CRYOGENIC ION VIBRATIONAL SPECTROSCOPY OF METAL COMPLEXES

By

Brett M. Marsh

A dissertation submitted in partial fulfillment of the requirements for the degree of

Doctor of Philosophy

(Chemistry)

at the

UNIVERSITY OF WISCONSIN-MADISON

2015

Date of final oral examination: 12/10/2015

The dissertation is approved by the following members of the Final Oral Committee:

Etienne Garand, Assistant Professor, Chemistry

F. Fleming Crim, Professor, Chemistry

John F. Berry, Professor, Chemistry

Timothy H. Bertram, Associate Professor, Chemistry

Edwin L. Sibert, Professor, Chemistry

CRYOGENIC ION VIBRATIONAL SPECTROSCOPY OF METAL COMPLEXES

Brett M. Marsh

Under the supervision of Professor Etienne Garand

at the University of Wisconsin-Madison

Metal complexes are involved in a wide variety of chemical transformations and processes vital to both industry and life. The study of the mechanisms of these transformations as well as the intermediate species involved is crucial to understanding and improving today's catalysts. However, the study of these species and their reactions is often complicated by the transient nature of the reactive intermediates involved. Furthermore, the nature of the solution phase means that there are typically several species present in a reaction mixture, further complicating the study of these species. In this work gas phase vibrational spectroscopy techniques are used to isolate and investigate catalytically relevant complexes.

In the first part of this work the behavior of hydrated MOH^+ clusters is investigated. These clusters, which serve to model interactions present in water oxidation intermediates, display a surprising dependence of the OH^- vibrational frequency on the identity of the metal center. This effect is attributed to a vibrational stark effect which is modulated by charge transfer between the OH^- moiety and metal center. Further solvation of the complexes is found to further modulate this shift.

In the second section we investigate the interactions present in a series of deprotonated glycine polypeptides as well as the behavior of two copper-glycine polypeptide complexes, one

of which, $[CuGly_4\text{-}4H]^{2-}$, has been shown to have catalytic activity in water oxidation reactions. In the case of the polypeptides the chain length is shown to have a significant influence on the interactions observed between the NH_2, COO^-, and amide N-H moieties. Surprisingly, the interaction between amide NH groups and the terminal NH_2 group is shown to have a profound effect on the stability and structure of the 3 and 4 residue peptides. In the case of the Cu-polypeptide complexes the peptide species bind to the copper in a planar fashion. Furthermore, the structure we observe for $[CuGly_4\text{-}4H]^{2-}$ is significantly different than that observed in previous solution phase studies.

Finally, we investigate the reaction of a platinum complex with methane. This reaction, which is an important step in the activation of alkane C-H bonds, is performed using our new cryogenic reaction trap. The resulting vibrational characterization shows that we have isolated the elusive σ-CH intermediate. This intermediate, which has been implicated in the selectivity of the C-H activation reaction, has never been directly observed in a reaction until now. The other postulated intermediate species, however, are not observed under these conditions.

Table of Contents

List of Figures

List of Tables

Acknowledgments

It is more likely than not that I owe my success in my studies to even more people than the ones I am about to list herein. To those people I acknowledge all of your contributions on my path to this point.

I should first thank my undergraduate mentor, Tim Zwier, and the graduate students I worked under, Evan Buchanan and Jacob Dean. Although they may not realize it they both taught how to (and sometimes how not to) approach graduate school. My graduate mentor my first year of grad school, Cornelia Heid, also contributed greatly to my growth as a scientist in the short time during which we worked together. My past and current coworkers in the Garand group have also helped me become a better scientist and mentor in so many ways. I am greatly indebted to them for that.

I must thank my first mentor in graduate school, F. Fleming Crim. Fleming's confidence in my scientific abilities was a very good thing to have when Cornelia and myself were replacing diffusion pump heaters once a month. His advice even after leaving his group has helped me immensely as I moved into a senior graduate student role and during my search for a postdoc.

I especially owe thanks to Etienne. When I first joined the Garand group I certainly felt intimidated by the thought of getting a lab running from nothing. With Etienne's guidance it felt as though I had been doing this my whole life. I especially owe him thanks for letting me pursue my own ideas in lab, whether it paid off (the MOH^+ clusters) or didn't quite work out (aminophenols).

I owe great thanks to my many friends I have made here and all over. I have to finish this thesis tonight so I couldn't possibly have the time to list them all but the support and advice they have given me over the years has been instrumental to my graduate career.

Finally, I must thank my family, and particularly Emma and Emily, for their unconditional support of my studies, even if they may not have the best grasp on the work I do. I am indebted to them for this.

On a final note, I am very excited to see the work that follows my departure. In the capable hands of all my lab mates I think the lab is going to do some truly remarkable things in the coming years.

Chapter 1

Introduction

Metal containing complexes play an important role in catalysis, synthetic chemistry, and biological systems. In particular, ionic metal-ligand complexes are important intermediates in a number of reactions including C-H activation,[1, 2] H_2O activation,[3, 4] and CO_2 reduction.[5, 6] The economic importance of catalysis has led to a great deal of scientific interest in the mechanisms and design of catalytic species. However, the mechanisms by which these complexes catalyze reactions are still unclear for most systems. This is made even more complicated by the questions about the roles of electron configuration and spin on the reactivity of catalytic species. Thus, characterizing the reaction pathways of these catalysts experimentally is an important problem in chemistry.

Theoretical studies of catalytic complexes are often complicated by the electronic structure of metal ions. Transition metals typically have large spin-orbit coupling, and can exist in high spin or low spin state depending on the local ligand environment. These spin states can also exhibit drastically different reactivity. In terms of performing accurate calculations, these open shell species must be calculated using either restricted open shell or unrestricted methods. In the case of unrestricted methods spin contamination can cause significant errors in the resulting values while restricted open shell methods are computationally expensive. The use of multireference methods to study these compounds is also limited in usefulness due to the computational cost of large systems. Thus, theoretical treatments alone are usually not sufficient in the study of these reactions and complexes.

Experimentally, solution phase spectroscopy measurements including UV/VIS,[3, 5, 7] infrared (IR)/ raman,[6, 8, 9] and electron paramagnetic resonance (EPR)[10]/nuclear magnetic resonance (NMR)[11] have been used to elucidate structures and reaction mechanisms, the measurements are often obscured by competing species in solution due to the lack of selectivity in these techniques. This is particularly troublesome when studying reaction pathways in which many intermediates may exist simultaneously. Furthermore, the most reactive species in the catalytic cycle may only exist transiently in the reaction mixture. This makes such species difficult to observe on the timescale of the experiment.

Mass spectrometry has been employed to overcome the issues of low number density and selectivity found in condensed phase experiments. However, the low volatility of most metal containing species makes them difficult to isolate in the gas phase. One common method used to produce these ions is laser desorption of a metal followed by entrainment of the resulting ions in a buffer gas.[12-15] While this method is capable of producing many simple complexes, the ligands that can be attached to the generated metal ions must be volatile or able to withstand the intense light used in the laser desorption process.[16] Therefore many species that are commonly studied in the solution phase cannot be generated with this technique.

To overcome this limitation, electrospray ionization (ESI) has been used to generate ions directly from solution.[17-19] Using ESI as the ion source allows for weakly bound complexes as well as complexes with fragile ligands to be preserved upon entering the gas phase.[20-27] Furthermore, ESI allows for direct abstraction of intermediates from a reaction mixture giving direct insight into the species present.[4, 28] While mass spectrometry is useful for providing information about masses of species in reactions as well as providing an isolated environment for

study, it does not provide sufficient detail about electronic structure or molecular geometry. In order to obtain these insights spectroscopic techniques must be employed.

While the low number densities in the gas phase preclude the use of typical absorption spectroscopy methods, there are many alternative techniques. In the case of ions, this can be accomplished by observing changes in the mass spectrum of a species due to photofragmentation upon irradiation. By integrating the intensity of the generated photofragments as a function of photofragmentation wavelength a spectrum can be generated. These photodissociation methods, which exploit the selectivity of mass spectrometry while providing structural information, have found use in a number of systems and have been implemented in numerous ways.

The energies of many covalent bonds are on the order of a UV/Vis photon which allows for single photon photodissociation. This results in linear spectra which can be compared to those produced by theoretical calculations. Furthermore UV/Vis spectroscopy is often used to study the species present in condensed phase reactions.[4, 7, 29] This means that meaningful comparisons can be made between the species observed in gas and condensed phases. However, the broadness associated with electronic transitions in the condensed phase limits their usefulness in structural determination. In the gas phase, spectra of some metal complexes can be reasonably resolved[30] but many complexes still show broad absorptions even when isolated.[26, 31, 32] Due to the short spin-orbit lifetimes of transition metals these broad bands may persist even at low temperatures.[33, 34] The loss of vibronic structure further complicates structural determination in these complexes. The need for a chromophore that can absorb accessible wavelengths of UV/Vis light also precludes the use of this technique on some systems such as non-aromatic peptides.

IR spectroscopy is an attractive option to study these ionic complexes due to the detailed structural information inherent in the spectrum collected. The IR region of the spectrum can generally be well resolved within the gas phase as well. However, the lower energies of IR photons are typically insufficient to fragment most species aside from weakly bound complexes. One method to overcome this is to bombard the ions of interest with a high flux of IR photons to induce multiphoton absorption events which lead to fragmentation.[35, 36] While this method is effective at generating spectra, the photon fluxes required are very high compared to other experiments. For example, to dissociate a methane C-H bond (bond dissociation energy = 35,700 cm^{-1}) would require 12 photons at the energy of the IR active C-H stretching mode (3019 cm^{-1}) or 28 photons corresponding to the energy of the lowest frequency bending mode (1306 cm^{-1}). Such photon fluxes require a bright light source such as a free-electron laser or synchrotron light source which makes doing such experiments very costly in terms of time. The inherent non-linearity of the multiphoton process also makes the resulting spectra difficult to compare to theoretical results.

Another experimental approach is to couple IR and UV/Vis photons to obtain a photofragmentation spectrum.[34, 37] This technique has some advantages over multiphoton techniques including the possibility of isomer selectivity and linear intensity spectra, but much like the pure UV/Vis techniques, this method requires a chromophore that absorbs in the accessible region. While this is feasible for most systems it does prevent the technique from being universally applicable.

A final method to overcome these challenges is predissociation spectroscopy, in which a weakly bound "messenger" species is removed from a complex by absorption of photons, typically in the IR energy range.[15, 38-41] By adding a weakly bound "tag" ion or molecule, such as

Ar or H_2, the complex can be dissociated with one IR photon.[42-44] While such adducts are readily formed in the cold conditions found in a supersonic expansion, ESI generated ions are typically formed near room temperature. To overcome this challenge the ions can be trapped and cryogenically cooled to allow attachment of very weakly bound (D_0 ~ 400 cm^{-1}) tags such as H_2. The low binding energy of such tags allows for spectra to be taken even in the low frequency "fingerprint region" (600 cm^{-1} -1500 cm^{-1}) of the spectrum. This technique generates cold and linear spectra which allow direct comparison to theoretical calculations.

In this work three types of systems are discussed. In the first section, Chapter 3, the spectroscopy of $MOH(H_2O)^+$ complexes (where M=Mn-Zn) is used to investigate charge transfer between the metal center and the OH^- ligand. The results show that the OH^- vibrational frequency is dependent on the electric field generated by the metal center, which is in turn dependent upon the amount of charge transferred between the metal and OH^-. Solvation further modulates both of these effects. These systems serve as models for the study of interactions found commonly in water oxidation catalysts and their intermediates.

In Chapter 4 hydrogen bonding interactions are studied using peptide systems. In section 4.1 the changing hydrogen bonding interactions induced by lengthening a peptide chain are explored using $[Gly_n\text{-}H]^-$ (n=1-4) peptides. These peptides serve as a model system for a typical peptide backbone. In section 4.2 tri- and tetraglycine peptides are coordinated to a Cu^{2+} metal center to investigate the effect of metal ions on peptide structure. In these systems the peptide is constrained by the Cu^{2+} center. This results in a planar structure for both of the oligoglycine peptides. The $[Cu(Gly)_4]^{2-}$ complex is especially of interest due to its reported activity as a water oxidation catalyst.[3]

In Chapter 5 the reaction of the platinum complex $[Pt(en)Cl]^+$ (en=ethylenediamine) with methane is explored. This reaction, which is important in C-H activation, has been the subject of several mechanistic studies. Here, we observe the so called "σ-CH" intermediate which has been implicated in the selectivity and rate of this reaction. We do not, however, observe any evidence of additional intermediates.

1.1 Predissociation Spectroscopy

1.1.1Principles of IR Predissociation Spectroscopy

IR spectroscopy is commonly used to probe the vibrational motion of atoms contained within a molecule or ion. In a typical experiment the fraction of IR light absorbed (A) by a sample is monitored and related to the absorption of a particular mode by the Beer's law:

$$A = \log\left(\frac{I}{I_0}\right) = \varepsilon b C \qquad \text{(eq. 1.1)}$$

where b is the sample path length, C is the concentration of the sample and ε is the extinction coefficient. The extinction coefficient is directly related to the absorption cross section of the mode with which it is associated. In the solution phase the number densities of the analyte species are typically very large which gives rise to a noticeable change in the light transmitted through a sample. However in many gas phase experiments the number density of molecules or ions is too low to observe a change in light intensity. In the case of ions electrostatic repulsion may result in an ion packet of thousands of ions compared to the 10^{12}-10^{16} photons present in a laser pulse. Thus a different scheme is needed to observe IR absorption in these cases.

The experiments in the following chapters utilize a type of predissociation spectroscopy known as cryogenic ion vibrational spectroscopy (CIVS) to overcome this problem. In these experiments a weakly bound D_2 tag molecule is placed onto cold ions which are then irradiated with light in the range of 600 cm^{-1} to 4000 cm^{-1}. When a photon is absorbed, the molecule undergoes statistical intramolecular vibrational energy redistribution on the order of picoseconds to nanoseconds, which eventually results in loss of the D_2 tag species. The resulting

photofragments intensities are collected in mass spectra for each wavelength and integrated to make an IR absorption spectrum.

The fragmentation behavior of the D_2 adducts can be described using the unimolecular reaction theory of Rice, Ramsberger, Kassel, and Marcus (known as RRKM theory), where the energy dependent rate constant ($k(\epsilon)$) is given by the equation

$$k(\epsilon) = \frac{N(\epsilon-\epsilon_0)}{h\rho(\epsilon)} \qquad \text{(eq. 1.2)}$$

where $N(\epsilon - \epsilon_0)$ is the number of states between energy ϵ and ϵ_0 (the barrier height of the reaction), h is Planck's constant, and $\rho(\epsilon)$ is the density of states at energy ϵ. If the vibrational energy levels of the system are known, the $N(\epsilon - \epsilon_0)$ and $\rho(\epsilon)$ terms can be calculated using a number of algorithms with the most common being that of Beyer and Swinehart.[45] In the case of photodissociation the binding energy of the photofragments can be substituted for the barrier height.

An example calculation of the unimolecular reaction rate for different tag binding energies of the complex $[PtCl(NH_3)_2OH_2]^+ \cdot D_2$ is shown in figure 1.1. The vibrational frequencies used were obtained from a harmonic frequency calculation on an optimized molecular geometry. The rate of dissociation of the complex must be on the order of the ion flight time between the laser and reflectron (~20 μs) in order to see photofragmentation signal upon photoexcitation. Due to the small binding energy of the D_2 tag to the ion (~400 cm^{-1}), even a 400 cm^{-1} photon is sufficient to induce photodissociation on the experimental timescale.

Once the spectra have been collected they are analyzed and assigned using *ab-initio* or density functional theory (DFT) electronic structure calculations. To perform these calculations

an optimized structure is found and the vibrational frequencies are calculated within the harmonic approximation. These frequencies are then compared to the experimental spectrum to assign a structure to the species of interest.

1.1.2 The Harmonic Oscillator Model and Vibrational Selection Rules

To simplify the calculation of vibrational energies the internuclear potential term of the Hamiltonian can be assumed to be harmonic with the form

$$V = \frac{1}{2}k(r - r_e) \quad \text{(eq 1.3)}$$

where k is a constant and r_e is the equilibrium bond length. The resulting wavefunctions upon solving the Schrodinger equation are

$$\psi_v = N_v H_v e^{-\frac{\sqrt{\mu k}(r-r_e)^2}{2\hbar}} \quad \text{(eq 1.4)}$$

where N_v is a normalization constant, H_v is the appropriate Hermite polynomial, and μ is the reduced mass of the vibrating atoms defined as

$$\mu = \frac{m_1 m_2}{m_1 + m_2} \quad \text{(eq 1.5)}$$

where m_1 and m_2 are the masses of the respective atoms. The resulting energy levels are

$$E_v = \left(v + \frac{1}{2}\right)h\nu \quad \text{(eq 1.6)}$$

with ν defined as:

$$\nu = \frac{1}{2\pi}\sqrt{\frac{k}{\mu}} \quad \text{(eq 1.7)}$$

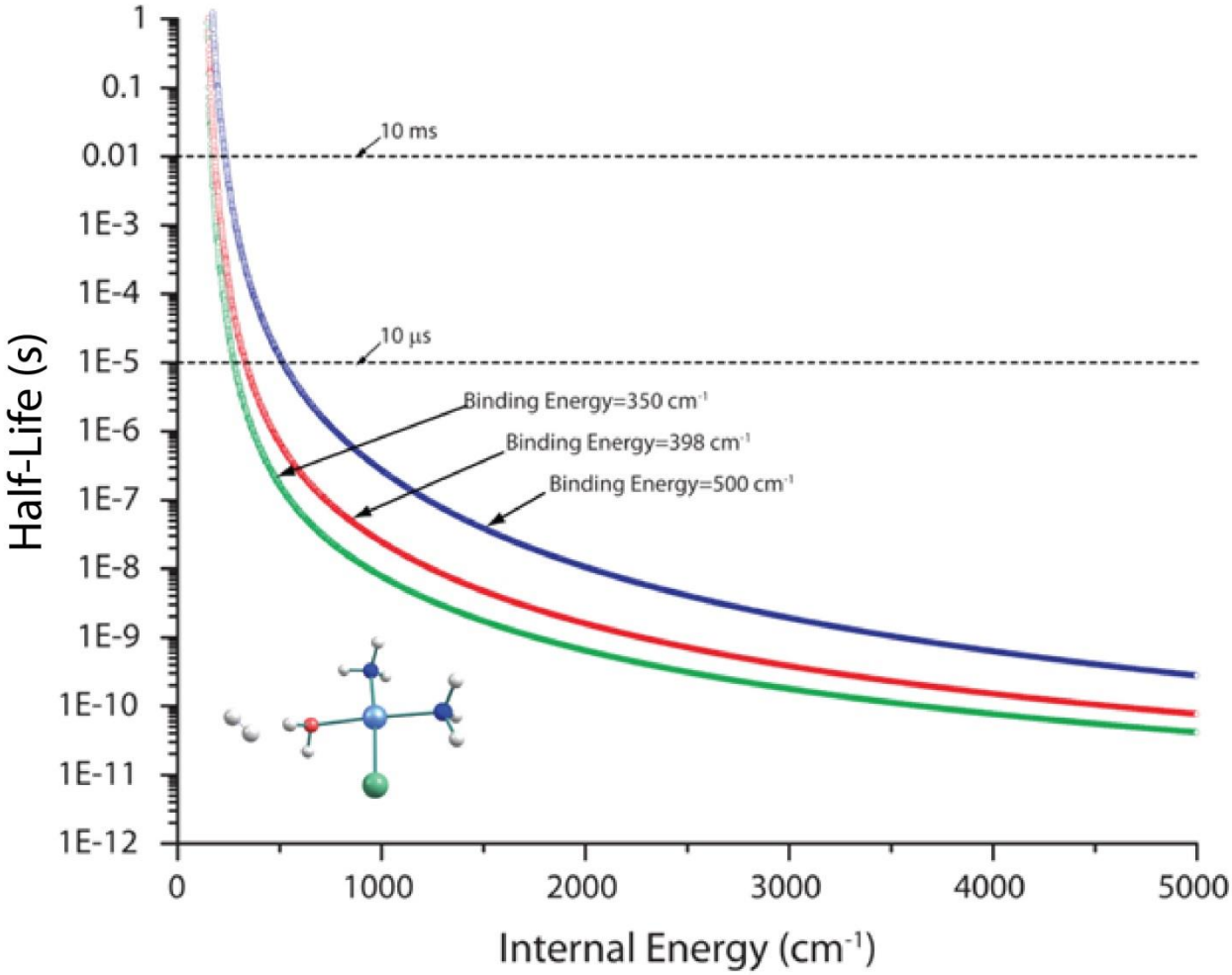

Figure 1.1-Results of RRKM calculations for the lifetimes of $[PtCl(NH_3)_2OH_2]^+ \cdot D_2$ as a function of ion internal energy for different binding energies of the D_2 tag. The line corresponding to 10 ms indicates the minimum half-life needed to perform the experiment. The line corresponding to 10 μs corresponds to the maximum half-life that produces observable photodissociation

Within this framework the selection rules for a vibrational transition can be derived. The intensity of absorption is related to the transition dipole moment (μ_v) by the equation

$$\mu_v = \langle \psi_v | \vec{\mu} | \psi_v' \rangle \quad \text{(eq 1.8)}$$

where $\vec{\mu}$ is the molecular dipole moment. $\vec{\mu}$ can be expanded in terms of the $(r - r_e)$ coordinates as

$$\vec{\mu} = \mu_{r_e} + \left(\frac{\partial \mu}{\partial r}\right)_{r_e} (r - r_e) + \cdots \quad \text{(eq 1.9)}$$

By inserting equation 1.8 and 1.3 into equation 1.8 it can be shown that μ_v is only non-zero for $\Delta v = \pm 1$. Furthermore, due to the presence of the $\left(\frac{\partial \mu}{\partial r}\right)_{r_e}$ term absorptions can only be observed for vibrations which induce a change in the molecular dipole moment.

Although nominally forbidden, in some systems overtone and combination bands can be observed.[46, 47] This is particularly noticeable in systems which are very anharmonic, such as water clusters.[48]

References:

1. J. A. Labinger and J. E. Bercaw, *Nature*, 2002, **417**, 507-514.

2. H. Heiberg, O. Swang, O. B. Ryan and O. Gropen, *The Journal of Physical Chemistry A*, 1999, **103**, 10004-10008.

3. M. T. Zhang, Z. F. Chen, P. Kang and T. J. Meyer, *Journal of the American Chemical Society*, 2013, **135**, 2048-2051.

4. D. E. Polyansky, J. T. Muckerman, J. Rochford, R. Zong, R. P. Thummel and E. Fujita, *Journal of the American Chemical Society*, 2011, **133**, 14649-14665.

5. J. M. Smieja, M. D. Sampson, K. A. Grice, E. E. Benson, J. D. Froehlich and C. P. Kubiak, *Inorganic Chemistry*, 2013, **52**, 2484-2491.

6. C. Matlachowski, B. Braun, S. Tschierlei and M. Schwalbe, *Inorganic Chemistry*, 2015, **54**, 10351-10360.

7. S. M. Barnett, K. I. Goldberg and J. M. Mayer, *Nat Chem*, 2012, **4**, 498-502.

8. J. D. Froehlich and C. P. Kubiak, *Journal of the American Chemical Society*, 2015, **137**, 3565-3573.

9. P. Christensen, A. Hamnett, A. V. G. Muir and J. A. Timney, *Journal of the Chemical Society, Dalton Transactions*, 1992, DOI: 10.1039/DT9920001455, 1455-1463.

10. N. V. Nagy, T. Szabó-Plánka, A. Rockenbauer, G. Peintler, I. Nagypál and L. Korecz, *Journal of the American Chemical Society*, 2003, **125**, 5227-5235.

11. L. Johansson, M. Tilset, J. A. Labinger and J. E. Bercaw, *Journal of the American Chemical Society*, 2000, **122**, 10846-10855.

12. J. M. Lisy, *International Reviews in Physical Chemistry*, 1997, **16**, 267-289.

13. A. D. Brathwaite, T. B. Ward, R. S. Walters and M. A. Duncan, *Journal of Physical Chemistry A*, 2015, **119**, 5658-5667.

14. K. S. Molek, T. D. Jaeger and M. A. Duncan, *Journal of Chemical Physics*, 2005, **123**.

15. J. M. Weber, *International Reviews in Physical Chemistry*, 2014, **33**, 489-519.

16. T. M. Ayers, B. C. Westlake, D. V. Preda, L. T. Scott and M. A. Duncan, *Organometallics*, 2005, **24**, 4573-4578.

17. J. B. Fenn, *Angewandte Chemie International Edition*, 2003, **42**, 3871-3894.

18. L. Batiste and P. Chen, *Journal of the American Chemical Society*, 2014, **136**, 9296-9307.

19. T. E. Hofstetter, C. Howder, G. Berden, J. Oomens and P. B. Armentrout, *J. Phys. Chem. B*, 2011, **115**, 12648-12661.

20. J. W. DePalma, P. J. Kelleher, C. J. Johnson, J. A. Fournier and M. A. Johnson, *Journal of Physical Chemistry A*, 2015, **119**, 8294-8302.

21. E. Garand, M. Z. Kamrath, P. A. Jordan, A. B. Wolk, C. M. Leavitt, A. B. McCoy, S. J. Miller and M. A. Johnson, *Science*, 2012, **335**, 694-698.

22. E. Garand, J. A. Fournier, M. Z. Kamrath, N. D. Schley, R. H. Crabtree and M. A. Johnson, *Physical Chemistry Chemical Physics*, 2012, **14**, 10109-10113.

23. A. Kamariotis, O. V. Boyarkin, S. R. Mercier, R. D. Beck, M. F. Bush, E. R. Williams and T. R. Rizzo, *Journal of the American Chemical Society*, 2006, **128**, 905-916.

24. M. J. DiTucci, S. Heiles and E. R. Williams, *Journal of the American Chemical Society*, 2015, **137**, 1650-1657.

25. M. H. Stockett, L. Musbat, C. Kjaer, J. Houmoller, Y. Toker, A. Rubio, B. F. Milne and S. Brondsted Nielsen, *Physical Chemistry Chemical Physics*, 2015, **17**, 25793-25798.

26. S. Xu and J. M. Weber, *The Journal of Physical Chemistry A*, 2015, DOI: 10.1021/acs.jpca.5b10488.

27. M. Katari, E. Payen de la Garanderie, E. Nicol, V. Steinmetz, G. van der Rest, D. Carmichael and G. Frison, *Physical Chemistry Chemical Physics*, 2015, **17**, 25689-25692.

28. J. A. Fournier, A. B. Wolk and M. A. Johnson, *Analytical Chemistry*, 2013, **85**, 7339-7344.

29. N. Mirbagheri, D. Wang, C. Peng, J. Wang, Q. Huang, C. Fan and E. E. Ferapontova, *ACS Catalysis*, 2014, **4**, 2006-2015.

30. Y. Inokuchi, T. Ebata and T. R. Rizzo, *The Journal of Physical Chemistry A*, 2015, **119**, 8097-8105.

31. J. C. Marcum and J. M. Weber, *The Journal of Chemical Physics*, 2009, **131**, 194309.

32. M. H. Stockett and S. Brøndsted Nielsen, *The Journal of Chemical Physics*, 2015, **142**, 171102.

33. L. Ferrand, S. Soorkia, G. Gregoire, M. Broquier, B. Soep and N. Shafizadeh, *Physical Chemistry Chemical Physics*, 2015, **17**, 25693-25699.

34. J. C. Dean, N. L. Burke, J. R. Hopkins, J. G. Redwine, P. V. Ramachandran, S. A. McLuckey and T. S. Zwier, *The Journal of Physical Chemistry A*, 2015, **119**, 1917-1932.

35. N. C. Polfer and J. Oomens, *Mass Spectrometry Reviews*, 2009, **28**, 468-494.

36. B. Chiavarino, M. E. Crestoni, S. Fornarini, D. Scuderi and J.-Y. Salpin, *Journal of the American Chemical Society*, 2013, **135**, 1445-1455.

37. T. R. Rizzo, J. A. Stearns and O. V. Boyarkin, *International Reviews in Physical Chemistry*, 2009, **28**, 481-515.

38. M. F. Vernon, D. J. Krajnovich, H. S. Kwok, J. M. Lisy, Y. R. Shen and Y. T. Lee, *The Journal of Chemical Physics*, 1982, **77**, 47-57.

39. A. B. Wolk, C. M. Leavitt, E. Garand and M. A. Johnson, *Accounts of Chemical Research*, 2014, **47**, 202-210.

40. M. A. Duncan, *International Reviews in Physical Chemistry*, 2003, **22**, 407-435.

41. J. T. O'Brien and E. R. Williams, *The Journal of Physical Chemistry A*, 2008, **112**, 5893-5901.

42. M. Z. Kamrath, E. Garand, P. A. Jordan, C. M. Leavitt, A. B. Wolk, M. J. Van Stipdonk, S. J. Miller and M. A. Johnson, *Journal of the American Chemical Society*, 2011, **133**, 6440-6448.

43. C. J. Johnson, A. B. Wolk, J. A. Fournier, E. N. Sullivan, G. H. Weddle and M. A. Johnson, *The Journal of Chemical Physics*, 2014, **140**, 221101.

44. T. D. Vaden, J. M. Lisy, P. D. Carnegie, E. Dinesh Pillai and M. A. Duncan, *Physical Chemistry Chemical Physics*, 2006, **8**, 3078-3082.

45. T. Beyer and D. F. Swinehart, *Commun. ACM*, 1973, **16**, 379.

46. D. P. Tabor, R. Kusaka, P. S. Walsh, E. L. Sibert and T. S. Zwier, *The Journal of Physical Chemistry Letters*, 2015, **6**, 1989-1995.

47. P. D. Carnegie, A. B. McCoy and M. A. Duncan, *The Journal of Physical Chemistry A*, 2009, **113**, 4849-4854.

48. A. B. McCoy, *The Journal of Physical Chemistry B*, 2014, **118**, 8286-8294.

Chapter 2

Experimental Details

2.1 Overview

The experimental apparatus (Shown in figure 2.1) is based upon the Yale photofragment spectrometer in the lab of Mark Johnson[1] and has undergone several modifications since being constructed in the spring of 2013. Improvements on the initial design include upgrades to the time-of-flight region as well as different versions of an accumulation and reaction trap preceding the primary 10K cold ion trap. Presented here is the most recent version of the machine incorporating a dual cold trap configuration which was assembled in September of 2015.

The species of interest in the experiment is produced *via* electrospray ionization (ESI)[2] of a solution containing the relevant ion or its precursor. The generated ions are introduced to the vacuum chamber through a ~0.3 mm ID capillary and guided through three differentially pumped stages into an octopole trap attached to the cold head of a liquid nitrogen cryostat. The ions are then extracted into a 3D quadrupole (Paul) trap attached to the cold finger of a liquid helium cryostat and cooled to 10 K. In this trap, buffer gas consisting of D_2 in He is pulsed into the trap and $M(D_2)_n$ adducts are formed. The front and back faces of the ion trap are pulsed at 10 Hz to extract the ions into a time-of-flight (TOF) region where the ions are mass selected using a gated deflector and then intersected with the output of a tunable OPO/OPA infrared light source to induce photodissociation. The parent and photofragments are then separated in a two-stage reflectron and impinged upon a multi-channel plate (MCP) detector. By monitoring the photofragment yield as a function of laser wavelength an infrared spectrum can be obtained.

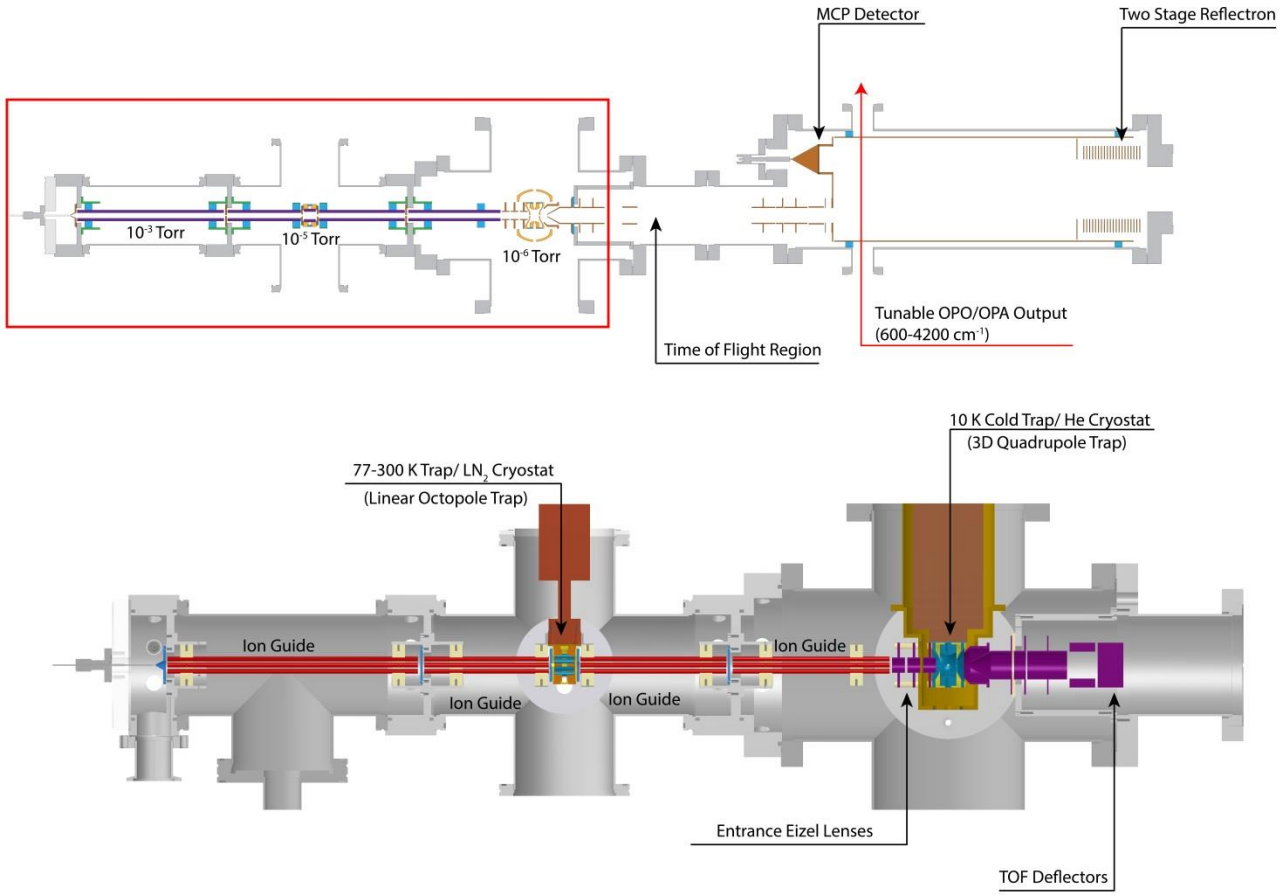

Figure 2.1- Experimental Apparatus. The top panel displays and overhead view of the instrument which includes the time of flight region of the machine. The bottom is a close-up side on view of the region outlined in the top figure which shows both the ion traps in the instrument. A section of the time of flight region has been removed from the top figure to save space.

2.2 Ion Source

The ionic species probed in the experiments described are generated by electrospray ionization of a solution containing the appropriate precursor. Typical solvents used include water, methanol, and acetonitrile. The solutions are placed in a Hamilton gas-tight syringe and fed through a 30 μm ID fused silica capillary (New Objective) at a rate of ~1-3 μL/min. The generated ions are introduced, by a 0.3 mm ID stainless steel capillary, to the first vacuum region held at 3 Torr. The capillary is mounted in a compression fitting which allows for adjustment and cleaning of the capillary without venting the chamber. The ions then pass through a skimmer to a second differentially pumped region, which is pumped by a 15 l/s mechanical pump to maintain a pressure on the order of 100 mTorr. The ions are guided by hexapole ion guides powered by RF supplies based on the design of O'Connor and coworkers.[3,4] It is important to note that changing the bias of the RF guide in this high pressure region can result in fragmentation of the species being studied. This voltage dependence is particularly useful when generating metal complexes of differing coordination such as the $MOH^+(H_2O)_n$ complexes described in chapter three.

After passing through a floated aperture, the ions arrive in the third stage of the chamber. This stage is pumped by a 300 l/s turbomolecular pump and held at an operating pressure of 10^{-4} Torr. Here the ions are guided by another hexapole guide into the first cooled accumulation trap.

2.3 Reaction Trap Region

The generated ions are collected in an accumulation trap mounted to a liquid nitrogen cryostat (Janis Research Company, VPF 100) in the 10^{-4} Torr region of the spectrometer. The ion trap is mounted on the cryostat using a thermally conductive ceramic to provide electrical

insulation. The trap itself consists of two copper apertures on either end of a copper octopole ion guide. The first aperture is held at a fixed DC voltage while the voltage of the exit aperture is pulsed to either trap or extract the ions at a rate of 10 Hz. Typically ions are held in the trap for 5-10 ms. To maintain alignment between the ion trap and hexapole ion guides upon cooling the cryostat, the ends of the entrance and exit ion guides are mated to the trap assembly.

The ions are collisionally cooled by a buffer gas (typically helium) thermalized to the temperature of the cryostat (variable from 77 K to 300 K). The buffer gas is typically pulsed in 1-2 ms after the start of the trapping cycle to give the maximum ion number densities. By adding small amounts of volatile solvents such as water, methanol, acetone, or acetonitrile to the buffer gas, the cooled ions can be solvated. Typically only a few drops of solvent is needed in the gas line to produce significant clustering. An example of the solvation of $GlyglyH^+$ by water is shown in figure 2.2. The largest amount of clustering is observed when the buffer gas is injected into the trap roughly 1-2 ms before the ions are extracted from the reaction trap. The delay between the gas pulse and extraction of the ions is somewhat dependent on the settings used. Higher voltages on the entrance aperture tend to increase clustering while a lower trap bias voltage will also give rise to larger clusters. Care must be used in generating the clusters as an overabundance of solvent can induce trap icing. It is also important to pump out the trap gas lines before switching solvents as even small amounts of solvent presence can lead to clustering. While previous work has shown that sizeable water clusters can be generated for select species using ESI,[5-7] this method is capable of producing significant hydration networks around even hydrophobic species.

The cooled reaction trap has also been utilized for gas phase ion-molecule reactions. In figure 2.3 the mass spectra of the $[Pt(en)Cl]^+$ complex are presented in the absence (B) and

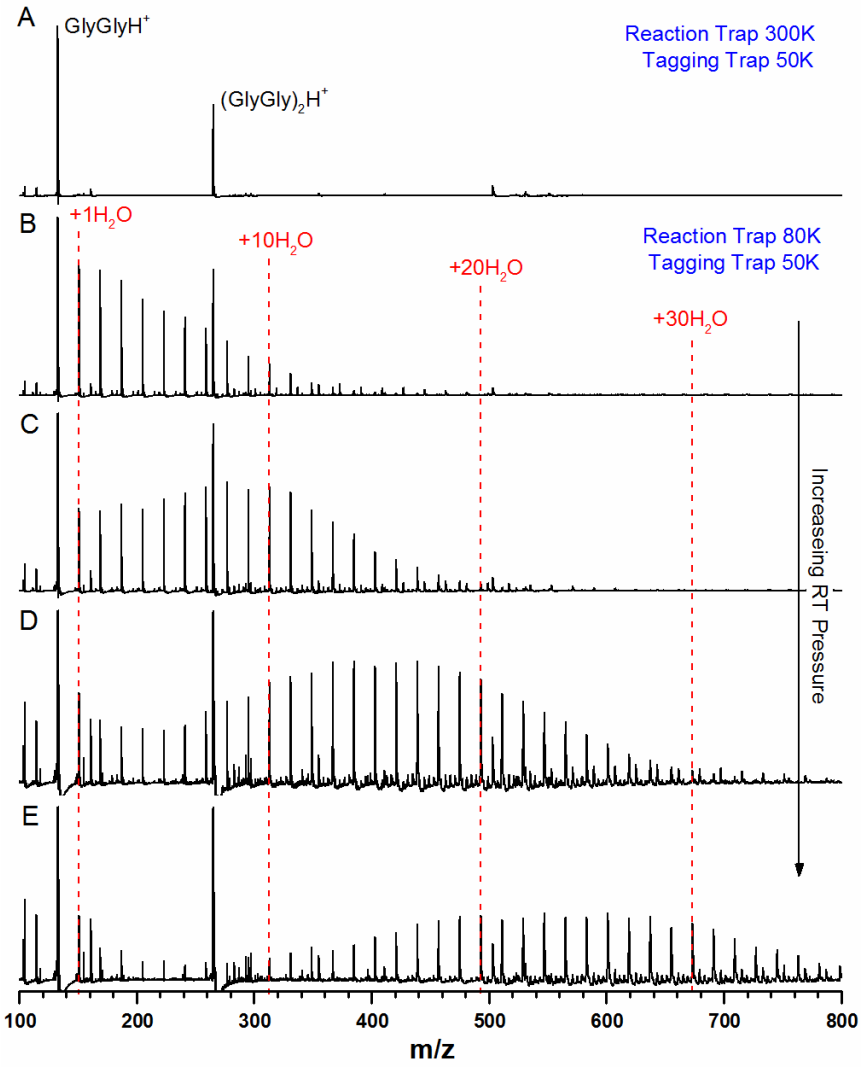

Figure 2.2- Mass spectra of $GlyGlyH^+$ with water seeded He buffer gas with the reaction trap at 300 K (A) and 50 K (B-E). As the pressure of the He/H_2O buffer gas is increased at 80 K the number of water adducts formed also increases.

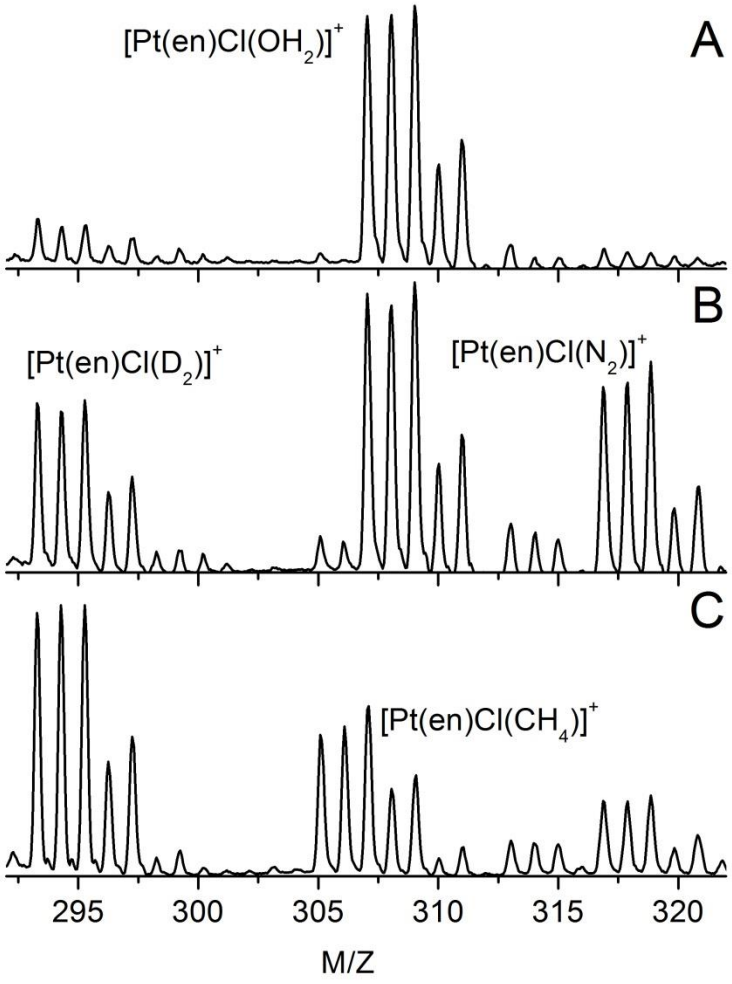

Figure 2.3- Mass spectra of $[Pt(en)Cl(X)]^+$ species under different conditions with a reaction trap temperature of 77 K and a tagging trap temperature of 35 K. In panel A the settings are such that minimal fragmentation is observed. In B the ions are significantly fragmented and in panel C the fragmented ions are exposed to a CH_4/He buffer gas, producing the desired $[Pt(en)Cl(CH_4)]^+$ product. Due to the presence of D_2 in the tagging trap gas mix the $[Pt(en)Cl(D_2)]^+$ complex is formed under fragmentation conditions.

presence (C) of methane gas at 77 K reaction trap temperature. The addition of methane causes significant conversion of $[Pt(en)Cl]^+$ to $[Pt(en)Cl(CH_4)]^+$ in the trapping region. As in the case of solvation, the most complete conversion is observed with the gas injection occurring slightly before ion ejection. It is also important to consider the boiling point and melting point of the neutral species used in the reaction to avoid icing of the reaction trap.

2.4 Main Trap Region

From the reaction trap, the ions are channeled through a hexapole guide into a region of the machine pumped by an 800 l/s turbomolecular pump. In this region is the 3D quadrupole "tagging" trap which is mounted to the cold head of a liquid helium cryostat.[8,9] The temperature of the ion trap can be varied from 4 K to 300 K using a cartridge heater and silicon diode to monitor the temperature. An aluminum radiation shield encloses the entire trap assembly to further aid in cooling. Due to thermal contraction and expansion, the entire cryostat is mounted on a linear translation stage to maintain alignment between the trap and the entrance ion guide and TOF optics.

The trap is typically held at 10 K while a He/D_2 buffer gas is injected into the trap. Ions are thermalized by collisions with the buffer gas and upon cooling the ions form adducts with the D_2 molecules present in the gas[39] as shown in figure 2.4. Although the buffer gas is pulsed in immediately after the end of the previous cycle, ions are not extracted from the trap typically until 90-100 ms after the cycle begins. Shorter holding times typically result in less satisfactory ion signal and less D_2 tagging.[10] At the end of the tagging cycle the endcaps of the 3D quadrupole ion trap are used as *de facto* Wiley-McLaren[11] plates and pulsed to extract the ions into the TOF region.

2.5 Time-of-Flight Region

The ions first pass through a grid electrode held at the TOF liner voltage (~1950V) and then are introduced into the first region of the TOF *via* a 3mm aperture. In this meter long flight tube the focus and position of the ion beam is controlled by two sets of einzel lenses and deflectors. The last deflector is used as a mass gate, and pulsed from the liner voltage to a lower voltage to select ions of a specific m/z for photofragmentation.

Once mass selected, the ions of interest are irradiated with the tunable output of an IR OPO/OPA laser (LaserVision) pumped by the 1064 nm output of a Nd:YAG laser (Continuum laser). In the event of a resonance between the laser frequency and a vibration in the molecule, an IR photon is absorbed and vibrational energy is redistributed throughout the ion which ultimately leads to ejection of a D_2 messenger tag (figure 2.5). The parent and fragment ions are separated in a two-stage reflectron at the end of the time-of-flight tube and impinged upon a micro-channel plate detector. Monitoring the formation of these photofragments as a function of the laser wavelength gives the resulting IR spectrum (figure 2.6).

2.6 Laser System

The laser setup used in the experiments described is a commercially available table-top laser system consisting of a Contiuum Powerlite Nd:YAG pump laser pulsed at 10 Hz and a LaserVision OPO/OPA which generates IR light in the range of 600 cm^{-1} to 4500 cm^{-1}. The laser output is guided into a purged enclosure which removes CO_2 and H_2O from the beam path and focused using a set of spherical mirrors. From here the beam is sent through a periscope and reflected onto a third spherical mirror which focuses the beam into the chamber. After passing

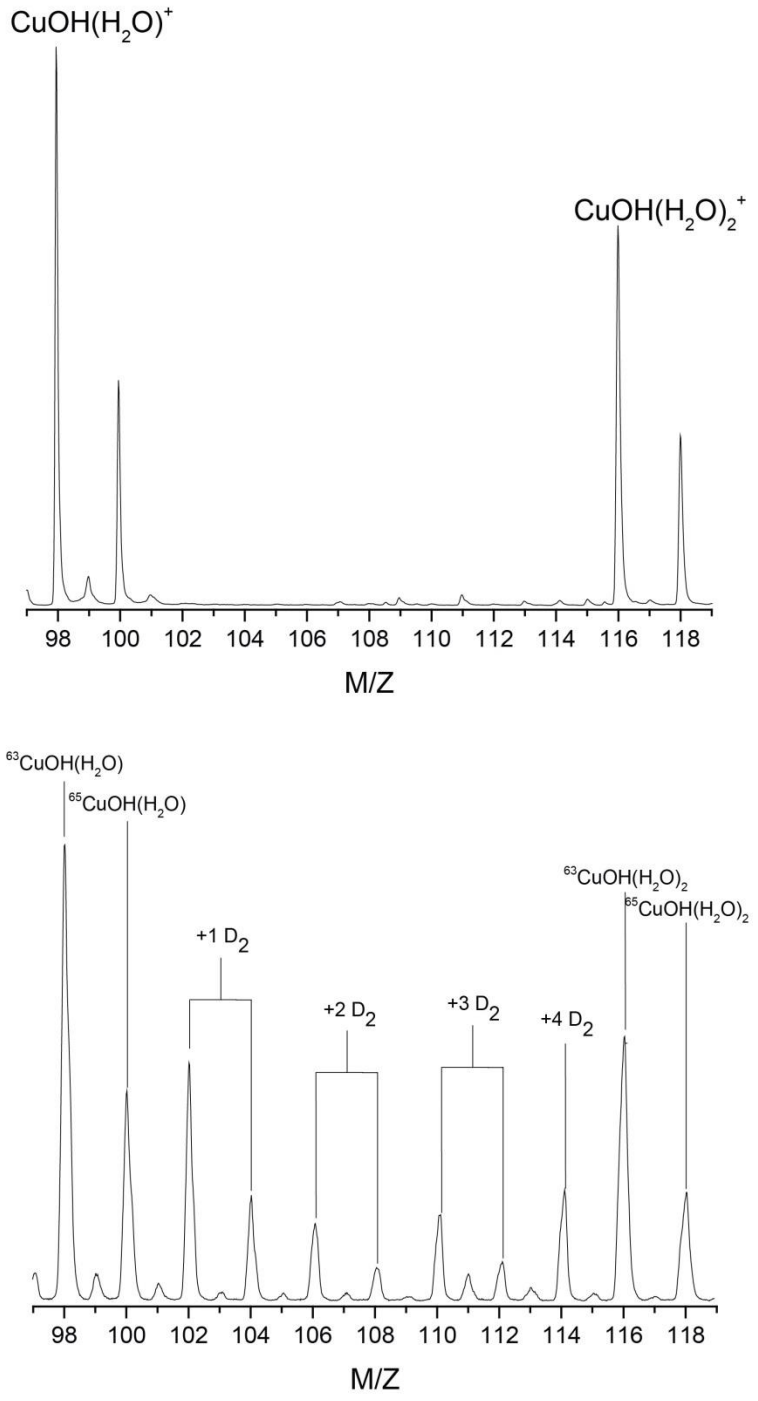

Figure 2.4- Mass spectra of $CuOH(H_2O)_n^+$ complexes at 10 K in the absence (top) and presence (bottom) of D_2 gas.

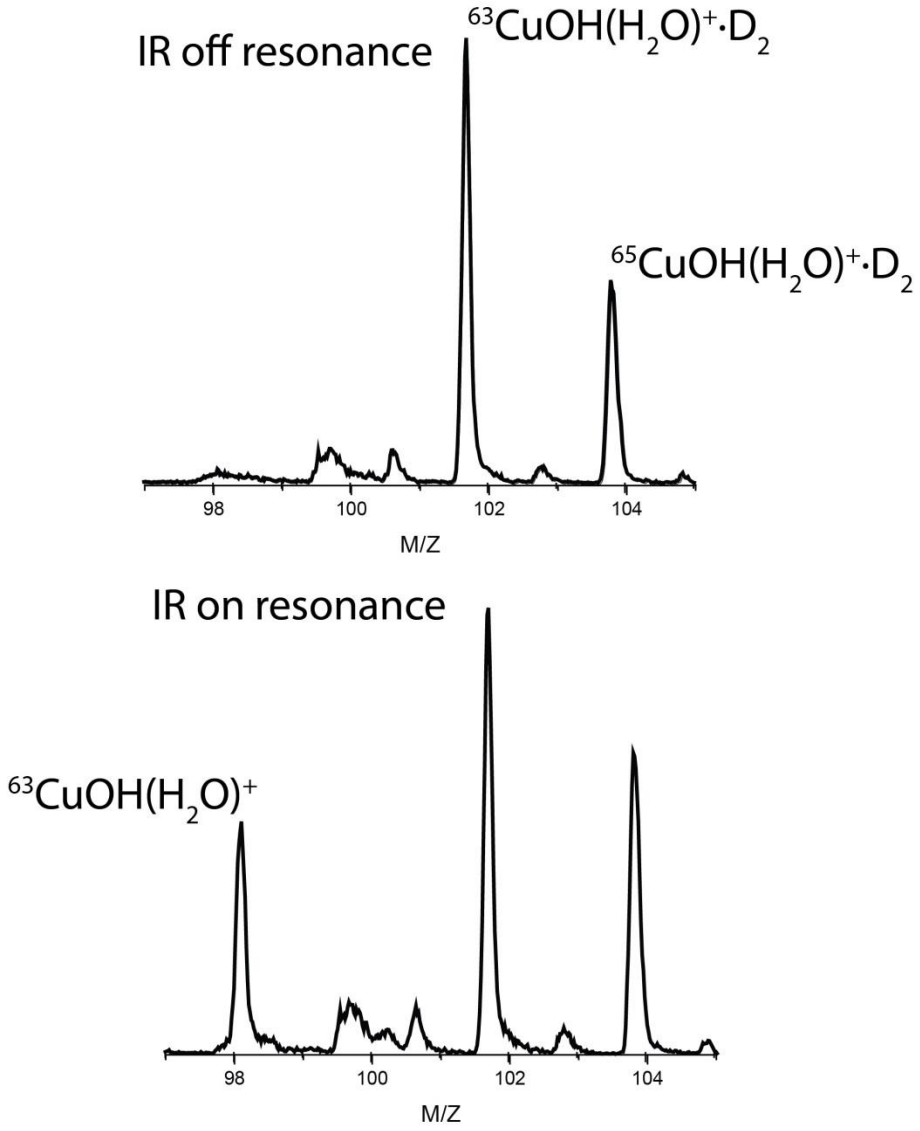

Figure 2.5- Mass spectra of $CuOH(H_2O)^+ \cdot D_2$ with the IR laser off resonance (top) and on resonance (bottom) showing the formation of the $^{63}CuOH(H_2O)^+$ photofragment.

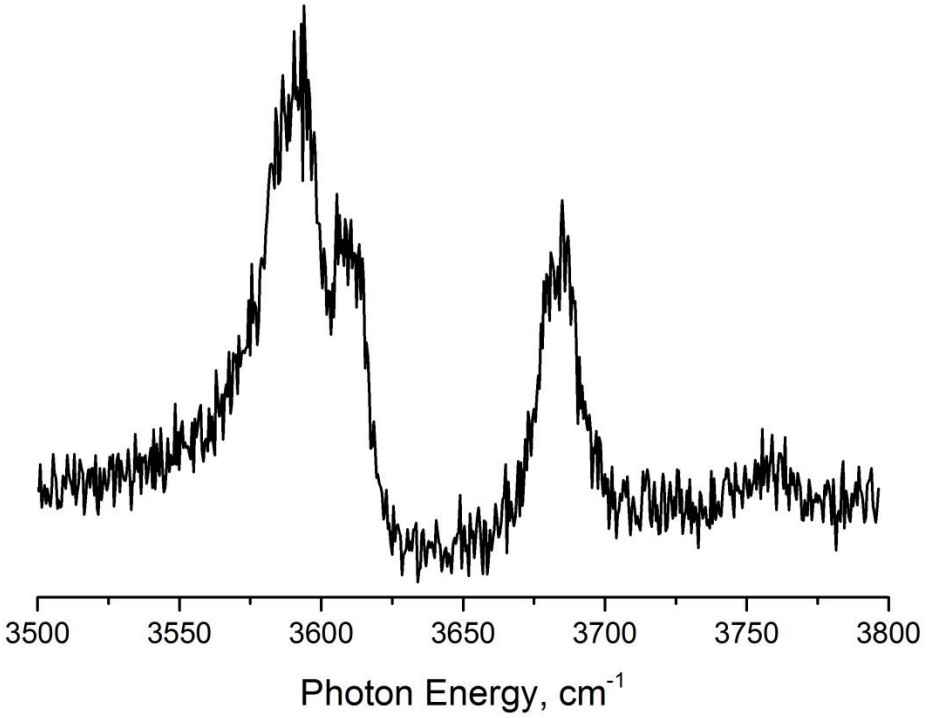

Figure 2.6- IR predissociation spectrum of $CuOH(H_2O)^+ \cdot D_2$ in the free OH stretching region

through the chamber the beam impinges upon a power meter to record a power curve for the scan.

The OPO/OPA generates light by splitting the 1064 nm (ω_0) input beam into two legs. In the first leg the 1064 nm light is passed through a $\lambda/4$ waveplate and into a β-barium borate (BBO) crystal for second harmonic generation of 532 nm ($2\omega_0$) light. This light is then passed into an OPO stage consisting of two potassium titanyl phosphate (KTP) crystals in an optical cavity. Here the 532 nm light is converted by an energy conserving process into two different wavelengths

$$2\omega_0 = \omega_s + \omega_i \quad \text{(eq 2.1)}$$

where ω_s and ω_I are known as the signal and idler frequency respectively. The signal, which is higher in frequency, and the idler are combined with the remaining split 1064 nm light and undergo conversion in the four KTP crystals of the OPA stage. In this stage the signal light and 1064 nm light are mixed and undergo a difference-frequency generation (DFG) process corresponding to the equation

$$\omega_{mid} = \omega_s - \omega_0 \quad \text{(eq 2.2)}$$

where ω_{mid} is between 2100 cm^{-1} and 4500 cm^{-1}. To obtain light only corresponding to the region from 2100 cm^{-1} to 4500 cm^{-1} the residual 1064 light is dumped from the beam path and the remaining light is sent through a polarized filter to remove the idler light and unconverted signal light. Typical power output in this region is ~30 mJ/pulse of 3900 cm^{-1} light.

Accessing the lower 600 cm^{-1} to 2400 cm^{-1} region requires removal of the output filter which removes idler light and insertion of a seventh silver gallium selenide (AgGaSe) crystal

into the optical path of the laser output. This crystal is positioned about one meter away from the OPO/OPA laser system in the purge box on the optical table to obtain good overlap between the ω_{mid} and ω_I outputs in the crystal . Once overlapped in the crystal the two beams interact to produce light by the DFG process

$$\omega_{far} = \omega_i - \omega_{mid} \quad \text{(eq 2.3)}$$

where ω_{far} is between 600 cm^{-1} and 2400 cm^{-1}. Residual light from this process is removed using either a ZnSe filter for the range of 1400 cm^{-1} to 2400 cm^{-1} or a 5.5 micron light filter for the range from 600 cm^{-1} to 1800 cm^{-1} directly after the AgGaSe crystal. Output power for this region are significantly lower than that of the 2100 cm^{-1} to 4500 cm^{-1} region with typical powers at 1594 cm^{-1} being 1.5 mJ/Pulse and 2 mJ/Pulse with the 5.5 micron or ZnSe filter, respectively. It is also important to note that due to the lack of a compensator crystal after the AgGaSe crystal, the beam path moves significantly at the extremes of the wavelength range.

2.7 Data Acquisition

The signal from the MCP detector is sent to a digital oscilloscope (PicoScope) which is connected to the data analysis computer. The mass spectrum and laser wavelength are recorded as the laser is scanned at 10 Hz using a homemade LabView program based around the Labview code provided with the PicoScope oscilloscope. The program consists primarily of a display panel that displays the signal from the oscilloscope and controls for the oscilloscope. The program in both mass spectrum and IR scan modes records the data that is displayed on the front panel of the program. The range of data that is displayed can be adjusted using the oscilloscope delay and sample width controls on the program front panel. Typically these settings can be set to reflect the time range displayed on the stand-alone oscilloscope. The voltage range control

should be set as to give the most dynamic range to the photofragment signal. This is typically slightly above the maximum observed signal. Within the file the scan type (MS or IR) is recorded for use with the analysis program.

The program communicates with the computer controlling the OPO/OPA system to start scan as well as collect wavelength values during an IR scan. These wavelength values are saved into the output file along with a mass spectrum for each wavelength. The range of time the mass spectrum is collected over is changed by adjusting the window and delay options on the program front panel. The laser scan rate, start wavelength, and end wavelength are also set on the front panel of the program. The start and end wavelength values must be entered in terms of the near IR wavelength that is output by the OPO/OPA computer instead of the actual output wavelength. While the data is collecting the photofragment peak can be selected using the cursors on the oscilloscope view and integrated on the fly to give a real time view of the spectrum. The scan will automatically end when the OPO/OPA computer reaches the end wavelength. The program will scan the laser position back to the start wavelength once the scan has stopped. If the number of scans requested is more than the number of scans which have been collected, the laser will begin scanning again after a user defined adjustable scan delay.

When only a mass spectrum is collected the file contains only individual mass spectra. The number of mass spectra collected is set by the user within the program. Once the requested number of individual mass spectra has been collected the program is ended.

The collected data are further processed in another homemade LabView program. For pure mass spectrum the collected individual mass spectra are averaged together to obtain a

composite mass spectrum. The program generates an output file consisting of the input file name with the extension ".dat" which contains the averaged mass spectrum.

For IR scans the photofragment peak of interest is selected and integrated in each mass spectrum. The results are recorded as a function of wavelength and displayed as a completed IR spectrum. This file is saved as a ".dat" file with the filename of the input file. The raw spectrum is then interpolated to give set point spacing in each scan. The interpolation settings can be controlled by the user but a typical interpolation step size is $1/10^{th}$ the scan rate. Typically the scan is interpolated over the entire scan range but this can also be adjusted by the user. These interpolated spectra are saved as ".dat.int" files with the filename of the input file. Each individual interpolated scan is then averaged together to give the final composite IR spectrum. A typical composite IR spectrum is composed of around 20-30 individual IR scans to give adequate signal to noise. It is not uncommon to use more scans in the lower energy (600-2400 cm^{-1}) region of the spectrum. This composite spectrum is saved in a user specified file when the program ends.

2.8 Experimental Timings

The experimental timings follow the scheme shown in figure 2.7. The trigger sequence is started when the pulsed valve of the main tagging trap is triggered by the T_0 output of a delay generator. This pulse also triggers a second delay generator which controls the reaction trap timings (Exit High, Exit Low, and pulse valve). The first delay generator controls the main trap trapping time as well as the firing of the laser flashlamps. Once the main trap power supply receives the trigger from this delay generator, the RF power to the trap is shut down. When the RF voltage is completely shut down, a process that can vary in time from cycle to cycle, a TTL

signal out is generated by the RF power supply. This then provides a trigger to the third delay generator which controls the post-extraction timings. This generator controls the pulses for the end caps of the ion trap which extract the ions. The mass gate and laser Q-switch timings are also controlled by this delay generator. The laser Q-switch timing is set to achieve optimal overlap with the ion packet while the laser flashlamp timing is adjusted to maintain a constant 1064 nm output power of 6 W. An example of timings for $[Pt(en)Cl(CH_4)]^+$ is shown in table 2.1.

2.9 Voltage Settings and Negative Ion Mode

An example of the voltages used for experiments on $[Pt(en)Cl(CH_4)]^+$ is shown in table 2.2. In general the voltages used throughout the experiment should decrease in magnitude from the capillary at the entrance to the tagging trap stage. Typically as the bias voltage on RF1 is increased in magnitude the ions become more fragmented. Lower reaction trap bias voltages typically serve to increase the amount of clustering observed on ions while higher voltages can lead to fragmentation. In the main trap the amount of tagging observed can be modulated by adjusting the voltages on the einzel lenses and the main trap bias voltage.

While the voltages in table 2.2 are for a positive ion, the spectrometer can also be used to study negative ions. In negative ion mode each power supply must be swapped to the opposite polarity that it has in positive mode. The MCP detector must also be floated in negative mode which requires the installation of a different voltage divider box than that used in the positive mode. The timing pulse polarities must also be switched from negative to positive for the reaction trap and Wiley-McLaren 2 pulses and from positive to negative for the Wiley-McLaren 1 and mass gate pulses.

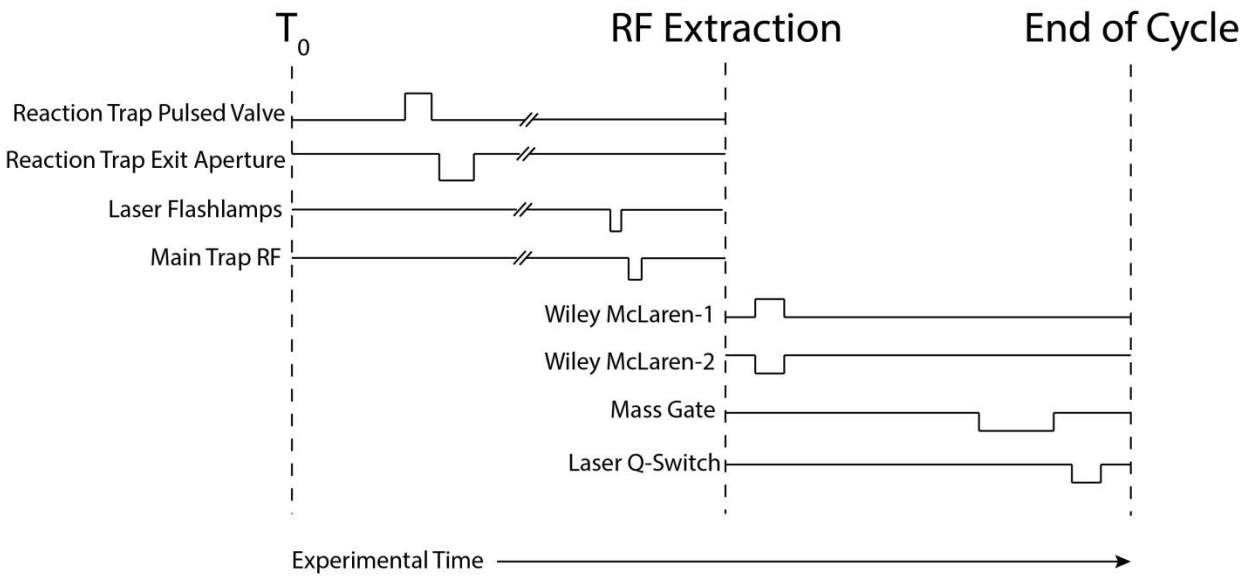

Figure 2.7- Schematic of the experimental timings for an experiment in positive ion mode. For negative ion mode the polarities of the reaction trap exit aperture, Wiley-McLaren 1, Wiley McLaren 2, and the mass gate are reversed.

Delay Generator 1 (DG1)	**Channel**	**Timing**
Main Trap Pulse Valve	T_0	-
Main Trap RF	A	T_0 + 95 ms
Laser Flash Lamps Delay	C	Channel A – 260 μs
Laser Flash Lamps Width	D	Channel C + 10 μs
Delay Generator 2 (DG2) (Triggered by T_0 of DG1)	**Channel**	**Timing**
Reaction Trap High	A	T_0 + 4 ms
Reaction Trap Low	B	Channel A + 2 ms
Reaction Trap Pulsed Valve	C	T_0 + 2 ms
Delay Generator 3 (DG3) (Triggered by Main Trap RF Supply)	**Channel**	**Timing**
Wiley McLaren 1 Low	A	0 + 500 ns
Wiley McLaren 1 High	B	Channel A + 500 μs
Wiley McLaren 2 High	C	0 + 500 ns
Wiley McLaren 2 Low	D	Channel C + 500 μs
Mass Gate High	E	0 + 39.5 μs
Mass Gate Low	F	Channel E + 100 μs
Laser Q-Switch	G	0 + 40.5 μs
Laser Q-Switch Width	H	Channel G + 10 μs

Table 2.1- Timings for $[Pt(en)Cl(CH_4)]^+$. The delay generator and channels that control each timing are listed as well as the triggers for each generator.

.

Supply	Voltage	Supply	Voltage
ESI	+1.5 kV	**HV1**	+51 V
MCP	-4.5kV	**HV2**	-305 V
Capillary	+109 V	**Liner**	-1.984 kV
Skimmer	+ 109 V	**Focus 1**	-0.43 kV
RF 1 Bias	+100 V	**L/R 1**	-2 kV
Aperture 1	+69 V	**U/D 1**	-2 kV
RF 2 Bias	+72.2 V	**Focus 2**	-1.02 kV
RT entrance	+74.1 V	**L/R 2**	-2.75 kV
RT bias	+68.1 V	**Mass gate 1**	-620 V
RT Exit High	+100 V	**Mass gate 2**	-2 kV
RT Exit Low	+68.5 V	**Reflectron 1**	-970 V
RF 3 Bias	+64.7 V	**Reflectron 2**	180 V
Aperture 2	-98 V	-	-
RF 4 Bias	+27.9 V	-	-
E1+E3	-96.7 V	-	-
E2	+36.6 V	-	-
Main Trap Bias	+50.6 V	-	-

Table 2.2- Voltage settings for $[Pt(en)Cl(CH_4)]^+$. The voltages on the left side of the table correspond to the source region while the voltages on the right side of the table correspond to the time-of-flight region. When the machine is in negative ion mode the polarities of all supplies should be flipped.

References:

1. M. Z. Kamrath, E. Garand, P. A. Jordan, C. M. Leavitt, A. B. Wolk, M. J. Van Stipdonk, S. J. Miller and M. A. Johnson, *Journal of the American Chemical Society*, 2011, **133**, 6440-6448.

2. J. B. Fenn, *Angewandte Chemie International Edition*, 2003, **42**, 3871-3894.

3. R. Mathur and P. B. O'Connor, *Review of Scientific Instruments*, 2006, **77**, -.

4. P. O'Connor, C. Costello and W. Earle, *J. Am. Soc. Spectrom.*, 2002, **13**, 1370-1375.
5. J. W. DePalma, P. J. Kelleher, C. J. Johnson, J. A. Fournier and M. A. Johnson, *Journal of Physical Chemistry A*, 2015, **119**, 8294-8302.

6. N. S. Nagornova, T. R. Rizzo and O. V. Boyarkin, *Science*, 2012, **336**, 320-323.

7. T. E. Cooper, J. T. O'Brien, E. R. Williams and P. B. Armentrout, *The Journal of Physical Chemistry A*, 2010, **114**, 12646-12655.

8. X.-B. Wang and L.-S. Wang, *Review of Scientific Instruments*, 2008, **79**.

9. M. Z. Kamrath, R. A. Relph, T. L. Guasco, C. M. Leavitt and M. A. Johnson, *International Journal of Mass Spectrometry*, 2011, **300**, 91-98.

10. A. B. Wolk, C. M. Leavitt, E. Garand and M. A. Johnson, *Accounts of Chemical Research*, 2014, **47**, 202-210.

11. W. C. Wiley and I. H. McLaren, *Review of Scientific Instruments*, 1955, **26**, 1150-1157.

Chapter 3: Infrared Spectroscopy of $MOH(H_2O)_n^+$ Clusters

In this chapter the spectroscopy of small hydrated metal hydroxide clusters is discussed. These complexes serve as model systems for interactions commonly thought to be present in water oxidation intermediates. In section 1 the behavior of small $CuOH^+$ clusters is discussed. Here we see a movement in the hydroxide stretching frequency of these complexes as a function of hydration.

The study of this system is expanded to other singly hydrated first row transition metal hydroxides in section 2. In this work we observed a significant metal-dependent trend in the hydroxide stretching frequency. Further investigation shows that the vibrational frequency is modulated by vibrational stark effect that is further influenced by charge transfer between the metal center and hydroxide ligand. Finally, in section 3, to assess the influence of solvation we investigate multiply hydrated metal hydroxide species. Here, similar to the copper case, we see the hydroxide stretching frequency is modulated by solvation. Interestingly it is observed that for all metals the hydroxide frequency tends to approach a value of 3700 cm^{-1} as solvation increases.

3.1 Vibrational Spectroscopy of Small Hydrated $CuOH^+$ Clusters

Published in**:** *Journal of Physical Chemistry A*, **118**, 2063-2071 (2014)

Abstract

Coordinated copper hydroxide centers can play an important role in copper catalyzed water oxidation reactions. In order to have a better understanding of the interactions involved in these complexes, we studied the vibrational spectra of D_2 tagged $CuOH^+(H_2O)_n$ clusters in the OH stretch region. These clusters are generated by electrospray ionization and probed via cryogenic ion vibrational spectroscopy. The results show that the copper center in the n=3 clusters has a distorted square planar geometry. The coordination in $CuOH^+(H_2O)_n$ is therefore more akin to $Cu^{2+}(H_2O)_n$ with four ligands in the first solvation shell than $Cu^+(H_2O)_n$ with two ligands in the first solvation shell. There is also no evidence of any strong axial ligand interactions. The well resolved experimental spectra enabled us to point out some discrepancies in the calculated spectra, which were found to be highly dependent on the level of theory used.

3.1.1 Introduction

Copper is an earth-abundant metal with a ubiquitous presence in homogeneous and heterogeneous catalysis. It also plays crucial roles in the field of biological oxygen chemistry. The versatility and reactivity of copper chemistry make it an appealing candidate for the development of rationally designed catalysts.[1] Very recently, several studies have found examples of coordinated copper complexes catalyzing water oxidation.[2-4] In one instance, the electrocatalytic water oxidation is driven by Cu(II) salts in a basic buffer solution, where the buffer anions coordinate to Cu(II) to prevent it from precipitating out of the solution.[2, 5] In the other two studies, the Cu(II) center is coordinated with polypeptide and bipyridine ligands.[3, 4] These catalytic systems are robust, simple to assemble, and have good reactivity. In all of these cases, the active species is thought to be a coordinated $CuOH^+$ core.

An important aspect of copper chemistry is its coordination with ligands and its solvation dynamics, which involve a combination of electrostatic, covalent, and hydrogen bonds. Understanding these interactions is necessary to understand and predict the reactivity of copper catalysts. In this respect, gas phase ion vibrational spectroscopy has proven to be one of the most powerful techniques in providing structural and bonding information on well-defined systems.[6-9] Here we use electrospray ionization to isolate microsolvated $CuOH^+ \cdot (H_2O)_n$ (n=1-3) clusters and study their structure and bonding by monitoring the spectral features in the OH stretching region.

Solvated copper systems have been subjected to several mass spectrometry studies. The sequential binding energies of H_2O molecules to Cu^+ have been determined via collision induced dissociation experiments.[10, 11] The solvation of Cu^{2+} ions was also studied via dissociation mass

spectrometry.[12-16] Furthermore, infrared photodissociation spectroscopy was applied to the study of $Cu^+(H_2O)_n$[17-19] and $Cu^{2+}(H_2O)_n$[20], yielding vibrational spectra that provided new insights into the coordination and solvation structure around the copper cation. One system that is rarely studied is the $CuOH^+\cdot(H_2O)_n$ complex. The interaction of the OH ligand and H_2O ligand creates an extra layer of complexity in the solvation dynamics. In one study, it was shown that the $CuOH^+\cdot(H_2O)$ loses an OH upon collisionally activated decomposition at low collision energy, whereas $CuOH^+\cdot(H_2O)_2$ loses an H_2O.[16] The second H_2O appears to bind more weakly to the copper, and brings to question whether the $CuOH^+\cdot(H_2O)_n$ complex would have a coordination number of 2, similar to $Cu^+(H_2O)_n$,[19] or a coordination number of 4, similar to $Cu^{2+}(H_2O)_n$.[20] Furthermore, with increasing attention paid to copper as a possible water oxidation catalyst, it is important to have a good understanding of the competing Cu-OH and Cu-H_2O interactions, as they may play crucial roles in the catalytic cycle.

In the present paper, $CuOH^+\cdot(H_2O)_n$ (n=1-3) clusters are studied via cryogenic ion vibrational spectroscopy. The OH stretch modes, which are used as a sensitive probe of the solvation network,[21] are monitored as a function of cluster size. Cryogenic cooling required for D_2 tagging also resulted in IR spectra that are relatively simple and well resolved. This greatly facilitates comparison with electronic structure calculations, and allows for unambiguous assignment of the observed features. The experimental data also highlights some shortcomings of various theoretical methods in relation to this open-shell system.

3.1.2 Experimental and theoretical details

The instrument used in these experiments has been described in detail in chapter 2. For these experiments the reaction trap stage contained only a single hexapole ion guide.

Additionally, the time-of-flight tube was a shorter, meter long, version. The $CuOH^+\cdot(H_2O)_n$ complexes were formed by the electrospray ionization (ESI) of a 1 mM solution of $CuSO_4$ in water.

Geometry optimization and vibrational frequency calculations for the $CuOH^+\cdot(H_2O)_n$ species in their doublet ground state were carried out using the cam-B3LYP, MP2 and CCSD methods and the TZVP basis set. Zero-point energy corrections were taken into account for the calculation of binding energies. For comparison with experimental spectra, the calculated harmonic frequencies obtained by each method were scaled by a factor of 0.953, 0.946, and 0.946 factor, respectively. These values are obtained by comparing the calculated stretch frequencies of an isolated H_2O molecule with experimental values of 3657 cm^{-1} and 3756 cm^{-1}. All the calculations were carried out using the Gaussian 09 program.[22]

3.1.3 Results

A typical positive mode mass spectrum (1 mM $CuSO_4$ in water) is shown in panel A of Figure 3.1. Each doublet pair corresponds to the ^{63}Cu and ^{65}Cu isotopes of copper, reflecting their natural abundances. The two lowest mass doublets are assigned to the bare Cu^+ and $Cu^+(H_2O)$. The three subsequent doublets are the $CuOH^+\cdot(H_2O)_n$ (n=1-3) species of interest. There is also very small amount of $CuO^{+\cdot}(H_2O)$ and $Cu^{+\cdot}(H_2O)_2$ which are visible around the two $CuOH^+\cdot(H_2O)$ peaks. Interestingly, very little bare $CuOH^+$ is present in the mass spectrum. Vukomanovic and Stone[16] have reported a very similar mass spectrum from the ESI of a similar $CuSO_4$ solution and showed that $Cu^+(H_2O)$ is the dominant fragmentation product of the $CuOH^+\cdot(H_2O)$ cluster at low collisional energies. The intensities we observe in our mass spectrum are in agreement with this result. When the ion trap temperature is lowered to 10 K, D_2

molecules condense onto the clusters, and further complex formation can be observed in the mass spectrum, as shown in Figure 3.2B. In this specific mass range, the clustering of D_2 molecules onto $CuOH^+\cdot(H_2O)$ forms ions tagged with up to four D_2, with larger clusters overlapping in mass with $CuOH^+\cdot(H_2O)_2$. The distribution of the tagged species was found to be very sensitive to experimental conditions such as the kinetic energy of the ions entering the trap and the pressure of buffer gas in the trap. This behavior is similar to what was observed in other cryogenic ion trap H_2 condensation studies.[23, 24] The distribution of tagged species is therefore more representative of the ion cooling and condensation kinetics in the trap than the relative stability of certain tagging numbers.

An overview of the infrared predissociation spectra of $CuOH^+\cdot(H_2O)_n$ with n=1-3 in the 2600 cm^{-1} to 3800 cm^{-1} range is presented in Figure 3.2. These spectra were acquired by monitoring the loss of D_2 from the corresponding singly tagged $CuOH^+\cdot(H_2O)_n\cdot D_2$ ions. The spectral features are concentrated in the free-OH region between 3550 and 3750 cm^{-1}. Specifically, Figure 3a shows the spectrum of the n=1 species, with three main peaks at 3590 cm^{-1}, 3612 cm^{-1} and 3684 cm^{-1}, as well as a weaker feature at 3758 cm^{-1}. These features have a full width at half maximum (FWHM) of 20-25 cm^{-1}, and they are on top of a slowly increasing background starting at ~2900 cm^{-1} with a dip at ~3600 cm^{-1} between the two partially resolved peaks. The spectrum is featureless below 3550 cm^{-1}, except for a small peak at 2733 cm^{-1}. The spectrum of the n=2 cluster, shown in Figure 3.2B, displays five distinct peaks of similar

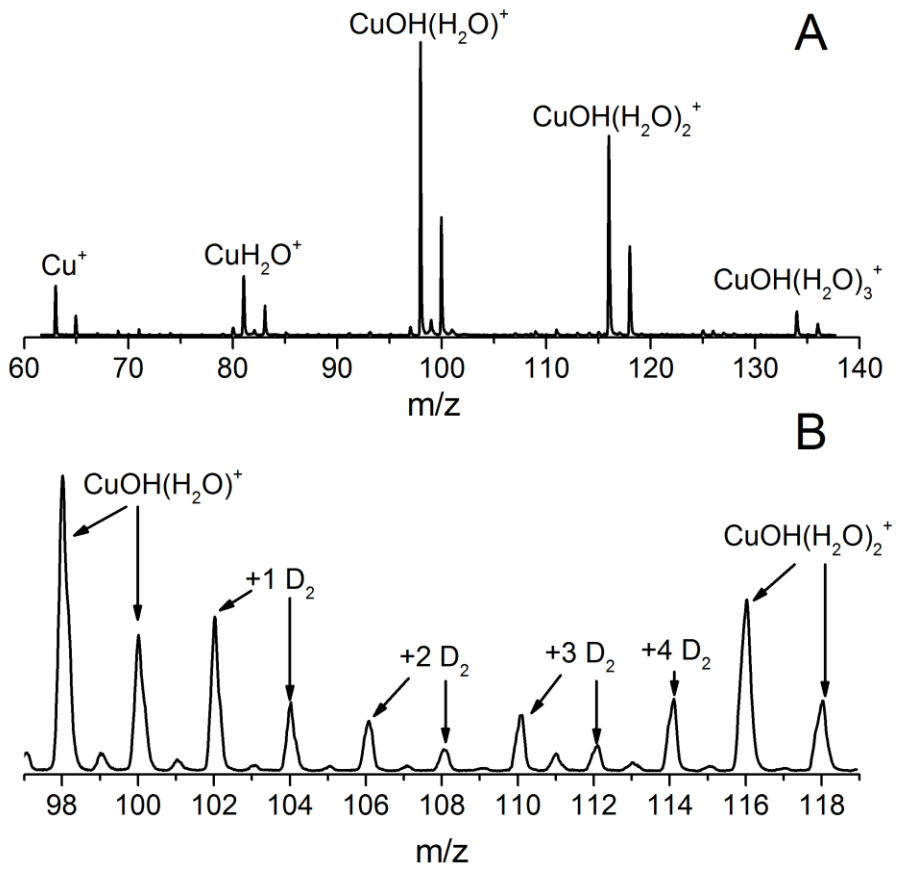

Figure 3.1- A) Mass spectrum obtained by ESI of a 1 mM $CuSO_4$ solution in water. B) Mass spectrum of D_2-tagging of $CuOH^+ \cdot (H_2O)$ obtained when the ion trap temperature is held at 10 K.

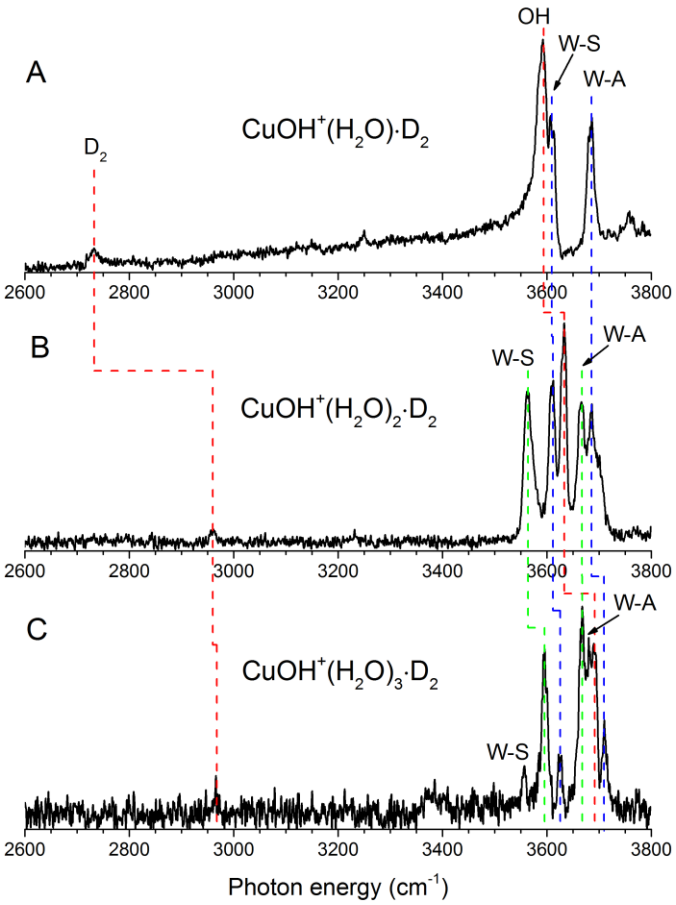

Figure 3.2- Overview of the infrared predissociation spectrum of A) $CuOH^+\cdot(H_2O)\cdot D_2$, B) $CuOH^+\cdot(H_2O)_2\cdot D_2$, and C) $CuOH^+\cdot(H_2O)_3\cdot D_2$. W-S denotes symmetric stretch of water, W-A denotes anti-symmetric stretch of water.

intensities centered at 3565 cm^{-1}, 3610 cm^{-1}, 3632 cm^{-1}, 3665 cm^{-1}, and 3685 cm^{-1}. These features are slightly sharper than those in the n=1 spectrum, with a FWHM of 15-20 cm^{-1}. A weak peak at 2960 cm^{-1} is also visible. Figure 3c shows the spectrum of the n=3 species. The resolved peaks in this spectrum have the narrowest widths of about 10 cm^{-1} FWHM. The more intense peak at 3595 cm^{-1} is surrounded by two weaker features at 3556 cm^{-1} and 3625 cm^{-1}. The broad feature at ~3680 cm^{-1} can be fitted nicely with three Gaussian peaks centered at 3667 cm^{-1}, 3681 cm^{-1} and 3692 cm^{-1} with FWHM of around 10 cm^{-1}. Lastly, the peak to the blue of the broad feature is situated at 3710 cm^{-1}.

Shown in Figure 3.3 is a series of spectra corresponding to increasing number of D_2 tags on the $CuOH^+ \cdot (H_2O)$ cluster, acquired to probe the perturbation caused by the D_2 tag at different binding sites. These spectra were obtained by monitoring the fragment corresponding to the loss of all tags. These results are particularly relevant for the small cluster because the under-coordinated open-shell metal center in this cluster might be reactive towards hydrogen. As can be seen from Figure 3.3, the sequential addition of D_2 molecules causes some noticeable changes in the IR spectrum. All four spectra show a common feature at 3590-3609 cm^{-1}, while the two other peaks gradually redshift as the number of tags is increased. They move from 3612 cm^{-1} and 3684 cm^{-1} to 3544 cm^{-1} and 3609 cm^{-1}, respectively, assuming that the bluest feature in the 4-tags spectrum consists of two overlapping peaks. The very weak feature at around 2750 cm^{-1} is present at about the same frequency for all four spectra, while a new stronger feature appears at 2956 cm^{-1} in the 4-tags spectrum.

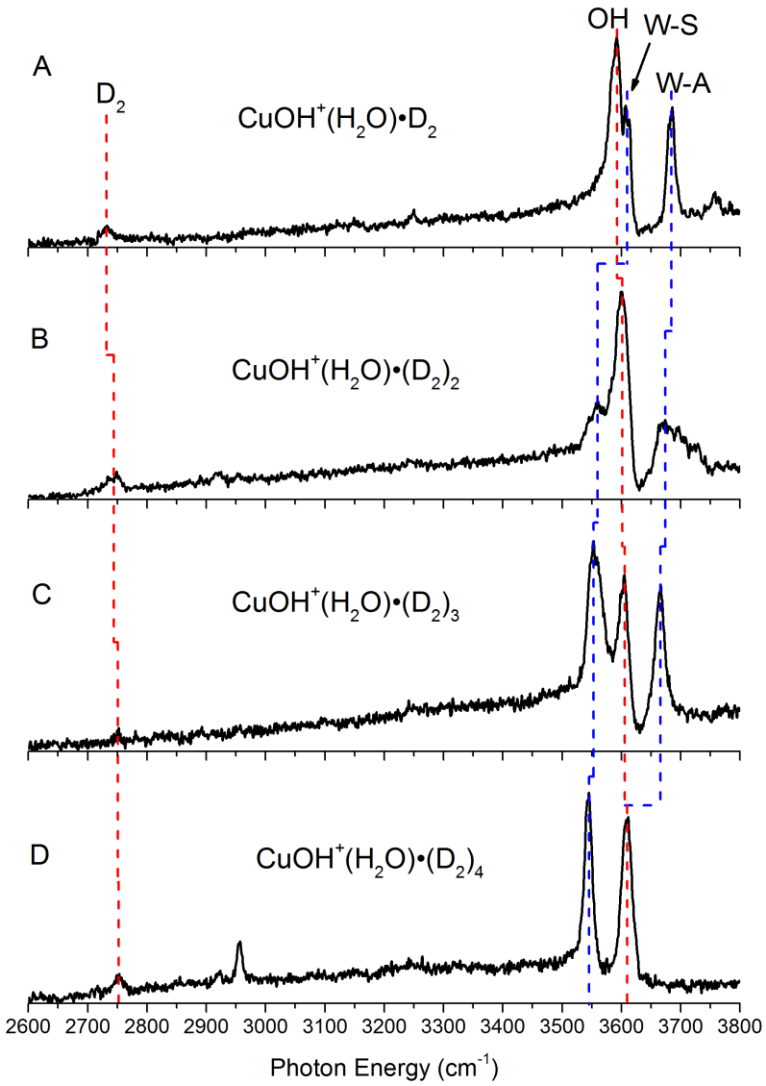

Figure 3.3- Overview of the infrared predissociation spectrum of $CuOH^+ \cdot (H_2O)$ with 1-4 D_2 tags.

3.1.4 Discussion

In order to have a better understanding of the coordination around the copper core, the effect of D_2 tagging on the observed vibrational frequencies, and the ability of electronic structure calculations to accurately predict structures and IR spectra, we start with a detailed analysis of the spectra of the $CuOH^+\cdot(H_2O)$ cluster with 1-4 D_2 tags presented in Figure 3.3.

The cam-B3LYP/TZVP optimized geometry of the lowest energy $CuOH^+\cdot(H_2O)$ structure is shown in Figure 3.4c. The water and hydroxide bind opposite of each other, forming an almost linear O-Cu-O bond with all the hydrogen atoms in the same plane. On the other hand, the calculated spectrum of the bare species shown in Figure 3.4C agrees well with the experiment. Computational searches yielded three available D_2 tag binding sites: directly on the copper center, on the water, and on the hydroxide. In the case of the 1-D_2 species, the strongest binding site is the copper site with a calculated binding energy of 1498 cm^{-1}. This is substantially larger than the typical value of 370-490 cm^{-1} found for H_2-tagging on protonated peptides.[23] The presence of the D_2 molecule distorts the O-Cu-O bond from linear to bent, as shown in Figure 3.4B. Nonetheless, the calculated spectrum is not very different from the bare species and is found to be in excellent agreement with the experimental spectrum. This allows us to assign the peak at 3590 cm^{-1} to mostly the hydroxide OH stretch with some contribution from the water symmetric stretch. This is 35 cm^{-1} higher than the vibrational frequency of the isolated hydroxide anion (3555 cm^{-1})[25], indicated in Figure 3.4A. The peaks at 3612 cm^{-1} and 3684 cm^{-1} are the symmetric and anti-symmetric stretches of the water ligand. They are redshifted with respect to the frequencies of free water (3657 cm^{-1} and 3756 cm^{-1}). The weak feature at 3758 cm^{-1} is not present in the calculated spectra. It is most likely a combination band involving the torsional mode and the anti-symmetric water stretch, as observed in similar Ar-

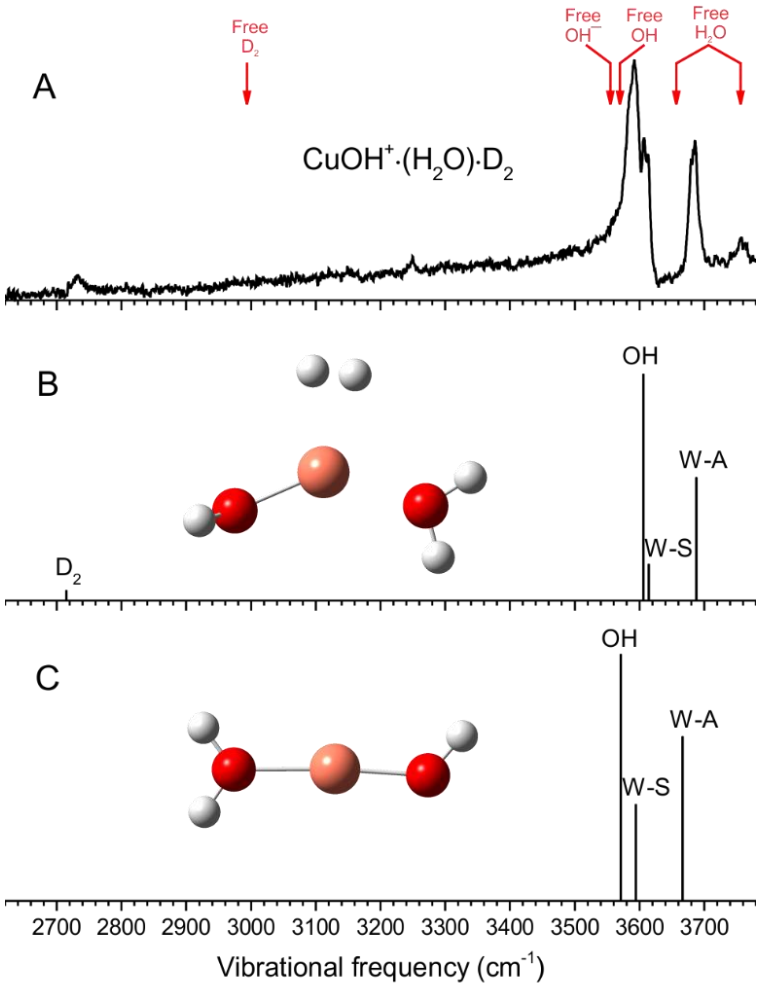

Figure 3.4- (A) Experimental spectra of $CuOH^+ \cdot (H_2O) \cdot D_2$. The red arrows indicate the gas phase positions of each free species. (B)-(C) Vibrations and optimized geometry of $CuOH^+ \cdot (H_2O) \cdot D_2$ and $CuOH^+ \cdot (H_2O)$ obtained at cam-B3LYP/TZVP level.

tagged spectra of $Cu^+(H_2O)$.[17] The weak feature at 2733 cm^{-1} is assigned to the nominally forbidden D_2 stretch which gains intensity from the perturbation induced by binding to the ion.[23, 24] It is redshifted by 261 cm^{-1} from the vibrational frequency of free D_2 at 2994 cm^{-1}.[26] The intensity and position of this transition are reproduced fairly well in the calculated spectrum.

The $CuOH^+\cdot(H_2O)\cdot D_2$ spectrum displays a slowly increasing background starting at ~2900 cm^{-1} with a dip at ~3600 cm^{-1}. Similar features are observed on the $CuOH^+\cdot(H_2O)$ species with more D_2 tags (see Figure 3.3), but not in any spectra of the larger $CuOH^+\cdot(H_2O)_n$ clusters. It is unlikely that the dip is due to further dissociation of the $CuOH^+\cdot(H_2O)$ photoproducts because the energy threshold for such process is calculated to be about 1.9 eV. The combination of the background and dip near the peaks is reminiscent of a Fano lineshape,[27, 28] which is due to a direct coupling between a vibrational mode and the dissociation continuum. It is not clear why this would be operative in the $CuOH^+\cdot(H_2O)$ spectra. The binding energy of the first tag is much larger than usual (and that of the other $CuOH^+\cdot(H_2O)_n$ species discussed below) which brings the dissociation threshold closer to the vibrations, possibly playing a role in the presence of the Fano lineshape. However, adequate theoretical treatment of such coupling is outside the scope of the present work.

We can now follow the evolution of the $CuOH^+\cdot(H_2O)$ experimental spectra as a function of increasing number of D_2 tags, shown in Figure 3.3. The optimized geometries and calculated vibrations at the cam-B3LYP/TZVP level are shown in Figure 3.5. Calculations found that the second D_2 can bind to either the Cu center or the water ligand with 544 cm^{-1} and 361 cm^{-1} binding energy, respectively. It appears that both isomers are present which would account for the broad appearances of the water modes in Figure 3.3B. The stepwise filling of these binding sites yields a structure for the 4-D_2 cluster in which two of the D_2 are on the Cu center and one

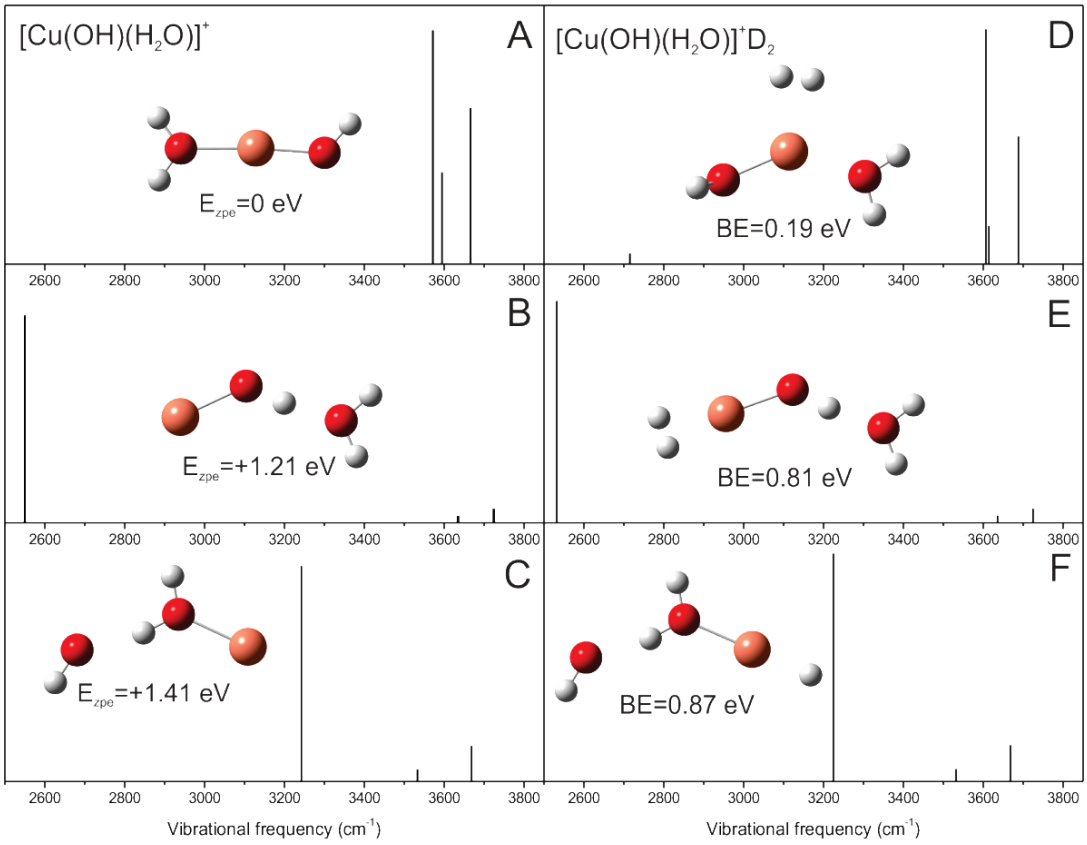

Figure 3.5- Calculated (cam-B3LYP/TZVP) energetics and vibrational spectra of different isomers of $CuOH^+\cdot(H_2O)$ (A-C) and $CuOH^+\cdot(H_2O)\cdot D_2$ (D-F). The spectra shown in panels A and D are the same as those in Figure 3.4. The relative energies, with zero-point correction, are listed in A-C. The binding energies of the D_2 tag are listed in D-E.

D_2 on each hydrogen of the water ligand. This scenario accounts for the redshifts of the water peaks and the slow and gradual blueshift of the hydroxide stretch as the number of tags increases. Lastly, we note that the good signal-to-noise ratio in the spectrum of the 4-D_2 species reveals three peaks in the 2700-3000 cm^{-1} region. These can be readily assigned to the vibration of the strongly-bound first D_2 on copper (2752 cm^{-1}), the weakly-bound second D_2 on copper (2921 cm^{-1}), and two weakly-bound D_2 on water (2956 cm^{-1}), by comparison with the calculated frequencies (Figure 3.6).

The cam-B3LYP/TZVP results for the $CuOH^+\cdot(H_2O)\cdot(D_2)_n$ species showed two noticeable deviations from the experimental spectra which are particularly visible in the 4-D_2 spectrum. First, the calculated frequency for the D_2-perturbed symmetric water vibration (W-S) is ~50 cm^{-1} lower than the experimental value. To probe this interaction in more detail, both cam-B3LYP/TZVP and CCSD/TZVP calculations were carried out for the $CuOH^+\cdot(H_2O)\cdot D_2$ cluster in which the D_2 binds to the water ligand with the results shown in Figure 3.7. The CCSD result yielded a D_2 binding energy of 148 cm^{-1} and a D_2-perturbed W-S vibration at 3561 cm^{-1}. On the other hand, cam-B3LYP yielded a D_2 binding energy of 441 cm^{-1} with a D_2-perturbed W-S vibration at 3450 cm^{-1}. This corroborates the experimental result that cam-B3LYP calculations overestimate the D_2 tag interaction, resulting in an overly redshifted water vibration. The second deviation is the calculated hydroxide vibration which is ~15 cm^{-1} higher in frequency

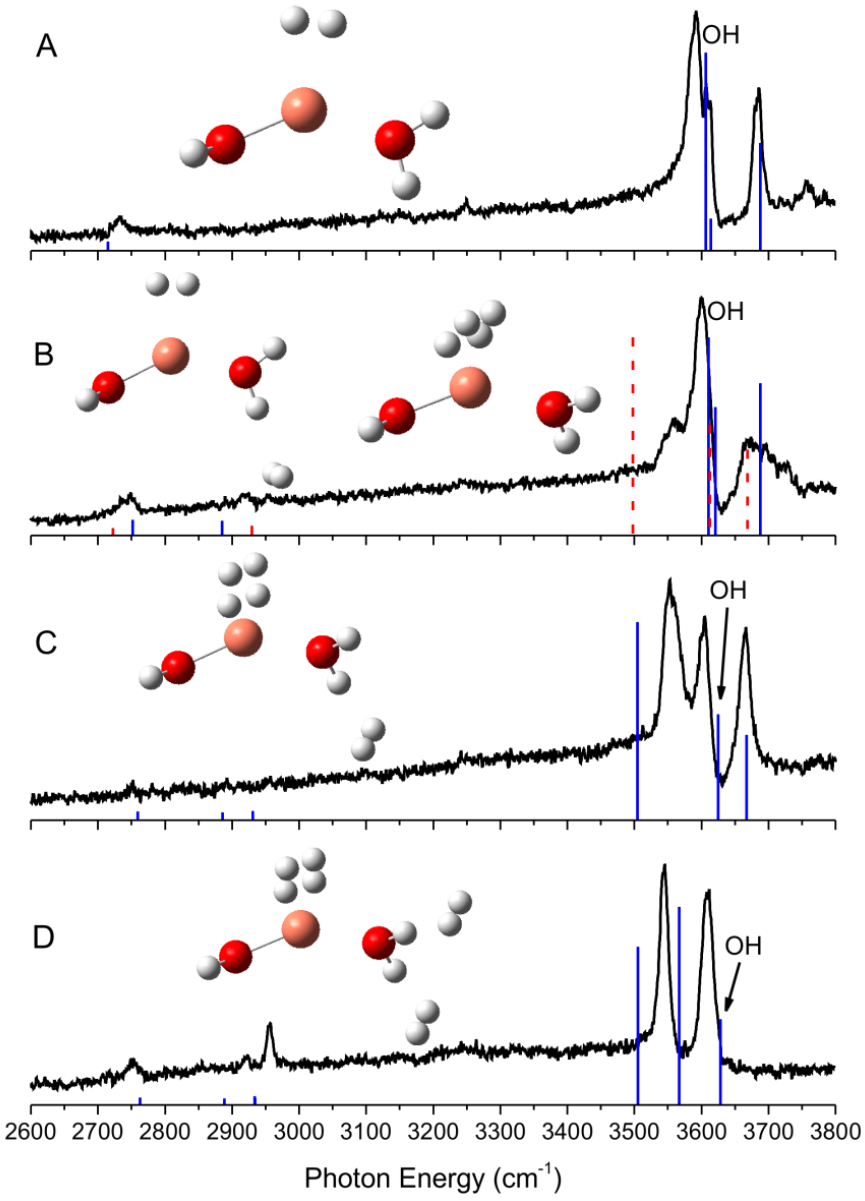

Figure 3.6- Experimental spectra (black) and calculated vibrations of $CuOH^{+}\cdot(H_2O)$ with 1-4 D_2 tags. The calculations are carried out at the cam-B3LYP/TZVP level. The red dashes in (B) correspond to the higher energy isomer at the left with one D_2 on Cu and one D_2 on water. The calculated position of the OH vibration is noted. The other two vibrations are the symmetric stretch (lower frequency) and anti-symmetric stretch (higher frequency) of water. D_2 vibrations are between 2700-3000 cm^{-1}.

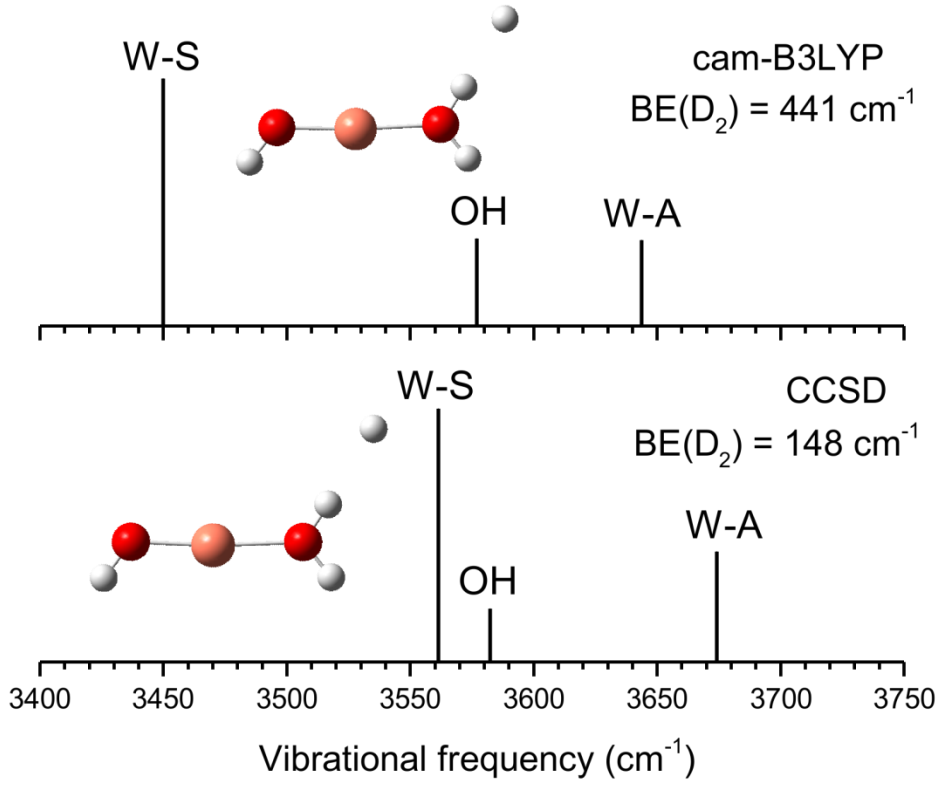

Figure 3.7- Calculated vibrational frequencies of $CuOH^+ \cdot (H_2O) \cdot D_2$ at the cam-B3LYP/TZVP and CCSD/TVZP level for D_2 tag binding to water.

than the experimental value in the cam-B3LYP result. This appears to be a systematic error present at all levels of theory because the CCSD result has an even higher frequency for the hydroxide vibration. In the interpretation of the infrared spectra of the larger clusters, these two discrepancies in the calculated spectrum will be considered when making assignments.

The spectrum of the $CuOH^+ \cdot (H_2O)_2 \cdot D_2$ cluster in the OH region, displayed in Figure 3.8A, shows five distinct peaks. The additional feature at 2960 cm^{-1} (Figure 3.2B) can be readily assigned to the vibration of a weakly bound D_2. This indicates that the strongly interacting Cu-D_2 motif of the n=1 species is not present here. The cam-B3LYP/TZVP calculation result for the bare $CuOH^+ \cdot (H_2O)_2$ is shown in Figure 3.8E. As expected, the additional water is found where the strongly bound D_2 was in the smaller cluster. This yields a geometry in which hydroxide and the two waters form an almost trigonal planar structure. The two water ligands differ slightly, where one has in-plane hydrogen atoms and one has out-of-plane hydrogen atoms. This causes the two waters to have slightly different vibrational frequencies and binding energies. The waters are labeled W_1 and W_2, which correspond to their clockwise position relative to the hydroxide in the structure displayed throughout Figure 3.8.

The weakly bound D_2 can bind to the copper center, the water ligand, or the hydroxide ligand, as discussed above. Structure, vibrational frequencies and binding energies calculated at the cam-B3LYP level for these three isomers are shown in Figure 3.8B-D. We note that two almost equivalent structures were found for the lowest energy isomer in which the D_2 binds to W_1. They correspond to D_2 binding to either of the two out-of-plane water hydrogens and yield slightly different spectra shown as solid and dashed lines in Figure 3.8B. Furthermore, all the starting geometries with D_2 on W_2 converged to the same two isomers as in Figure 3.8B.

Taking into account that the cam-B3LYP calculations overestimate the redshift of the D_2-perturbed W_1-S mode and the frequency of the hydroxyl stretch, we find the calculated spectra of the two isomers in Figure 3.8B give the best match with the experimental spectrum. Moreover, the slight differences in the vibrational spectra of these two isomers would account for the broader and asymmetrical appearance of the features at 3565 cm^{-1} and 3685 cm^{-1}. While the presence of isomers depicted in Figure 3.8C or 3.8D cannot be completely ruled out, they are certainly not major contributors because neither reproduces the lowest frequency OH band. Consequently, we make the following assignments: water anti-symmetric stretch at 3685 cm^{-1} and 3665 cm^{-1}, hydroxide stretch at 3632 cm^{-1}, and water symmetric stretch at 3610 cm^{-1} and 3565 cm^{-1}. We note that this assignment, similar to the $CuOH^+ \cdot (H_2O)$ clusters, yields an underestimation of ~50 cm^{-1} for the W_1-S (D_2-bound OH) mode and an overestimation of 18 cm^{-1} for the hydroxide stretch in the cam-B3LYP calculation.

There may be a couple of reasons why the isomer in Figure 3.8B dominates the experimental spectrum. First, the calculations indicate it is the lowest energy isomer. Even though isomers 3.8C and 3.8D are not significantly higher in energy, the potential energy surface is likely quite flat, allowing the clusters to reach the lowest energy isomer during collisional cooling. Furthermore, there are four almost equivalent binding sites for D_2 on the water ligand, whereas there is only one binding site on hydroxide and at most two on copper. Therefore, the isomer in Figure 3.8B is also favored from a statistical point of view.

We now turn our attention to the larger $CuOH^+ \cdot (H_2O)_3$ cluster. If the additional water bonds to another water molecule and forms a second solvation shell, it would give rise to the typical H-bonded water transitions in the 3100-3400 cm^{-1} region.[18, 29] No feature in that range is observed in the experimental spectrum of the n=3 cluster. Therefore, the n=3 cluster has three

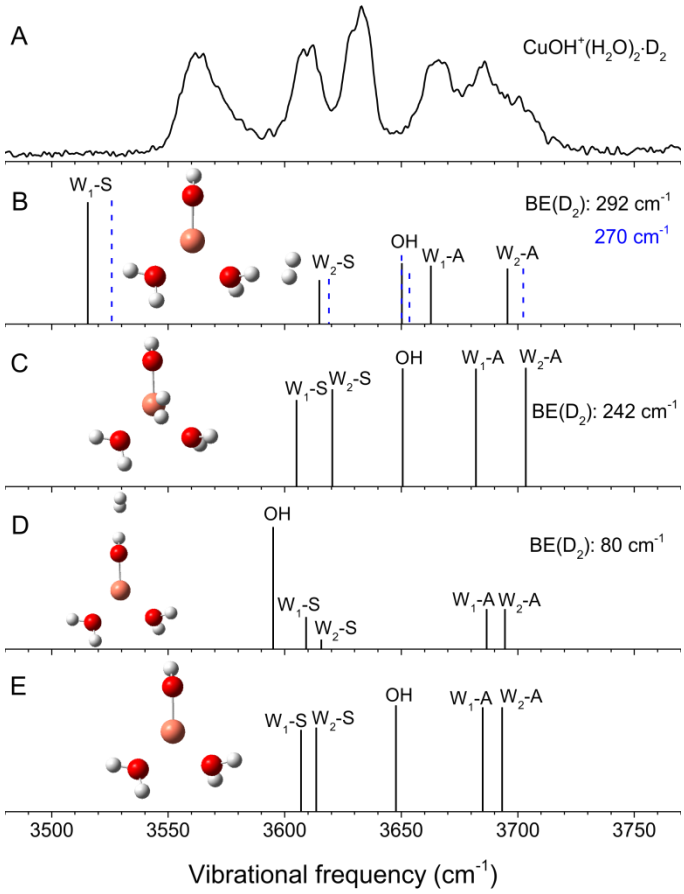

Figure 3.8- (A) The experimental spectrum of $CuOH^+ \cdot (H_2O)_2 \cdot D_2$. (B)-(D) Optimized geometries and vibrations calculated at cam-B3LYP/TZVP level. Shown in blue dashes in (B) are the vibrations corresponding to D_2 binding on the other binding site on the same water. (E) Optimized geometries and vibrations of the untagged cluster. The waters are labeled W_1 and W_2, corresponding to their clockwise position relative to the hydroxide.

waters and a hydroxide group on the copper center. The cam-B3LYP calculations produced a cluster with an almost square planar geometry, shown in Figure 3.9D along with its infrared spectrum. We again used the same W_1, W_2 and W_3 labeling, corresponding to the clockwise position starting from hydroxide. The arrangement of the ligands around the copper center is more akin to $Cu^{2+}(H_2O)_n$[12, 20] than $Cu^{+}(H_2O)_n$[19] in which only 2 water molecules are present in the primary solvation shell. The hydroxide acts as a slight hydrogen bond acceptor for the neighboring W_1 water, which distorts the ligand arrangement and yields three non-equivalent waters.

Again, we found that D_2 binding to water gives the lowest energy structures. Because the $CuOH^{+}\cdot(H_2O)_2$ cluster showed only contributions from this binding site, we will only consider these D_2 binding isomers in detail here. The cam-B3LYP calculations yielded four possible D_2 tag isomers, in which D_2 binds to W_2 (Figure 3.9C) or W_3 (Figure 3.9B). Starting geometries with D_2 on W_1 all produced rearrangements leading to the structure in Figure 3.9B. As expected, the calculated D_2 binding energies for all the species are essentially the same. However, none of the calculated spectra present a very good match with the experiment. The best agreement comes from isomer 3.9B (solid black lines), if we use the same calibrations for the calculated frequency as before. We can assume that the frequency of the hydroxide is once again overestimated by ~15 cm^{-1} and the frequency of the D_2-bound W_3-S is underestimated by ~50 cm^{-1}. This yields a good agreement for the 6 highest frequency peaks with the following assignments: water anti-symmetric stretch at 3710 cm^{-1}, 3681 cm^{-1}, and 3667 cm^{-1}, hydroxide stretch at 3692 cm^{-1}, and water symmetric stretch at 3625 cm^{-1} and 3595 cm^{-1}. This only leaves the small peak at 3556 cm^{-1} to be the W_1-S peak, calculated to be 90 cm^{-1} lower in frequency. This vibration is redshifted due to W_1 forming a hydrogen bond donor interaction with the

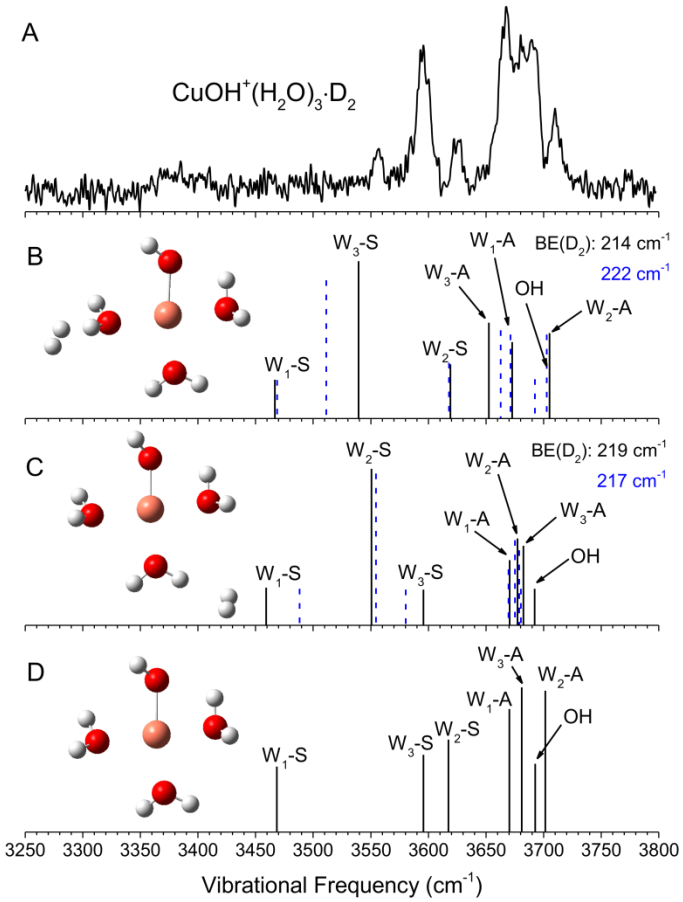

Figure 3.9- (A) The experimental spectrum of $CuOH^+ \cdot (H_2O)_3 \cdot D_2$. (B)-(C) Optimized geometries and vibrations calculated at cam-B3LYP level. Shown in blue dashes are the vibrations corresponding to D_2 binding on the other binding site on the same water. (D) Optimized geometries and vibrations of the untagged cluster.

nearby oxygen of the hydroxide. It is conceivable that, similar to the D_2 binding induced shift, the calculations overestimate the effect of this interaction in the infrared spectrum. Although the presence of the other isomers cannot be completely ruled out, the narrow 10 cm^{-1} FWHM of all the peaks indicates that a single isomer is probably responsible for all the features in the experimental spectrum.

From the assigned spectra, we can see some interesting trends in the evolution of the clusters. First, the hydroxide stretch blueshifts by ~100 cm^{-1} with increasing number of water ligands, moving from 3590 cm^{-1} in n=1 to 3692 cm^{-1} in n=3. A similar trend, but of smaller magnitude, is also observed in the spectra of $CuOH^+ \cdot (H_2O) \cdot (D_2)_n$ in which the hydroxide peak shifts from 3590 cm^{-1} to 3609 cm^{-1} as the number of D_2 tags is increased. Interestingly, the hydroxide vibration for the smallest cluster studied here is already at a higher frequency than either the isolated hydroxyl radical (3570 cm^{-1}) or hydroxide anion (3555 cm^{-1}). In fact, as solvation increases around the Cu center, this vibration is moving towards the typical frequency of a free OH in water or alcohol (~3700 cm^{-1}).[30] This can be seen in Figure 3.2C, where the hydroxide stretch is only 18 cm^{-1} lower in frequency than the anti-symmetric stretch of the "free" water in the n=3 cluster. Very similar behavior of the hydroxide mode has been observed before in the infrared spectra of small $OH^-(H_2O)_n$ clusters.[31] On the other hand, the vibrational frequencies of the "free" water ligand, i.e., not hydrogen-bonded or D_2-bonded, are much less sensitive to the increasing solvation. These modes show almost no shift from n=1 (3612/3684 cm^{-1}) to n=2 (3610/3685 cm^{-1}), but slightly blueshifts in n=3 (3625/3710 cm^{-1}), moving closer to the gas phase H_2O vibrations (3657/3756 cm^{-1}). The calculation at the cam-B3LYP level yielded incremental water binding energies of 2.18 eV, 1.26 eV and 0.94 eV for the first, second and third water, respectively. The redshift of the free water ligand is thus not directly related to the

binding energy. A possible explanation is that the vibrational frequency shift is mostly due to the electric field induced by the charged $CuOH^+$ ion core.[32]

Although the copper center in the clusters studied here has a formal oxidation state of +2, NBO analysis determined that the copper center has a charge varying from +1.05 to +1.14 as the number of water increases. This is not surprising considering that the ionic charge-separated state is likely to be much higher in energy for these small clusters. However, the square planar arrangement of the ligands around the copper center found in this work is similar to $Cu^{2+}(H_2O)_n$[12, 20] and not $Cu^+(H_2O)_n$[19] in which only 2 water molecules are present in the primary solvation shell. While the second and third water have significantly lower binding energies than the first water, it is not sufficient to force them into the second solvation shell. We did not observe any significant intensity in the mass spectrum for clusters containing more than 3 water ligands. This indicates that the fourth water, whether binding on the axial Cu site or hydrogen bonding to the primary water ligand, has a much lower binding energy. The closure of the first solvation shell at 3 water would be consistent with the square planar coordination observed for the $Cu^{2+}(H_2O)_n$ clusters.

The well resolved spectra afforded by the cryogenic ion vibrational spectroscopy technique have enabled us to point out some subtle discrepancies between the cam-B3LYP calculated spectrum and the experimental results. We briefly studied the effects of different calculation methods in order to explore the origin of these discrepancies. We found that the calculated structures and vibrational spectra were very dependent on the calculation method. An example of this is shown in Figure 3.10 which compares the structures and spectra of the $CuOH^+ \cdot (H_2O)_2 \cdot D_2$ cluster at the cam-B3LYP, MP2, and CCSD methods using the same TZVP basis

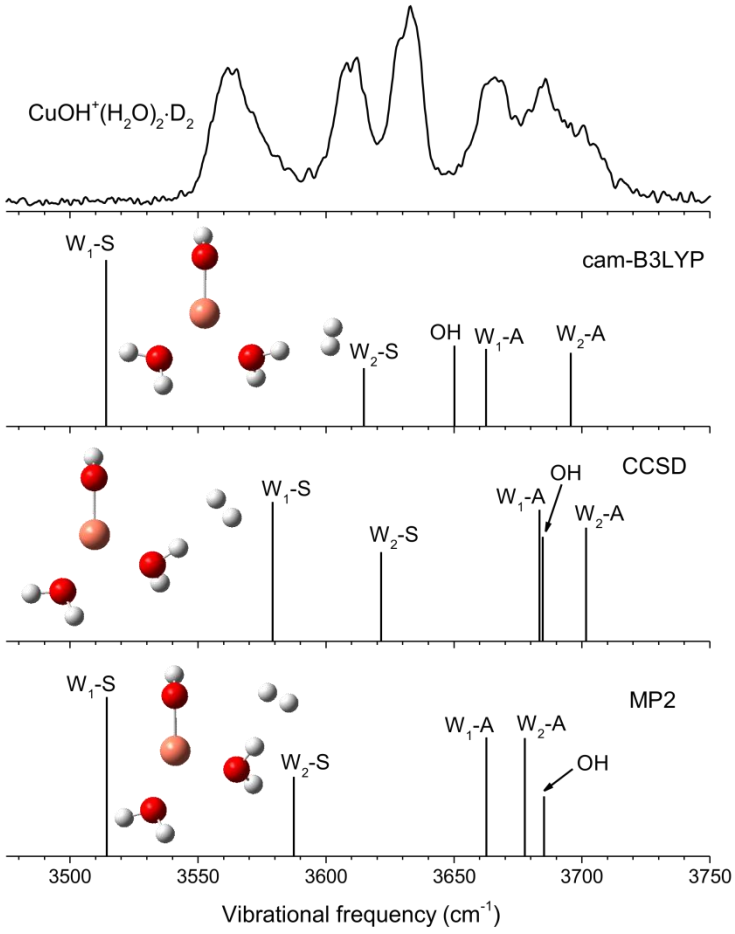

Figure 3.10- Comparison of the calculation results at cam-B3LYP, MP2, and CCSD levels with experimental result. All calculations used the TZVP basis set.

set. As discussed before, the cam-B3LYP calculation gives a geometry close to a trigonal planar ligand arrangement for this species. On the other hand, MP2 yields an almost T-shaped geometry, while the CCSD result is somewhere between the two. In assigning the experimental spectra, we noted that cam-B3LYP calculations consistently overestimate the hydroxide frequency by ~15 cm^{-1}. Interestingly, both MP2 and CCSD, with a more T-shaped geometry, yielded a hydroxide mode ~35 cm^{-1} higher than the cam-B3LYP calculation. This suggests that the geometry for the n=2 cluster might be even closer to symmetrically trigonal planar than predicted by cam-B3LYP. However, while cam-B3LYP may be closest in obtaining the correct hydroxide frequency, it fails in predicting the correct interaction strength for both the D_2-H_2O interaction and the slight hydrogen bond in the n=3 cluster. The CCSD calculation is better at accounting for these weak intermolecular interactions despite not having the right geometry. The cause of these method dependent geometries is not clear. One possibility is the open-shell nature of these Cu complexes which can cause spin-contamination problems. However, in the case of the calculations shown in Figure 3.10, we found S^2 to be very close to the expected 0.75 value (0.758 for cam-B3LYP, and 0.754 for MP2 and CCSD). Furthermore, the T-shaped MP2 structure is closer to the linear coordination expected for Cu^+ centers. This suggests that differences between the various calculation methods might stem from the different treatment of charge transfer between the Cu^{2+} center and the OH^- ligand.

We note that similar method dependent geometries have previously been reported for other Cu complexes. Wang *et al.*[33] have reported significantly different geometries for Cu-(2,2'-bipyridine) and Cu-(4,4'-bipyridine) complexes calculated using MP2 and B3LYP. Comparison with high resolution photoelectron spectra indicated that the structure of Cu-(2,2'-bipyridine) was correctly predicted by B3LYP while the structure of Cu-(4,4'-bipyridine) was best described

by MP2. Rios-Font *et al.*[34] have also found significant effects by the amount of exact exchange in DFT functional for the description of $Cu^{2+}(H_2O)_n$ water clusters.

3.1.5 Conclusion

The $CuOH^+\cdot(H_2O)_n$ (n=1-3) clusters were isolated using electrospray ionization and studied by cryogenic ion vibrational spectroscopy. The resolution afforded in the OH region allowed for a detailed analysis and assignment of the experimental spectra. The results showed that the copper center in the $CuOH^+\cdot(H_2O)_3$ cluster has a distorted square planar geometry. The coordination in $CuOH^+\cdot(H_2O)_n$ is found to be more akin to $Cu^{2+}(H_2O)_n$ with four ligands in the first solvation shell than $Cu^+(H_2O)_n$ with two ligands in the first solvation shell. The under-coordinated $CuOH^+\cdot(H_2O)$ cluster showed a high reactivity, binding strongly to the D_2 tag and significantly shifting the D_2 stretch. The larger $CuOH^+\cdot(H_2O)_2$ and $CuOH^+\cdot(H_2O)_3$ clusters did not show such a strong interaction. The well resolved spectra also enabled us to point out some discrepancies between the calculated spectra and the experimental results, which were found to be highly dependent on the level of theory used. Care is needed for proper simulation of the coordinated copper complexes.

References

1. A. E. Wendlandt, A. M. Suess and S. S. Stahl, *Angew. Chem.-Int. Ed.*, 2011, **50**, 11062-11087.

2. Z. F. Chen and T. J. Meyer, *Angew. Chem.-Int. Ed.*, 2013, **52**, 700-703.

3. M. T. Zhang, Z. F. Chen, P. Kang and T. J. Meyer, *J. Am. Chem. Soc.*, 2013, **135**, 2048-2051.

4. S. M. Barnett, K. I. Goldberg and J. M. Mayer, *Nat. Chem.*, 2012, **4**, 498-502.

5. Z. F. Chen, P. Kang, M. T. Zhang, B. R. Stoner and T. J. Meyer, *Energy Environ. Sci.*, 2013, **6**, 813-817.

6. K. R. Asmis and D. M. Neumark, *Acc. Chem. Res.*, 2012, **45**, 43-52.

7. O. Dopfer, *Z. Phys. Chem.*, 2005, **219**, 125-168.

8. M. A. Duncan, *International Reviews in Physical Chemistry*, 2003, **22**, 407-435.

9. N. C. Polfer and J. Oomens, *Mass Spectrometry Reviews*, 2009, **28**, 468-494.

10. N. F. Dalleska, K. Honma, L. S. Sunderlin and P. B. Armentrout, *J. Am. Chem. Soc.*, 1994, **116**, 3519-3528.

11. T. F. Magnera, D. E. David, D. Stulik, R. G. Orth, H. T. Jonkman and J. Michl, *J. Am. Chem. Soc.*, 1989, **111**, 5036-5043.

12. B. J. Duncombe, K. Duale, A. Buchanan-Smith and A. J. Stace, *J. Phys. Chem. A*, 2007, **111**, 5158-5165.

13. A. J. Stace, N. R. Walker and S. Firth, *J. Am. Chem. Soc.*, 1997, **119**, 10239-10240.

14. A. A. Shvartsburg and K. W. M. Siu, *J. Am. Chem. Soc.*, 2001, **123**, 10071-10075.

15. J. A. Stone and D. Vukomanovic, *Int. J. Mass Spectrom.*, 1999, **185**, 227-229.

16. D. Vukomanovic and J. A. Stone, *Int. J. Mass Spectrom.*, 2000, **202**, 251-259.

17. P. D. Carnegie, A. B. McCoy and M. A. Duncan, *J. Phys. Chem. A*, 2009, **113**, 4849-4854.

18. T. Iino, K. Ohashi, K. Inoue, K. Judai, N. Nishi and H. Sekiya, *J. Chem. Phys.*, 2007, **126**.

19. T. Iino, K. Ohashi, Y. Mune, Y. Inokuchi, K. Judai, N. Nishi and H. Sekiya, *Chem. Phys. Lett.*, 2006, **427**, 24-28.

20. J. T. O'Brien and E. R. Williams, *J. Phys. Chem. A*, 2008, **112**, 5893-5901.

21. W. H. Robertson and M. A. Johnson, *Annu. Rev. Phys. Chem.*, 2003, **54**, 173-213.

22. M. J. Frisch, G. W. Trucks, H. B. Schlegel, G. E. Scuseria, M. A. Robb, J. R. Cheeseman, G. Scalmani, V. Barone, B. Mennucci, G. A. Petersson, H. Nakatsuji, M. Caricato, X. Li, H. P. Hratchian, A. F. Izmaylov, J. Bloino, G. Zheng, J. L. Sonnenberg, M. Hada, M. Ehara, K. Toyota, R. Fukuda, J. Hasegawa, M. Ishida, T. Nakajima, Y. Honda, O. Kitao, H. Nakai, T. Vreven, J. A. Montgomery, Jr., J. E. Peralta, F. Ogliaro, M. Bearpark, J. J. Heyd, E. Brothers, K. N. Kudin, V. N. Staroverov, R. Kobayashi, J. Normand, K. Raghavachari, A. Rendell, J. C. Burant, S. S. Iyengar, J. Tomasi, M. Cossi, N. Rega, N. J. Millam, M. Klene, J. E. Knox, J. B. Cross, V. Bakken, C. Adamo, J. Jaramillo, R. Gomperts, R. E. Stratmann, O. Yazyev, A. J. Austin, R. Cammi, C. Pomelli, J. W. Ochterski, R. L. Martin, K. Morokuma, V. G. Zakrzewski, G. A. Voth, P. Salvador, J. J. Dannenberg, S. Dapprich, A. D. Daniels, Ö. Farkas, J. B. Foresman, J. V. Ortiz, J. Cioslowski and D. J. Fox, *Journal*, 2009, **Revision D.01**.

23. M. Z. Kamrath, E. Garand, P. A. Jordan, C. M. Leavitt, A. B. Wolk, M. J. Van Stipdonk, S. J. Miller and M. A. Johnson, *J. Am. Chem. Soc.*, 2011, **133**, 6440-6448.

24. M. Z. Kamrath, R. A. Relph, T. L. Guasco, C. M. Leavitt and M. A. Johnson, *Int. J. Mass Spectrom.*, 2011, **300**, 91-98.

25. N. H. Rosenbaum, J. C. Owrutsky, L. M. Tack and R. J. Saykally, *J. Chem. Phys.*, 1986, **84**, 5308-5313.

26. G. D. Dickenson, M. L. Niu, E. J. Salumbides, J. Komasa, K. S. E. Eikema, K. Pachucki and W. Ubachs, *Phys. Rev. Lett.*, 2013, **110**.

27. U. Fano, *Physical Review*, 1961, **124**, 1866-1878.

28. U. Fano and J. W. Cooper, *Physical Review*, 1965, **137**, 1364-&.

29. B. Bandyopadhyay, K. N. Reishus and M. A. Duncan, *J. Phys. Chem. A*, 2013, **117**, 7794-7803.

30. J. W. Shin, N. I. Hammer, E. G. Diken, M. A. Johnson, R. S. Walters, T. D. Jaeger, M. A. Duncan, R. A. Christie and K. D. Jordan, *Science*, 2004, **304**, 1137-1140.

31. W. H. Robertson, E. G. Diken, E. A. Price, J. W. Shin and M. A. Johnson, *Science*, 2003, **299**, 1367-1372.

32. J. S. Prell, J. T. O'Brien and E. R. Williams, *J. Am. Chem. Soc.*, 2011, **133**, 4810-4818.

33. X. Wang, J. S. Lee and D.-S. Yang, *Can. J. Chem.*, 2013, **91**, 613-620.

34. R. Rios-Font, M. Sodupe, L. Rodriguez-Santiago and P. R. Taylor, *J. Phys. Chem. A*, 2010, **114**, 10857-10863.

3.2 Charge Transfer in $MOH(H_2O)^+$ (M=Mn, Fe, Co, Ni, Cu, Zn) Complexes Revealed by Vibrational Spectroscopy of Mass-Selected Ions

Published in: *Physical Chemistry Chemical Physics*, **17**, 25786-25792 (2015)

Abstract

Charge transfer between a metal and its ligand is fundamental for the structure and reactivity of a metal complex as it directly dictates the distribution of electron density within the complex. To better understand such charge transfer interactions, we studied the vibrational spectra of mass-selected $MOH(H_2O)^+$ (M=Mn, Fe, Co, Ni, Cu, or Zn) complexes, acquired using cryogenic ion infrared predissociation spectroscopy. We find that there is a partial charge transfer from the hydroxide anion to the metal center for these first-row transition metals, the extent of which is in the order of Mn < Fe < Co < Ni < Cu > Zn, dictated by the 2^{nd} ionization energy of the bare metal. This gradual change across the metal series points to the complexity in the electronic structures of these transition metal complexes. Interestingly, the hydroxide ligand in these complexes also serves as an in-situ sensitive probe of this charge transfer. Its vibrational frequency varies by >150 cm^{-1} for different metal species, and it is dependent on the electric field produced by the charged metal center. This dramatic vibrational Stark shift is further modulated by the charge present on the hydroxide itself, providing a well-defined relationship between the observed hydroxide frequency and the effective electric field.

3.2.1 Introduction

Charge transfer is a fundamental process present in metal-ligand interactions.[1-5] While metal-centered complexes are typically designated by their formal charge states, it is often unclear how the electrons are delocalized within the complex.[6, 7] On the other hand, the functionality of an active site, whether in a catalyst or an enzyme, depends heavily on the exact electronic structure present.[8-10] Therefore a better understanding of the driving forces behind the electron transfer process, as well as an in-situ sensitive probe of the charge states present in a complex, would provide deeper insights into this vital metal-ligand interaction. Here, we use infrared predissociation spectroscopy of mass-selected $MOH(H_2O)^+$ (M=Mn, Fe, Co, Ni, Cu, Zn) complexes to directly probe the charge transfer in these species. We find that the vibrational frequency of the hydroxide ligand is extremely sensitive to the electric field generated by the charge on the metal center.

The $(M^{2+})(OH^-)$ ion pair, where the positively charged metal center directly interacts with the negatively charged hydroxide ligand, serves as a relatively simple example of metal-ligand charge transfer interaction. Recently, our group[11] probed the vibrational structure of the microsolvated $CuOH^+$ clusters[12] in an effort to better understand a new group of self-assembling copper-centered water oxidation catalysts.[13-16] Shortly after, Johnson *et al.*[17] reported the gas phase IR study of solvated $MgOH^+$ and $CaOH^+$ clusters. Surprisingly, these two studies showed dramatic differences between the vibrational spectrum of the alkaline earth and the copper complexes. Most notably, the vibrational frequency of the hydroxide (OH^-) moiety in $CaOH(H_2O)^+$ and $MgOH(H_2O)^+$ was found to be blueshifted with respect to the free hydroxide frequency by nearly 200 cm^{-1} and 300 cm^{-1}, respectively, while the same hydroxide vibration in

$CuOH(H_2O)^+$ is blueshifted by only 35 cm^{-1}. Additionally, the Mg and Ca complexes show a redshifting trend for the hydroxide vibration with increasing number of surrounding water molecules, while the Cu complex shows the exact opposite trend. These results highlight the possibility that the electronic structure of these complexes involve more than a simple $M^{2+}OH^-$ contact ion pair configuration.

This prompted us to use cryogenic ion vibrational spectroscopy to systematically investigate the late first-row transition metal complexes of the form $MOH(H_2O)^+$ (M=Mn, Fe, Co, Ni, Cu, or Zn). We focus on the OH stretching region to reveal the metal-dependent trends in the frequencies of the hydroxide and H_2O stretch vibrations. The use of D_2 tagging affords cryogenically cooled complexes, yielding well-resolved vibrational features for facile assignment as well as direct comparison with electronic structure calculations. We find that the extent of charge transfer between the hydroxide ligand and the metal center depends highly on the metal species. Furthermore, the main driver of the hydroxide vibrational frequency is the modulation of the vibrational Stark effect induced by the charged metal center.

3.2.2 Experimental and Computational Details

The instrument used in these experiments has been described in detail in chapter 2. For these experiments the reaction trap stage contained only a single hexapole ion guide. Additionally, the time-of-flight tube was a shorter, meter long, version. The ions of interest were generated via electrospray ionization of ~1 mM aqueous solutions of the corresponding metal sulfates.

To aid the analysis of the experimental spectra, electronic structure calculations were performed using the Gaussian 09 computational package.[18] Geometry optimizations, with Gaussian 09 standard tight convergence criteria, and harmonic frequency calculations were

carried out at the cam-B3LYP/def2TZVP level of theory. Previous works have shown that the cam-B3LYP functional yields accurate binding energies[19] and vibrational spectra[11] for $CuOH(H_2O)^+$. For comparison to the experimental vibrational spectrum, the harmonic frequencies are scaled by a factor of 0.955. The atomic charges in these complexes were obtained using Natural population analysis with the NBO 6 program.[20]

3.2.3 Results and Analysis

The vibrational predissociation spectra of $MOH(H_2O)^+ \cdot D_2$ (M=Mn, Fe, Co, Ni, Cu, Zn) complexes in the 3200-3800 cm^{-1} region are shown in Figure 3.11. The spectrum of $CuOH(H_2O)^+ \cdot D_2$ has been reported and analyzed previously,[11] but is reproduced here for comparison. In this spectral region there are two or three intense features present in each spectrum. Specifically, the $MnOH(H_2O)^+ \cdot D_2$ spectrum displays two sharp features at 3598 cm^{-1} and 3745 cm^{-1} while a third broad feature extends from 3634 cm^{-1} to 3720 cm^{-1}. This feature has resolved maxima at 3654 cm^{-1}, 3692 cm^{-1} and 3711 cm^{-1}. The spectrum of the Fe complex has three sharp features at 3593 cm^{-1}, 3659 cm^{-1} and 3733 cm^{-1}. The spectrum of Co complex is similar, with three peaks at 3593 cm^{-1}, 3661 cm^{-1}, and 3680 cm^{-1}. On the other hand, the $NiOH(H_2O)^+ \cdot D_2$ spectrum shows only two features, one narrow peak at 3597 cm^{-1} and a slightly broader feature at 3671 cm^{-1}. The spectrum of Cu complex again shows three features at 3590 cm^{-1}, 3612 cm^{-1} and 3684 cm^{-1}. Finally, the $ZnOH(H_2O)^+ \cdot D_2$ spectrum shows three strong features at 3582 cm^{-1}, 3646 cm^{-1}, and 3664 cm^{-1} as well as two additional small peaks at 3689 cm^{-1} and 3709 cm^{-1}.

The calculated lowest energy structure and corresponding vibrational spectrum for each complex are also shown in Figure 3.11, and the structural parameters are summarized in Table 3.1. For each complex, we considered several different spin multiplicities. We found that the

ground states have the same multiplicity as the corresponding bare M^{2+} ion,[21] namely sextet for $MnOH(H_2O)^+ \cdot D_2$, quintet for $FeOH(H_2O)^+ \cdot D_2$, quartet for $CoOH(H_2O)^+ \cdot D_2$, triplet for $NiOH(H_2O)^+ \cdot D_2$, doublet for $CuOH(H_2O)^+ \cdot D_2$, and singlet for $ZnOH(H_2O)^+ \cdot D_2$. For the bare $MOH(H_2O)^+$ complexes, all the calculated ground state structures have a nearly linear O-M-O geometry. Upon interaction with the D_2 tag, which binds to the metal center, the O-M-O bond distorts to a bent geometry, as shown in Figure 3.11. The extent of the distortion varies depending on the metal species, with the Cu complex being the most bent and the Zn complex closest to linear.

The calculated vibrational frequencies of the lowest energy structure of the Mn complex has a good agreement with the experimental spectrum. This yields the assignment of the peak at 3598 cm^{-1} to the H_2O symmetric stretch and the peak at 3745 cm^{-1} to the hydroxide stretch, which leaves the broad feature at 3634-3720 cm^{-1} to be assigned as the H_2O antisymmetric stretch. The harmonic calculation does not reproduce the complexity of this feature, but the calculated frequency is close to the lowest resolved maxima at 3654 cm^{-1}. The substantial broadening of the H_2O antisymmetric stretch can be attributed to the coupling of this vibration with the hindered internal rotation of the water ligand. Such coupling has been observed previously for other M-H_2O type of complexes.[22-25] The calculated barrier for the water rotation in the $MnOH(H_2O)^+ \cdot D_2$ complex is only ~15 cm^{-1}, making it feasible to give rise to the progression observed here.

The calculated spectrum for the $FeOH(H_2O)^+ \cdot D_2$ and $CoOH(H_2O)^+ \cdot D_2$ complexes have excellent agreement with the experimental spectrum. In both cases, the two lower frequency peaks are assigned to the H_2O symmetric and antisymmetric stretch while the highest frequency peak is assigned to the hydroxide stretch. Unlike the Mn complex, the antisymmetric H_2O stretch

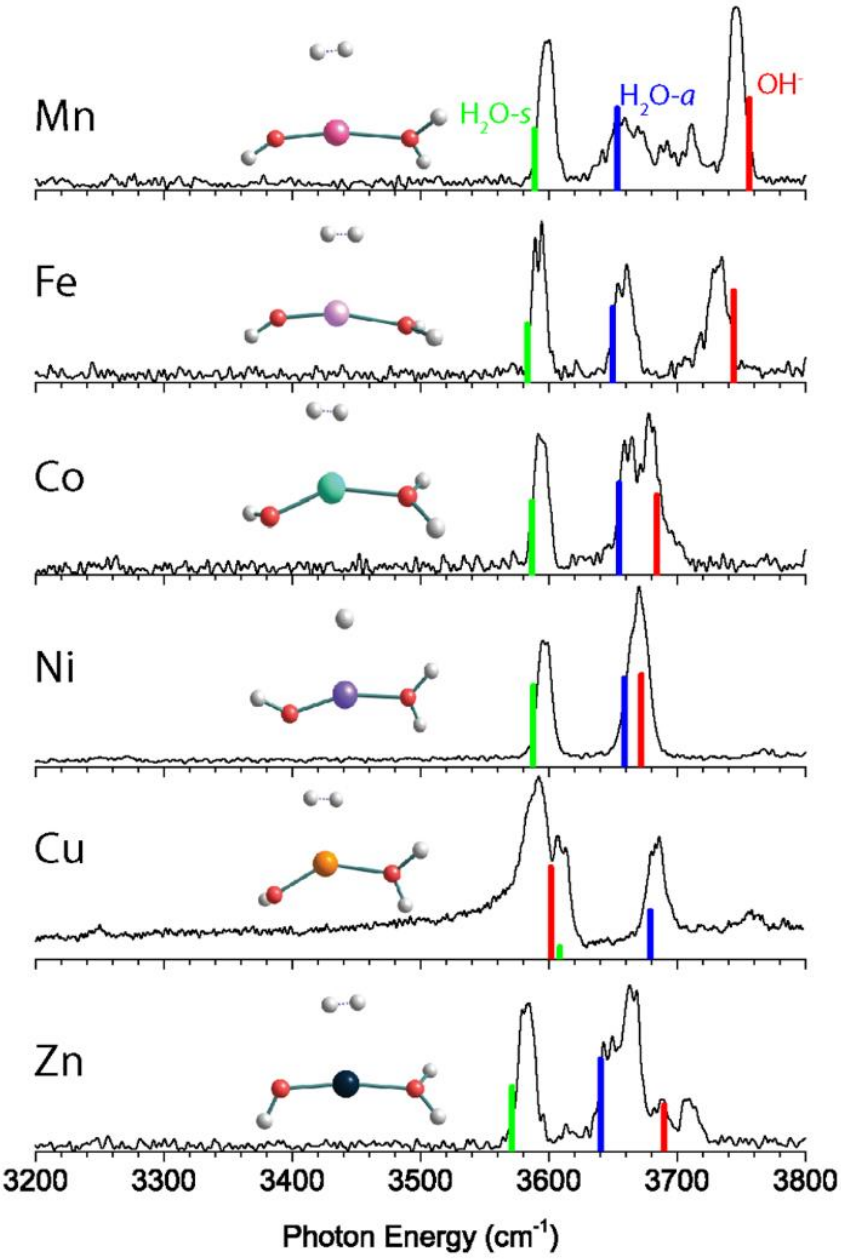

Figure 3.11- Experimental vibrational predissociation spectra and calculated (cam-B3LYP/def2TZVP) harmonic infrared spectra of the $MOH(H_2O)^+ \cdot D_2$ (M=Mn, Fe, Co, Ni, Cu, Zn) complexes.

of these two species remains a sharp peak, indicating higher H_2O hindered rotor barriers. For the $NiOH(H_2O)^+ \cdot D_2$ complex, the experimental spectrum shows only two features in the OH stretch region. The calculation indicates that this is because the hydroxide stretch and the H_2O antisymmetric stretch are nearly degenerate, and they both appear under the slightly broader feature at 3670 cm^{-1}. The lower frequency feature at 3597 cm^{-1} is then assigned to the H_2O symmetric stretch mode. The spectrum of the $CuOH(H_2O)^+ \cdot D_2$ species has been assigned previously.[11] In contrast to all the other species considered here, the calculation predicts that the hydroxide frequency is lower in frequency than the H_2O stretch modes. The peak at 3590 cm^{-1} is assigned to the hydroxide stretch and the peaks at 3608 cm^{-1} and 3680 cm^{-1} are assigned to the H_2O symmetric and antisymmetric stretches, respectively.

Finally, we consider the only closed-shell singlet species in the series, the $ZnOH(H_2O)^+ \cdot D_2$ complex. The calculated spectrum, shown in Figure 3.11, allows us to assign the lowest frequency feature at 3582 cm^{-1} to the H_2O symmetric mode. The assignment of the remaining features is more difficult. The complexity in the 3600-3750 cm^{-1} region is akin to the spectrum of the Mn complex, and is likely due to a similar coupling of the H_2O internal rotation with the antisymmetric stretch. Similar to the Mn complex, the structure of $ZnOH(H_2O)^+ \cdot D_2$ is quasi-linear with a calculated H_2O rotational barrier of only 14 cm^{-1}. Therefore, we tentatively assign the feature at 3646 cm^{-1} and the two small peaks at 3689 cm^{-1} and 3709 cm^{-1} to the H_2O antisymmetric stretch coupled to the H_2O internal rotation. These two small peaks are at approximately the same frequency as the partially resolved features in the hindered rotor progression of the Mn complex. This assignment leaves the peak at 3664 cm^{-1} to be the hydroxide stretching mode. The discrepancy between the calculated and experimental frequencies of this mode is 25 cm^{-1}, significantly larger than those of the other complexes (< 12

cm^{-1}). We note that although the calculated hydroxide frequency coincides with the small 3689 cm^{-1} feature, that assignment would leave the much more intense 3664 cm^{-1} peak unassignable. Furthermore, calculations yielded similar vibrational frequencies (within ~10 cm^{-1}) for all the low-lying conformers, making it unlikely that the observed spectral complexity is due to the presence of multiple conformers.

3.2.4 Discussion

Figure 3.12 highlights the progression of the hydroxide and H_2O stretch vibrational frequencies as a function of the metal species. The plot also includes values for the Mg and Ca complexes reported by Johnson *et al.*[17] Note that the $CaOH(H_2O)^+ \cdot D_2$ complex has a calculated O-M-O angle of ~100º, making its geometry distinctively different than the other complexes. We can see from Figure 3.12 that the hydroxide frequency is particularly sensitive to the nature of the metal center, shifting from a high value of 3856 cm^{-1} in $MgOH(H_2O)^+ \cdot D_2$ to a low value of 3590 cm^{-1} in $CuOH(H_2O)^+ \cdot D_2$. On the other hand, the H_2O stretch frequencies display a much more modest dependence on the metal center, varying by no more than 43 cm^{-1} for all the species considered here. Interestingly, for the transition metal species, the water frequencies generally blueshifts as the hydroxide vibration redshifts.

The observed trend in the hydroxide frequency is consistent with the Irving-Williams series which ranks the stability of complexes containing high-spin metal dications in the order of Mn < Fe < Co < Ni < Cu > Zn.[26, 27] The ordering of this series is attributed to the 2nd ionization energies of the metal center, which should also dictate the extent of charge transfer between the hydroxide and the metal center. Figure 3.13 shows that the observed hydroxide frequencies indeed has a clear linear dependence on the 2nd ionization energies[21] of the transition metal center. This relationship points to electron transfer from the hydroxide to the metal center as the

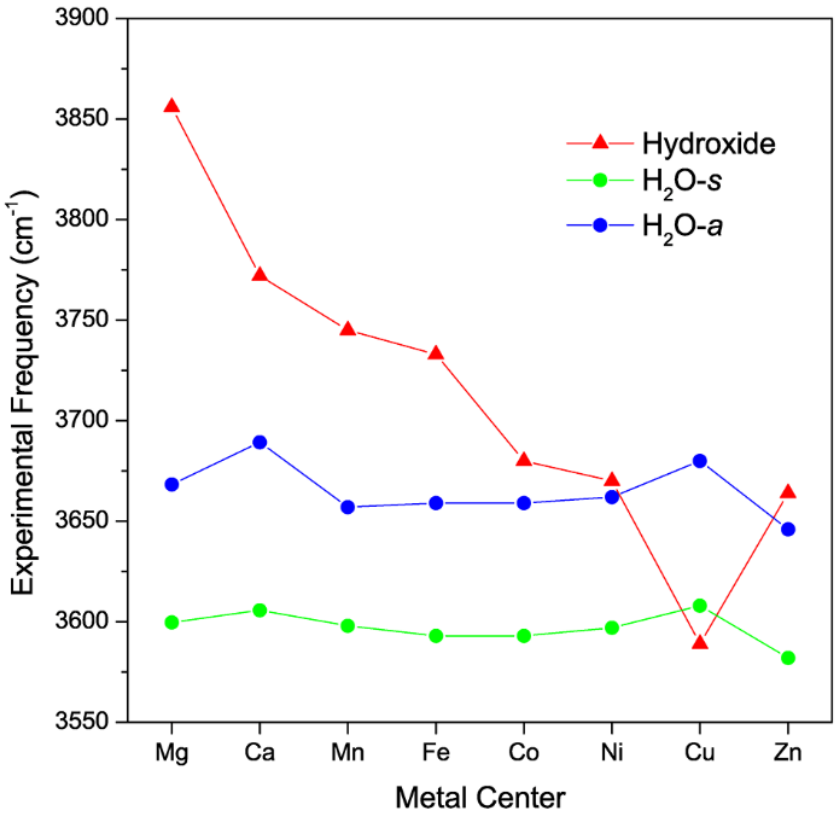

Figure 3.12- Experimental vibrational frequencies of the $MOH(H_2O)^+ \cdot D_2$ complexes as a function of the metal species. The values for the Mg and Ca complexes are obtained from ref. [17].

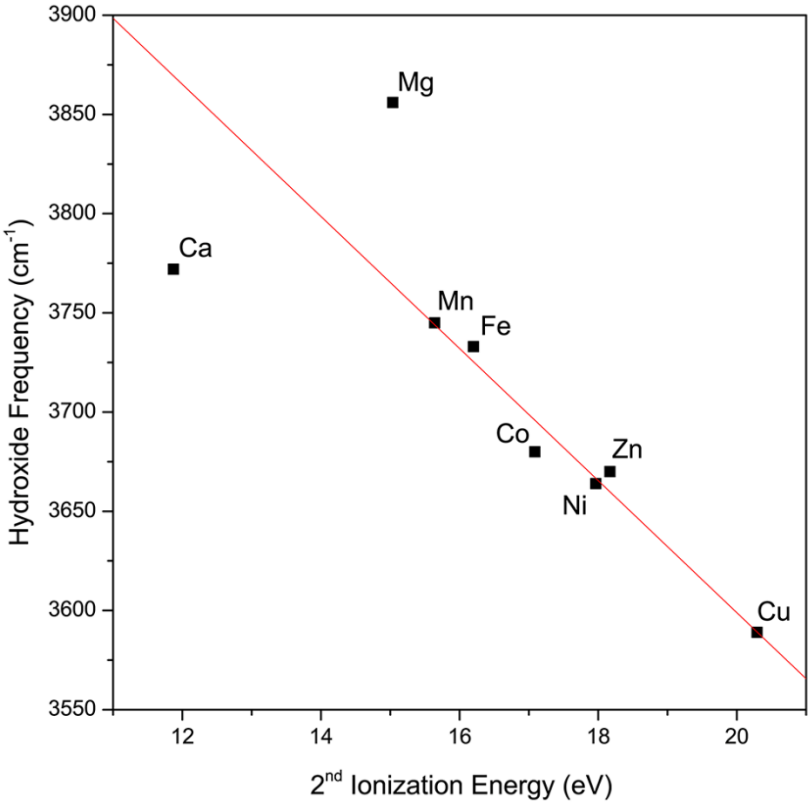

Figure 3.13- Experimental hydroxide vibrational frequency in the $MOH(H_2O)^+ \cdot D_2$ complexes as a function of the 2nd ionization energy of the bare metal. The experimental values for the hydroxide frequency of the Mg and Ca complexes are obtained from ref. [17]. The red line is a linear fit of the data points excluding the Mg and Ca values.

main cause for the observed frequency shift. However, we note that this trend does not hold well for the two alkaline earth metal species.

The good agreement between the calculated and the experimental vibrational spectra shows that the cam-B3LYP method is able to reproduce the observed trends. We therefore use the same level of theory to perform natural population analysis (NPA) on the $MOH(H_2O)^+ \cdot D_2$ complexes, taking a closer look at how the electron densities are distributed within these clusters.

The localized NPA charges on the metal center, hydroxide and H_2O ligand for each complex are listed in Table 3.1. The positive charge on the metal center decreases from +1.54e in Mn to +1.20e in Cu and then increases again to +1.61e in Zn. This change is mirrored by the negative charge on the hydroxide fragment which decreases from -0.64e in Mn to -0.32e in Cu and then increases again to -0.72e in Zn. On the other hand, the charge on H_2O is fairly constant, varying only between 0.07e and 0.09e for the different metal species. Table 3.1 also lists the NBO charges for the Mg and Ca complexes which shows that, as expected, these two species are much closer to a $M^{2+}OH^-$ contact ion pair with a charge of +1.84e on both alkaline earth metal centers.

The NPA charges indicates that, across the late first row transition metals, there is a gradual change in the electron transfer between the metal and hydroxide. To visualize this, electron density difference plots (isovalue=0.007), obtained by subtracting the SCF densities of the individual OH^- and $[M\text{-}OH_2]^{2+}$ fragments from the entire $MOH(H_2O)^+$ complex, are shown in Figure 3.14. For simplicity sake these plots were generated without the D_2 tag. Going from Mn to Cu, these SCF difference plots indicate that there is increasing electron density moving from the hydroxide to both the metal center and the M-OH bond. For the Mn complex, most of the electron density goes into the M-OH bond. This is true for the Fe complex as well, but it also

gains electron density in the metal d-orbitals. The increasing gain of electron density in the metal d-orbitals continues for Co, Ni and Cu complexes, which shows concurrent increase in electron withdrawal from the hydroxide moiety. For the Zn complex, the electron density moves into the metal s orbital, consistent with Zn having a filled 3d shell. These SCF difference plots also show the rearrangement of the electron densities upon M-OH interaction, as indicated, for example, by the changes in the d-orbital occupation. This significant reorganization as well as the gradual charge transfer highlights the complexity of the electronic structures in these transition metal complexes.

From the above discussion, it appears that the electron transfer from the hydroxide to the metal center should be responsible for the observed variation in hydroxide frequency. However, varying the partial charge on the hydroxide alone cannot account for the >150 cm^{-1} shift in its frequency. Specifically, the free hydroxyl radical has a vibrational frequency[28] of 3570 cm^{-1} while the free hydroxide anion has a slightly blueshifted frequency[29] of 3556 cm^{-1}. The experimental hydroxide frequencies for all the species considered here lie above those values, making the partial charge on the hydroxide seemingly irrelevant. The insensitivity of the hydroxide frequency to its own charge is consistent with the fact that the extra electron on the hydroxide anion occupies a non-bonding orbital, and therefore has minimal effect on the O-H bond length and frequency.

$MOH(H_2O)^+ \cdot D_2$	O-M-O Angle	M-O-H Angle	M-OH Bond (Å)	$M-OH_2$ Bond (Å)	O-H Bond (Å)	M Charge q_M (e)	OH Charge q_{OH} (e)	H_2O Charge (e)
$MgOH(H_2O)^+ \cdot D_2$	156.1	164.6	1.723	1.974	0.951	1.84	-0.90	0.04
$CaOH(H_2O)^+ \cdot D_2$	101.4	179.2	1.930	2.331	0.956	1.84	-0.86	0.02
$MnOH(H_2O)^+ \cdot D_2$	169.1	150.7	1.758	2.058	0.957	1.54	-0.64	0.07
$FeOH(H_2O)^+ \cdot D_2$	165.9	151.6	1.717	2.011	0.958	1.46	-0.58	0.08
$CoOH(H_2O)^+ \cdot D_2$	151.4	134.3	1.723	1.978	0.962	1.41	-0.55	0.08
$NiOH(H_2O)^+ \cdot D_2$	159.1	136.0	1.695	1.937	0.963	1.31	-0.47	0.09
$CuOH(H_2O)^+ \cdot D_2$	142.2	127.5	1.754	1.954	0.969	1.20	-0.32	0.07
$ZnOH(H_2O)^+ \cdot D_2$	171.8	120.5	1.740	1.919	0.962	1.61	-0.72	0.08

Table 3.1- Calculated structural parameters and NBO charges of the $MOH(H_2O)^+ \cdot D_2$ complexes at the cam-B3LYP/def2TZVP level.

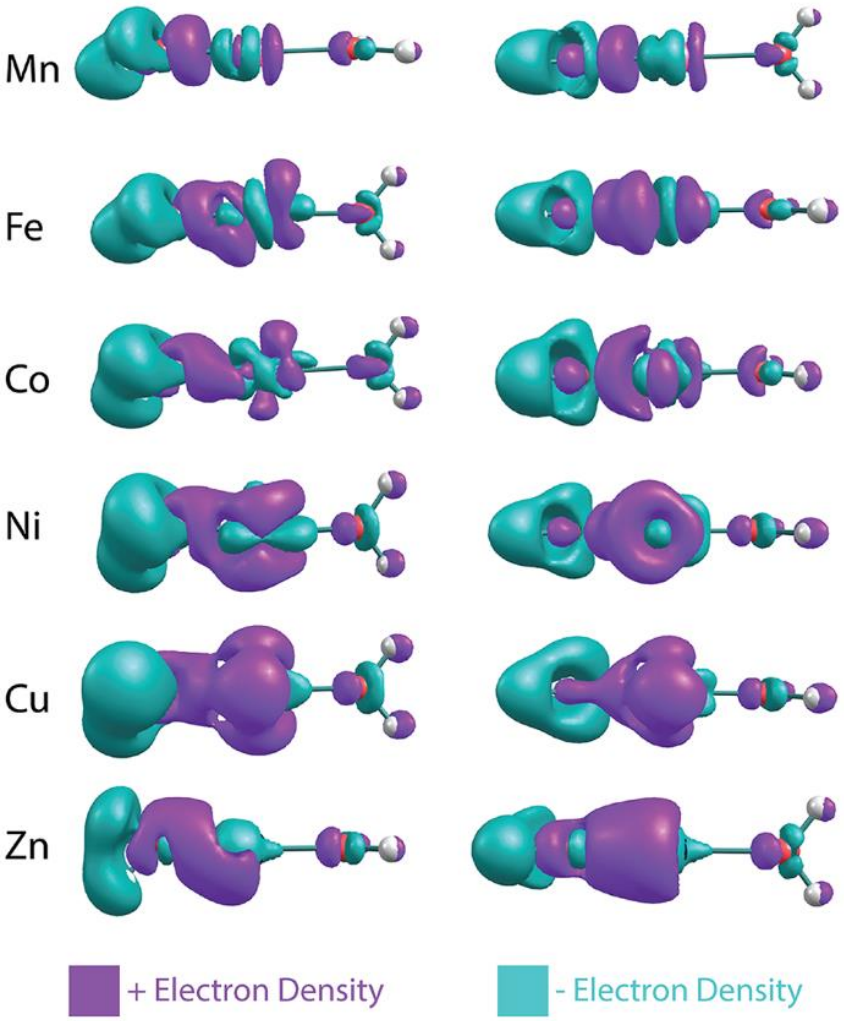

Figure 3.14- SCF electron density difference map of the $MOH(H_2O)^+$ complexes. The contour isovalue is 0.007. The difference map is obtained by subtracting the SCF densities of the individual OH^- and $[M\text{-}OH_2]^{2+}$ fragments from the entire $MOH(H_2O)^+$ complex.

There is an additional way in which the charge transfer can affect the hydroxide frequency. The metal center, with its varying degree of localized charge, can exert a strong electric field on the surrounding ligands and induce a vibrational Stark shift.[30-36] For example, the vibrational frequency of the free OH stretch in ion-containing water clusters have been observed to be modulated by the charge of the central ion.[34, 35] In order to explore this further, we performed CCSD/aug-cc-pVTZ calculations of water, hydroxide anion and hydroxyl radical in the presence of a +1e point charge. We choose this particular method over DFT because it generally produce more accurate dipole moment and polarizability. In all cases, the point charge was placed on the O atom side of the molecule in a co-linear fashion and the geometry was allowed to relax. The calculated harmonic vibrational frequencies as a function of $1/R^2$, where R is the distance from the point charge to the middle of the O-H bond, is plotted in Figure 3.15. This rather simplified picture does qualitatively reproduce several of the observed experimental trends. First, the hydroxide anion shows the most sensitivity to the electric field generated by the point charge, with the change in its frequency being more than five times greater than that of H_2O. The hydroxyl radical, on the other hand, is almost completely insensitive to the electric field. Also reproduced here is the opposing trend in the hydroxide and H_2O frequencies as a function of the electric field. As the electric field strength increases, the hydroxide stretch blueshifts whereas both H_2O stretch redshifts. The behavior of the hydroxide and water frequencies as a function of electric field are in agreement with the more detailed theoretical studies of Hermansson.[37-39]

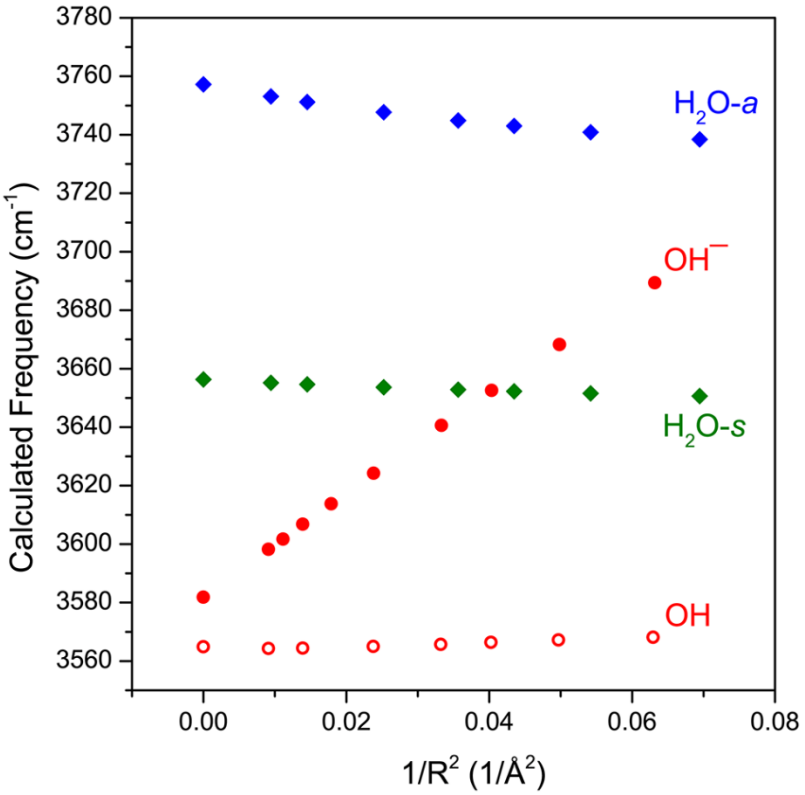

Figure 3.15- The calculated (CCSD/aug-cc-pVTZ) vibrational frequencies of OH^-, OH, and symmetric/antisymmetric H_2O at various distances from a point charge (+1e). The harmonic frequencies are scaled by 0.949.

Figure 3.15 shows that the vibrational frequency of the hydroxide anion varies nearly linearly with the field strength, in agreement with previous vibrational Stark shift studies.[30, 32] In order to assess the effect of the electric field on the hydroxide frequency in the $MOH(H_2O)^+$ complexes, we must take into account two effects of the M-OH charge transfer. First, increasing electron transfer reduces the effective partial charge on the metal center (q_M), yielding an electric field which is proportional to q_M/R^2. At the same time, decreasing charge on the hydroxide ligand also lowers the Stark tuning rate (Stark tuning rate is effectively the slope of Figure 3.15) to nearly zero as the hydroxide anion becomes a hydroxyl radical. Therefore, as the electric field from the metal center weakens, the hydroxide ligand concurrently becomes less sensitive to the field. If we assume that the Stark tuning rate is proportional to the partial charge on the hydroxide (q_{OH}) then the hydroxide frequency shift should be proportional to:

$$\Delta\omega \propto q_{OH}q_M/R^2$$

Figure 3.16 plots the hydroxide frequency of all the $MOH(H_2O)^+ \cdot D_2$ complexes considered here as a function of $q_{OH}q_M/R^2$. One can clearly see that as the electron transfer increases and the effective electric field from the metal center weakens, the observed hydroxide frequency correspondingly redshifts, going towards the free hydroxyl radical frequency. The linear dependence indicates that this frequency shift is mainly due to the modulation of the vibrational Stark shift as a function of the charge transfer between the hydroxide ligand and the metal center. The Mg and Ca complexes also follow the same trend and the difference in their hydroxide frequencies can be explained by their different M-OH bond lengths. Specifically, the Ca complex has a much longer M-OH bond, and its hydroxide ligand effectively experiences a weaker field from the same +1.84e charge on the metal. For the transition metals, the M-OH

bonds all have similar length, and the differences in the hydroxide frequency can be mostly accounted for by the different amount of charge transfer.

The Zn complex is the only species that falls outside the linear trend in Figure 3.16. There are two possible explanations for this discrepancy. First, the calculated hydroxide frequency for the Zn complex shows the largest deviation from the experimental value. It is therefore possible that DFT has a larger error in calculating the amount of charge transfer in this complex. This is supported by the fact that Zn has a similar 2nd ionization energy as Ni and their respective complexes also have similar experimental hydroxide frequencies. From these two facts, one would expect a similar amount of charge transfer for both species, but DFT calculation gives much less charge transfer for the Zn complex. Another possibility for the different behavior of the Zn complex is the involvement of the 4s orbital in the charge transfer, as highlighted in Figure 3.14. This different electron distribution might lead to a different effective electric field than the other species. In the case of the Mg and Ca complexes, since little charge transfer occurs, this may not play as much of a role. We also note that our analysis relies on the calculated atomic charges which varies depending on the method used. The NPA approach used here tends to be more reliable for ionic compounds such as the metal hydroxide complexes, however, we note that we found a similar trend using the Mulliken charges.

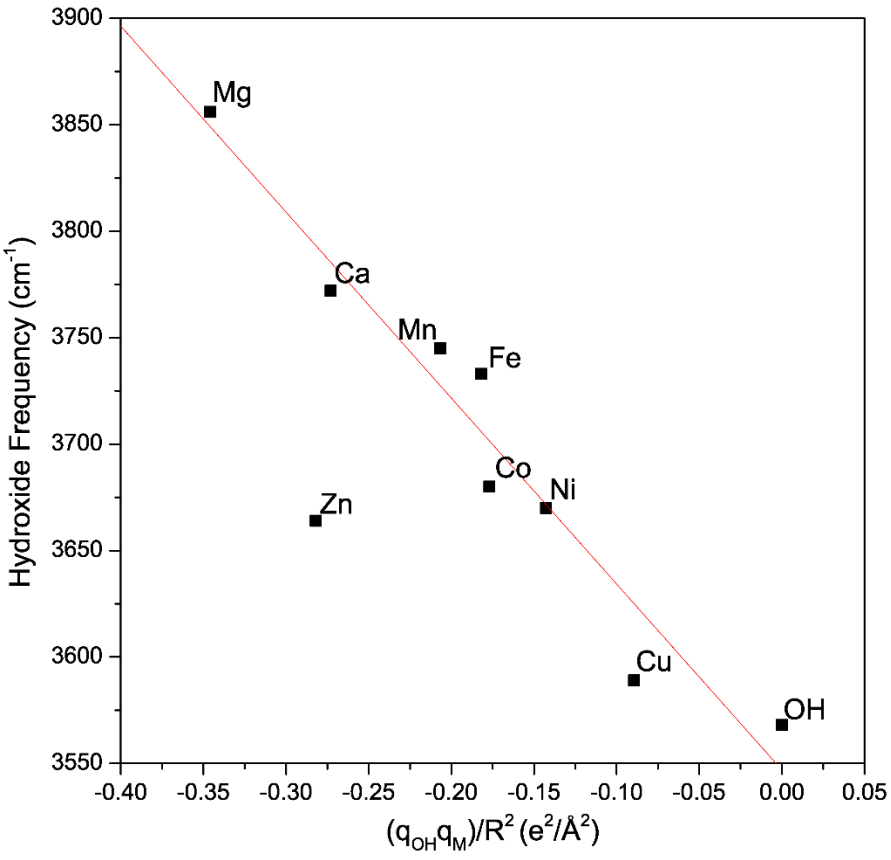

Figure 3.16- The experimental hydroxide frequency as a function of the field induced by the metal center multiplied by the charge present on the hydroxide. The gas phase vibrational frequency of the hydroxyl radical is also included. The experimental values for the hydroxide frequency of the Mg and Ca complexes are obtained from ref. [17]. The red line is a linear fit of the data points excluding the Zn complex.

3.2.5 Conclusion

The vibrational spectra of mass-selected $MOH(H_2O)^+ \cdot D_2$ (M=Mn, Fe, Co, Ni, Cu, or Zn) complexes, acquired using cryogenic ion infrared predissociation spectroscopy, are presented. This series of transition metals bridge the gap between the Mg and Ca complexes studied by Johnson *et al.*[17] and the Cu complex studied previously in our group[11]. The evolution of the vibrational frequencies of the hydroxide and water ligands as a function of the metal center sheds light on the gradual charge transfer behavior of this series of metals. The interaction between the hydroxide ligand and the metal center was found to be more ionic in the Mg, Ca, and Mn complexes, while becoming more covalent in character for the Fe, Co, Ni and Cu complexes. The hydroxide vibration was found to be highly sensitive to the electric field generated by the charge on the metal center, giving rise to abnormally high frequencies for this moiety. Two correlated effects, charge on the metal center and electron density on the hydroxide ligand, yielded a linear dependence of the hydroxide frequency on $q_{OH}q_M/R^2$. This description of M-OH interaction provides a framework for future investigation of charge transfer and vibrational spectroscopy of these metal complexes. Additionally, the well-resolved experimental spectra can serve as a benchmark for electronic structure calculations to provide better description of these complex transition metal species.

References:

1. K. Ando, *J. Phys. Chem. B*, 2008, **112**, 250-256.

2. A. Hoffmann, S. Binder, A. Jesser, R. Haase, U. Flörke, M. Gnida, M. Salomone Stagni, W. Meyer-Klaucke, B. Lebsanft, L. E. Grünig, S. Schneider, M. Hashemi, A. Goos, A. Wetzel, M. Rübhausen and S. Herres-Pawlis, *Angew. Chem. Int. Ed.*, 2014, **53**, 299-304.

3. M. Y. M. Pau, M. I. Davis, A. M. Orville, J. D. Lipscomb and E. I. Solomon, *J. Am. Chem. Soc.*, 2007, **129**, 1944-1958.

4. J. Roithova and D. Schroder, *Coord. Chem. Rev.*, 2009, **253**, 666-677.

5. J. Šima and J. Makáňová, *Coord. Chem. Rev.*, 1997, **160**, 161-189.

6. S. Bonhommeau, N. Pontius, S. Cobo, L. Salmon, F. M. F. de Groot, G. Molnar, A. Bousseksou, H. A. Durr and W. Eberhardt, *Phys. Chem. Chem. Phys.*, 2008, **10**, 5882-5889.

7. T. Petrenko, K. Ray, K. E. Wieghardt and F. Neese, *J. Am. Chem. Soc.*, 2006, **128**, 4422-4436.

8. L. S. Levitt, *Science*, 1954, **120**, 33-35.

9. J. Rittle and M. T. Green, *Science*, 2010, **330**, 933-937.

10. X. Shan and L. Que Jr, *J. Inorg. Biochem.*, 2006, **100**, 421-433.

11. B. M. Marsh, J. Zhou and E. Garand, *Journal of Physical Chemistry A*, 2014, **118**, 2063-2071.

12. A. F. Sweeney, J. T. O'Brien, E. R. Williams and P. B. Armentrout, *Int. J. Mass Spectrom.*, 2014, DOI: http://dx.doi.org/10.1016/j.ijms.2014.08.037, http://dx.doi.org/10.1016/j.ijms.2014.1008.1037.

13. S. M. Barnett, K. I. Goldberg and J. M. Mayer, *Nat. Chem.*, 2012, **4**, 498-502.

14. Z. F. Chen, P. Kang, M. T. Zhang, B. R. Stoner and T. J. Meyer, *Energy Environ. Sci.*, 2013, **6**, 813-817.

15. Z. F. Chen and T. J. Meyer, *Angew. Chem. Int. Ed.*, 2013, **52**, 700-703.

16. M. T. Zhang, Z. F. Chen, P. Kang and T. J. Meyer, *J. Am. Chem. Soc.*, 2013, **135**, 2048-2051.

17. C. J. Johnson, L. C. Dzugan, A. B. Wolk, C. M. Leavitt, J. A. Fournier, A. B. McCoy and M. A. Johnson, *J. Phys. Chem. A*, 2014, **118**, 7590-7597.

18. M. J. Frisch, G. W. Trucks, H. B. Schlegel, G. E. Scuseria, M. A. Robb, J. R. Cheeseman, G. Scalmani, V. Barone, B. Mennucci, G. A. Petersson, H. Nakatsuji, M. Caricato, X. Li, H. P. Hratchian, A. F. Izmaylov, J. Bloino, G. Zheng, J. L. Sonnenberg, M. Hada, M. Ehara, K. Toyota, R. Fukuda, J. Hasegawa, M. Ishida, T. Nakajima, Y. Honda, O. Kitao, H. Nakai, T. Vreven, J. A. Montgomery, Jr., J. E. Peralta, F. Ogliaro, M. Bearpark, J. J. Heyd, E. Brothers, K. N. Kudin, V. N. Staroverov, R. Kobayashi, J. Normand, K. Raghavachari, A. Rendell, J. C. Burant, S. S. Iyengar, J. Tomasi, M. Cossi, N. Rega, N. J. Millam, M. Klene, J. E. Knox, J. B. Cross, V. Bakken, C. Adamo, J. Jaramillo, R. Gomperts, R. E. Stratmann, O. Yazyev, A. J. Austin, R. Cammi, C. Pomelli, J. W. Ochterski, R. L. Martin, K. Morokuma, V. G. Zakrzewski, G. A. Voth, P. Salvador, J. J. Dannenberg, S. Dapprich, A. D. Daniels, Ö. Farkas, J. B. Foresman, J. V. Ortiz, J. Cioslowski and D. J. Fox, *Journal*, 2009, **Revision D.01**.

19. A. F. Sweeney and P. B. Armentrout, *Journal of Physical Chemistry A*, 2014, **118**, 10210-10222.

20. E. D. Glendening, J. K. Badenhoop, A. E. Reed, J. E. Carpenter, J. A. Bohmann, C. M. Morales, C. R. Landis and F. Weinhold, *Journal*, 2013.

21. A. Kramida, Y. Ralchenko, J. Reader and NIST_ASD_Team, *Journal*, 2014.

22. P. D. Carnegie, B. Bandyopadhyay and M. A. Duncan, *J. Chem. Phys.*, 2011, **134**, 014302.

23. A. L. Nicely, D. J. Miller and J. M. Lisy, *J. Mol. Spectrosc.*, 2009, **257**, 157-163.

24. T. D. Vaden, B. Forinash and J. M. Lisy, *J. Chem. Phys.*, 2002, **117**, 4628-4631.

25. N. R. Walker, R. S. Walters, E. D. Pillai and M. A. Duncan, *J. Chem. Phys.*, 2003, **119**, 10471-10474.

26. S. I. Gorelsky, L. Basumallick, J. Vura-Weis, R. Sarangi, K. O. Hodgson, B. Hedman, K. Fujisawa and E. I. Solomon, *Inorg. Chem.*, 2005, **44**, 4947-4960.

27. H. Irving and R. J. P. Williams, *J. Chem. Soc.*, 1953, DOI: 10.1039/JR9530003192, 3192-3210.

28. J. P. Maillard, J. Chauville and A. W. Mantz, *J. Mol. Spectrosc.*, 1976, **63**, 120-141.

29. J. C. Owrutsky, N. H. Rosenbaum, L. M. Tack and R. J. Saykally, *J. Chem. Phys.*, 1985, **83**, 5338-5339.

30. S. S. Andrews and S. G. Boxer, *J. Phys. Chem. A*, 2000, **104**, 11853-11863.

31. S. G. Boxer, *J. Phys. Chem. B*, 2009, **113**, 2972-2983.

32. S. H. Brewer and S. Franzen, *J. Chem. Phys.*, 2003, **119**, 851-858.

33. T. Mani, D. C. Grills and J. R. Miller, *J. Am. Chem. Soc.*, 2015, **137**, 1136-1140.

34. J. T. O'Brien and E. R. Williams, *J. Am. Chem. Soc.*, 2012, **134**, 10228-10236.

35. J. S. Prell, J. T. O'Brien and E. R. Williams, *J. Am. Chem. Soc.*, 2011, **133**, 4810-4818.

36. D. M. Walker, R. Wang and L. J. Webb, *Phys. Chem. Chem. Phys.*, 2014, **16**, 20047-20060.

37. K. Hermansson, *Chemical Physics*, 1993, **170**, 177-184.

38. K. Hermansson, *International Journal of Quantum Chemistry*, 1993, **45**, 747-758.

39. K. Hermansson, P. A. Bopp, D. Spångberg, L. Pejov, I. Bakó and P. D. Mitev, *Chemical Physics Letters*, 2011, **514**, 1-15.

3.3 Coordination Structure and Charge Transfer in Microsolvated Transition Metal Hydroxide Clusters $[MOH]^+(H_2O)_{1-4}$

Published in: *Physical Chemistry Chemical Physics*, **17**, 23195-23206 (2015)

Abstract

Infrared vibrational predissociation spectra of transition metal hydroxide clusters, $[MOH]^+(H_2O)_{1-4}\cdot D_2$ with M = Mn, Fe, Co, Ni, Cu, and Zn, are presented and analyzed with the aid of density functional theory calculations. For the $[MnOH]^+$, $[FeOH]^+$, $[CoOH]^+$ and $[ZnOH]^+$ species, we find that the first coordination shell contains three water molecules and the four ligands are arranged in a distorted tetrahedral geometry. $[CuOH]^+$ can have either two or three water molecules in the first shell arranged in a planar arrangement, while $[NiOH]^+$ has an octahedral ligand geometry with the first shell likely closed with five water molecules. Upon closure of the first coordination shell, characteristic stretch frequencies of hydrogen-bonded OH in the 2500-3500 cm^{-1} region are used to pinpoint the location of the water molecule in the second shell. The relative energetics of different binding sites are found to be metal dependent, dictated by the first-shell coordination geometry and the charge transfer between the hydroxide and the metal center. Finally, the frequency of the hydroxide stretch is found to be sensitive to the vibrational Stark shift induced by the charged metal center, as observed previously for the smaller $[MOH]^+(H_2O)$ species. Increasing solvation modulates this frequency by reducing the extent of the charge transfer while elongating the M-OH bond.

3.3.1 Introduction

Interactions between a metal center and its ligands are important for the stability of the complex as well as its functionality. While such interactions can be modified by functional groups on the ligand, it can be further altered by the presence of solvent molecules. For example, the extent of charge transfer between a metal center and a ligand group can be influenced by interactions with nearby polar solvents,[1-4] and the structural arrangement of the ligand groups can also vary depending on local solvent environment. Two recent studies highlight the intricacies present in such solvent-driven changes in metal-ligand interactions for the simple case of $[MOH]^+$ complexes. In a vibrational predissociation study by Johnson et al,[5] they found that the hydroxide frequency redshifts with increasing solvation in the $[MgOH]^+(H_2O)_{1-5}$ and $[CaOH]^+(H_2O)_{1-5}$ clusters. On the other hand, the same hydroxide stretch blueshifts with increasing solvation in the $[CuOH]^+(H_2O)_{1-3}$ clusters.[6] Furthermore, these complexes have rather different solvation structures, distinctive from each other when surrounded by three or more water molecules.

In an effort to understand the differences manifested in these prototypical ion pair metal complexes, we recently probed the charge transfer between the metal and hydroxide ligand in the small $[MOH]^+(H_2O)$ complexes for the Mn-Zn series.[7] Interestingly, we found that the degree of charge transfer is mainly dictated by the 2nd ionization potential of the transition metal, although such a trend does not hold for the alkali earth metals. Additionally, the vibrational frequency of the hydroxide ligand demonstrates a high sensitivity to the local charge environment, varying by >150 cm^{-1} depending on the electric field induced by the metal center. This dramatic vibrational Stark shift provides a well behaved correlation between the observed hydroxide frequency and the extent of charge transfer. This trend holds true for $[MgOH]^+$ and $[CaOH]^+$ as well, allowing

the hydroxide frequency to serve as an effective in-situ probe of charge transfer. Therefore, the observed opposing trends in the hydroxide stretch for $[MgOH]^+(H_2O)_{1-5}$, $[CaOH]^+(H_2O)_{1-5}$, and $[CuOH]^+(H_2O)_{1-3}$ clusters are likely reflecting different solvent-driven changes in the metal-ligand charge transfer.

Another open question is how the presence of a charged ligand affects the solvation structure of the metal complex. There are only a few studies on the stepwise solvation of ion pairs,[3, 5-8] but many reports have focused on the molecular-level interactions controlling solvation of isolated alkali and transition metal ions. Gas-phase studies of these singly and doubly charged clusters have proven an essential tool for understanding fundamental solvation processes. Specifically, coordination numbers and sequential binding energies of water have been previously determined by collision-induced-dissociation mass spectrometry (CID-MS) for the singly charged transition metals Ti – Cu[9] as well as for Ca^{2+}, Mg^{2+}, and Fe^{2+}, and Zn^{2+}.[10-14] Additionally, structures of hydrated singly and doubly charged alkali and transition metal clusters have been very well characterized by photodissociation spectroscopy.[15-26]

Building on these results of solvated metal ions, we extend our study of the $[MOH]^+$ species to larger clusters to probe the effect of solvation on the M-OH charge transfer as well as to determine how the coordination sphere is influenced by the charged hydroxide ligand. Specifically, we present the infrared predissociation spectroscopy of mass-selected $[MOH]^+(H_2O)_{1-4}$ clusters, with M = Mn, Fe, Co, Ni, Cu, and Zn. The experimental spectra are analyzed with the help of density functional theory calculations. The vibrations in the OH stretch region, between 2600 cm^{-1} and 3800 cm^{-1}, are used to reveal the coordination number and solvation structure of these clusters. Particularly, several hydration motifs are found for these transition metal clusters, with their relative energies dependent on the metal-hydroxide

interaction. We also find a progression of hydroxide frequency behavior as a function of solvation, which is related to the modulation of the vibrational Stark shift. The results point to the water molecules acting as a polarizable medium that affects the charge-transfer interaction even in the molecular solvation regime.

3.3.2 Experimental and Computational Details

The vibrational predissociation spectra of D_2-tagged $[MOH]^+(H_2O)_n$ (M = Mn-Zn) complexes were acquired using a homebuilt cryogenic ion photofragment spectrometer, described in detail previously.[6] Ions of interest were generated via electrospray ionization of ~1 mM aqueous solution of the corresponding metal sulfate, guided by hexapole ion guides through three differentially pumped stages, and collected in a 3D quadrupole ion trap (Jordan TOF) held at 10K. Buffer gas, consisting of 10% D_2 in a balance of helium, was pulsed into the ion trap for collisional cooling and formation of D_2 adducts, which serve as messengers for vibrational predissociation spectroscopy. After a 90 ms delay allowing for the evacuation of the buffer gas, the cooled ions were extracted from the trap into a time-of-flight mass spectrometer. The species corresponding to the m/z of the $[MOH]^+(H_2O)_n \cdot D_2$ ions were isolated using a mass gate and intersected with the output of a Nd:YAG pumped tunable OPO/OPA laser system (Laservision). When the IR photon energy is resonant with a vibrational transition, the absorption of a single photon is sufficient to induce the evaporation of the weakly bound D_2 tag. Photofragment ions corresponding to the bare $[MOH]^+(H_2O)_n$ species were then separated from the parent ions in a two-stage reflectron. The resulting photofragment intensity as a function of the photon energy yielded linear IR spectra. The final intensities of the experimental spectra were normalized to the laser output power.

To aid the analysis of the experimental spectra, electronic structure calculations were performed using the Gaussian 09 computational package.[27] Geometry optimizations, with Gaussian 09 standard tight convergence criteria, and harmonic frequency calculations were carried out at the cam-B3LYP/def2TZVP level of theory. Previous works[7, 28] have shown that the cam-B3LYP functional yields reasonable binding energies and more importantly, harmonic vibrational spectra (scaled by a factor of 0.955) that showed good agreement with experiment for $[MOH]^+(H_2O)_n$. Charge analysis on the metal and hydroxide were carried out using natural population analysis of NBO 6.[29] Lastly, isomer searches were guided by chemical intuition. Various binding sites for each additional water molecule were explored with geometry optimization carried out at normal convergence criteria. Similar structures were eliminated before tight convergence was applied.

3.3.3 Results and Analysis

The vibrational spectra of $[MOH]^+(H_2O)_n$, with M = Mn, Fe, Co, Ni, Cu, Zn, are shown in Figures 3.17-3.22. For all the metal species studied here, most of the vibrational features are in the 3600-3800 cm^{-1} free OH region. For the larger n=4 clusters, all metal species show additional features between 2500-3500 cm^{-1}, characteristic of hydrogen-bonded (H-bonded) OH vibrations. All the experimental peak positions and assignments are summarized in Table 3.2. The ground states of the $[MOH]^+(H_2O)_n$ species have the same spin multiplicity as the bare M^{2+} ion. This yields sextet for Mn, quintet for Fe, quartet for Co, triplet for Ni, doublet for Cu, and singlet for Zn.

The experimental vibrational spectra of the singly hydrated clusters and the $[CuOH]^+(H_2O)_{1-3}$ clusters have been analyzed in detail previously.[6, 7] The data are reproduced

$[MOH]^+$ $(H_2O)_n$	$[MnOH]^+$	$[FeOH]^+$	$[CoOH]^+$	$[NiOH]^+$	[CuOH]+	$[ZnOH]^+$	Assignment
n=2	2905	2810		2845	2960	2950	D_2
	3589_{OH}			3525_{OH}	3565_{D2}	3545_{D2}	H_2O-s
	3614	3610	3611	3610	3610	3602	H_2O-s
	3678			3672	3665	3657	H_2O-as
	3697	3685	3686	3688	3685	3678	H_2O-as
	3753	3744	3686	3688	3632	3695	Hydroxide
n=3		2960	2960		2963		D_2
	3568_{OH}	3562_{OH}	3545_{OH}	3493_{OH}	3370/3555	3543_{OH}	H_2O-s
	3597_{D2}	3586_{D2}	3586_{D2}	3606	3593_{D2}	3580_{D2}	H_2O-s
	3624	3615	3619	3626	3625	3614	H_2O-s
	3681						H_2O-as
	3694	3681	3673	3680	3663-3688	3684	H_2O-as
	3705	3691	3700	3691	3706	3698	H_2O-as
	3756	3745	3700	3709	3688	3714	Hydroxide
n=4			2962	2972	2965	2964	D_2
	$\sim 2650_{H2O}$		$\sim 2650_{H2O}$		~3370	$\sim 2600_{H2O}$	H_2O-s
	$\sim 3150_{OH}$	$\sim 3400_{H2O}$	$\sim 3280_{OH}$		$\sim 3485_{H2O}$	$\sim 3230_{OH}$	H_2O-s
	3597_{D2}	3593_{D2}	3592_{D2}	3378_{OH}		3590_{D2}	H_2O-s
	3623	3620	3617	3612	3615	3612/3625	H_2O-s
	3685-3720	3680-3716	3680-3717	3685-3711	3650-3690	3674,3692,3720	H_2O-as
	3735	3734/3751	3717	3711	3690	3720	Hydroxide

Table 3.2- Experimental frequencies and assignments of the $[MOH]^+(H_2O)_{2\text{-}4}$ clusters. The subscript denotes the group to which the H-bond is donated.

here for comparison. The assignment process here is similar to that carried out in the previous studies, where the harmonic vibrational spectra calculated at the cam-B3LYP/def2TZVP level serve as the main guidance. The cam-B3LYP functional yielded harmonic vibrational spectra with good agreement with experimental spectra, except for two previously[6] noted systematic deviations. First, the hydroxide stretch frequency, which is extremely sensitive to the charge transfer between the metal center and the hydroxide, is typically overestimated by ~10-30 cm^{-1}. Second, the strength of the D_2-H_2O interaction is overestimated, resulting in an overly red-shifted symmetric stretch for the D_2 tagged water. This error may arise from anharmonic nature of this weak interaction,[30] which is not captured by our harmonic calculations. As discussed in detail in our earlier report on $CuOH^+(H_2O)_n$ clusters[6], higher level ab-initio calculations, such as CCSD, can provide a better description of the D_2-H_2O interaction, but the hydroxide frequency is worse. While error in D_2-H_2O interaction only affects that specific water, the error in hydroxide frequency reflects improper treatment of the charge transfer which is likely to affect the whole cluster. For this reason, we rely on the cam-B3LYP calculated harmonic spectra. To simplify the figures and the discussion, only the assigned isomers and their calculated spectra are shown here.

Finally, for the calculated spectra presented here, the D_2 tag is not included once it binds on the water. In our previous study of the $[CuOH]^+$ system, it was found that the D_2 tag binds to the metal center for the smaller clusters and moves onto one of the water molecules when the coordination sphere of the metal is filled. This can be deduced from the experimental spectra by looking at the frequency of the weak (nominally forbidden) D_2 stretch. Namely, D_2 interacting directly with the metal center has a frequency lower than 2900 cm^{-1} while D_2 interacting with a water has a frequency around 2960 cm^{-1}. Additionally, the D_2-perturbed water has a symmetric

stretch in the 3580-3600 cm^{-1} region, ~30 cm^{-1} redshifted from the unperturbed symmetric stretch. The exclusion of D_2 in the larger cluster calculations is mainly due to the aforementioned error in the D_2-H_2O interaction. The calculated IR spectra including the D_2 tag typically show greater deviations from experimental spectra than the bare cluster, and therefore do not add any useful information for making assignments. Note that when comparing calculated spectrum of the bare cluster to the experimental spectrum, the most noticeable differences are the lack of D_2 stretch and an additional H_2O stretch in the 3580-3600 cm^{-1} region.

a) $[MnOH]^+(H_2O)_n$

The experimental IR predissociation spectra of $[MnOH]^+(H_2O)_{1-4}$ with corresponding calculated spectra and geometries are shown in Figure 3.17. The experimental spectrum of the singly hydrated species has three bands in the OH stretch region corresponding to the H_2O symmetric (H_2O-s) and antisymmetric (H_2O-as) stretch and the hydroxide (OH) stretch. These three bands remain well-separated up to the n=3 cluster. Note that the additional features around 3700 cm^{-1} in the n=1 spectrum is due to coupling of the H_2O-as stretch with hindered internal rotation.

The n=2 cluster has the two water molecules and hydroxide arranged in a quasi-planar T geometry with a weak HO-H_2O interaction. This gives rise to a doublet for the H_2O-s and H_2O-as modes. The bare n=3 cluster has a distorted tetrahedral geometry with two weak HO-H_2O interactions, again giving rise to H_2O-s and H_2O-as doublets. The feature at 3597 cm^{-1} is assigned to D_2 perturbed H_2O-s while the feature at 3568 cm^{-1} is assigned to H_2O-s with HO-H_2O interaction. The experimental spectrum of the n=4 cluster shows two broad and redshifted H-bonding features centered around 2650 cm^{-1} and 3150 cm^{-1}, indicating that the metal

coordination shell is closed at n=3. The two lowest energy isomers, in which the fourth water is interacting directly with the hydroxide moiety, are found to be present in the experimental spectrum. The first isomer has a four-membered H-bond ring, with the second-shell water accepting an H-bond from a water and donating an H-bond to the hydroxide (AD configuration). This geometry gives rise to the very broad feature at ~2650 cm^{-1} corresponding to the H_2O-H_2O H-bond, and a feature at ~3150 cm^{-1} corresponding to the HO-H_2O interaction. The other isomer, 251 cm^{-1} higher in energy, has the second-shell water in a double acceptor-single donor (AAD) configuration. Its presence is responsible for the very broad and asymmetric appearance of the ~3150 cm^{-1} feature. Notably, the broad shoulder at ~3300 cm^{-1} is likely due to this isomer, corresponding to the two H_2O-H_2O H-bonds. In the ~3600 cm^{-1} region, the calculated H_2O-s of the free water molecules for both isomers have the same frequency, and it agrees well with the experimental feature at 3623 cm^{-1}. The 3597 cm^{-1} feature is therefore assigned to H_2O-s of the D_2 tagged water. The ~3700 cm^{-1} region of the experimental spectrum has several partially resolved peaks, which correspond to the H_2O-as stretch of water (or the non H-bonded OH of a water). Lastly, calculations also yielded similar hydroxide stretch frequencies for both isomers, and the bluest experimental feature at 3735 cm^{-1} is assigned to this vibration.

b) $[FeOH]^+(H_2O)_n$

Figure 3.18 shows the experimental IR spectra and calculated results for $[FeOH]^+(H_2O)_{1-4}$. Similar to $[MnOH]^+$, the $[FeOH]^+$ series has three distinct bands in the OH stretch region corresponding to the H_2O-s, the H_2O-as, and the hydroxide stretch. With increasing solvation, the H_2O-as band and hydroxide stretch move towards each other, but they do not yet overlap in the n=4 spectrum.

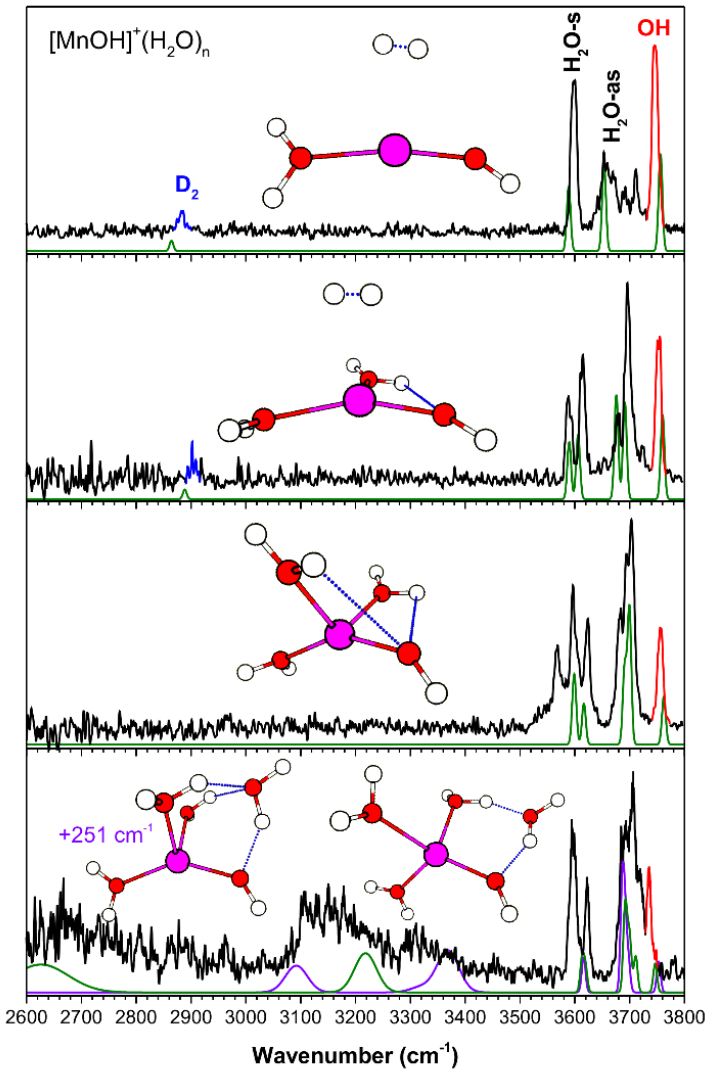

Figure 3.17- The experimental (black) and calculated (purple/green, cam-B3LYP/def2TZVP) vibrational spectra of $[MnOH]^+(H_2O)_n \cdot D_2$. Highlighted in red is the hydroxide stretch and in blue is the D_2 stretch.

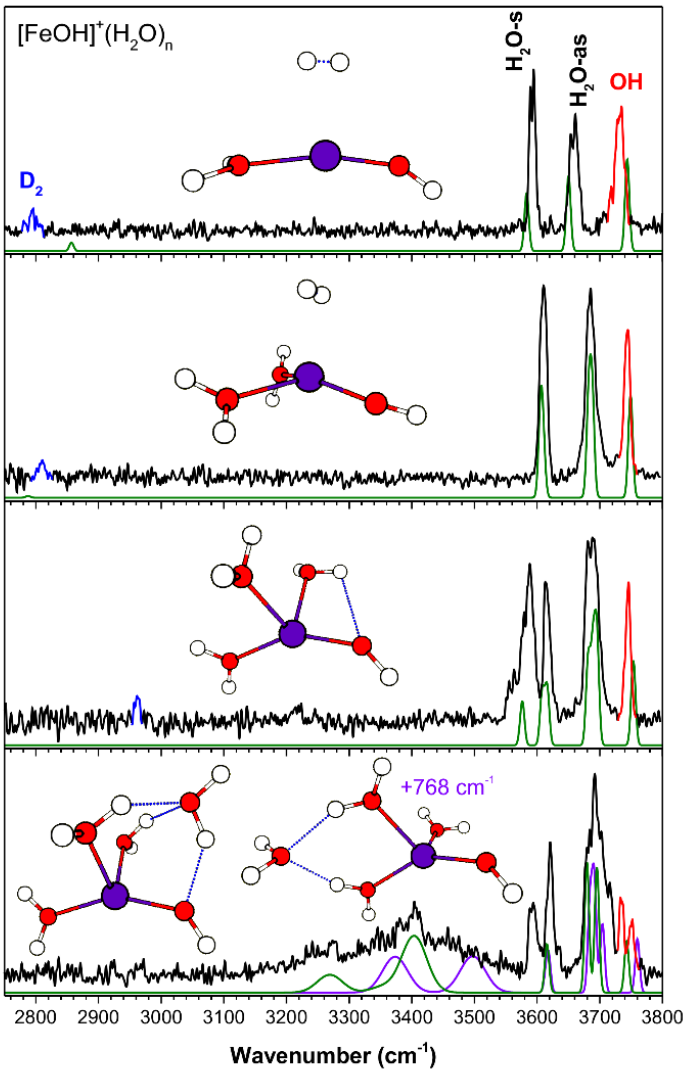

Figure 3.18- The experimental (black) and calculated (purple/green, at cam-B3LYP/def2TZVP) vibrational spectra of $[FeOH]^+(H_2O)_n \cdot D_2$. Highlighted in red is the hydroxide stretch and in blue is the D_2 stretch.

The calculated spectrum of the lowest energy isomer of the n=2 cluster shows excellent agreement with the experimental spectrum. The water molecules and hydroxide are arranged in a distorted trigonal planar geometry, with the two water molecules essentially equivalent. This results in a simple spectrum with three narrow features slightly blueshifted from those in the n=1 spectrum. The bare n=3 cluster is tetrahedral in shape with one weak HO-H_2O interaction. The appearance of the spectrum is very similar to that of $[MnOH]^+(H_2O)_3$, and the assignments are similar as well, with the D_2 tag moving onto a water ligand and giving rise to the additional feature at 3586 cm^{-1}.

The experimental spectrum of the n=4 cluster shows contributions from at least two isomers. This is indicated primarily by the two distinct features in the hydroxide stretch region around 3740 cm^{-1}. The lowest energy isomer has an AAD water interacting directly with the hydroxide. Its calculated spectrum accounts for part of the intensity in the 3200-3500 cm^{-1} region, as well as the 3734 cm^{-1} hydroxide peak. The second isomer, 768 cm^{-1} higher in energy, has the second shell water in an AA configuration accepting two H-bonds from the water ligands opposite the hydroxide. The hydroxide moiety here only has a weak interaction with a nearby water, resulting in the higher frequency 3751 cm^{-1} feature. No other isomers within ~1000 cm^{-1} can account for this peak. This isomer also has two calculated transitions at 3373 and 3497 cm^{-1} which result in the very broad appearance of the feature at ~3400 cm^{-1}. The relative intensity of the two hydroxide features indicates an almost equal presence of both isomers, despite the large calculated energy difference. The lack of any intensity around ~2600 cm^{-1} indicates that the isomer with an AD second shell water (lowest energy isomer in $[MnOH]^+(H_2O)_4$) is not present here, even though it is calculated to only be 257 cm^{-1} higher in energy than the AAD isomer. It should be noted that the errors in the calculated energetics appear to be larger for the Fe species

compared to the other metal species studied here. Lastly, although all the experimentally observed intensities can be accounted for by the two isomers discussed above (the 3593 cm^{-1} feature correspond to the D_2 perturbed H_2O-s), minor contributions from an additional isomer, with all four water molecules in the first shell, cannot be eliminated.

c) $[CoOH]^+(H_2O)_n$

The experimental and calculated IR spectra of $[CoOH]^+(H_2O)_{1-4}$ are shown in Figure 3.19. Even for the smallest cluster, the hydroxide stretch is only partially resolved from the H_2O-as band, and they are completely overlapped for the larger clusters. The assigned geometry of the n=2 cluster, a distorted trigonal planar structure with two nearly equivalent water molecules, is similar to that of $[FeOH]^+$. This gives rise to a very simple experimental spectrum, where the 3611 cm^{-1} feature is assigned to the H_2O-s stretch and the slightly broader 3686 cm^{-1} feature is assigned to the hydroxide and H_2O-as stretch. This isomer is 100 cm^{-1} higher in energy than the isomer with a planar T structure, which involves a slight HO-H_2O interaction. Such an interaction would result in a splitting of each water peak, clearly not present in the experimental spectrum. The higher signal-to-noise ratio of the n=2 spectrum also reveals several small features in the 2900-3300 cm^{-1} region, and are not reproduced in the calculations. Similar features are observed occasionally in the other experimental spectra presented here, and are likely due to combination/overtone bands. Specifically, the feature at 3250 cm^{-1} is likely the overtone of the H_2O bend vibration. Small features are also visible above 3720 cm^{-1}, likely due to combination bands of the water stretch and low frequency libration modes.[31] The n=3 cluster has a distorted tetrahedral geometry, similar to that of the $[MnOH]^+$ and $[FeOH]^+$ species. One of the water molecules interacts with hydroxide, resulting in the 3545 cm^{-1} feature. The 3586 cm^{-1} feature is assigned to the D_2-tagged H_2O-s, while the 3619 cm^{-1} feature is the unperturbed

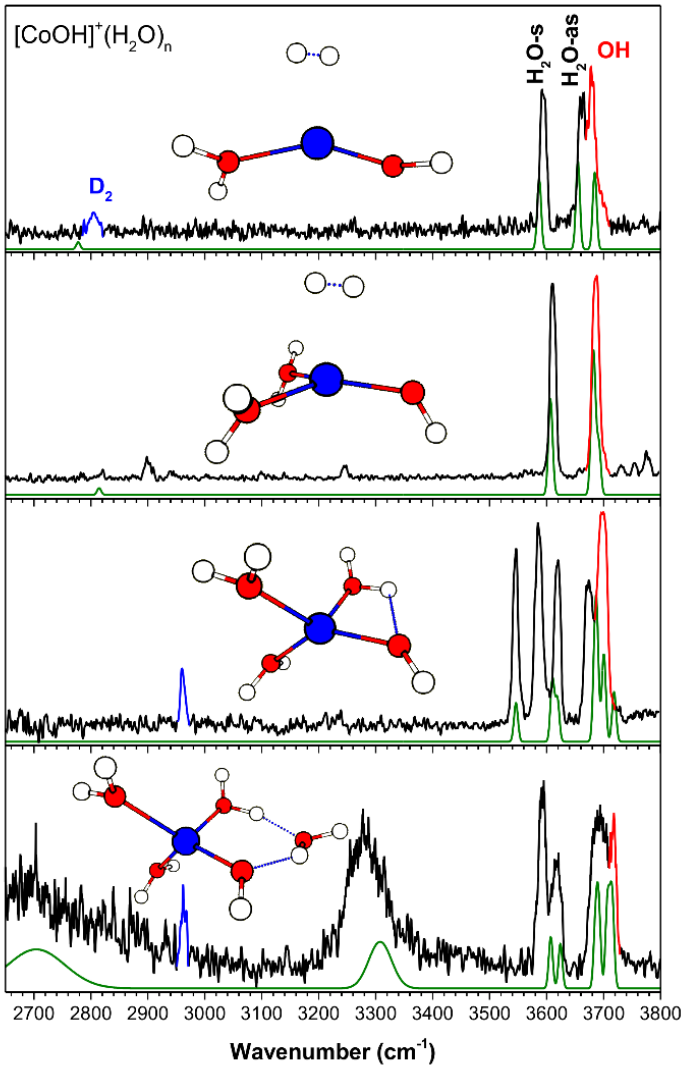

Figure 3.19- The experimental (black) and calculated (green, at cam-B3LYP/def2TZVP) vibrational spectra of $[CoOH]^+(H_2O)_n \cdot D_2$. Highlighted in red is the hydroxide stretch and in blue is the D_2 stretch.

H_2O-s. The partially resolved doublet at 3673 cm^{-1} and 3700 cm^{-1} is assigned to the H_2O-as stretches and the overlapping hydroxide stretch.

The coordination shell closes at n=3 for $[CoOH]^+$ as well. The calculated spectrum of the lowest energy isomer of the n=4 cluster shows an excellent agreement with the experiment, accounting for all the observed spectral features. The geometry of this isomer has the second shell water in an AD configuration, forming an H-bond ring with the hydroxide moiety. The H_2O-H_2O H-bond accounts for the broad 2650 cm^{-1} feature, and the HO-H_2O H-bond accounts for the 3280 cm^{-1} feature. The hydroxide stretch is assigned to the higher frequency side of the broad partially resolved H_2O-as band. Isomers with the second shell water in an AAD or AA configuration similar to those of $[FeOH]^+(H_2O)_4$ are calculated to be 555 cm^{-1} and 573 cm^{-1} higher in energy. They both have calculated intensities in the 3400-3500 cm^{-1} region, and therefore do not have significant presence in the experimental spectrum.

d) $[NiOH]^+(H_2O)_n$

Figure 3.20 shows the experimental and calculated IR spectra for the n=1-5 clusters of $[NiOH]^+(H_2O)_n$. Similar to the $[CoOH]^+$ species, the hydroxide stretch of $[NiOH]^+$ is overlapped with the H_2O-as band, giving rise to only two bands centered at ~3600 cm^{-1} and ~3700 cm^{-1} for the n=1 species. However, there is an additional distinct isolated feature which progressively redshifts with increasing solvation. Furthermore, even in the spectrum of the larger n=5 cluster, there are no very intense redshifted features, clearly making the solvation of $[NiOH]^+$ different than the other metal species presented thus far.

In the n=2 cluster, the water molecules and hydroxide are in a T-shaped planar geometry. The ~90˚ angle between the water and the hydroxide results in a stronger HO-H_2O interaction,

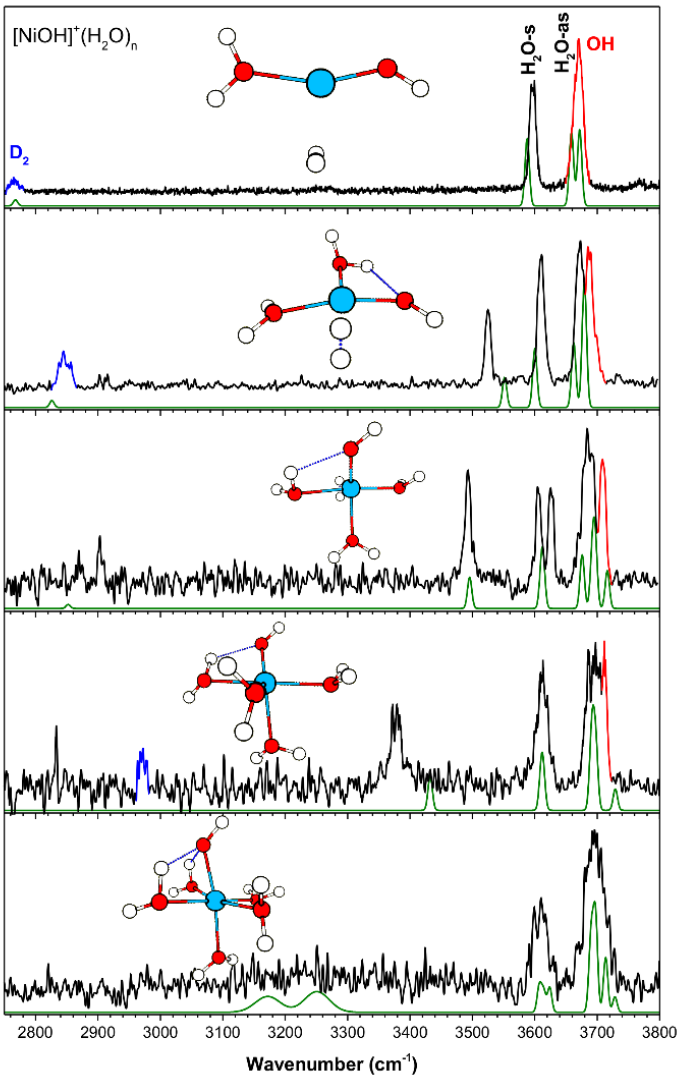

Figure 3.20- The experimental (black) and calculated (green, at cam-B3LYP/def2TZVP) vibrational spectra of $[NiOH]^+(H_2O)_n \cdot D_2$. Highlighted in red is the hydroxide stretch and in blue is the D_2 stretch.

giving rise to the redshifted feature at 3525 cm^{-1}. The calculation cannot fully capture this interaction, but the other spectral features have good agreement with the experiment. This isomer is calculated to be 126 cm^{-1} higher in energy than the lowest energy structure found, which has D_2 on an axial location similar to that of $[MnOH]^+$, $[FeOH]^+$, and $[CoOH]^+$. That geometry, however, does not have an HO-H_2O interaction and cannot account for the 3525 cm^{-1} experimental feature. In the n=3 cluster, the water replaces the D_2 in the equatorial position, and the additional repulsion results in a yet stronger HO-H_2O interaction and a redshifted peak at 3493 cm^{-1}. Here, the calculation shows a good overall agreement with the experiment, but the doublet at 3606/3626 cm^{-1} is calculated to have the same frequency. The increasing HO-H_2O interaction trend continues in the n=4 cluster, with the fourth water still interacting with the Ni center. We note that the strong HO-H_2O interaction in the n=4 cluster gives rise to a vibrational feature at 3378 cm^{-1}, which is of similar frequency as that of the H-bonded water stretch due to second shell formation for the other metal species. However, the $[NiOH]^+$ feature has comparably narrow width and low intensity in the experimental spectrum, pointing to the difference in its H-bond. The calculated geometry for the n=5 cluster has an octahedral arrangement, with all six ligands in the first solvation shell. The structure has two water molecules strongly interacting with the hydroxide, with calculated frequencies of 3172 cm^{-1} and 3251 cm^{-1}. Interestingly, these redshifted features suddenly broaden out in the n=5 cluster, such that they almost disappear into the baseline. This is similar to the spectra of the n=4 and 5 clusters of $[MgOH]^+(H_2O)_n$ and $[CaOH]^+(H_2O)_n$.[5] Note that for the alkali earth species, the extremely broad feature spanning >500 cm^{-1} arises from a similar HO-H_2O interaction arranged in an octahedral geometry. Isomers with the fifth water in the second shell are all calculated to be ~1000 cm^{-1} higher in energy, with significant intensities in the 2500-3400 cm^{-1} region. Due to

insufficient ion signal, the spectrum of $[NiOH]^+(H_2O)_6$ cluster could not be collected. This drop in intensity in the mass spectrum from n=5 to n=6 suggests the completion of the first coordination shell at n=5.

e) $[CuOH]^+(H_2O)_n$

The assignment and analysis of the solvated $[CuOH]^+$ clusters have been previously published by us for n=1-3,[6] and by Sweeney *et al.*[32] for n=2-9. Recent improvements allowed us to acquire a better signal-to-noise spectrum for the n=3 cluster and a vibrational spectrum for the n=4 cluster. Figure 3.21 shows the entire n=1-4 series. In contrast to the metal species discussed so far, the hydroxide stretch in the singly hydrated $[CuOH]^+$ lies below the H_2O-s and blueshifts to overlap with the H_2O-as in the n=3 and 4 clusters. Furthermore, the D_2 tag is already on the water ligand for n=2 and gives rise to a comparably complex spectrum. The most stable isomer of the n=3 cluster has a nearly square planar geometry and is the dominant species contributing to the experimental spectrum. The enhanced signal-to-noise spectrum for n=3 now clearly shows an additional H-bonded feature at 3370 cm^{-1}, indicating the presence of a second isomer as pointed out by Sweeney *et al.*.[32] This isomer, calculated to be 432 cm^{-1} higher in energy here, has the third water in the second shell bonded to two water ligands in an AA configuration, yielding the distinctive H-bond feature.

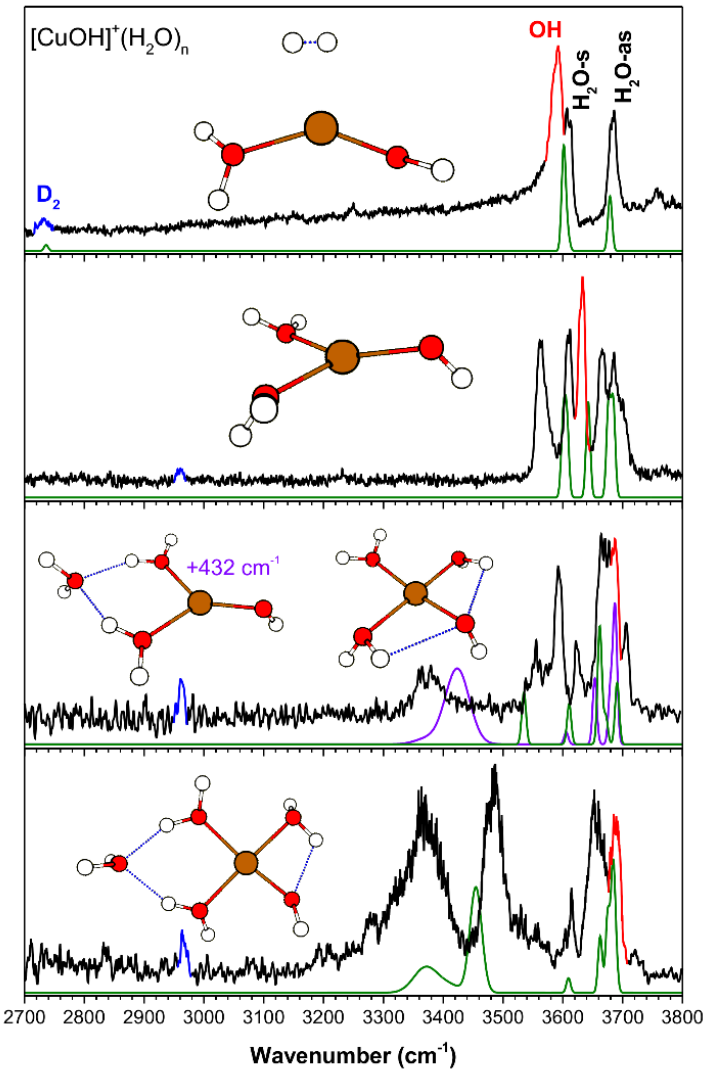

Figure 3.21- The experimental (black) and calculated (green, at cam-B3LYP/def2TZVP) vibrational spectra of $[CuOH]^+(H_2O)_n \cdot D_2$. Highlighted in red is the hydroxide stretch and in blue is the D_2 stretch.

The calculated spectrum of the lowest energy isomer for the n=4 cluster agrees well with the experimental spectrum. This is also the lowest energy isomer found by Sweeney *et al.*.[32] This isomer, also planar, has three water molecules in the primary metal coordination shell and the fourth water in an AA configuration between two water ligands. It is an extension of both n=3 isomers. The double H-bond interaction gives rise to the two intense features observed at 3370 cm^{-1} and 3485 cm^{-1}. Calculations also indicate that the hydroxide stretch is now the highest frequency vibration, overlapped with several H_2O-as vibrations, and they are all assigned to the partially resolved 3690 cm^{-1} feature. The other low energy isomers reported by Sweeney *et al.*[32] have calculated intensities below 3200 cm^{-1} and do not appear to contribute to the experimental spectrum observed here.

f) $[ZnOH]^+(H_2O)_n$

Figure 3.22 shows the experimental and calculated results for $[ZnOH]^+(H_2O)_{1-4}$. As pointed out for the singly hydrated species,[7] the calculated results for $[ZnOH]^+$ has a slightly larger error (~20-30 cm^{-1}) for the hydroxide stretch frequency compared to the other metal species. This is true for the larger clusters as well. Furthermore, similar to the Mn species, the H_2O-as feature in Zn n=1 is complicated by coupling of this stretch with hindered internal rotation. The n=2 cluster has a planar T geometry with the two water molecules nearly equivalent. The calculated spectrum of the bare cluster does not show a good agreement with the experiment, which has a similar appearance to the corresponding $[CuOH]^+$ cluster. This similarity points to the D_2 tag residing on a water ligand, yielding the differences between calculation and experiment. Specifically, the 3602 cm^{-1} feature is assigned to the free H_2O-s, which, similar to the n=1 cluster, is slightly blueshifted from the calculated frequency. The broader and asymmetric feature at 3545 cm^{-1} is then assigned to the D_2 perturbed H_2O-s. The

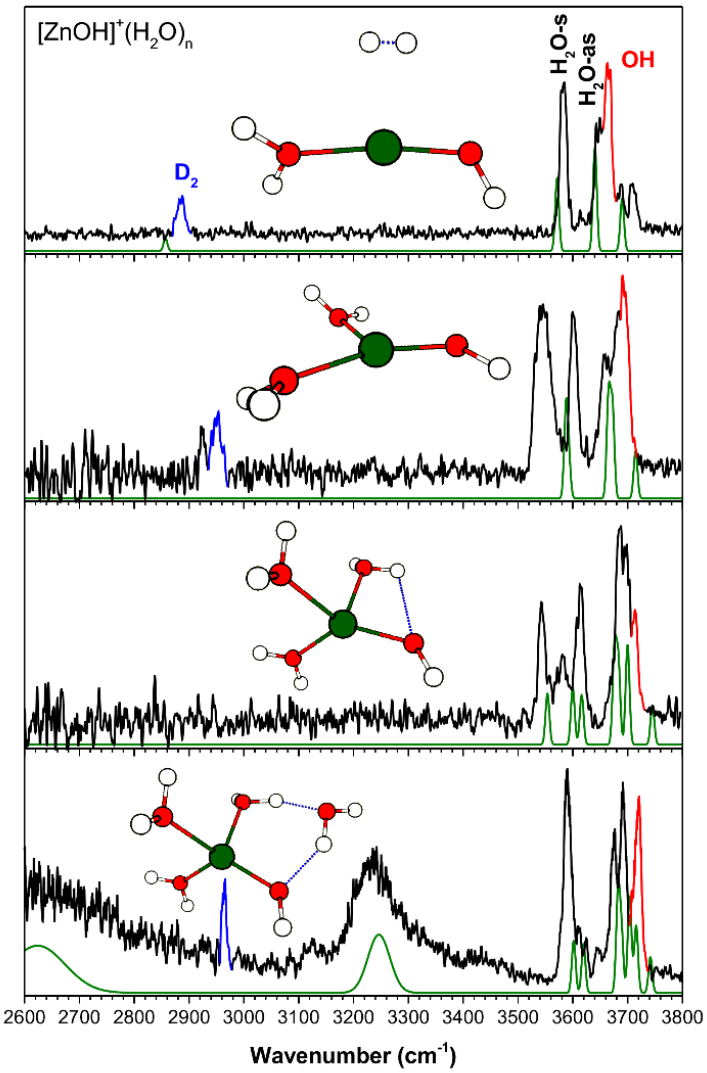

Figure 3.22- The experimental (black) and calculated (green, at cam-B3LYP/def2TZVP) vibrational spectra of $[ZnOH]^+(H_2O)_n \cdot D_2$. Highlighted in red is the hydroxide stretch and in blue is the D_2 stretch.

H_2O-as stretch is also perturbed by the D_2 tag, similar to $[CuOH]^+(H_2O)_2$, giving rise to the partially resolved band at 3650-3700 cm^{-1}. The highest frequency side of this band is assigned to the hydroxide stretch.

The experimental spectrum of the n=3 cluster is similar in appearance to the corresponding $[MnOH]^+$, $[FeOH]^+$, and $[CoOH]^+$ species, in agreement with its calculated geometry being a quasi-tetrahedral structure. The HO-H_2O interaction here gives rise to the feature at 3543 cm^{-1}. The peak at 3580 cm^{-1} is assigned to the D_2 tagged water stretch and the 3614 cm^{-1} feature is assigned to the free H_2O-s. The H_2O-as features are again only partially resolved from each other and the 3714 cm^{-1} hydroxide stretch. Similar to the other tetrahedral species, the Zn coordination shell is complete at n=3, and the spectrum of the n=4 cluster has broad and intense features at ~2600 cm^{-1} and ~3230 cm^{-1}. The lowest energy isomer for n=4 has the second shell water in an AD configuration between a water and the hydroxide. This isomer has two redshifted features in excellent agreement with the experimental features, and it accounts for most of the intensities in the 3600-3800 cm^{-1} region as well. Minor presence of an additional isomer, with the second shell water in an AAD configuration, cannot be ruled out.

3.3.4 Discussion

a) Coordination and solvation structure

The assigned vibrational spectra allow us to take a closer look at the different trends in the coordination geometry and solvation structure. To aid the discussions, we present the experimental spectra and calculated structures of the $[MOH]^+(H_2O)_{2\text{-}4}$ clusters grouped by solvation (i.e. n=2, 3, and 4) in Figures 3.23, 3.24 and 3.25.

For the n=2 clusters, shown in Figure 3.23, all the metal species have a relatively similar trigonal structure. Specifically, the two water molecules in the $[FeOH]^+$ and $[CoOH]^+$ clusters are both free and have the same vibrational frequencies. In the $[MnOH]^+$ and $[NiOH]^+$ clusters, one of the water molecules has a weak interaction with the hydroxide, leading to a splitting in the H_2O-s and H_2O-as modes. In $[CuOH]^+$ and $[ZnOH]^+$, the water modes are split due to the presence of the D_2 tag on a water, and these features are correspondingly broader and more asymmetrical.

The IR spectra of the n=3 clusters, displayed in Figure 3.24, highlight the different coordination behaviors of the various species. The $[MnOH]^+$, $[FeOH]^+$, $[CoOH]^+$, and $[ZnOH]^+$ clusters all have a distorted tetrahedral geometry and the proximity of the ligands leads to one water weakly interacting with the hydroxide. This interaction gives rise to a feature in the 3540-3570 cm^{-1} region. On the other hand, both the $[NiOH]^+$ and the dominant $[CuOH]^+$ isomer have a quasi-square-planar geometry. With this structure, the $[NiOH]^+$ cluster has the strongest HO-H_2O interaction, with a redshifted frequency of 3493 cm^{-1}. The minor isomer of $[CuOH]^+$ yields the first H-bonded OH stretch for this series of $[MOH]^+$ clusters. For all the species except Ni, the D_2 tag now resides on a water, and a feature ~30 cm^{-1} redshifted from the free H_2O-s is observed in the experimental spectra.

The vibrational spectra of the n=4 clusters, in the broader 2400-3800 cm^{-1} region, are shown in Figure 3.25. Unlike the smaller clusters, there is now significant activity in the H-bonding region. $[NiOH]^+$ is the unique species here, with the fourth water residing in the first solvation shell. The proximity of the ligands in the octahedral coordination leads to a redshifted feature at 3378 cm^{-1}, resulting from the HO-H_2O interaction. This frequency indicates that the interaction is almost as strong as some H_2O-H_2O interactions in the other metal species, though it

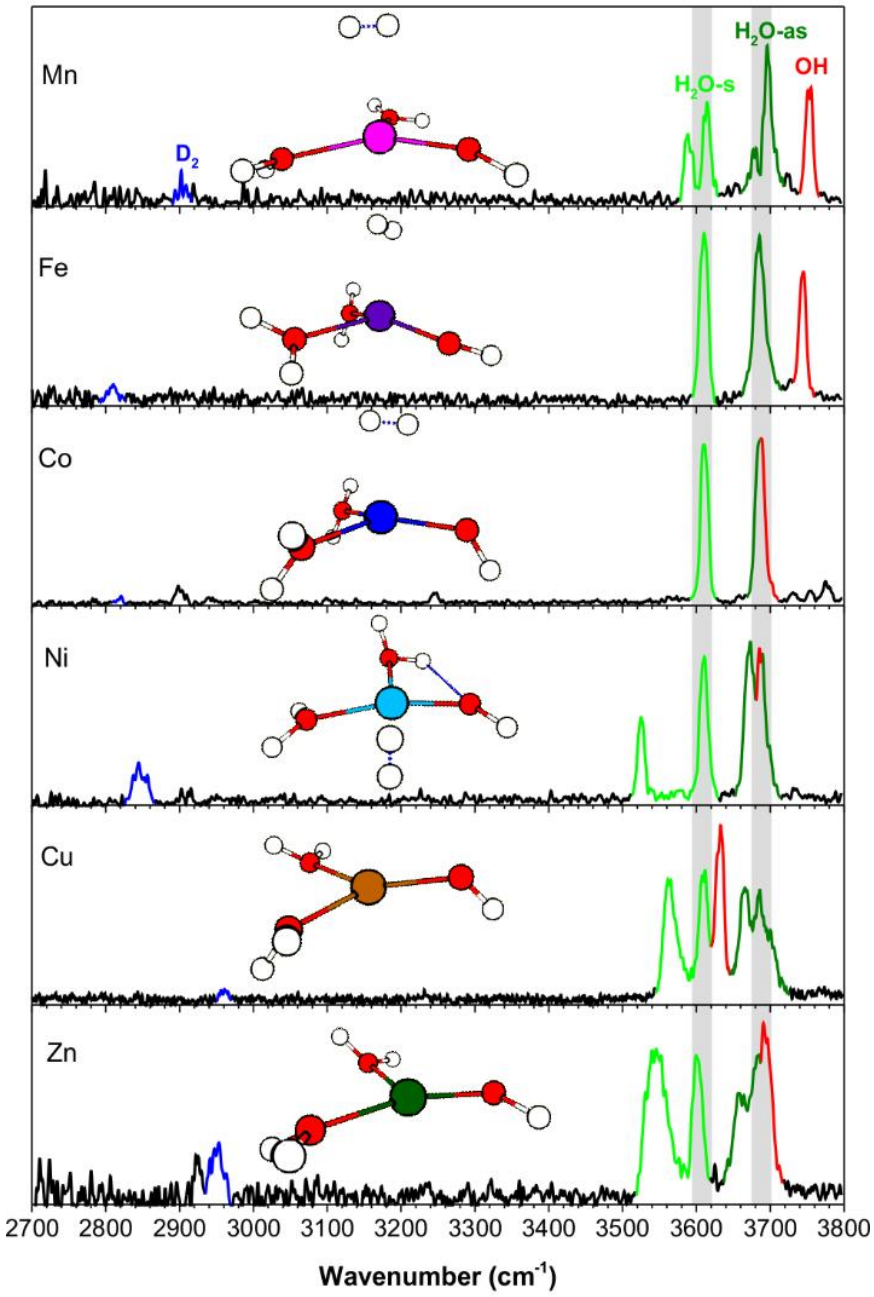

Figure 3.23- The assigned experimental spectra of $[MOH]^+(H_2O)_2$. Highlighted in blue is the D_2 stretch, in green are the H_2O-s and H_2O-as stretches, and in red is the hydroxide stretch. The grey bars allow for comparison of the H_2O-s and H_2O-as bands for different metals (highlighting the higher frequency edge of the bands).

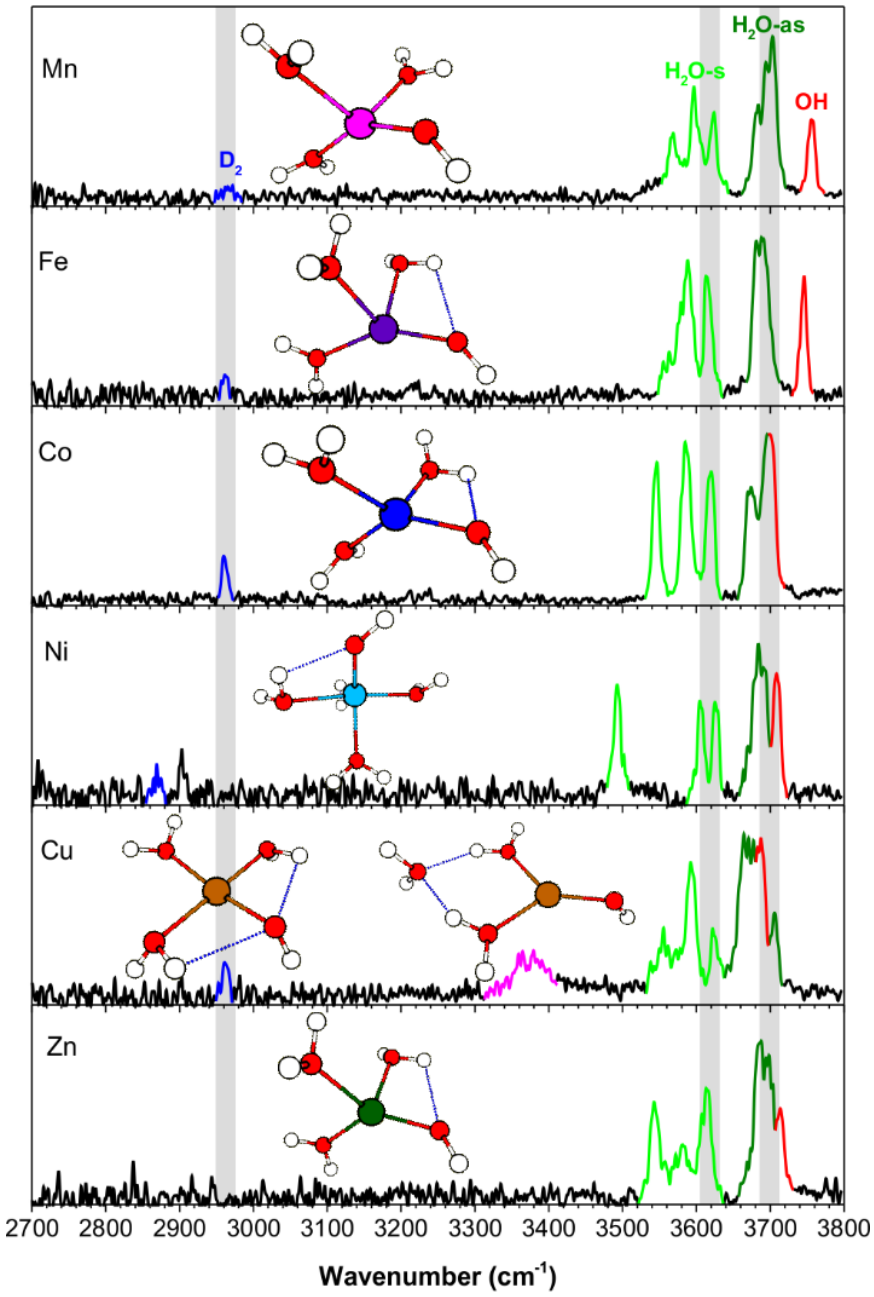

Figure 3.24- The assigned experimental spectra of $[MOH]^+(H_2O)_3$. Highlighted in blue is the D_2 stretch, in green are the H_2O-s and H_2O-as stretches, in red is the hydroxide stretch, and in magenta are the H-bonded OH stretch involving the second shell water. The grey bars allow for comparison of the D_2, H_2O-s_and H_2O-as bands for different metals (highlighting the higher frequency edge of the bands).

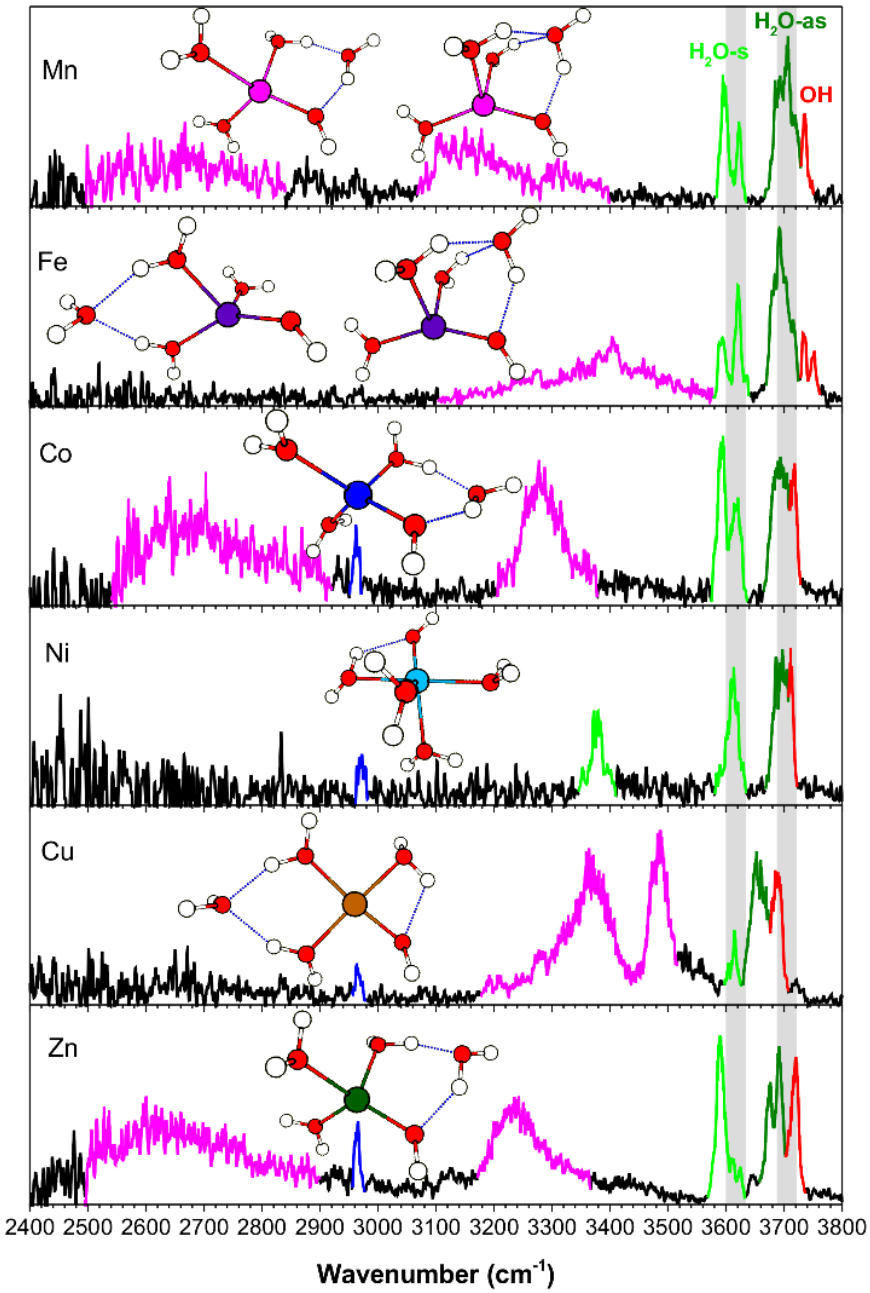

Figure 3.25- The experimental spectra of $[MOH]^+(H_2O)_4 \cdot D_2$ complexes in the 2400-3800 cm^{-1} region. Highlighted in blue is the D_2 stretch, in green are the H_2O-s and H_2O-as stretches, in red is the hydroxide stretch, and in magenta are the H-bonded OH stretches involving the second shell water. The grey bars allow for comparison of the H_2O-s and H_2O-as bands for different metals (highlighting the higher frequency edge of the bands).

remains a rather narrow feature with relatively low intensity. For all the other $[MOH]^+(H_2O)_4$ clusters, the fourth water resides in the second shell, giving rise to characteristic broad and intense redshifted H-bonded features. The experimental spectra point to two distinct binding sites for the second shell water. First, the $[MnOH]^+$, $[CoOH]^+$, and $[ZnOH]^+$ spectra all have a very broad feature spanning 2500-2900 cm^{-1}, which is absent in the $[FeOH]^+$ and $[CuOH]^+$ spectra. Calculations show that this feature is due to the second shell water in an AD configuration, forming a ring between a water and the hydroxide. The H_2O-H_2O H-bond in this ring is very strong, giving rise to this low frequency feature. The corresponding HO-H_2O H-bond yields the ~3200 cm^{-1} feature. A related motif in which the second shell water is in an AAD configuration between two water molecules and the hydroxide is found for one of the $[FeOH]^+$ and $[MnOH]^+$ isomers. This configuration has the all the H-bonded features in the 3100-3400 cm^{-1} region. The weaker H_2O-H_2O interaction here is due to the distribution of the interaction over two equivalent H-bonds. We note that the HO-H_2O interaction here creates a motif in which simple proton transfer to the adjacent oxygen would effectively transfer the location of the hydroxide in the first coordination sphere. The other distinct location for the second shell water is at the opposite side of the cluster, in an AA configuration between two water ligands. This H-bond is of a more typical water-water interaction, and gives rise to features in the 3300-3500 cm^{-1} region for $[CuOH]^+$ and one of the $[FeOH]^+$ isomers.

The position and binding motif of the second shell water reveals the relative strength of the H_2O-H_2O and HO-H_2O interactions for the different metal species. As discussed for the singly hydrated species,[7] electron transfer from the hydroxide to the metal center varies as a function of the 2nd ionization energy of the metal. This makes $[CuOH]^+$ the species with the

largest charge transfer and therefore the smallest residual charge on the hydroxide (see Table 3.3). With less charge on the hydroxide, the HO-H_2O interaction becomes less energetically favorable and the second shell water preferably binds in an AA configuration between two water ligands. The $[MnOH]^+$, $[FeOH]^+$, $[CoOH]^+$ and $[ZnOH]^+$ species have larger ($\geq$0.7e) NPA charge on the hydroxide ligand, which favors the interaction of the second shell water with the hydroxide. $[FeOH]^+$ is different than the other species because it has the AAD motif as a dominant configuration. This can be explained by the geometry of the first coordination shell. The distorted tetrahedral geometry of $[FeOH]^+$ has the smallest H_2O-M-H_2O angle in the n=3 cluster, at about 85°. This favors the AAD interaction, which has a smaller H_2O-M-H_2O angle than the AD motif. Furthermore, the absence of the AD isomer and the strong presence of the AA isomer suggest that the charge on hydroxide is also a factor here, especially considering that $[FeOH]^+$ has the second lowest calculated NPA charge on its hydroxide. Similarly, structural considerations may also play a part in the relative stability of the $[CuOH]^+$ isomers, where the square planar structure is more strained when accommodating the second shell water in an AD configuration. Altogether, it appears that the solvation structures of $[MOH]^+$ are influenced by a combination of charge transfer and coordination geometry.

The coordination behavior of the $[MOH]^+$ complexes can also be compared to that of the corresponding $M^+(H_2O)_n$ and $M^{2+}(H_2O)_n$ complexes, summarized in Table 3.4. Previous studies of $M^{2+}(H_2O)_n$ clusters by Williams and coworkers[22, 23, 33] show that the average coordination numbers (CNs) of Mn^{2+}, Fe^{2+}, Co^{2+}, and Ni^{2+} ions complexed with water are all approximately 6. Cu^{2+} and Zn^{2+} complexes were found to have CN = 4 and CN = 5, respectively. Studies of $M^+(H_2O)_n$ complexes [18, 19, 24] showed that Co^+ and Zn^+ complexes have CN = 3 while Ni^+ has CN = 3 or 4[20]. Fe^+ and Cu^+ clusters both have CN = 2 predominantly, with $Fe^+(H_2O)_n$ possibly

$[MOH]^+$	n=1			n=2			n=3			n=4		
$(H_2O)_n$	M (e)	OH (e)	M-OH (Å)	M (e)	OH (e)	M-OH (Å)	M (e)	OH (e)	M-OH (Å)	M (e)	OH (e)	M-OH (Å)
$[MgOH]^+$	1.84	-0.90	1.723	1.83	-0.91	1.740	1.82	-0.91	1.789	1.81	-0.89	1.833
$[CaOH]^+$	1.84	-0.86	1.930	1.83	-0.87	1.958	1.85	-0.90	2.016	1.86	-0.89	2.139
$[MnOH]^+$	1.54	-0.64	1.758	1.55	-0.70	1.804	1.58	-0.74	1.836	1.61	-0.76	1.878
$[FeOH]^+$	1.46	-0.58	1.717	1.45	-0.62	1.755	1.50	-0.67	1.778	1.52	-0.70	1.818
$[CoOH]^+$	1.41	-0.55	1.723	1.42	-0.62	1.761	1.49	-0.68	1.787	1.52	-0.71	1.816
$[NiOH]^+$	1.31	-0.47	1.695	1.36	-0.57	1.752	1.42	-0.67	1.791	1.47	-0.71	1.808
$[CuOH]^+$	1.20	-0.32	1.754	1.29	-0.43	1.741	1.40	-0.64	1.811	1.42	-0.67	1.814
$[ZnOH]^+$	1.61	-0.72	1.740	1.65	-0.76	1.758	1.69	-0.81	1.794	1.71	-0.82	1.823

Table 3.3- The calculated (cam-B3LYP/def2TZVP) metal (M) NPA charge, hydroxide (OH) NPA charge, and M-OH bond length for the optimized geometries shown in Figures 3.17-3.22. For species where multiple isomers are present in the experimental spectrum, the dominant species is listed. In the case of n=4 cluster for FeOH, the AAD isomer is listed.

M	M^+	M^{2+}	$[MOH]^+$
Mn	-	6 (ref. [23])	4
Fe	2 or 4 (ref.[17])	6 (ref.[23])	4
Co	3 (ref. [18])	6 (ref.[23])	4
Ni	3 or 4 (ref. [20])	6 (ref.[23])	6
Cu	2 (ref. [21])	4 (ref.[22])	3 or 4
Zn	3 (ref. [19])	5 or 6 (ref. [33])	4

Table 3.4- Coordination numbers of M^+, M^{2+}, and $[MOH]^+$ complexes with water molecules.

having 4 coordinate geometries as well[17, 21]. The $[MOH]^+$ species, on the other hand, seem to have CNs somewhere in between the two extremes. Namely, $[MnOH]^+$, $[FeOH]^+$, $[CoOH]^+$, and $[ZnOH]^+$ have CN = 4, which is larger than that of the $M^+(H_2O)_n$ clusters but smaller than that of the known $M^{2+}(H_2O)_n$ clusters. Interestingly, $[CuOH]^+$ and $[NiOH]^+$ have the same coordination numbers as the corresponding M^{2+} ions despite having the lower NPA charge on the metal center. This indicates that neither the formal charge nor NPA charge are sufficient to predict the coordination environment around the metal center, especially when a charged ligand is located in the coordination sphere.

b) Hydroxide frequency

In our previous study on the $[MOH]^+(H_2O)$ species, we found that the frequency of the hydroxide stretch has a strong dependence on the metal species.[7] This was attributed to the vibrational Stark shift[34-42] induced by the charged metal center, with charge transfer between the metal ion and the hydroxide ligand being the most important factor in two ways. First, electron transfer from the hydroxide to the metal center reduces the magnitude of the electric field. Second, depletion of the excess electron on the hydroxide reduces the Stark tuning rate, because, unlike the hydroxide anion, the hydroxyl radical frequency is almost insensitive to electric field. Overall the hydroxide frequency was found to be linearly proportional to $q_{OH}q_M/R^2$ where q_{OH} and q_M are the charge on the hydroxide and the metal, respectively, and R is the distance between the metal and the center of the hydroxide O-H bond.

Here we can look at the effect of solvation on this trend, which is summarized in Figure 3.26. The top panel shows that the metal dependence of the hydroxide frequency observed for the n=1 species continues for the larger clusters. However, the range of the hydroxide frequency

narrows significantly with each additional water molecule, and it converges toward ~3700 cm^{-1} for all the metal species studied here. Even though the solvation occurs predominately around the metal, the hydroxide frequency shows a high sensitivity to the solvation environment for some species. Notably there is a progression of behavior from $[CuOH]^+$ to $[MgOH]^+$. The hydroxide frequencies of $[CuOH]^+$, $[ZnOH]^+$, $[NiOH]^+$ and $[CoOH]^+$ all blueshift with increasing number of water. On the other hand, the hydroxide frequencies redshift in $[MgOH]^+$ and $[CaOH]^+$ with increasing solvation.[5] Finally, hydroxide frequencies of $[FeOH]^+$ and $[MnOH]^+$ remain fairly constant as a function of solvation.

We carried out a similar natural population analysis (NPA) for these larger solvation clusters as in our previous study. (Note: for species where multiple isomers are present in the experimental spectrum, the dominant species is considered. In the case of $[FeOH]^+(H_2O)_4$, the AAD isomer is considered.) The localized charge on the metal center and the hydroxide moiety are listed in Table 3.3. The bottom panel of Figure 3.26 shows the plot of the hydroxide frequency as a function of $q_{OH}q_M/R^2$, including the $[MgOH]^+$ and $[CaOH]^+$ species studied by Johnson *et al.* [5]. With the exception of $[ZnOH]^+$, all the other species follow the linear $q_{OH}q_M/R^2$ relationship found for the n=1 clusters. The offset in the $[ZnOH]^+$ series is due to errors in the calculation of the Zn-OH interaction and NPA charges as discussed previously for the singly solvated species.[7] This is partly reflected in the discrepancy between calculated and experimental hydroxide frequencies as discussed in section III-f. The more scattered appearance of the data points in the center of the plot is likely due to the inherent errors in the charge analysis as well as additional HO-H_2O interactions that affect the hydroxide stretch independent of the electric field. Furthermore, although the $[MgOH]^+$ and $[CuOH]^+$ species start at the opposite ends of the plot in the n=1 cluster, they both move toward the center with increasing

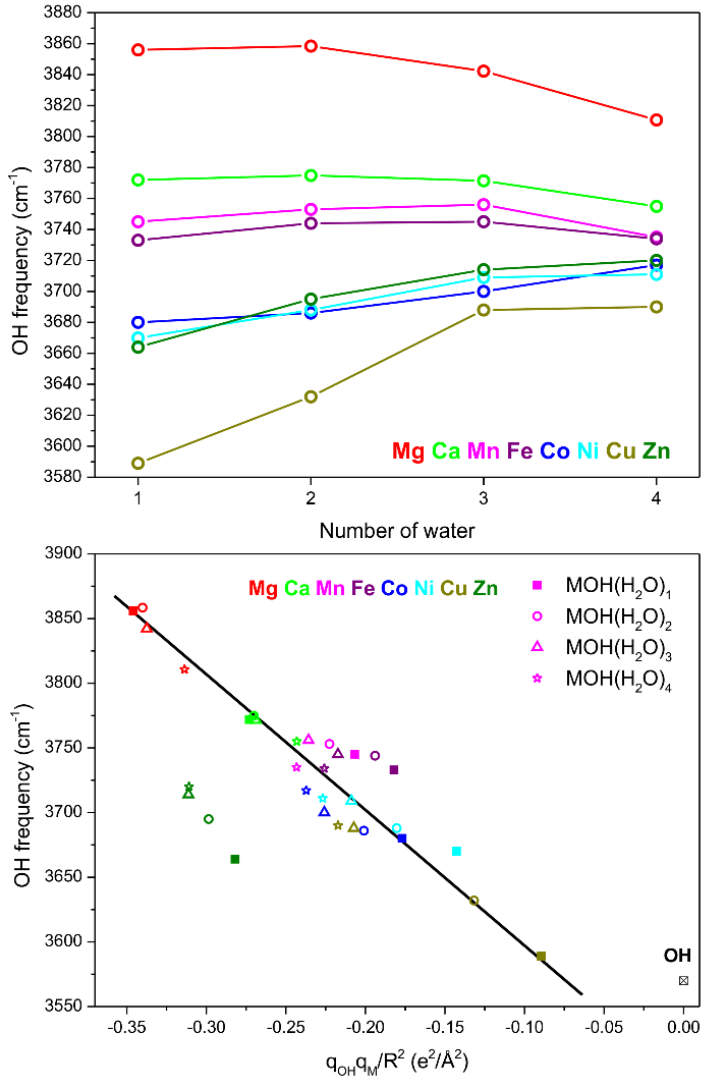

Figure 3.26- Top panel: Hydroxide frequency in $MOH^+(H_2O)_n$ as a function of n. Bottom panel: Hydroxide frequency as a function of $q_{OH}q_M/R^2$ where q_{OH} and q_M are the charge on the hydroxide and the metal, respectively, and R is the distance between the metal and the center of the O-H bond. The data for $[MgOH]^+$ and $[CaOH]^+$ are from ref 5. The straight line serves as a visual guidance.

number of water molecules. For the n=4 clusters, all the metal species except for $[MgOH]^+$ and $[ZnOH]^+$ are congregated around a $q_{OH}q_M/R^2$ of about -0.22 $e^2/Å^2$. This linear relationship indicates that modulation of the Stark shift is the primary reason behind the solvation dependent hydroxide frequency in these $[MOH]^+$ complexes, and provides an explanation for the opposing redshift/blueshift trends.

The reason for this behavior is twofold. First, as shown in Table 3.3, the magnitude of electron transfer between the hydroxide and the metal center is reduced with increasing solvation (i.e., the respective charges on the metal and hydroxide increases). This can be explained by dielectric charge stabilization from the water molecules surrounding the metal center. This effect is more pronounced for the species with larger charge transfer in the small clusters. For example, in $[CuOH]^+$ the charge on the metal goes from 1.20 in n=1 to 1.42 in n=4. This reduced charge transfer increases both the strength of the electric field and the Stark tuning rate of the hydroxide, leading to a blueshift of the hydroxide frequency. At the same time, a more crowded coordination around the metal center leads to a gradual lengthening of the M-OH bond for all metal species considered here. The longer bond lengths lead to reduced electric field, and a redshift of the hydroxide frequency. This is the dominant effect for the already charge-separated species such as $[MgOH]^+$ and $[CaOH]^+$. For the $[MnOH]^+$ and $[FeOH]^+$ species, these two opposing trends effectively cancel out each other, resulting in a relatively constant hydroxide frequency as a function of solvation.

3.3.5 Conclusion

The vibrational spectra of $[MOH]^+(H_2O)_n \cdot D_2$ (M = Mn, Fe, Co, Ni, Cu and Zn; n = 2-4), acquired using cryogenic ion infrared predissociation spectroscopy are presented. The formation

of the second coordination shell is observed for all the metals species except $[NiOH]^+$. For $[MnOH]^+$, $[FeOH]^+$, $[CoOH]^+$, and $[ZnOH]^+$, the second shell begins with the addition of the fourth water. On the other hand, $[CuOH]^+$ can have either a 3-coordinate or a 4-coordinate first shell, with the 4-coordinate shell energetically favored for the n=4 cluster. $[NiOH]^+$ is found to have an octahedral geometry with the first shell likely closed at n=5. The different coordination numbers also correspond to different geometries, with $[CuOH]^+$ adopting a planar structure, $[NiOH]^+$ adopting an octahedral structure, and the other species adopting a quasi-tetrahedral structure. For the second shell water, characteristic H-bonded OH vibrations are observed in the 2500-3500 cm^{-1} region, pointing to different binding sites for different metal species. Specifically, the water molecule in the second shell can adopt either an AD or AAD configuration, interacting directly with the hydroxide moiety, or an AA configuration, interacting only with two water molecules. The relative energetics of different binding sites are found to be dictated by the first shell coordination geometry and the local charge present on the hydroxide. Finally, the hydroxide frequency exhibits very high sensitivity to metal species as well as solvation. Specifically, the $[ZnOH]^+$, $[CuOH]^+$, $[CoOH]^+$ and $[NiOH]^+$ clusters showed a blueshifting hydroxide stretch with increasing solvation whereas $[FeOH]^+$ and $[MnOH]^+$ clusters showed a fairly constant hydroxide stretch for n=1-4. The modulation of this frequency is dominated by the vibrational Stark shift observed for the n = 1 clusters, despite the increasing and varying H-bonding interactions around the hydroxide moiety.

References

1. A. M. Ricks, A. D. Brathwaite and M. A. Duncan, *The Journal of Physical Chemistry A*, 2013, **117**, 11490-11498.

2. E. M. Duffy, B. M. Marsh and E. Garand, *The Journal of Physical Chemistry A*, 2015, DOI: 10.1021/acs.jpca.5b04778.

3. R. J. Cooper, S. Heiles and E. R. Williams, *Physical Chemistry Chemical Physics*, 2015, **17**, 15963-15975.

4. B. J. Knurr and J. M. Weber, *The Journal of Physical Chemistry A*, 2015, **119**, 843-850.
5. C. J. Johnson, L. C. Dzugan, A. B. Wolk, C. M. Leavitt, J. A. Fournier, A. B. McCoy and M. A. Johnson, *The Journal of Physical Chemistry A*, 2014, **118**, 7590-7597.

6. B. M. Marsh, J. Zhou and E. Garand, *The Journal of Physical Chemistry A*, 2014, **118**, 2063-2071.

7. B. M. Marsh, J. Zhou and E. Garand, *Physical Chemistry Chemical Physics*, 2015, DOI: 10.1039/C5CP01522G.

8. L. Jiang, T. Wende, R. Bergmann, G. Meijer and K. R. Asmis, *Journal of the American Chemical Society*, 2010, **132**, 7398-7404.

9. N. F. Dalleska, K. Honma, L. S. Sunderlin and P. B. Armentrout, *Journal of the American Chemical Society*, 1994, **116**, 3519-3528.

10. D. R. Carl, R. M. Moision and P. B. Armentrout, *International Journal of Mass Spectrometry*, 2007, **265**, 308-325.

11. D. R. Carl and P. B. Armentrout, *The Journal of Physical Chemistry A*, 2012, **116**, 3802-3815.

12. D. R. Carl and P. B. Armentrout, *ChemPhysChem*, 2013, **14**, 681-697.

13. T. E. Cooper, D. R. Carl and P. B. Armentrout, *The Journal of Physical Chemistry A*, 2009, **113**, 13727-13741.

14. T. E. Hofstetter and P. B. Armentrout, *The Journal of Physical Chemistry A*, 2013, **117**, 1110-1123.

15. Y. Inokuchi, K. Ohshimo, F. Misaizu and N. Nishi, *The Journal of Physical Chemistry A*, 2004, **108**, 5034-5040.

16. M. F. Bush, J. T. O'Brien, J. S. Prell, C.-C. Wu, R. J. Saykally and E. R. Williams, *Journal of the American Chemical Society*, 2009, **131**, 13270-13277.

17. K. Ohashi, J. Sasaki, G. Yamamoto, K. Judai, N. Nishi and H. Sekiya, *The Journal of Chemical Physics*, 2014, **141**, 214307.

18. K. Furukawa, K. Ohashi, N. Koga, T. Imamura, K. Judai, N. Nishi and H. Sekiya, *Chemical Physics Letters*, 2011, **508**, 202-206.

19. B. Bandyopadhyay, K. N. Reishus and M. A. Duncan, *The Journal of Physical Chemistry A*, 2013, **117**, 7794-7803.

20. R. S. Walters, E. D. Pillai and M. A. Duncan, *Journal of the American Chemical Society*, 2005, **127**, 16599-16610.

21. T. Iino, K. Ohashi, Y. Mune, Y. Inokuchi, K. Judai, N. Nishi and H. Sekiya, *Chemical Physics Letters*, 2006, **427**, 24-28.

22. J. T. O'Brien and E. R. Williams, *The Journal of Physical Chemistry A*, 2008, **112**, 5893-5901.

23. J. T. O'Brien and E. R. Williams, *The Journal of Physical Chemistry A*, 2011, **115**, 14612-14619.

24. P. D. Carnegie, B. Bandyopadhyay and M. A. Duncan, *The Journal of Physical Chemistry A*, 2011, **115**, 7602-7609.

25. J. Fenn, M. Mann, C. Meng, S. Wong and C. Whitehouse, *Science*, 1989, **246**, 64-71.

26. J. B. Fenn, M. Mann, C. K. Meng, S. F. Wong and C. M. Whitehouse, *Mass Spectrometry Reviews*, 1990, **9**, 37-70.

27. M. J. Frisch, G. W. Trucks, H. B. Schlegel, G. E. Scuseria, M. A. Robb, J. R. Cheeseman, G. Scalmani, V. Barone, B. Mennucci, G. A. Petersson, H. Nakatsuji, M. Caricato, X. Li, H. P. Hratchian, A. F. Izmaylov, J. Bloino, G. Zheng, J. L. Sonnenberg, M. Hada, M. Ehara, K. Toyota, R. Fukuda, J. Hasegawa, M. Ishida, T. Nakajima, Y. Honda, O. Kitao, H. Nakai, T. Vreven, J. A. Montgomery Jr., J. E. Peralta, F. Ogliaro, M. J. Bearpark, J. Heyd, E. N. Brothers, K. N. Kudin, V. N. Staroverov, R. Kobayashi, J. Normand, K. Raghavachari, A. P. Rendell, J. C. Burant, S. S. Iyengar, J. Tomasi, M. Cossi, N. Rega, N. J. Millam, M. Klene, J. E. Knox, J. B. Cross, V. Bakken, C. Adamo, J. Jaramillo, R. Gomperts, R. E. Stratmann, O. Yazyev, A. J. Austin, R. Cammi, C. Pomelli, J. W. Ochterski, R. L. Martin, K. Morokuma, V. G. Zakrzewski, G. A. Voth, P. Salvador, J. J. Dannenberg, S. Dapprich, A. D. Daniels, Ö. Farkas, J. B. Foresman, J. V. Ortiz, J. Cioslowski and D. J. Fox, *Journal*, 2009.

28. A. F. Sweeney and P. B. Armentrout, *Journal of Physical Chemistry A*, 2014, **118**, 10210-10222.

29. E. D. Glendening, J. K. Badenhoop, A. E. Reed, J. E. Carpenter, J. A. Bohmann, C. M. Morales, C. R. Landis and F. Weinhold., *Journal*, 2013.

30. M. J. Frisch, G. W. Trucks, H. B. Schlegel, G. E. Scuseria, M. A. Robb, J. R. Cheeseman, G. Scalmani, V. Barone, B. Mennucci, G. A. Petersson, H. Nakatsuji, M. Caricato, X. Li, H. P. Hratchian, A. F. Izmaylov, J. Bloino, G. Zheng, J. L. Sonnenberg, M. Hada, M. Ehara, K. Toyota, R. Fukuda, J. Hasegawa, M. Ishida, T. Nakajima, Y. Honda, O. Kitao, H. Nakai, T. Vreven, J. A. Montgomery, J. E. Peralta, F. Ogliaro, M. Bearpark, J. J. Heyd, E. Brothers, K. N. Kudin, V. N. Staroverov, R. Kobayashi, J. Normand, K. Raghavachari, A. Rendell, J. C. Burant, S. S. Iyengar, J. Tomasi, M. Cossi, N. Rega, J. M. Millam, M. Klene, J. E. Knox, J. B. Cross, V. Bakken, C. Adamo, J. Jaramillo, R. Gomperts, R. E. Stratmann, O. Yazyev, A. J. Austin, R. Cammi, C. Pomelli, J. W. Ochterski, R. L. Martin, K. Morokuma, V. G. Zakrzewski, G. A. Voth, P. Salvador, J. J. Dannenberg, S. Dapprich, A. D. Daniels, Farkas, J. B. Foresman, J. V. Ortiz, J. Cioslowski and D. J. Fox, *Journal*, 2009, DOI: citeulike-article-id:9096580.

31. P. D. Carnegie, A. B. McCoy and M. A. Duncan, *The Journal of Physical Chemistry A*, 2009, **113**, 4849-4854.

32. A. F. Sweeney, J. T. O'Brien, E. R. Williams and P. B. Armentrout, *International Journal of Mass Spectrometry*, 2015, **378**, 270-280.

33. T. E. Cooper, J. T. O'Brien, E. R. Williams and P. B. Armentrout, *The Journal of Physical Chemistry A*, 2010, **114**, 12646-12655.

34. K. Hermansson, P. A. Bopp, D. Spångberg, L. Pejov, I. Bakó and P. D. Mitev, *Chemical Physics Letters*, 2011, **514**, 1-15.

35. K. Hermansson, *International Journal of Quantum Chemistry*, 1993, **45**, 747-758.

36. K. Hermansson, *Chemical Physics*, 1993, **170**, 177-184.

Chapter 4: Infrared Spectroscopy of Peptide Based Systems

This chapter covers the behavior of a series of glycine peptides as well as two polyglycine-Cu complexes. In section 1 the influence of chain length on hydrogen bonding motifs in $[Gly_n\text{-}H]^-$ (n=1-4) polypeptides are studied. It is found that with additional residues the interaction between amide groups and the terminal NH_2 group becomes important to the structure.

In section 2 the spectra of $[CuGly_4\text{-}4H]^{2-}$ and $[CuGly_3\text{-}3H]^-$ are investigated to further expand on the importance of hydrogen bonding interactions. Comparison to the previously studied glycine peptides indicates that the C=O region is significantly red-shifted in the CuGly complexes. This shift is attributed to the charged environment induced by deprotonation and the metal center. The structure of $[CuGly_4\text{-}4H]^{2-}$ is shown to differ from previous solution phase experiments.

4.1 Intramolecular Hydrogen Bonding Motifs in Deprotonated Glycine Peptides Studied by Cryogenic Ion Infrared Spectroscopy

Published in: *Journal of Physical Chemistry A*, **118**, 3906-3912 (2014)

Abstract

The infrared spectra of deprotonated glycine peptides, $(G_n\text{-}H)^-$ with n=1-4, in the 1200-3500 cm^{-1} spectral region are presented. Comparisons between the experimental and calculated spectra reveal the chain length dependent hydrogen bonding motifs which define the geometries of these species. First, an interaction between the terminal carboxylate and the neighboring amide N-H is present in all the peptide structures. This interaction is strong enough to align this amide group in the same plane as the carboxylate. However, we found that the vibrational frequency shift of this hydrogen bonded N-H group is not well reproduced in the calculations. Second, in the longer $(G_3\text{-}H)^-$ and $(G_4\text{-}H)^-$ species, the peptide chain folds such that the terminal NH_2 group also interacts with the carboxylate. Both of these folded structures display an interaction between the terminal NH_2 and the neighboring N-H as well. Lastly, an amide-amide interaction is observed in the longest $(G_4\text{-}H)^-$ structure. Analysis of the N-H peak positions reveals the interplay among the different hydrogen bonds, especially around the negatively charged carboxylate moiety.

4.1.1 Introduction

The three-dimensional structures of proteins arise from hydrogen bonding within the peptide backbone. Probing such interactions at the residue level can provide insights into the formation of these geometries. In this regard, infrared vibrational spectroscopy is a valuable tool in determining molecular structures and the strength of intramolecular forces. Specifically, positions of the characteristic amide vibrational modes are useful indicators of the effect of local structure on these interactions.[1, 2] In this paper, we present the infrared spectroscopic study of intramolecular hydrogen bonding in isolated deprotonated glycine peptides as a function of chain length.

There have been numerous investigations of peptide vibrations, many of which involved solution phase spectroscopy,[3-7] such as the recent growth in popularity of 2D-IR spectroscopy as a probe for secondary structures.[8-12] For glycine peptides, its conformations have been relatively well explored in the condensed phase.[6, 7, 13] On the other hand, gas phase experiments allow individual vibrational modes to be studied in detail. Such studies of peptides were greatly aided by the advent of electrospray ionization (ESI),[14, 15] which enabled fragile solution phase species to be brought into the gas phase for spectroscopic analysis. Peptides[16-22] and even proteins[23] have been studied in the gas phase, with techniques including infrared multiple photon dissociation (IRMPD) spectroscopy,[16, 17, 22, 23] IR-UV double resonance photofragment spectroscopy,[24-26] and resonant two-photon ionization (R2PI) spectroscopy[18, 21]. Most of these experiments involved cationic[16, 19, 20] or neutral[18] species, whereas anions have been considerably less explored[22]. A recently developed technique, involving H_2-tagging in a cryogenic ion-trap, allows for infrared spectroscopy of cold mass-selected ions without the need for a powerful free-electron laser or the presence of a UV chromophore.[19, 20, 27] Moreover, the single-photon nature

of the predissociation process and cryogenic temperature required for H_2-tagging yield well-resolved linear spectra which greatly facilitate comparison with calculations.

Here we present infrared spectra of deprotonated glycine chains, $(G_n\text{-}H)^-$ with n = 1-4, obtained by cryogenic ion vibrational spectroscopy. DFT calculations aid peptide structure determination and spectral assignments. We monitor the relative strength of intramolecular hydrogen bonding as a function of chain length using the vibrational frequencies of the H-bond donating N-H groups and H-bond accepting C=O groups. The changes in the N-H peak positions as a function of peptide length also reveal the interplay between the different hydrogen bonds, especially around the negatively charged carboxylate moiety.

4.1.2 Experimental and computational details

The apparatus used in these experiments is described in detail in chapter two. In these experiments the reaction trap stage contained only a hexapole ion guide. The time-of-flight region also used a shorter 1 m long flight tube.

Glycine peptides were obtained from Sigma-Aldrich (purity >98%) and dissolved in methanol to a concentration of 1 mM. The solutions were then adjusted to pH ~8 using a small amount of 1 M KOH in H_2O. Tetraglycine, which was initially insoluble in methanol, dissolved fully upon the addition of KOH. The methanol solvent was chosen because it yielded a more stable ion signal, which is desirable for the spectroscopy experiments.

Optimized structures and vibrational frequencies of each peptide were calculated at the cam-B3LYP/aug-cc-pVTZ level of theory using the Gaussian 09 software package.[28] The long-range corrected functional was chosen because of the importance of hydrogen bonding in the species studied here. Frequencies were scaled by factors of 0.948 in the 2800-3500 cm^{-1} region

and 0.963 in the 1200-1800 cm^{-1} region. These scaling factors were obtained by comparing the calculated and experimental N-H (3498 cm^{-1}) and C=O (1707 cm^{-1}) stretching frequencies of isolated N-methyl acetamide.[29] The structures of deprotonated glycine and diglycine are simple enough that a thorough conformer search could be performed manually. For the larger deprotonated triglycine and tetraglycine, a conformer search was carried out using MacroModel 10.1 (Schrödinger) with the OPLS_2005 force field. A large set of resulting low energy conformers was first optimized at the cam-B3LYP/3-21G level. Conformers within a ~0.5 eV window were further refined at the cam-B3LYP/6-31+G(d,p) level, and the final optimization and vibrational frequency calculations were carried out for the 5 lowest energy conformers at the cam-B3LYP/aug-cc-pVTZ level.

4.1.3 Results

An overview of the infrared predissociation spectra of the four deprotonated glycine peptides, $(G_n\text{-}H)^-$ (n=1-4), in the 1200-3500 cm^{-1} range is shown in Figure 4.1. These spectra were acquired by monitoring the loss channel of two D_2 tags from the corresponding $(G_n\text{-}H)^- \cdot (D_2)_2$ ions. As expected, peaks are observed in the N-H stretch (amide A) region, C-H stretch region, C=O stretch (amide I) region, and the C=N stretch (amide II) region for each peptide species. In the N-H stretch region, from 3100 cm^{-1} to 3500 cm^{-1}, a generally increasing number of peaks are observed as the peptide chain lengthens, corresponding to increasing number of N-H bonds. In the spectrum of $(G\text{-}H)^-$, only a weak feature is observed at 3258 cm^{-1}. For $(G_2\text{-}H)^-$, a much more intense feature is observed at 3223 cm^{-1}, while a weaker feature remains at 3270 cm^{-1}. The $(G_3\text{-}H)^-$ spectrum displays three intense features in the N-H region, two broad peaks at 3172 cm^{-1} and 3291 cm^{-1}, and a narrower feature at 3355 cm^{-1}. The $(G_4\text{-}H)^-$ spectrum also displays three intense peaks in the N-H region, at 3125 cm^{-1}, 3329 cm^{-1} and 3371 cm^{-1}. A clear

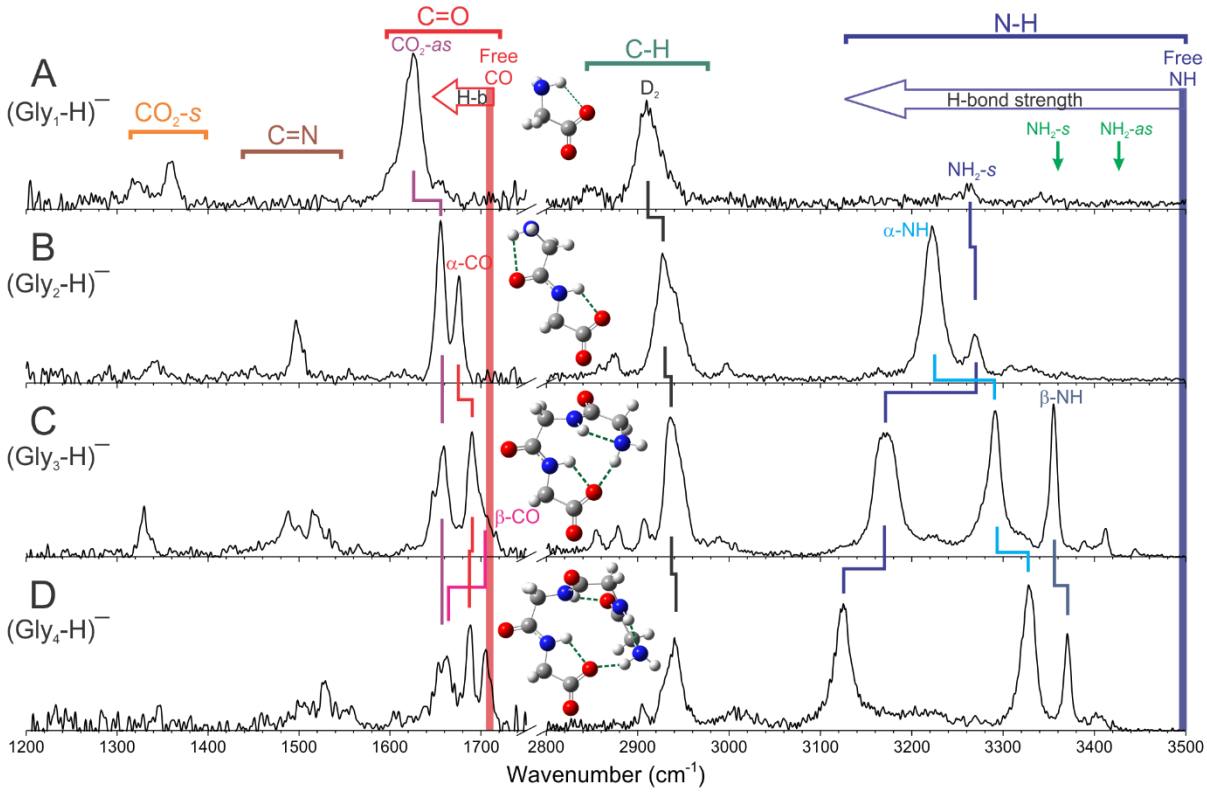

Figure 4.1- Overview of the infrared predissociation spectra of (A) $(G\text{-}H)^-$, (B) $(G_2\text{-}H)^-$, (C) $(G_3\text{-}H)^-$, (D) $(G_4\text{-}H)^-$. The green arrows indicate the frequencies of the free R-NH_2 stretches.

overall trend can be seen in this spectral region, where the lowest frequency N-H peak redshifts while all the other features appear at progressively higher frequencies as the glycine peptide lengthens.

The C-H stretch region, between 2800 cm^{-1} and 3000 cm^{-1}, is also where the D_2 stretching mode is expected to appear. For all four species, this spectral range is dominated by a relatively broad and asymmetric peak whose maximum slowly shifts from about 2911 cm^{-1} in $(G_1\text{-}H)^-$ to about 2939 cm^{-1} in $(G_4\text{-}H)^-$. There are also several weak features at lower frequencies with no discernable trend with increasing peptide length.

The most intense peaks in the lower frequency part of the spectrum all appear in the C=O region between 1600 cm^{-1} and 1750 cm^{-1} (amide I and carboxylate antisymmetric stretch). The number of peaks in this region proportionally increase from 1 in $(G_1\text{-}H)^-$ to 4 in $(G_4\text{-}H)^-$. However, unlike the N-H stretch region, these peaks all progressively blueshift as the peptide size increases. Several weaker peaks appear below 1600 cm^{-1}, especially in the C=N stretch (amide II) region between 1450 cm^{-1} and 1600 cm^{-1}.

4.1.4 Analysis

Electronic structure calculations were carried out to aid the assignment of the observed infrared predissociation spectra and to determine the structure of the deprotonated glycine peptides. Oomens and Steill[22] have shown that the singly deprotonated trialanine obtained by electrospray ionization corresponds to the carboxylate species. Therefore, we only considered this deprotonation site in our theoretical study of the glycine peptides. We begin this section by comparing the calculation results with the experimental spectrum of each individual species.

For the simple deprotonated glycine amino acid, only one energy minimum was found. The calculated structure is shown in Figure 4.2 along with the calculated and experimental spectra. In this structure, one of the N-H bonds is aligned in the carboxylate plane and interacts with the nearby oxygen. The calculated spectrum is in very good agreement with the experimental results, with the peak at 2911 cm^{-1}, which is not reproduced in the calculation, as the only significant discrepancy. This peak can be readily assigned to the nominally forbidden D_2 stretch which gains intensity from the perturbation induced by binding to the anion. The observed D_2 vibration is redshifted by 84 cm^{-1} from the frequency of free D_2 at 2994 cm^{-1}.[30] Calculations on the tagged $(G_1\text{-}H)^-\cdot(D_2)_n$ ions in figure 4.3 show that D_2 binds to the negatively charged carboxylate moiety similarly to its interaction with deprotonated carboxylic acids.[31] The addition of one or two D_2 tags did not significantly perturb any of the glycine vibrations in the calculated spectra, and thus we can directly compare the calculated spectrum of the bare species with the experimental results.

The assignment of the $(G_1\text{-}H)^-$ spectrum is straightforward. In the N-H stretch region, the weak peak at 3258 cm^{-1} is assigned to the NH_2 symmetric stretch. The corresponding antisymmetric stretch is calculated to be much weaker and is thus tentatively assigned to the very weak feature at 3341 cm^{-1}. In the C-H stretch region, the peak at 2849 cm^{-1} is assigned to the CH_2 symmetric stretch. The main peak at 1625 cm^{-1} in the C=O stretch region is assigned to two modes corresponding to a mixture of the antisymmetric CO_2 stretch and NH_2 bend. These two modes are too close to each other to be resolved in the experimental spectrum. Lastly, the weak peaks at 1323 cm^{-1} and 1359 cm^{-1} are assigned to the NH_2 wag and the CO_2 symmetric stretch, respectively.

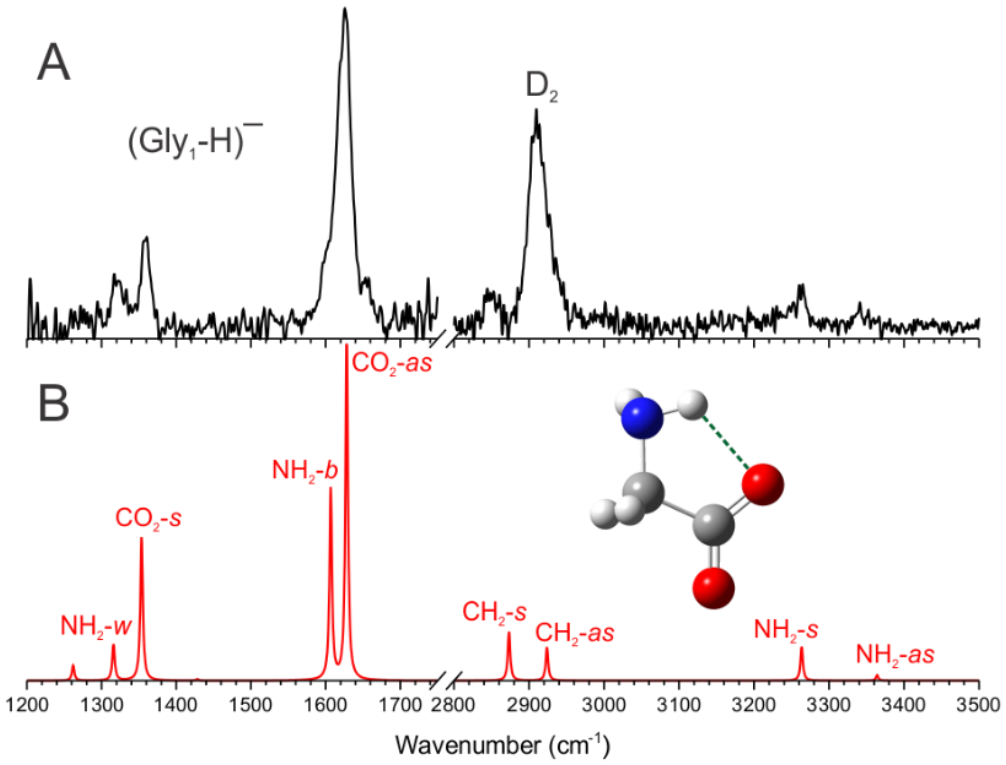

Figure 4.2- The experimental (A) and calculated (B) vibrational spectrum of $(G\text{-}H)^-$.

as=antisymmetric stretch, *s*=symmetric stretch, *b*=bend, *w*=wag.

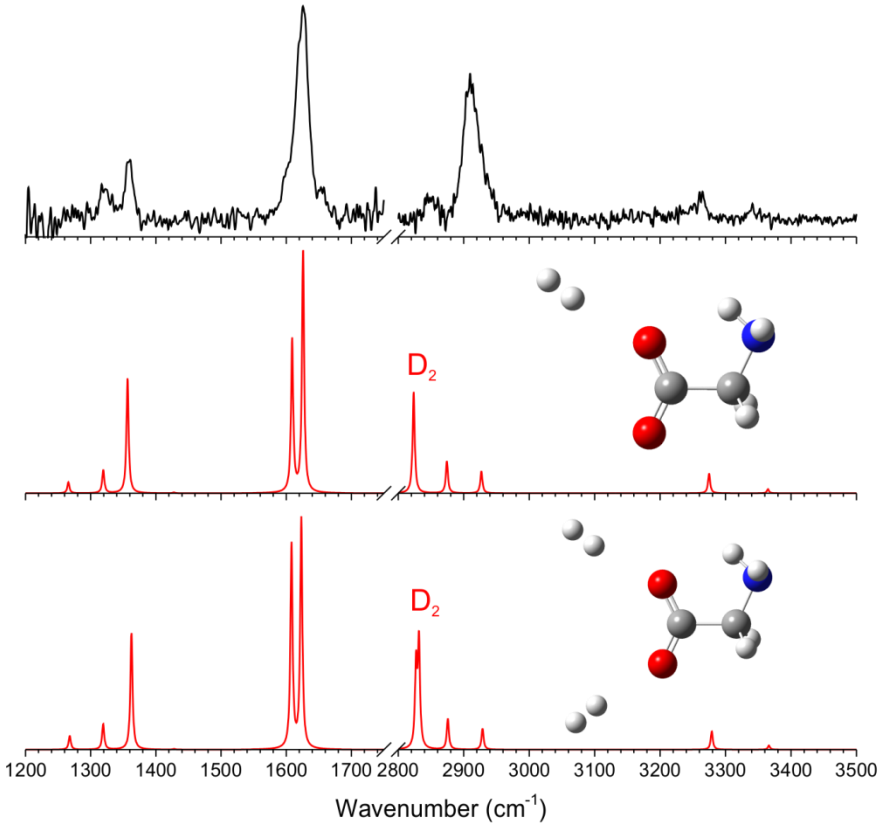

Figure 4.3- Experimental spectrum of $(G\text{-}H)^-$ and CAM-B3LYP/aug-cc-pVTZ calculated spectra of $(G\text{-}H)(D_2)^-$, and $(G\text{-}H)(D_2)_2^-$

The computational search for $(G_2\text{-}H)^-$ conformers yielded two low-lying structures which are shown in Figure 4.4 together with the calculated and experimental spectra. The lowest energy conformer has a fully extended geometry which contains two internal hydrogen bonds. One of them is between the CO_2 and the nearby amide α-N-H group, and the second one is between the terminal NH_2 and the amide α-C=O. The next conformer is merely 206 cm^{-1} higher in energy and only differs in the rotation of the terminal CH_2NH_2 group, breaking the second weak H-bond. The corresponding calculated spectra are very similar, except for small shifts in the N-H region. For the lower frequency part of the spectrum, both conformers are in excellent agreement with the experimental spectrum. This allows us to assign the peaks at 1341 cm^{-1} and 1656 cm^{-1} to the symmetric and antisymmetric CO_2 modes, respectively. The two other peaks at 1675 cm^{-1} and 1498 cm^{-1} are assigned to the amide I (C=O) and amide II (C=N) modes, respectively.

The agreement between the calculated and experimental spectra is not as good in the N-H region of $(G_2\text{-}H)^-$. Both conformers are predicted to have a single intense feature corresponding to the α-N-H interacting with the neighboring CO_2 at either 3267 cm^{-1} or 3282 cm^{-1}. The experimental spectrum instead shows an intense peak at 3223 cm^{-1} and a weaker peak at 3270 cm^{-1}. None of the higher lying conformers produced a more reasonable fit. One possible assignment is that both conformers in Figure 4.4 are present in the experiment, and the two observed N-H peaks correspond to the two α-N-H vibrations. However, this would imply that the calculation overestimates the frequency of the α-N-H vibration by 43 cm^{-1} for the conformer

in Figure 4.4B and 13 cm^{-1} for the conformer in Figure 4.4C. Given that the interaction between α-N-H and CO_2 is essentially the same for these two structures, it is unlikely the overestimation

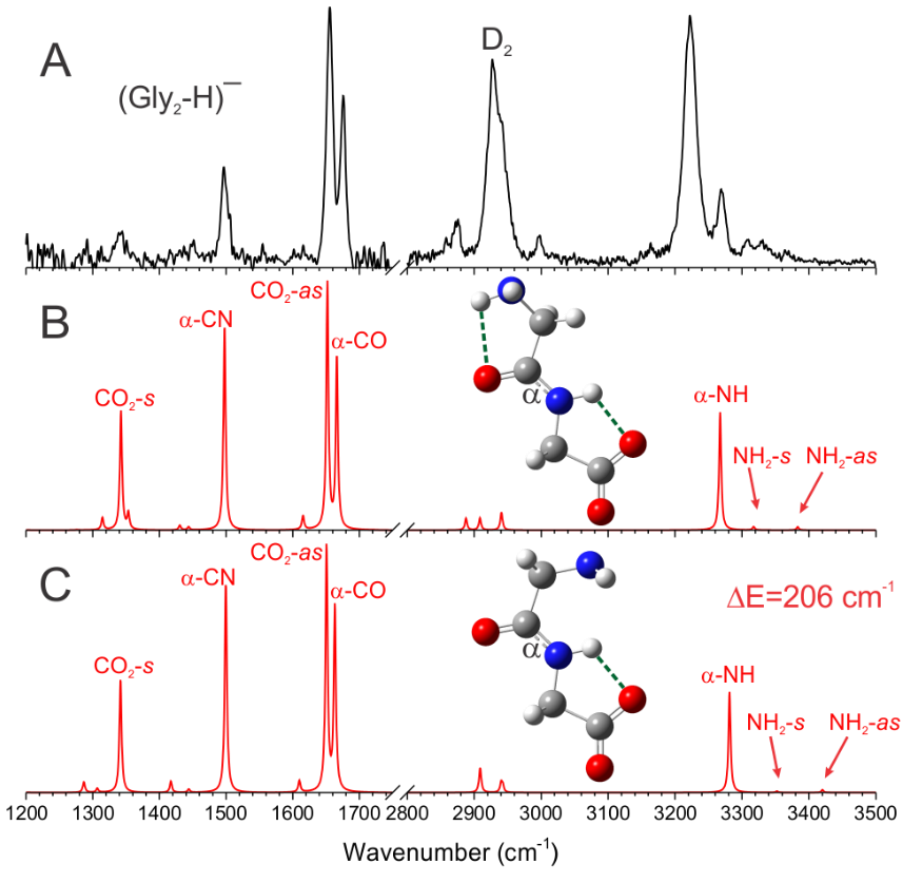

Figure 4.4- The experimental (A) and calculated (B)-(C) vibrational spectrum of $(G_2-H)^-$ with their relative energies. *as*=antisymmetric stretch, *s*=symmetric stretch. The location of the □-amide group is indicated on the molecule.

would be so different. A more plausible assignment is that the two observed peaks are the α-N-H and the symmetric NH_2 stretch of the lowest energy conformer, implying that both hydrogen bond interactions are underestimated in the calculation. This interpretation is reinforced by the observation of a very similar discrepancy in the calculated position of the α-N-H band in the $(G_3\text{-}H)^-$ and $(G_4\text{-}H)^-$ spectra, as discussed below. Additional calculations at the MP2/6-31+G(d,p) level were carried out for the lowest energy conformers of $(G_2\text{-}H)^-$, $(G_3\text{-}H)^-$ and $(G_4\text{-}H)^-$ (Figures 4.5-4.7), which yielded similar frequencies for the α-N-H stretch vibration. This indicates that the discrepancy is probably due to anharmonicity. We performed anharmonic calculations at the cam-b3lyp/aug-cc-pVTZ for structure 3B which yielded an improved frequency of 3230 cm^{-1} for this band. This assignment does not rule out the presence the conformer in Figure 4.4C whose α-N-H stretch would appear at essentially the same frequency. However, because the two conformers are connected through a simple bond rotation, it is unlikely that the higher energy conformer can survive the collisional cooling in the ion trap.

We now turn our attention to the deprotonated triglycine molecule. An extensive conformer search yielded many possible structures, and the two lowest energy ones are shown in Figure 4.8 along with their respective calculated spectrum. To facilitate the discussion, we label the two amides α and β, starting from the C-terminus. The two lowest energy conformers have a folded structure with a hydrogen bond between the terminal NH_2 and CO_2 groups. They differ in geometry by the hydrogen-bonding motif of the α and β amide groups. In the lowest energy structure (Figure 4.8B), the terminal NH_2 is also an H-bond acceptor for the β-N-H while the α-N-H interacts with the CO_2, similar to the $(G_2\text{-}H)^-$ conformers. On the other hand, conformer 4C, which is 438 cm^{-1} higher in energy, has only an H-bond between the β-N-H and the CO_2. In the experimental spectrum, the three intense peaks in the 3100 cm^{-1} to 3400 cm^{-1} N-H stretch region

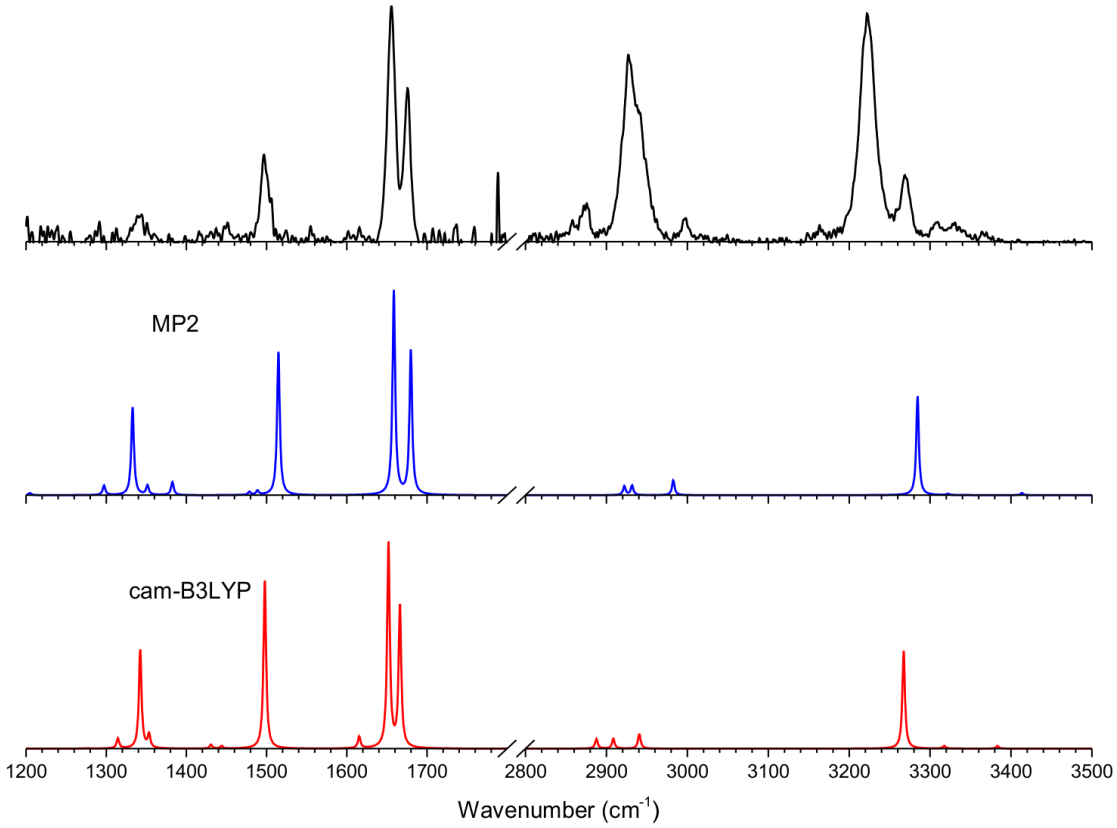

Figure 4.5- Comparison of the experimental spectrum of $(G_2\text{-}H)^-$ (top) with calculated spectrum of the lowest energy conformer at MP2/6-31+G(d,p) and cam-B3LYP/aug-cc-pVTZ levels of theory.

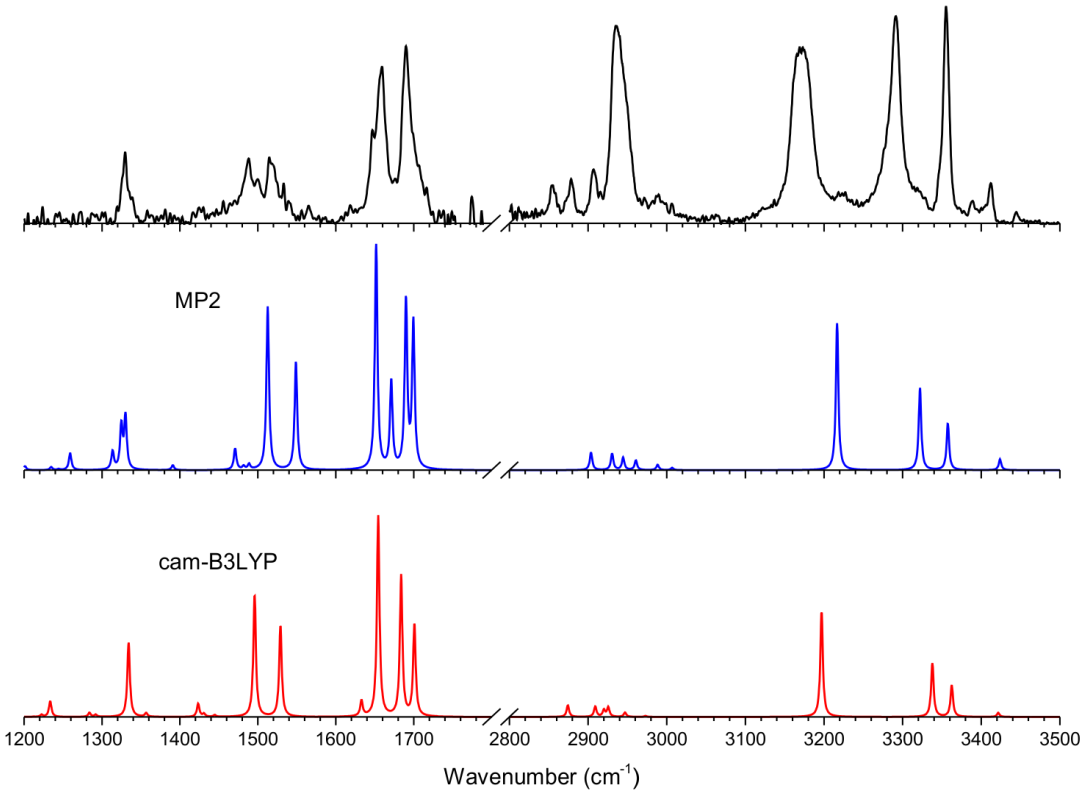

Figure 4.6- Comparison of the experimental spectrum of $(G_3\text{-}H)^-$ (top) with calculated spectrum of the lowest energy conformer at MP2/6-31+G(d,p) and cam-B3LYP/aug-cc-pVTZ levels of theory.

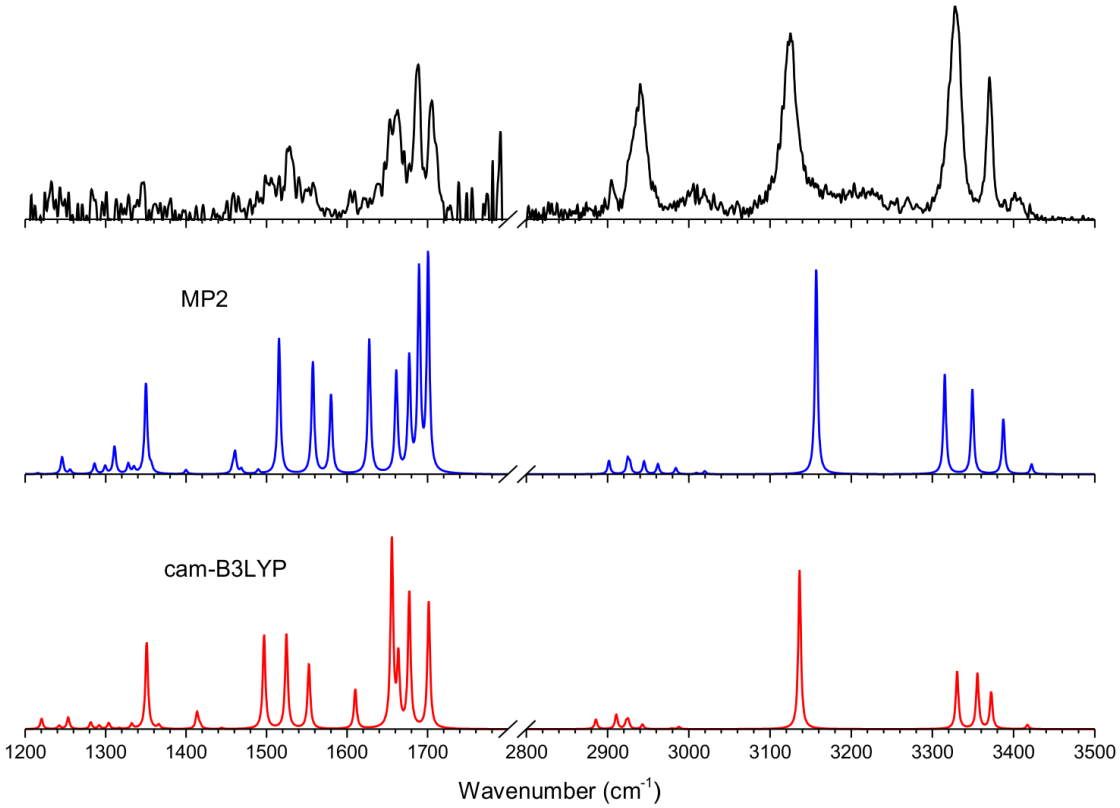

Figure 4.7- Comparison of the experimental spectrum of $(G_4\text{-}H)^-$ (top) with calculated spectrum of the lowest energy conformer at MP2/6-31+G(d,p) and cam-B3LYP/aug-cc-pVTZ levels of theory.

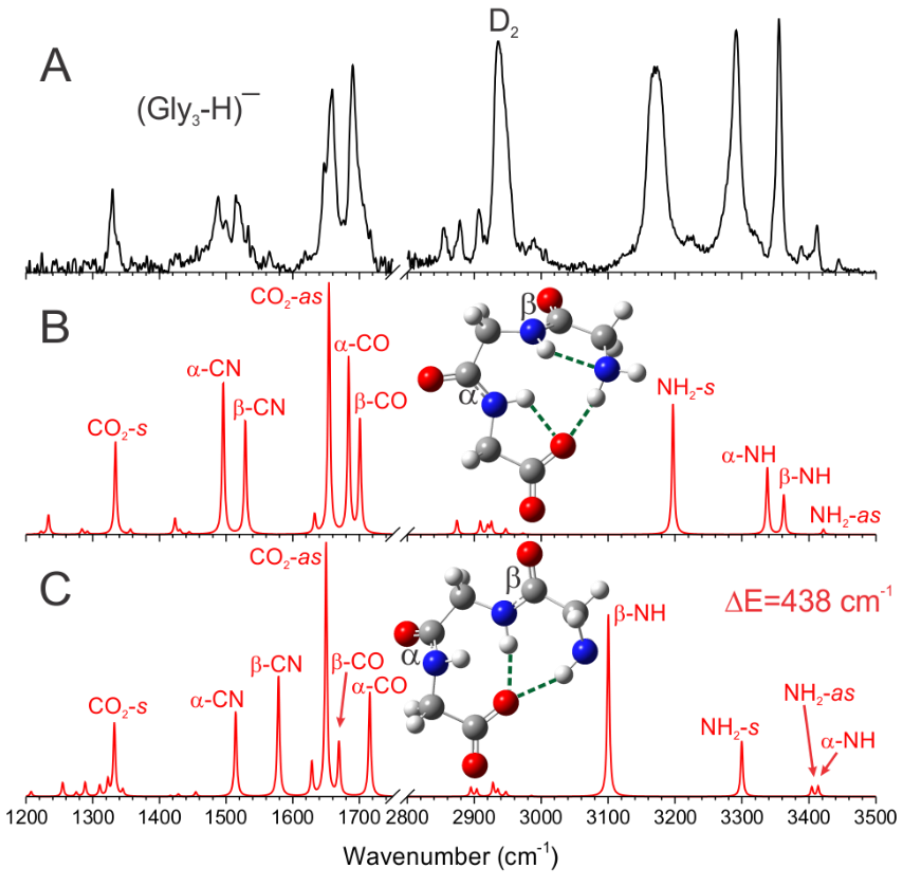

Figure 4.8- The experimental (A) and calculated (B)-(C) vibrational spectrum of (G_3-H)- with their relative energies. *as*=antisymmetric stretch, *s*=symmetric stretch. The locations of the α and β-amide groups are indicated on the molecule.

indicate the presence of three hydrogen bonds with varying degrees of interaction strength, and rules out the presence of conformer 4C. The calculated spectrum of conformer 4B is in good agreement with the experimental spectrum. The main discrepancy is again the frequency of the α-N-H stretch, which is overestimated by 46 cm^{-1} in the calculated spectrum. This discrepancy and the associated H-bond interaction involving the α-N-H and CO_2 is the same as in the $(G_2\text{-}H)^-$ species. Therefore, the three intense peaks at 3172 cm^{-1}, 3291 cm^{-1} and 3355 cm^{-1} are assigned to the NH_2 symmetric stretch, α-N-H stretch and β-N-H stretch, respectively. The weak peak at 3411 cm^{-1} is assigned to the antisymmetric NH_2 stretch.

In the lower frequency region, the good agreement between the experiment and calculated spectrum of the lowest energy conformer allows for a straightforward assignment. The peak at 1690 cm^{-1} and its shoulder at 1707 cm^{-1} are assigned to the α-C=O and β-C=O stretch, respectively. The symmetric and antisymmetric CO_2 stretches are found at 1330 cm^{-1} and 1658 cm^{-1}, respectively. Lastly, the α-C=N and β-C=N stretches are at 1487 cm^{-1} and 1519 cm^{-1}, respectively.

Finally, we consider the infrared predissociation spectrum of the deprotonated tetraglycine molecule, shown in Figure 4.9. Once again, we label each amide group α, β, and γ, keeping the α-amide next to the C-terminus and the β-amide next to the N-terminus, with the new γ-amide in the center of the peptide. The extensive conformer search yielded the two lowest energy structures of $(G_4\text{-}H)^-$ shown in Figure 4.9B and 4.9C, which have a similar folded motif as the $(G_3\text{-}H)^-$ conformer discussed above. In both structures, the CO_2 interacts with both the terminal NH_2 and the α-N-H. In addition, the conformer shown in Figure 4.9B has two other H-

bond interactions, between the β-N-H and terminal NH_2 and between the β-C=O and γ-N-H. On the other hand, conformer 4.9C has only one additional H-bond between the β-N-H and CO_2. Once again the calculated spectrum of the lowest energy conformer is in excellent agreement with the experimental spectrum, with the frequency of the α-N-H stretch as the only exception. Its calculated position falls between the two observed peaks at 3329 cm^{-1} and 3371 cm^{-1}, assigned to the γ-N-H and β-N-H stretches, respectively. If a similar ~45 cm^{-1} correction is made as in the case of $(G_2\text{-}H)^-$ and $(G_3\text{-}H)^-$, which display the same interaction motif between the α-N-H and CO_2, this peak would appear at about 3310 cm^{-1} and overlap with the γ-N-H stretch. This is consistent with the broad and intense appearance of the band at 3329 cm^{-1}. A close inspection of the N-H region indicates that the conformer in Figure 4.9C, even though only 192 cm^{-1} above the minimum energy structure, does not contribute to the observed spectrum. For this conformer, the calculation predicts two intense features between 3200 cm^{-1} and 3300 cm^{-1}, which are clearly absent in the experimental spectrum.

In the lower frequency region, the good agreement between the experimental spectrum and calculated spectrum of the lowest energy conformer yields straightforward assignments. The broad feature at 1660 cm^{-1} is assigned to the overlapping CO_2 antisymmetric stretch and β-C=O. The peaks at 1687 cm^{-1} and 1706 cm^{-1} are assigned to the α-C=O and γ-C=O modes, respectively. All the assigned experimental peak positions are summarized in Table 4.1.

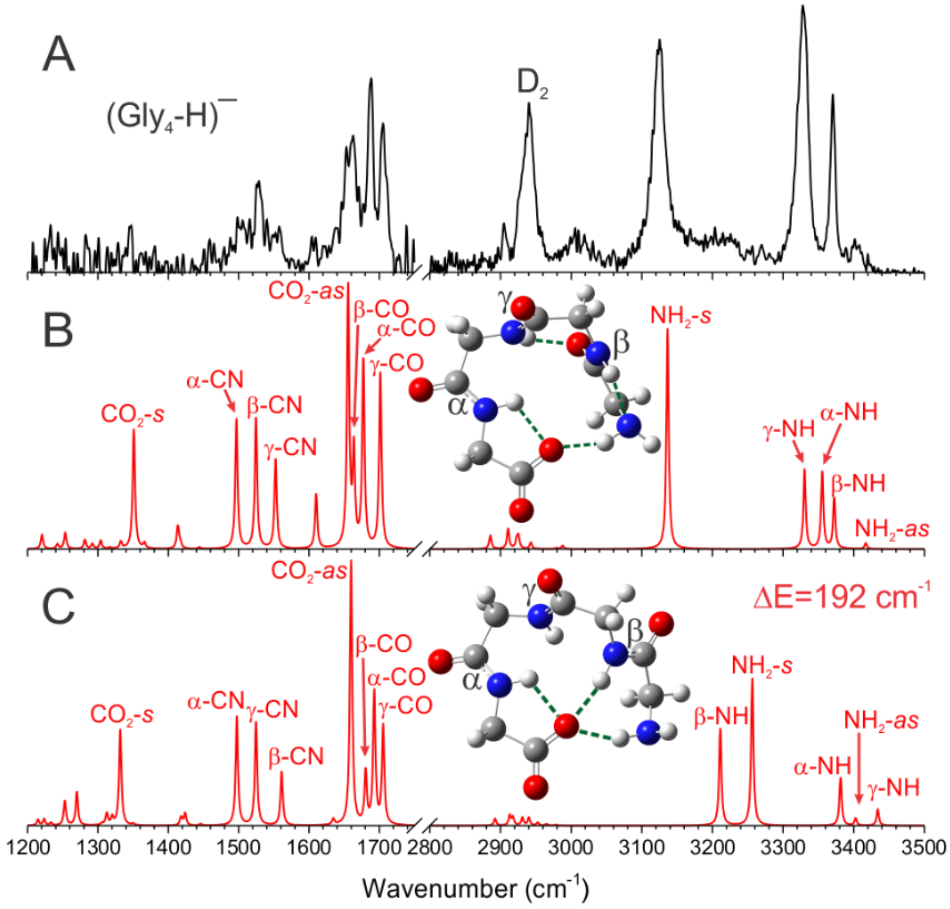

Figure 4.9- The experimental (A) and calculated (B)-(C) vibrational spectrum of $(G_4\text{-}H)^-$ with their relative energies. For the peak labels in (B)-(C): *as*=antisymmetric stretch, *s*=symmetric stretch, *b*=bend. The locations of the α, β, and γ-amide groups are indicated on the molecule.

4.1.5 Discussion

The well-resolved experimental spectra and well-defined structures offer a clear look at the evolution of the intramolecular hydrogen bonding as a function of peptide length. Several hydrogen bonding interactions appear in the structure of deprotonated glycine peptides and define the overall geometry. First, the interaction between the α-N-H and the CO_2 is present in all the peptide structures and is strong enough to align the α-amide group in the same plane as the carboxylate group. Second, while $(G_1\text{-}H)^-$ and $(G_2\text{-}H)^-$ have extended structures, the peptide chain is folded in the longer $(G_3\text{-}H)^-$ and $(G_4\text{-}H)^-$ such that the terminal NH_2 group interacts with the terminal CO_2 group. Furthermore, $(G_3\text{-}H)^-$ and $(G_4\text{-}H)^-$ also display an interaction between the terminal NH_2 and the neighboring β-N-H. Lastly, the an amide-amide interaction is first observed in the $(G_4\text{-}H)^-$ structure.

The N-H stretch vibrations can serve as sensitive probes for the local hydrogen bonding environment. In general, the frequency shift of an X-H hydrogen bond donor is proportional to the square of the hydrogen bonding interaction energy.[32-34] The vibrational frequencies of the free symmetric R-NH_2 (3361 cm^{-1}) and amide N-H (3498 cm^{-1}) are indicated in Figure 4.1 and serve as our reference points for estimating the interaction strength. These values are taken from the vibrational spectra of gas phase methylamine[35] and N-methyl acetamide isolated in a cryogenic matrix.[29] In the extended $(G_2\text{-}H)^-$ structure, the strongest interaction is between the α-N-H and CO_2, which causes a 275 cm^{-1} redshift of the amide N-H. When the chain folds in $(G_3\text{-}H)^-$, the interaction between the terminal NH_2 and CO_2 causes a 189 cm^{-1} shift of the NH_2 frequency, while at the same time reduces the α-N-H redshift to 207 cm^{-1}. This trend continues in $(G_4\text{-}H)^-$ in which the NH_2 is shifted by 236 cm^{-1} and the α-N-H by 169 cm^{-1}. The overlapping

Mode	Experimental position			
	$[G-H]^-$	$[G_2-H]^-$	$[G_3-H]^-$	$[G_4-H]^-$
NH_2-as			3411	
NH_2-s	3258	3270	3172	3125
α-NH	--	3223	3291	~3329
β-NH	--	--	3355	3371
γ-NH	--	--	--	~3329
D_2	2911	2928	2936	2939
α-CO	--	1675	1690	1687
β-CO	--	--	~1707	~1660
γ-CO	--	--	--	1706
α-C=N	--	1498	1487	1503
β-C=N	--	--	1519	1528
γ-C=N	--	--	--	1555
CO_2-as	1625	1656	1658	~1660
CO_2-s	1359	1341	1330	

Table 4.1- Summary of the observed peak positions

α-N-H and γ-N-H peaks in $(G_4\text{-H})^-$ indicate that the strength of the α-N-H CO_2 interaction is reduced to approximately the same as a neutral amide-amide H-bond. We attribute the higher NH_2-CO_2 hydrogen bonding strength in $(G_4\text{-H})^-$ to simply a reduced bending strain in the longer peptide chain. In return, this H-bond creates an increased charge transfer from the CO_2 to the terminal NH_2, which progressively reduces the CO_2's interaction with the neighboring α-N-H. This progressive charge transfer effect can also be observed through the frequency of the nominally forbidden D_2 stretch. The D_2 tag binds to the charge center and the shift from the free D_2 frequency of 2994 cm^{-1} [30] is a good indicator of the binding energy and thus of the effective charge on the CO_2. As the chain length increases and the charge on CO_2 becomes stabilized by stronger interactions, the frequency of the D_2 stretch blueshifts from about 2910 cm^{-1} to 2940 cm^{-1}, consistent with a reduced effective charge.

The amide I mode (C=O stretch) can also be an indication of the hydrogen bonding environment. In general, when the C=O acts as an H-bond acceptor, the frequency redshifts from the free value of about 1707 cm^{-1}.[29] However, the amplitude of the shift is much more modest than the N-H modes. Moreover, the positions of peaks in this spectral region can be complicated by coupling between nearby C=O modes.[21] In $(G_2\text{-H})^-$, the α-C=O interacts with the terminal NH_2 group, and its frequency is redshifted by 33 cm^{-1}. This is approximately the expected shift induced by a neutral hydrogen bond.[36, 37] However, it is unexpected in this case given that the difference in energy between conformer 3B and 3C indicates that this H-bonding interaction is only about 200 cm^{-1}. Furthermore, even though the α-C=O is free in $(G_3\text{-H})^-$ and $(G_4\text{-H})^-$, its frequency is still anomalously redshifted by about 20 cm^{-1}. On the other hand, the free β-C=O in $(G_3\text{-H})^-$ and the free γ-C=O in $(G_4\text{-H})^-$ have frequencies that are very close to the free C=O at 1707 cm^{-1}. Inspection of the normal mode displacements in the calculated structures

of $(G_3\text{-H})^-$ and $(G_4\text{-H})^-$ rules out couplings as a source of the redshifted position of the α-C=O. Therefore, we attribute the redshifting of the α-C=O vibration to charge transfer from the interaction of the α-N-H with the negatively charged CO_2. Support for this conclusion comes from the calculated spectra of conformers in Figure 4.8B and 4.8C, in which the immediate environment around α-C=O differs only by the presence of the α-N-H/CO_2 interaction. When this interaction is not present (4.8C) the position of the α-C=O vibration is calculated to fall in the expected free C=O region. It thus appears that in addition to driving the folding of the peptide chain, the presence of a negatively charged carboxylate group also has a strong electronic effect on the neighboring amide group.

The well resolved spectra also enable us to probe the behavior of the amide II bands. The calculated normal modes for the longer $(G_3\text{-H})^-$ and $(G_4\text{-H})^-$ show that the amide II vibrations are strongly coupled together in these structures and that the splitting of these features probably mostly comes from this coupling. In Figures 4.4, 4.8, and 4.9, we labelled these peaks according to the amide that is the main contributor to the displacements. This analysis shows that the lowest frequency amide II in these structures belongs to the α-amide group. According to the behavior of the corresponding N-H peaks, this is the amide group with the strongest hydrogen bond. On the other hand, the free γ-amide in $(G_4\text{-H})^-$ has the highest frequency. Therefore, it appears that the amide II vibrations have a qualitatively similar behavior as the amide I vibrations with regard to hydrogen-bonding. We note that the overall positions of the amide II bands shift to slightly higher frequencies as the number of glycine units increases. This is consistent with the behavior of the amide N-H peaks shifting toward higher frequency in the larger peptides, indicating weaker amide hydrogen bond.

4.1.6 Conclusion

Infrared spectra of deprotonated glycine peptides, with 1-4 residues, are presented. Comparison with calculated spectra revealed the structures of these species, allowing a closer look at the intramolecular hydrogen bonding motifs present in these peptides. Consistent trends are seen as the deprotonated glycine peptide chain lengthens, which come to define the overall geometry. First, there is an interaction between the CO_2 and the neighboring α-N-H, which is present in all the peptide structures and is strong enough to keep the α-amide group in the same plane as the carboxylate. We found that the shift in the vibrational frequency of the α-N-H stretch induced by this interaction is not well reproduced in the cam-B3LYP or MP2 calculations. Nonetheless, the experimental frequencies of the α-N-H stretch provide a clear picture of the changes in the strength of this hydrogen bond as other intramolecular hydrogen bonds come into play. As the peptide increases in length, the longer $(G_3\text{-}H)^-$ and $(G_4\text{-}H)^-$ species begin to fold such that the terminal NH_2 group is also interacting with the CO_2 group. This interaction quickly becomes the strongest hydrogen bond, giving rise to an intense redshifted NH_2 stretch, while at the same time weakening the interaction between α-N-H and CO_2. Both $(G_3\text{-}H)^-$ and $(G_4\text{-}H)^-$ also display a comparably weaker interaction between the terminal NH_2 and the neighboring β-N-H. The first amide-amide interaction appears in the $(G_4\text{-}H)^-$ structure, and its strength is on par with the α-N-H/CO_2 interaction. Further analysis of the frequencies of the C=O stretches reveals the effects of the electrostatic interactions in the peptide chains, particularly around the negatively charged carboxylate moiety.

References:

1. A. Barth and C. Zscherp, *Q. Rev. Biophys.*, 2002, **35**, 369-430.
2. E. Vass, M. Hollósi, F. Besson and R. Buchet, *Chem. Rev.*, 2003, **103**, 1917-1954.
3. P. I. Haris and D. Chapman, *Biopolymers*, 1995, **37**, 251-263.
4. C. L. Nesloney and J. W. Kelly, *Biorg. Med. Chem.*, 1996, **4**, 739-766.
5. J. Kubelka, R. Huang and T. A. Keiderling, *J. Phys. Chem. B*, 2005, **109**, 8231-8243.
6. S. Bykov and S. Asher, *J. Phys. Chem. B*, 2010, **114**, 6636-6641.
7. S. Ohnishi, H. Kamikubo, M. Onitsuka, M. Kataoka and D. Shortle, *J. Am. Chem. Soc.*, 2006, **128**, 16338-16344.
8. Z. Ganim, H. S. Chung, A. W. Smith, L. P. Deflores, K. C. Jones and A. Tokmakoff, *Acc. Chem. Res.*, 2008, **41**, 432-441.
9. S. Roy, J. Lessing, G. Meisl, Z. Ganim, A. Tokmakoff, J. Knoester and T. L. C. Jansen, *J. Chem. Phys.*, 2011, **135**, 234507.
10. A. Ghosh and R. M. Hochstrasser, *Chem. Phys.*, 2011, **390**, 1-13.
11. Y. S. Kim and R. M. Hochstrasser, *J. Phys. Chem. B*, 2009, **113**, 8231-8251.
12. S. D. Moran, A. M. Woys, L. E. Buchanan, E. Bixby, S. M. Decatur and M. T. Zanni, *Proc. Natl. Acad. Sci. U. S. A.*, 2012, **109**, 3329-3334.
13. C. H. Bamford, L. Brown, E. M. Cant, A. Elliott, W. E. Hanby and B. R. Malcolm, *Nature*, 1955, **176**, 396-397.
14. J. B. Fenn, M. Mann, C. K. Meng, S. F. Wong and C. M. Whitehouse, *Science*, 1989, **246**, 64-71.
15. J. B. Fenn, M. Mann, C. K. Meng, S. F. Wong and C. M. Whitehouse, *Mass Spectrom. Rev.*, 1990, **9**, 37-70.
16. W. Ronghu and T. B. McMahon, *J. Phys. Chem. B*, 2009, **113**, 8767-8775.
17. D. Scuderi, C. F. Correia, O. P. Balaj, G. Ohanessian, J. Lemaire and P. Maitre, *ChemPhysChem*, 2009, **10**, 1630-1641.
18. J. C. Dean, E. G. Buchanan and T. S. Zwier, *Journal of the American Chemical Society*, 2012, **134**, 17186-17201.
19. C. M. Leavitt, A. B. Wolk, J. A. Fournier, M. Z. Kamrath, E. Garand, M. J. Van Stipdonk and M. A. Johnson, *J. Phys. Chem. Lett.*, 2012, **3**, 1099-1105.

20. C. M. Leavitt, A. B. Wolk, M. Z. Kamrath, E. Garand, M. J. Van Stipdonk and M. A. Johnson, *Journal of the American Society for Mass Spectrometry*, 2011, **22**, 1941-1952.
21. E. G. Buchanan, W. H. James, S. H. Choi, L. Guo, S. H. Gellman, C. W. Muller and T. S. Zwier, *Journal of Chemical Physics*, 2012, **137**.
22. J. Oomens and J. D. Steill, *Journal of the American Society for Mass Spectrometry*, 2010, **21**, 698-706.
23. J. Oomens, N. Polfer, D. T. Moore, L. van der Meer, A. G. Marshall, J. R. Eyler, G. Meijer and G. von Helden, *PCCP*, 2005, **7**, 1345-1348.
24. N. S. Nagornova, T. R. Rizzo and O. V. Boyarkin, *Angew. Chem.*, 2013, **52**, 6002-6005.
25. J. A. Stearns, S. Mercier, C. Seaiby, M. Guidi, O. V. Boyarkin and T. R. Rizzo, *J. Am. Chem. Soc.*, 2007, **129**, 11814-11820.
26. T. R. Rizzo, J. A. Stearns and O. V. Boyarkin, *Int. Rev. Phys. Chem.*, 2009, **28**, 481-515.
27. M. Z. Kamrath, E. Garand, P. A. Jordan, C. M. Leavitt, A. B. Wolk, M. J. Van Stipdonk, S. J. Miller and M. A. Johnson, *Journal of the American Chemical Society*, 2011, **133**, 6440-6448.
28. M. J. Frisch, G. W. Trucks, H. B. Schlegel, G. E. Scuseria, M. A. Robb, J. R. Cheeseman, G. Scalmani, V. Barone, B. Mennucci, G. A. Petersson, H. Nakatsuji, M. Caricato, X. Li, H. P. Hratchian, A. F. Izmaylov, J. Bloino, G. Zheng, J. L. Sonnenberg, M. Hada, M. Ehara, K. Toyota, R. Fukuda, J. Hasegawa, M. Ishida, T. Nakajima, Y. Honda, O. Kitao, H. Nakai, T. Vreven, J. A. Montgomery, Jr., J. E. Peralta, F. Ogliaro, M. Bearpark, J. J. Heyd, E. Brothers, K. N. Kudin, V. N. Staroverov, R. Kobayashi, J. Normand, K. Raghavachari, A. Rendell, J. C. Burant, S. S. Iyengar, J. Tomasi, M. Cossi, N. Rega, N. J. Millam, M. Klene, J. E. Knox, J. B. Cross, V. Bakken, C. Adamo, J. Jaramillo, R. Gomperts, R. E. Stratmann, O. Yazyev, A. J. Austin, R. Cammi, C. Pomelli, J. W. Ochterski, R. L. Martin, K. Morokuma, V. G. Zakrzewski, G. A. Voth, P. Salvador, J. J. Dannenberg, S. Dapprich, A. D. Daniels, Ö. Farkas, J. B. Foresman, J. V. Ortiz, J. Cioslowski and D. J. Fox, *Journal*, 2009, **Revision D.01**.
29. S. Ataka, H. Takeuchi and M. Tasumi, *J. Mol. Struct.*, 1984, **113**, 147-160.
30. H. Bredohl and G. Herzberg, *Can. J. Phys.*, 1973, **51**, 867-887.
31. M. Z. Kamrath, R. A. Relph, T. L. Guasco, C. M. Leavitt and M. A. Johnson, *Int. J. Mass spectrom.*, 2011, **300**, 91-98.

32. A. V. Iogansen, *Spectrochim. Acta, Part A*, 1999, **55**, 1585-1612.
33. M. Rozenberg, A. Loewenschuss and Y. Marcus, *PCCP*, 2000, **2**, 2699-2702.
34. M. Rozenberg, G. Shoham, I. Reva and R. Fausto, *PCCP*, 2005, **7**, 2376-2383.
35. T. Shimanouchi, *Tables of Molecular Vibrational Frequencies Consolidated Volume I,* National Bureau of Standards, 1972.
36. E. Garand, M. Z. Kamrath, P. A. Jordan, A. B. Wolk, C. M. Leavitt, A. B. McCoy, S. J. Miller and M. A. Johnson, *Science*, 2012, **335**, 694-698.
37. A. B. Wolk, E. Garand, I. M. Jones, A. D. Hamilton and M. A. Johnson, *J. Phys. Chem. A*, 2013, **117**, 5962-5969.

4.2 Vibrational Spectroscopy of Isolated Copper(II) Complexes with Deprotonated Triglycine and Tetraglycine Peptides

Published in: *RSC Advances*, **5**, 1790-1795 (2015)

Abstract

The gas-phase vibrational predissociation spectra of deprotonated copper-triglycine ($[Cu+G_3-3H]^-$) and deprotonated copper-tetraglycine ($[Cu+G_4-4H]^{2-}$), a known water oxidation catalyst, are presented. Unambiguous determination of the coordination structure in these complexes is made by comparison of the experimental spectra with calculations. We found both complexes to have an approximately square planar geometry in which all the amide groups are deprotonated and coordinating to the Cu center. Our experimentally determined structure for $[Cu+G_3-3H]^-$, in which the terminal carboxylate and amine groups provide the additional coordination interaction, agrees with previous studies. However, the $[Cu+G_4-4H]^{2-}$ complex is found to have the carboxylate group coordinated to the Cu center rather than NH_2, as determined in previous solution-phase studies. Our results also highlight the sensitivity of the amidate C=O stretch frequencies to the charge and coordination environment in these complexes. The observed experimental frequencies alone are capable of providing qualitative information on the interactions present in these species.

4.2.1 Introduction

Copper is an earth-abundant and biorelevant transition metal with a ubiquitous presence in homogeneous and heterogeneous catalysis. Particularly, the ability of copper containing enzymes to reduce oxygen[1, 2] has led to recent discoveries of several nitrogen ligated copper catalysts that show promise for oxygen reduction and water oxidation.[3-6] One such catalyst, consisting of a Cu(II) center coordinated with a deprotonated tetraglycine molecule, has been found to have remarkable activity towards water oxidation.[6] This complex, noted for its proton transfer[7, 8] and oxidative properties[9], has been studied via X-ray crystallography[10], solution-phase electron paramagnetic resonance (EPR)[11] and solution-phase infrared (IR) spectroscopy[12]. However, in the condensed phase, spectral analysis and structural assignment is complicated by the simultaneous presence of several pH-dependent species as well as perturbations arising from interactions with counter-ions. On the other hand, gas phase vibrational spectroscopy is capable of isolating the species of interest to probe the structure and interactions in detail. Such studies have been carried out for a variety of amino acids,[13-15] peptides,[16-23] as well as metallated amino acids and peptides[24-27].

In this paper, we present the infrared vibrational predissociation[18, 28] study of isolated Cu(II) triglycine complex $[Cu+G_3-3H]^-$ and tetraglycine complex $[Cu+G_4-4H]^{2-}$. The species are isolated using electrospray ionization and cryogenically cooled prior to photo predissociation, yielding well-resolved vibrational spectra and allows for detailed comparison with density functional theory (DFT) calculations. Particular attentions are paid to the C=O and N-H stretch frequencies, which have been found to be highly indicative of molecular structures and intramolecular interactions in previous solution and gas phase investigations.[24, 29] Furthermore,

comparison of the amidate C=O stretch modes in $[Cu+G_3-3H]^-$ and $[Cu+G_4-4H]^{2-}$ showed notable sensitivity to the Cu bonding environment.

4.2.2 Experimental and Theoretical Details

The apparatus used in these experiments has been described in detail in chapter 2. For these experiments the reaction trap stage contained only a single hexapole ion guide. Additionally, the time-of-flight tube was a shorter, meter long, version. The ions studied here were generated via electrospray ionization (ESI) of a 1 mM $CuSO_4$ solution containing 1 mM triglycine (or tetraglycine) in a 65:35 acetonitrile:water mixture. The solution was adjusted to a pH of 9 with KOH, similar to previous work on these complexes.[11, 12, 30]

Electronic structure calculations were carried out using Gaussian 09.[31] Optimized geometries and harmonic frequencies of the gas phase species were calculated at the cam-B3LYP/6-311++G(d,p) level. The reported relative energies include zero-point corrections. The harmonic vibrational frequencies were scaled by a factor of 0.959 for the 1200-1800 cm^{-1} range, and 0.948 for the 2800-3600 cm^{-1} range. These scaling factors were obtained by comparing calculated values (cam-B3LYP/6-311++G(d,p)) of the N-H and C=O stretch frequencies of N-methyl acetamide with their experimental values.[32] It should be noted that calculations yielded very similar vibrational spectrum for the bare and tagged species, with the major difference being the additional presence of the weak D_2 stretch band. For simplicity, the calculated results of the bare complexes are used for the analysis of experimental spectra.

4.2.3 Results

The gas-phase vibrational predissociation spectrum of $[Cu+G_3-3H]^-$ in the 1200-1800 cm^{-1} and 2800-3600 cm^{-1} range is shown in Figure 1. The three strongest features appear in the

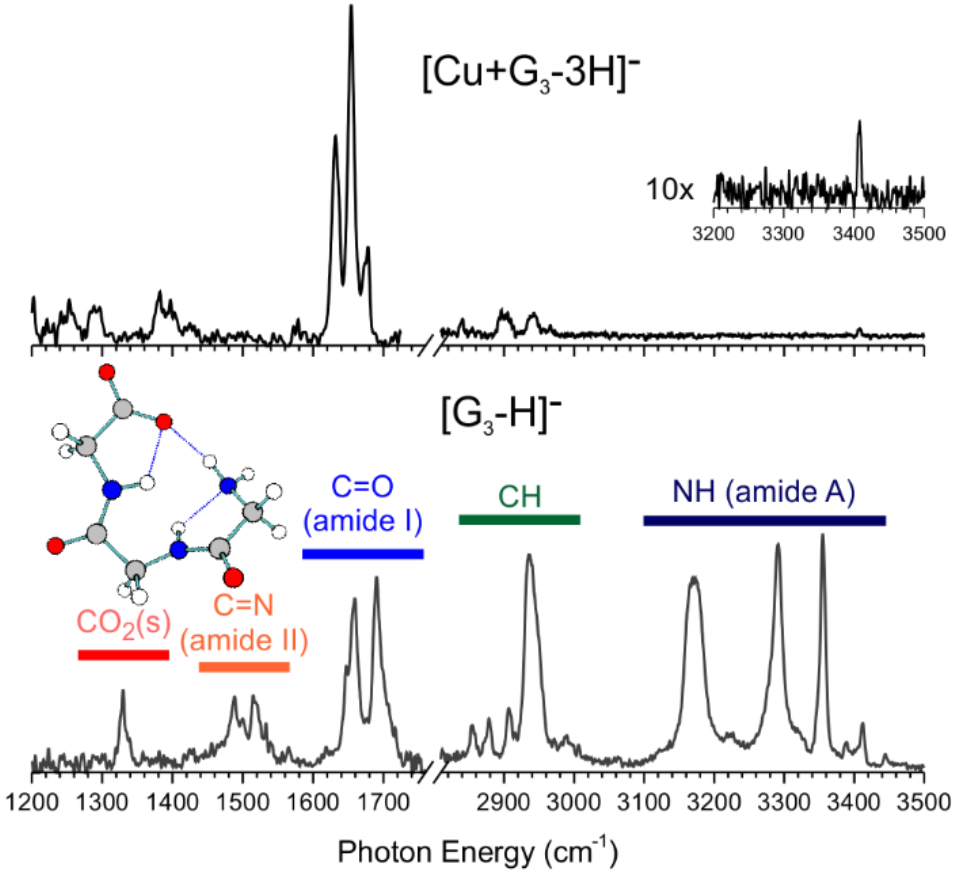

Figure 4.10- Experimental IR spectra of $[Cu+G_3-3H]^-$ (top) and $[G_3-H]^-$ (bottom). The spectrum of $[G_3-H]^-$ is analyzed in detail in section 4.1.

C=O stretch region at 1632 cm^{-1}, 1654 cm^{-1} and 1672 cm^{-1}. Four weak features are observed at lower frequencies, at 1252 cm^{-1}, 1293 cm^{-1}, 1380 cm^{-1} and 1393 cm^{-1}. All the features in the higher frequency region are very weak. Several peaks are observed in the 2800-3000 cm^{-1} region where the CH stretch modes and the D_2 stretch mode are expected to appear. The nominally forbidden D_2 stretch becomes weakly allowed when the centrosymmetry is broken by binding to the ion. A single weak peak is found at 3408 cm^{-1} in the N-H stretch region.

The vibrational spectrum of the $[Cu+G_3-3H]^-$ complex can be compared to the spectrum of the singly deprotonated triglycine species $[G_3-H]^-$, presented in the bottom panel of Figure 1. The spectrum analysis and structure of this species has been described in detail previously.[19] Briefly, it forms a cyclic structure in which the terminal carboxylate and NH_2 groups are linked by hydrogen bonding. Cursory inspection of the spectra in Figure 1 reveals several differences between the two species. First, the three intense peaks between 3100 cm^{-1} and 3400 cm^{-1} in the $[G_3-H]^-$ spectrum, assigned to the two hydrogen-bonded amide N-H and the hydrogen-bonded N-H in NH_2, are completely absent in $[Cu+G_3-3H]^-$. The experimental spectrum of $[Cu+G_3-3H]^-$ only displays a single weak peak in the free N-H region. In the lower frequency region, between 1450 cm^{-1} and 1550 cm^{-1}, the peaks assigned to the amide II modes in $[G_3-H]^-$ are also absent in $[Cu+G_3-3H]^-$. The amide II mode in peptides contains significant contributions from N-H bending motion.[29] The disappearance of the amide A and amide II features clearly indicate the deprotonation of both amides in the $[Cu+G_3-3H]^-$ complex. Another notable difference between the two species is the ~25 cm^{-1} redshift of the peaks in the C=O stretch region of $[Cu+G_3-3H]^-$ compared to $[G_3-H]^-$. This effect has been observed in previous studies of metallated peptides.[12, 33]

The gas-phase vibrational predissociation spectrum of $[Cu+G_4-4H]^{2-}$, in the 1200-1800 cm^{-1} and 2800-3600 cm^{-1} range, is shown in Figure 2. It is qualitatively similar to the spectrum of the $[Cu+G_3-3H]^-$ complex. The predominant feature is a set of four intense peaks at 1566 cm^{-1}, 1601 cm^{-1}, 1609 cm^{-1} and 1632 cm^{-1}. Two additional weaker features are observed at 1326 cm^{-1} and 1407 cm^{-1}. Again, only weak features are found in the higher frequency region. A group of peaks is observed between 2800 cm^{-1} and 3100 cm^{-1} where the CH stretch and nominally forbidden D_2 stretch vibrations are expected. Very little activity is found in the N-H region, with only two very weak peaks at 3271 cm^{-1} and 3351 cm^{-1}.

The vibrational spectrum of the $[Cu+G_4-4H]^{2-}$ complex can be compared with the spectrum of the singly deprotonated tetraglycine species $[G_4-H]^-$, presented in the bottom panel of Figure 2. The structure of this species, which has been described in detail previously,[19] is also cyclic in which the terminal carboxylate and NH_2 groups are linked by hydrogen bonding. Comparison of the $[Cu+G_4-4H]^{2-}$ and $[G_4-H]^-$ spectra shows the same trends observed for the triglycine species. The most apparent difference is the disappearance of the intense hydrogen-bonded N-H stretch peaks in the 3100-3400 cm^{-1} range which again suggest that all three amide groups of the tetraglycine ligand are deprotonated in $[Cu+G_4-4H]^{2-}$. Lastly, the redshift of the C=O stretch peaks in $[Cu+G_4-4H]^{2-}$ compared to $[G_4-H]^-$ is ~90 cm^{-1}, significantly more than that of the triglycine species.

4.2.4 Analysis

From the experimental spectra presented in the previous section, it appears that all the amide groups are deprotonated in $[Cu+G_3-3H]^-$ and $[Cu+G_4-4H]^{2-}$. Therefore, only starting geometries in which the amide and carboxylic acid groups are deprotonated were considered in the

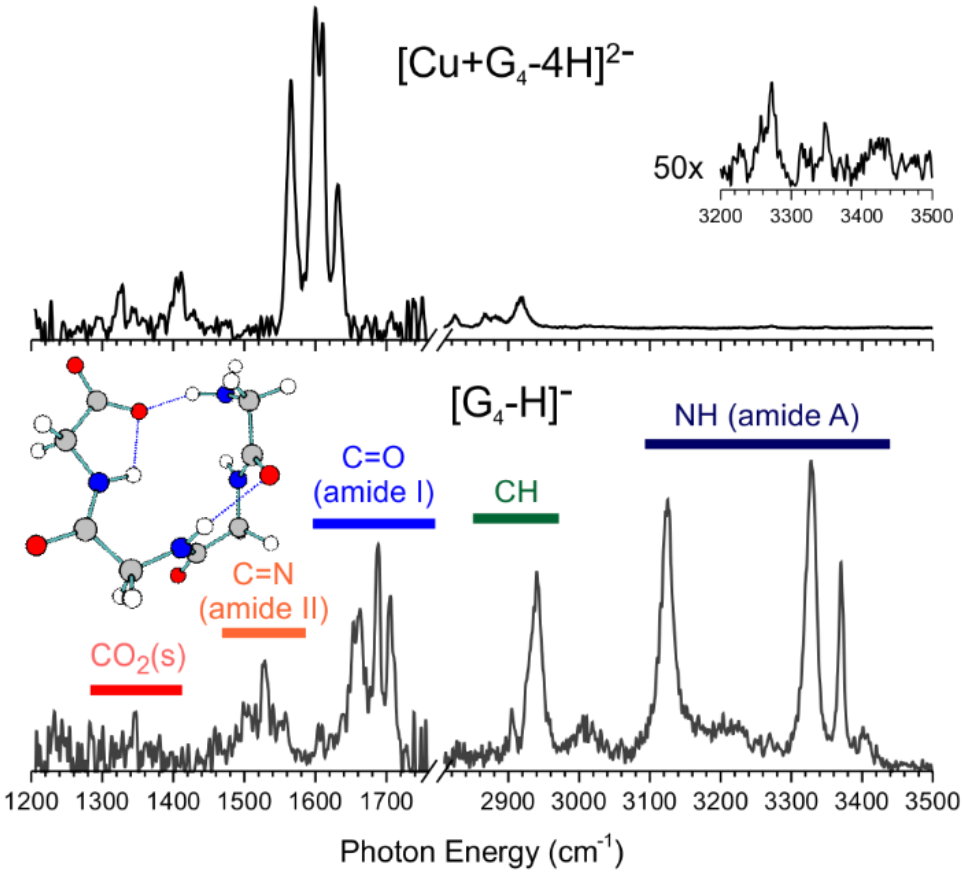

Figure 4.11- Experimental IR spectra of $[Cu+G_4-4H]^-$ (top) and $[G_4-H]^-$ (bottom). The spectrum of $[G_4-H]^-$ is analyzed in detail in section 4.1.

electronic structure calculations. For the $[Cu+G_3-3H]^-$ complex, all the starting geometries converged to the same structure, shown in Figure 3, in which the triply deprotonated triglycine ligand wraps around Cu(II) metal center in an approximately square planar geometry. The peptide is bound to the Cu via one of the carboxylate oxygens, the two nitrogens of the amidate groups and the nitrogen of the terminal NH_2 group. This geometry agrees well with the structure obtained from solution phase measurements.[11, 12] To facilitate the discussion, we label the two amidate groups α and β, starting from the terminal carboxylate.

The calculated vibrational spectrum (Figure 3 bottom panel) has an excellent agreement with the experimental spectrum, allowing for unambiguous assignment of the observed features. In the C=O stretch region, the peaks at 1675 and 1654 cm^{-1} are assigned to a mixture of the CO_2 antisymmetric stretch and the β-C=O stretch. The feature at 1632 cm^{-1} is assigned to the α-C=O stretch. The two peaks at 1380 cm^{-1} and 1393 cm^{-1} are assigned to CH_2 bending motions. The lower frequency peak at 1293 cm^{-1} is assigned to a mixture of the CO_2 symmetric stretch and CH_2 wag modes. The features in the region of 2800-3100 cm^{-1} can be assigned to various CH_2 stretching modes. The peak at 2942 cm^{-1}, which is absent in the calculation, is assigned to the D_2 stretch of the tags. This frequency is close to the free D_2 stretch at 2994 cm^{-1}, indicating very weakly interacting tags. Finally, the weak feature at 3408 cm^{-1} can be assigned to the antisymmetric stretch of the NH_2 group. The corresponding symmetric NH_2 stretch, calculated to appear at 3353 cm^{-1}, is significantly weaker than the antisymmetric stretch and is not observed in the experimental spectrum.

Calculations revealed four low-lying structures for the $[Cu+G_4-4H]^{2-}$ complex. The structures are shown in Figure 4 (I-IV), along with their respective calculated spectra. Once again, we label the three amidate groups α, β and γ, starting from the terminal carboxylate.

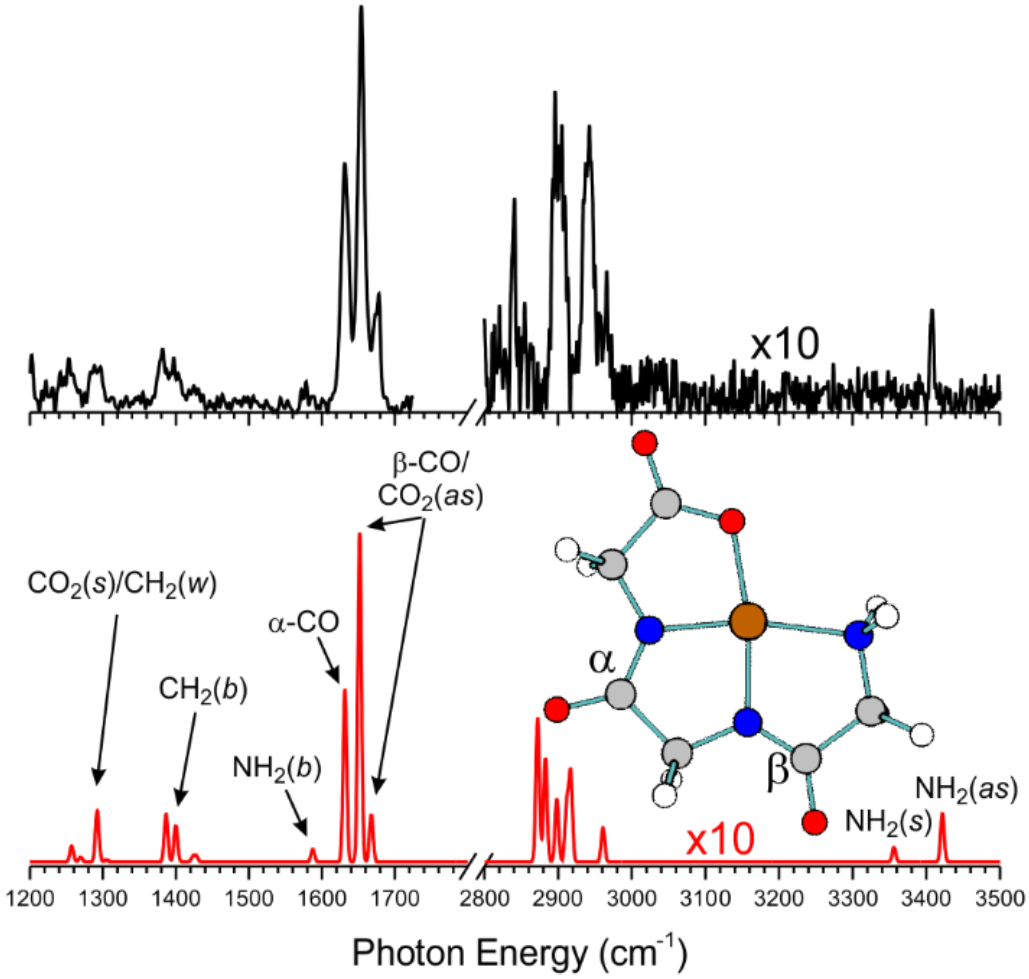

Figure 4.12- Experimental (top) and calculated (bottom) spectra of the $[Cu+G_3-3H]^-$ complex. For both spectra, the intensity in the 2800-3500 cm^{-1} region is multiplied by 10 to clearly show the weak features. For the labels: *as*=antisymmetric stretch, *s*=symmetric stretch, *b*=bend, *w*=wag. The position of the α and β amide group is indicated on the structure.

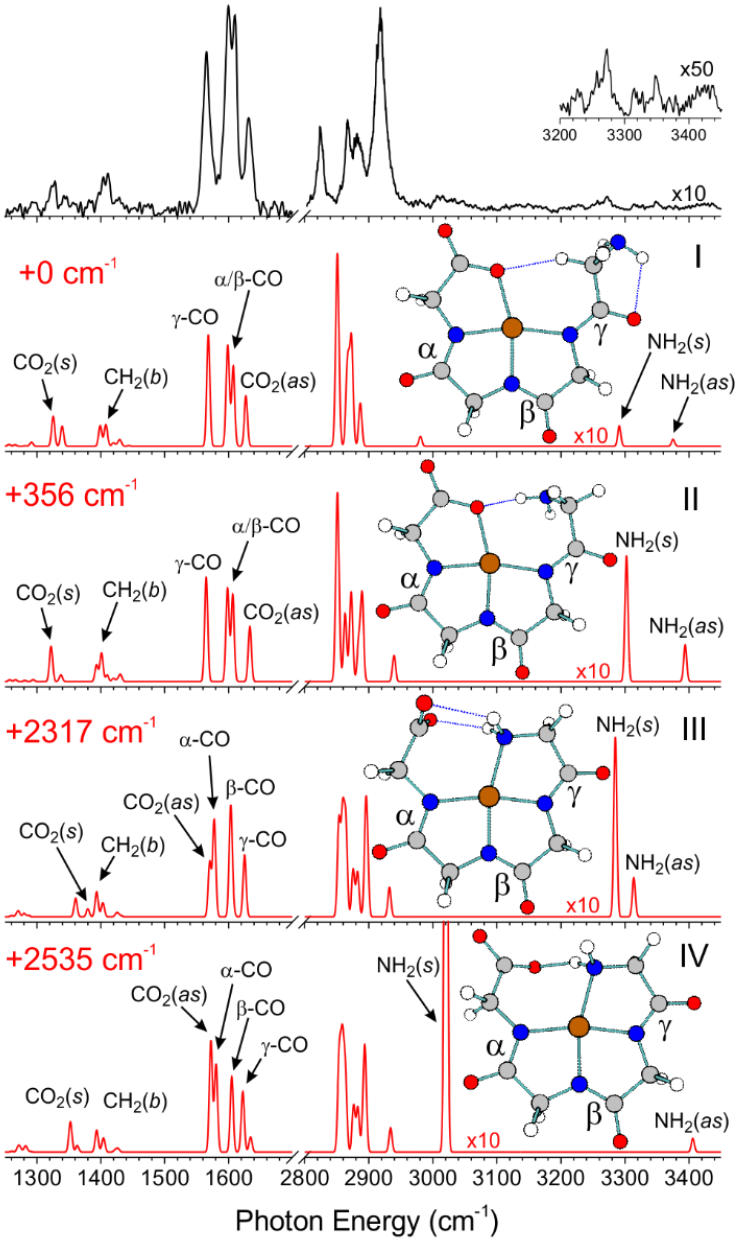

Figure 4.13- Experimental (top) and calculated (I-IV) spectra of the $[Cu+G_4-4H]^-$ complex. For all spectra, the intensity in the 2800-3500 cm^{-1} region is multiplied by 10 to clearly show the weak features. For the labels: *as*=antisymmetric stretch, *s*=symmetric stretch, *b*=bend, *w*=wag. The position of the α, β, and γ amide group is indicated on the structures.

All four conformers have an approximately square planar geometry with the three nitrogen on the amidate groups bound to the Cu center. In the two lowest energy structures (I and II), the fourth coordination comes from the carboxylate oxygen. In conformer I, the NH_2 is weakly interacting with the neighboring γ-C=O. In conformer II, calculated to be 356 cm^{-1} higher in energy, the NH_2 is hydrogen bonded to the carboxylate group. In conformers III and IV, calculated to be 2319 cm^{-1} and 2535 cm^{-1} higher in energy, respectively, the fourth coordination is with the NH_2 group. For both structures, the carboxylate is hydrogen bonded to the NH_2 group. This coordination motif is similar to those assigned in previous work on $[Cu+G_4-4H]^{2-}$.[11, 12]

In the C=O stretch region, 1550-1650 cm^{-1}, the calculated spectra for conformers I and II are very similar, and both show excellent agreement with the experimental spectrum. On the other hand, the peak pattern in the C=O region of conformers III and IV do not agree as well with the experiment. There are further differences between the calculated spectra in the 3000-3500 cm^{-1} N-H stretch region. For conformers II-IV, N-H stretch features with intensities comparable to or greater than the C-H stretch modes (2800-2900 cm^{-1}) are present at various frequencies. This is clearly not observed in the experimental spectrum. Only conformer I is calculated to have the correct relative intensities for the symmetric and antisymmetric NH_2 stretch modes. The calculated frequencies are also in good agreement with the two observed very weak features at 3271 cm^{-1} and 3351 cm^{-1}. These clear differences allow us to rule out the presence of conformers II-IV and assign all observed features to conformer I.

In the C=O stretch region, the feature at 1632 cm^{-1} is assigned to the CO_2 antisymmetric stretch. The doublet at 1609 and 1601 cm^{-1} correspond to a mixture of the α and β C=O stretch and the peak at 1566 cm^{-1} is assigned to the γ-C=O stretch. The peak at 1407 cm^{-1} corresponds to

the CH_2 bending vibrations whereas the feature at 1325 cm^{-1} corresponds to the CO_2 symmetric stretch. The features between 2800 and 2900 cm^{-1} are assigned to various CH_2 symmetric and antisymmetric stretch modes. The large feature at 2917 cm^{-1}, which is absent in the calculated spectrum, is assigned to the D_2 stretch mode of the tags. This frequency is again close to the free D_2 stretch, but slightly redshifted compared to those in $[Cu+G_3-3H]^-$. The D_2 tag frequency difference indicate a stronger binding energy to the doubly charged $[Cu+G_4-4H]^{2-}$ than the singly charged $[Cu+G_3-3H]^-$. This is confirmed by calculations which show that the D_2 tags have a binding energy of about 100 cm^{-1} (1.2 kJ/mol) in $[Cu+G_3-3H]^-\cdot D_2$ compared to 300 cm^{-1} (3.6 kJ/mol) in $[Cu+G_4-4H]^{2-}\cdot D_2$.

4.2.5. Discussion

The four-fold coordination present in the $[Cu+G_3-3H]^-$ and $[Cu+G_4-4H]^{2-}$ complexes is similar to other Cu(II) complexes.[34, 35] It also agrees with previous studies of these species in the solution phase.[11, 12] However, for $[Cu+G_4-4H]^{2-}$, the solution phase studies concluded that the four equatorial coordination groups are the three amidates and the NH_2 group, with structures similar to conformer III and IV. Specifically, in the EPR experiments performed by Nagy et al.,[11] the carboxylate group is determined to not directly interact with the copper center. This geometry was based on various ESR parameters extracted from spectral deconvolution. In the solution-phase IR spectroscopy work of Kim and Martell,[12] it was determined that the carboxylate group resided on the axial position. This was based on the observation of two amide I bands at 1610 cm^{-1} and 1570 cm^{-1}, which were assigned to the amidate C=O and a weakly coordinated carboxylate group, respectively. However, no such stable geometry could be found in our calculation search. In order for the carboxylate to reach the axial coordination position, the α-amidate group has to be rotated out the equatorial plane, severely straining its

bond with the copper. In addition, the calculated spectra in Figure 4 show that geometries involving either NH_2 or CO_2 coordination at the fourth equatorial site would produce IR spectra with very similar appearance in the C=O region, especially at low resolution. The non-coordinating CO_2 in conformers III and IV does indeed appear at ~1570 cm^{-1}, but at the same time, all the conformers are predicted to have an amidate C=O band at about the same frequency.

This different coordination motif observed in our experiments can be explained by several experimental parameters. For instance, we use an acetonitrile/water mixture rather than a pure aqueous solution. However, the most obvious reason is that our measurements were carried out in the gas phase where all the solvents are removed. In order to investigate the effect of solvation on the geometry, we have performed additional calculations on the $[Cu+G_4-4H]^{2-}$ complex to include implicit water and acetonitrile solvent interactions through the PCM model[36]. We found the same four low energy structures as shown in Figure 4, and interestingly, the PCM results indicate that conformers I and IV are the two lowest energy conformers in solution and they are nearly isoenergetic. Conformer I is still the lowest energy conformer by 45 cm^{-1} (0.49 kJ/mol) in acetonitrile, but we found conformer IV to be the ground state by 21 cm^{-1} (0.25 kJ/mol) in water. Such large relative solvent stabilization of conformer IV, in which the NH_2 group is coordinated to the metal, thus provide the likely cause of the different structure found here. The large solvation energy of the charged carboxylate compared to the neutral NH_2 makes it less favorable to be coordinated in solution. However in the absence of any solvent, the carboxylate coordinated conformer I becomes more energetically favorable. The small calculated energy differences between conformer I and IV would suggest that both species might be present in solution. More accurate determination of the relative energy of these conformers would require the inclusion of explicit solvent molecules which is beyond the scope of the

present work. However, we note that the fact that we only observe conformer I in our experimental spectrum suggest that the barriers between these structures is relatively small and easily overcome during the electrospray ionization or collisional cooling process in the ion trap.

Also of interest is the sensitivity of the C=O stretch bands to the coordination environment of the Cu(II) complex. This is illustrated in Figure 5, which focuses on the 1300-1800 cm^{-1} region of both $[Cu+G_3-3H]^-$ and $[Cu+G_4-4H]^{2-}$ species. For comparison, Figure 5 also includes the calculated C=O stretch frequencies of a free amide and a free amidate anion using N-methyl acetamide as a model. The free amidate C=O stretch has a calculated frequency of 1569 cm^{-1}, 138 cm^{-1} lower than the free amide C=O stretch (1707 cm^{-1}). The origin of this shift can be understood by examining the differences in bond lengths between the amide and amidate species. Upon deprotonation, the C=O bond length is increased from 1.217 Å to 1.264 Å, while the C-N bond is shortened from 1.358 Å to 1.313Å. This shows that the negative charge is delocalized through a $[^-O\text{-}C{=}N] \leftrightarrow [O{=}C\text{-}N^-]$ resonance structure. The C=O frequencies can therefore be used as a probe of the charge transfer upon coordination to the Cu center.

The observed C=O stretch modes in $[Cu+G_4-4H]^{2-}$ are at lower frequencies than their corresponding modes in $[Cu+G_3-3H]^-$. This implies that each amidate group in $[Cu+G_4-4H]^{2-}$ has less charge transfer to the Cu center and a structure that is closer to the free amidate anion. The calculated geometries, shown in Figure 5, agree with that assessment. Notably, the Cu-N bond lengths in $[Cu+G_4-4H]^{2-}$ are all longer than those in $[Cu+G_3-3H]^-$. Upon closer inspection, we can see that the γ-amidate in $[Cu+G_4-4H]^{2-}$ has the longest Cu-N bond length of 1.988 Å, and its C=O stretch is the lowest frequency at 1566 cm^{-1}. This C=O stretch is not significantly perturbed by its weak interaction with the NH_2 group, as shown by conformer II in Figure 4 which has a similar frequency for its free γ-C=O stretch. The two other amidate groups in

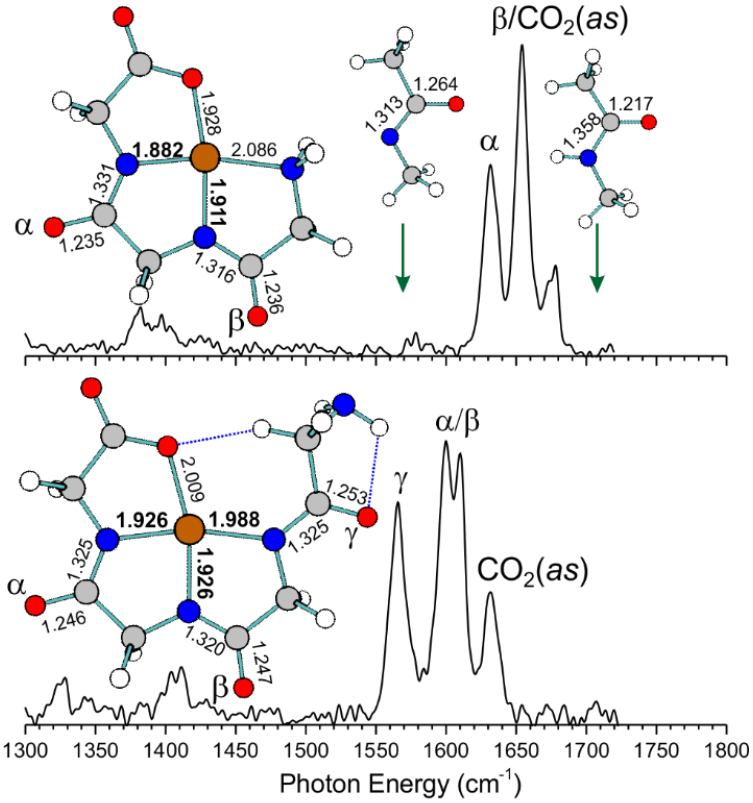

Figure 4.14- Experimental IR specta of $[Cu+G_3-3H]^-$ (top) and $[Cu+G_4-4H]^{2-}$ (bottom) in the amide I region. In each panel are the corresponding calculated (cam-B3LYP/6-311++G(d,p)) structure and bond lengths. Also shown are the free amide and amidate frequencies (green arrows) with calculated structures.

$[Cu+G_4-4H]^{2-}$ have a Cu-N bond length of 1.926 Å, giving rise to similar C=O and C-N bond lengths and C=O stretches at similar frequencies around 1600 cm^{-1}. The shorter Cu-N bond lengths in $[Cu+G_3-3H]^-$, 1.882 Å and 1.911 Å, correspond to higher frequency C=O stretches at 1632 cm^{-1} and 1654 cm^{-1}. The stronger Cu-N interactions in $[Cu+G_3-3H]^-$ is likely due to the fact that there are only two amidate groups interacting with Cu. The total charge transfer to the copper center is spread over a smaller number of amidate groups, leading to a larger charge transfer per Cu-N bond. The amide I region is often considered to be diagnostic of the peptide structure.[29, 37] Here, we have shown the ability of well-resolved IR spectroscopy to yield information on the charge and coordination of metal-center complexes. This capability will be useful in future studies of related complexes involved in the water oxidation, as well as larger structures where detailed calculations are less feasible.

4.1.6 Conclusions

The vibrational predissociation spectra of two isolated Cu(II) oligoglycine complexes, $[Cu+G_3-3H]^-$ and $[Cu+G_4-4H]^{2-}$, are presented. Analysis of the experimental spectra is aided by DFT calculations. For each species, a single structural conformer is responsible for all the observed features, all of which can be readily assigned. For $[Cu+G_3-3H]^-$, the two amidate, NH_2 and carboxylate groups are coordinated with the Cu center, in agreement with previous studies. On the other hand, the $[Cu+G_4-4H]^{2-}$ complex is found to have the carboxylate group as the fourth coordination in contrast to previous solution-phase assignments in which the NH_2 is involved in the coordination. However, electronic structure calculations with implicit solvent suggest that both species may be present in solution. Furthermore, we find the frequencies of the amidate C=O modes to be very sensitive to the charge and coordination environment of the metal

complexes. The observed experimental frequencies alone are capable of providing qualitative information on the interactions present in these complex species.

References:

1. E. A. Lewis and W. B. Tolman, *Chem. Rev.*, 2004, **104**, 1047-1076.
2. L. M. Mirica, X. Ottenwaelder and T. D. P. Stack, *Chem. Rev.*, 2004, **104**, 1013-1045.
3. S. M. Barnett, K. I. Goldberg and J. M. Mayer, *Nat Chem*, 2012, **4**, 498-502.
4. T. Zhang, C. Wang, S. Liu, J.-L. Wang and W. Lin, *J. Am. Chem. Soc.*, 2013, **136**, 273-281.
5. M. Zhao, H.-B. Wang, L.-N. Ji and Z.-W. Mao, *Chem. Soc. Rev.*, 2013, **42**, 8360-8375.
6. M. T. Zhang, Z. F. Chen, P. Kang and T. J. Meyer, *Journal of the American Chemical Society*, 2013, **135**, 2048-2051.
7. M. P. Youngblood, K. L. Chellappa, C. E. Bannister and D. W. Margerum, *Inorg. Chem.*, 1981, **20**, 1742-1747.
8. M. P. Youngblood and D. W. Margerum, *Inorg. Chem.*, 1980, **19**, 3072-3077.
9. J. L. Kurtz, G. L. Burce and D. W. Margerum, *Inorg. Chem.*, 1978, **17**, 2454-2460.
10. H. C. Freeman and M. R. Taylor, *Acta Crystallographica*, 1965, **18**, 939-952.
11. N. V. Nagy, T. Szabo-Planka, A. Rockenbauer, G. Peintler, I. Nagypal and L. Korecz, *J. Am. Chem. Soc.*, 2003, **125**, 5227-5235.
12. M. K. Kim and A. E. Martell, *J. Am. Chem. Soc.*, 1966, **88**, 914-918.
13. D. Scuderi, C. F. Correia, O. P. Balaj, G. Ohanessian, J. Lemaire and P. Maitre, *ChemPhysChem*, 2009, **10**, 1630-1641.
14. B. C. Dian, J. R. Clarkson and T. S. Zwier, *Science*, 2004, **303**, 1169-1173.
15. J. A. Stearns, S. Mercier, C. Seaiby, M. Guidi, O. V. Boyarkin and T. R. Rizzo, *J. Am. Chem. Soc.*, 2007, **129**, 11814-11820.

16. E. G. Buchanan, W. H. James, S. H. Choi, L. Guo, S. H. Gellman, C. W. Muller and T. S. Zwier, *J. Chem. Phys.*, 2012, **137**, 094301.

17. J. C. Dean, E. G. Buchanan and T. S. Zwier, *Journal of the American Chemical Society*, 2012, **134**, 17186-17201.

18. M. Z. Kamrath, E. Garand, P. A. Jordan, C. M. Leavitt, A. B. Wolk, M. J. Van Stipdonk, S. J. Miller and M. A. Johnson, *Journal of the American Chemical Society*, 2011, **133**, 6440-6448.

19. B. M. Marsh, E. M. Duffy, M. T. Soukup, J. Zhou and E. Garand, *J. Phys. Chem. A*, 2014, **118**, 3906-3912.

20. N. S. Nagornova, T. R. Rizzo and O. V. Boyarkin, *Angew. Chem.*, 2013, **52**, 6002-6005.

21. J. Oomens and J. D. Steill, *J. Am. Soc. Mass. Spectrom.*, 2010, **21**, 698-706.

22. W. Ronghu and T. B. McMahon, *J. Phys. Chem. B*, 2009, **113**, 8767-8775.

23. J. A. Stearns, C. Seaiby, O. V. Boyarkin and T. R. Rizzo, *PCCP*, 2009, **11**, 125-132.

24. R. C. Dunbar, N. C. Polfer, G. Berden and J. Oomens, *International Journal of Mass Spectrometry*, 2012, **330**, 71-77.

25. T. E. Hofstetter, C. Howder, G. Berden, J. Oomens and P. B. Armentrout, *J. Phys. Chem. B*, 2011, **115**, 12648-12661.

26. J. T. O'Brien, J. S. Prell, J. D. Steill, J. Oomens and E. R. Williams, *Journal of Physical Chemistry A*, 2008, **112**, 10823-10830.

27. J. S. Prell, T. G. Flick, J. Oomens, G. Berden and E. R. Williams, *Journal of Physical Chemistry A*, 2010, **114**, 854-860.

28. A. B. Wolk, C. M. Leavitt, E. Garand and M. A. Johnson, *Acc. Chem. Res.*, 2014, **47**, 202-210.

29. A. Barth and C. Zscherp, *Q. Rev. Biophys.*, 2002, **35**, 369-430.

30. E. Garribba and G. Micera, *J. Chem. Educ.*, 2007, **84**, 832-835.

31. M. J. Frisch, G. W. Trucks, H. B. Schlegel, G. E. Scuseria, M. A. Robb, J. R. Cheeseman, G. Scalmani, V. Barone, B. Mennucci, G. A. Petersson, H. Nakatsuji, M. Caricato, X. Li, H. P. Hratchian, A. F. Izmaylov, J. Bloino, G. Zheng, J. L. Sonnenberg, M. Hada, M. Ehara, K. Toyota, R. Fukuda, J. Hasegawa, M. Ishida, T. Nakajima, Y. Honda, O. Kitao, H. Nakai, T. Vreven, J. A. Montgomery, J. E. Peralta, F. Ogliaro, M. Bearpark, J. J. Heyd, E. Brothers, K. N. Kudin, V. N. Staroverov, R. Kobayashi, J. Normand, K. Raghavachari, A. Rendell, J. C. Burant, S. S. Iyengar, J. Tomasi, M. Cossi, N. Rega, J. M. Millam, M. Klene, J. E. Knox, J. B. Cross, V. Bakken, C. Adamo, J. Jaramillo, R. Gomperts, R. E. Stratmann, O. Yazyev, A. J. Austin, R. Cammi, C. Pomelli, J. W. Ochterski, R. L. Martin, K. Morokuma, V. G. Zakrzewski, G. A. Voth, P. Salvador, J. J. Dannenberg, S. Dapprich, A. D. Daniels, Farkas, J. B. Foresman, J. V. Ortiz, J. Cioslowski and D. J. Fox, *Journal*, 2009.

32. S. Ataka, H. Takeuchi and M. Tasumi, *J. Mol. Struct.*, 1984, **113**, 147-160.

33. M. K. Kim and A. E. Martell, *Biochemistry*, 1964, **3**, 1169-1174.

34. B. M. Marsh, J. Zhou and E. Garand, *Journal of Physical Chemistry A*, 2014, **118**, 2063-2071.

35. J. T. O'Brien and E. R. Williams, *J. Phys. Chem. A*, 2008, **112**, 5893-5901.

36. J. Tomasi, B. Mennucci and R. Cammi, *Chem. Rev.*, 2005, **105**, 2999-3093.

37. Z. Ganim, H. S. Chung, A. W. Smith, L. P. Deflores, K. C. Jones and A. Tokmakoff, *Acc. Chem. Res.*, 2008, **41**, 432-441.

5.1 The Reaction of Methane with a Platinum Coordination Complex

Abstract

The conversion of relatively inert alkane species to useful chemical building blocks by Pt(II) catalysts is a well-studied catalytic reaction. While the mechanism of the reaction has been inferred from various studies, the key intermediate species have yet to be observed. Analogs of one such species, known as the σ-CH complex, have been synthesized but have not shown catalytic activity. In this work we isolate the product of a reaction between the ionic Pt complex $[Pt(en)Cl]^+$ and methane using a dual cryogenic ion trap mass spectrometer. The product species is characterized using infrared photodissociation (IRPD) spectroscopy and analyzed using density functional theory (DFT) calculations. Comparison of the experimental spectrum to theory indicates that we have obtained solely the σ-CH complex. Calculations of reaction potential energy surface indicate that the barriers to interconversion along the surface are ~6500 cm^{-1}-7500 cm^{-1}. These energies preclude the interconversion between species at the temperature of our experiment (~80 K).

5.1.1 Introduction

The conversion of relatively inert alkane species, such as methane, to more synthetically useful species has long been a goal of chemists.[1-4] The strength of C-H bonds in most alkanes, as well as the lack of selectivity in most oxidation reactions, has rendered this problem one of the most difficult in chemistry. One of the earliest successes in this field is known as the "Shilov System".[5, 6] This reaction, which uses a Pt(II) salt as a catalyst, has been extensively studied in an attempt to understand the mechanism involved.[7-11] The postulated mechanism consists of docking an alkane molecule on the Pt(II) complex to form the so called σ-CH complex. This σ-CH complex can undergo oxidative addition of the alkane followed by reductive elimination to remove the activated hydrogen from the complex.[8] Alternatively, the σ-CH complex can undergo a metathesis reaction to remove the activated hydrogen from the complex without undergoing oxidative addition.[12]

Despite the intensive study of this system, the σ-CH complex, which has been theorized to control the selectivity of the reaction,[13] has not been directly observed. Many model chemistries have been employed to isolate this complex with some success.[14-16] However, these species are not active towards C-H activation. The difficulty in characterizing this intermediate arises from the endothermic nature of the ligand exchange needed to go from the Pt-solvent to the Pt-alkane complexes.

This limitation can be overcome by studying the reaction in the gas phase. In particular studies by Chen and Schwarz have utilized mass spectrometry coupled with collision induced dissociation to produce products from reactions of Pt and hydrocarbon molecules.[9, 17, 18] Mass spectrometry and gas phase spectroscopy have also been used to characterize the reactions of

alkanes with a number of other metal ions.[18-22] However, these studies have also failed to isolate the rate-determining σ-CH complex.

In this work we have isolated an intact Pt(II)-Methane complex for the first time using a recently developed dual cryogenic ion trap mass spectrometer.[23] The resulting complex has been characterized structurally using infrared spectroscopy. Comparisons with density functional theory (DFT) calculations indicate that the species observed is the heretofore elusive σ-CH complex. There is no evidence of the oxidative addition or metathesis products observed in the collected spectrum.

5.1.2 Experimental

The experimental setup has been described in detail in Chapter 2. In these experiments the $[Pt(en)Cl(OH_2)]^+$ (en=ethylenediamine) ions were generated by electrospray ionization of an aqueous 1 mM solution of $Pt(en)Cl_2$ salt. The solutions were allowed to sit for 24 hours to ensure complete dissolution of the complex. The $[Pt(en)Cl(CH_4)]^+$ complex was generated by fragmentation of the $[Pt(en)Cl(OH_2)]^+$ complex in the ~100 mTorr region of the machine followed by exposure to methane gas in the temperature controlled reaction trap stage of our instrument. The maximum ion signal was observed when the trap was held at 77 K and a 10% CH_4/He buffer gas mix was used as the trapping gas. The resulting mass spectra are shown in Figure 5.1. The IRPD spectra that were collected were corrected for power and combined to create the composite spectra shown.

Analysis of the data was performed using the Gaussian 09 software package. Geometry optimizations and harmonic frequency calculations were performed using the cam-B3LYP functional and 6-311+g(d,p) basis set for all atoms except Pt, which was calculated using the

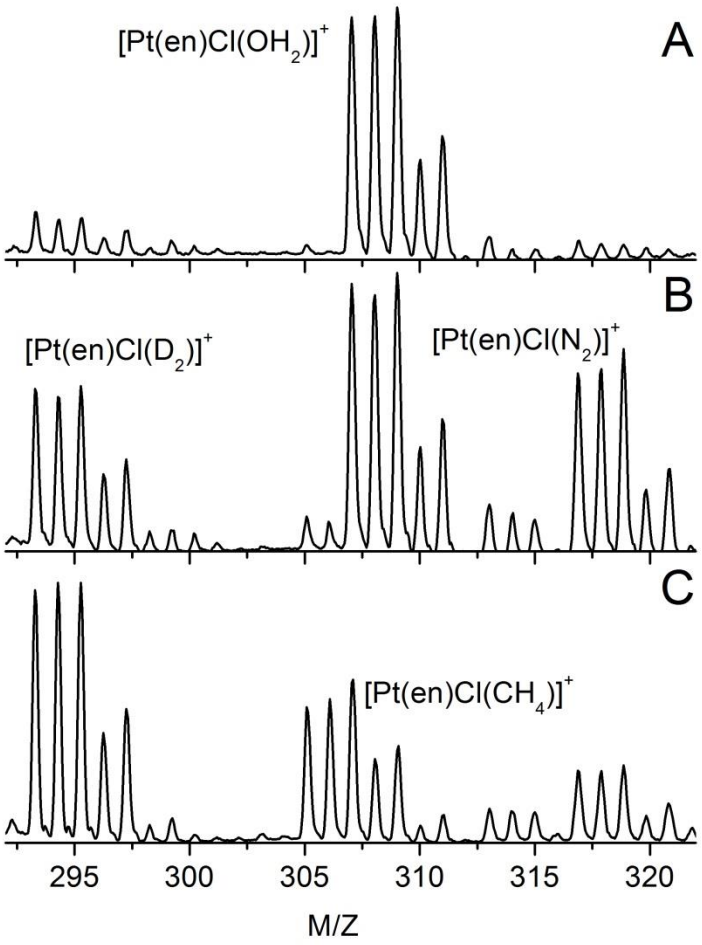

Figure 5.1- Mass spectra of $[Pt(en)Cl(X)]^+$ species under different conditions with a reaction trap temperature of 77 K and a tagging trap temperature of 35 K. In panel A the settings are such that minimal fragmentation is observed. In B the ions are significantly fragmented and in panel C the fragmented ions are exposed to a CH_4/He buffer gas, producing the desired $[Pt(en)Cl(CH_4)]^+$ product. Due to the presence of D_2 in the tagging trap gas mix the $[Pt(en)Cl(D_2)]^+$ complex is formed under fragmentation conditions.

SDD pseudopotential. Frequencies from 2000 cm^{-1} to 3800 cm^{-1} were scaled by a factor of 0.943 while frequencies from 1000 cm^{-1} to 2000 cm^{-1} were scaled by a factor of 0.963.

5.1.3 Results

IR spectra of $[Pt(en)Cl(OH_2)]^+ \cdot (D_2)_2$ and $[Pt(en)Cl(CH_4)]^+ \cdot (D_2)_2$ are shown in Figure 5.2. The $[Pt(en)Cl(OH_2)]^+ \cdot (D_2)_2$ spectrum is included for comparison with the $[Pt(en)Cl(CH_4)]^+ \cdot (D_2)_2$ spectrum to ascertain which modes are associated with the ethylenediamine backbone. The spectrum of $[Pt(en)Cl(OH_2)]^+ \cdot (D_2)_2$ shows strong activity in the 1000 -1700 cm^{-1} region. The brightest features are found in the NH_2 and OH_2 bending region between 1550 cm^{-1} and 1650 cm^{-1}. In the 3200 - 3800 cm^{-1} N-H/O-H stretching region, six particularly bright features are observed. Two smaller features are observed in the C-H stretching region from 2800 cm^{-1} to 3200 cm^{-1}.

The spectrum of $[Pt(en)Cl(CH_4)]^+ \cdot (D_2)_2$ is shown in the bottom panel of Figure 5.2. This spectrum is noticeably similar to that of $[Pt(en)Cl(OH_2)]^+ \cdot (D_2)_2$ in the 3200 - 3500 cm^{-1} N-H stretching region. In the higher frequency O-H stretching region the two intense features at 3493 cm^{-1} and 3553 cm^{-1} have diminished in intensity. The presence of these features is attributed to residual signal from the $[Pt(en)Cl(OH_2)]^+ \cdot (D_2)_2$ complex.

In the region from 1000 cm^{-1} to 1650 cm^{-1} the $[Pt(en)Cl(CH_4)]^+ \cdot (D_2)_2$ spectrum is largely similar to the spectrum of $[Pt(en)Cl(OH_2)]^+ \cdot (D_2)_2$ save for a new feature which appears at 1389 cm^{-1} and a change in the intensity of the feature at 1290 cm^{-1}. The feature at 1642 cm^{-1} in the water complex also shows a noticeable drop in intensity in the methane complex spectrum. In the region from 1800 cm^{-1} to 2800 cm^{-1} a single weak feature is observed at 2278 cm^{-1}.

5.1.4 Analysis

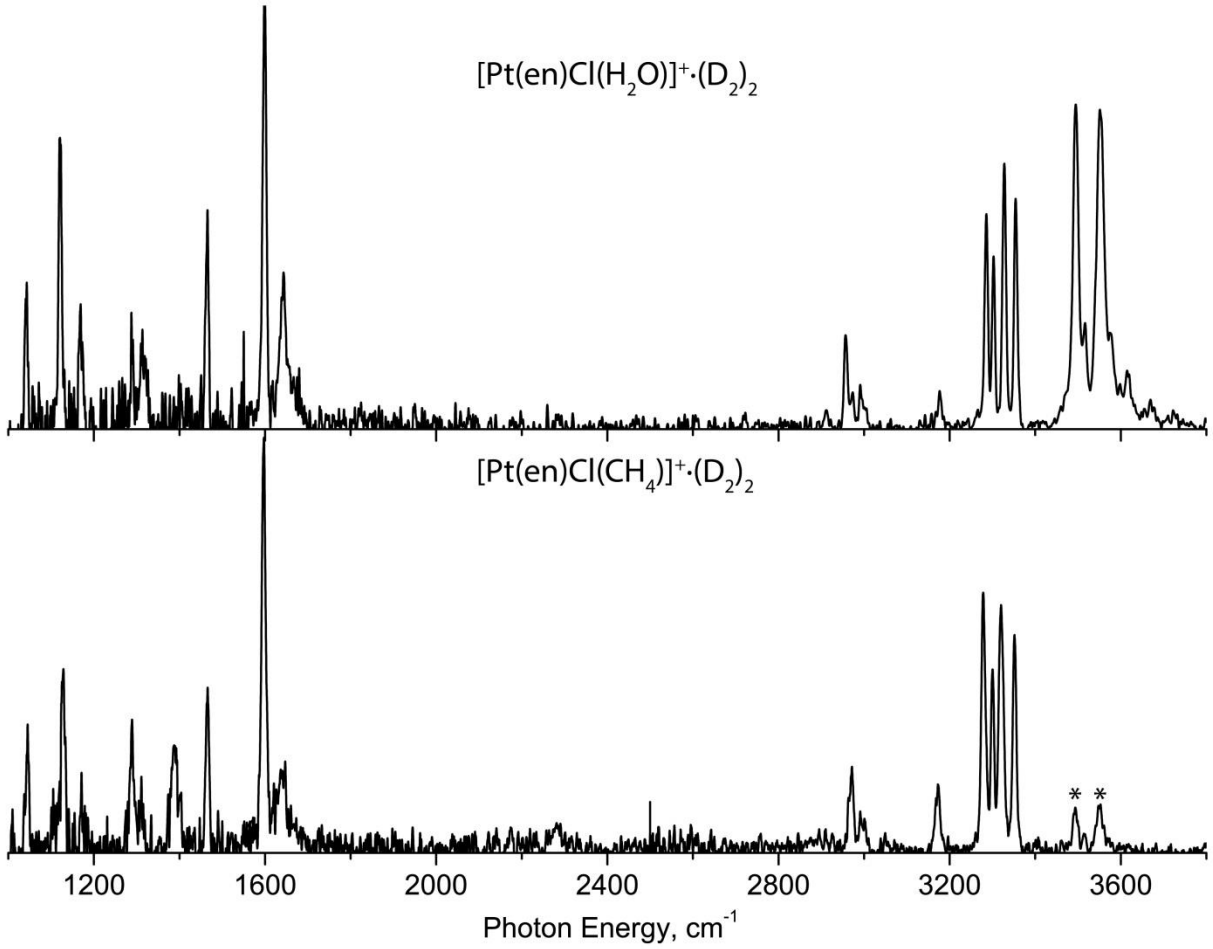

Figure 5.2- IRPD spectra of $[Pt(en)Cl(OH_2)]^+\cdot(D_2)_2$ (top) and $[Pt(en)Cl(CH_4)]^+\cdot(D_2)_2$ (bottom) complexes from 1000 cm^{-1} to 3800 cm^{-1}. The peaks marked with an asterisk (*) in the bottom panel are residual signal from the $[Pt(en)Cl(OH_2)]^+\cdot(D_2)_2$ complex.

The spectrum of $[Pt(en)Cl(OH_2)]^+ \cdot (D_2)_2$ is shown in Figure 5.3 (top) along with the calculated harmonic spectrum (bottom). The intense features are assigned as the symmetric and asymmetric O-H stretching modes of the water. The overestimated red-shift of the O-H frequencies arises from errors in the calculation of the O-H$\cdots$$D_2$ interaction.[24-27] The four features between 3200 cm^{-1} and 3500 cm^{-1} are assigned as combinations of the symmetric and asymmetric N-H stretching modes while the lower features around 2957 cm^{-1} are assigned as the D_2 stretch and C-H stretches. The feature at 3177 cm^{-1} is not observed in the calculated spectrum. This peak may be an overtone of the intense feature observed at 1590 cm^{-1} in the lower energy region.

The peak observed at 1640 cm^{-1} is assigned as the H_2O bend while the feature at 1590 cm^{-1} is assigned as a combination of the NH_2 bends. The peak at 1464 cm^{-1} is assigned to the CH_2 bending modes of the ethylenediamine ligand. The peaks observed at 1311 cm^{-1} correspond to combinations of CH_2 and NH_2 wagging modes. The intense feature at 1129 cm^{-1} is assigned to the C-N stretches of the ethylenediammine ligand while the feature at 1043 cm^{-1} is assigned as the C-C stretching vibration.

Before assigning the $[Pt(en)Cl(CH_4)]^+ \cdot (D_2)_2$ it is beneficial to consider the relative energies of the intermediates and the heights of the barriers involved along the reaction pathway. The calculated potential energy surface of the gas phase reaction is shown in Figure 5.4. The pathways corresponding to the metathesis and oxidative addition pathways are shown in red and blue respectively. The σ-CH complex is the most stable species on the surface by over 3000 cm^{-1}. The barrier to transition between the σ-CH complex and the oxidative addition complex is 4677 cm^{-1} while the barrier to convert between the σ-CH and metathesis species is significantly higher at 6573 cm^{-1}. Despite the nearly 2000 cm^{-1} difference in barrier heights the σ-CH-

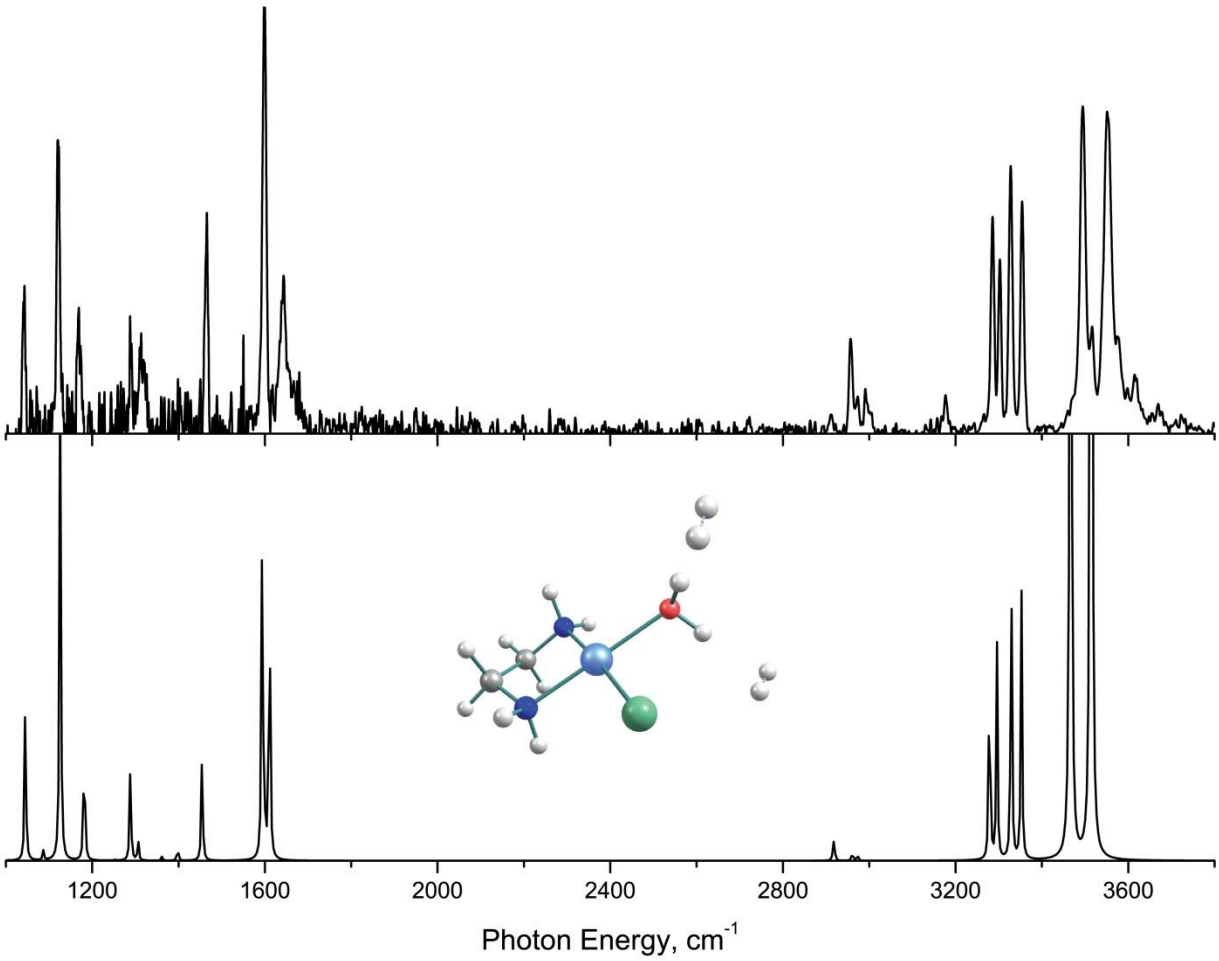

Figure 5.3- Experimental (top) and calculated (bottom) spectra for $[Pt(en)Cl(OH_2)]^+ \cdot (D_2)_2$.

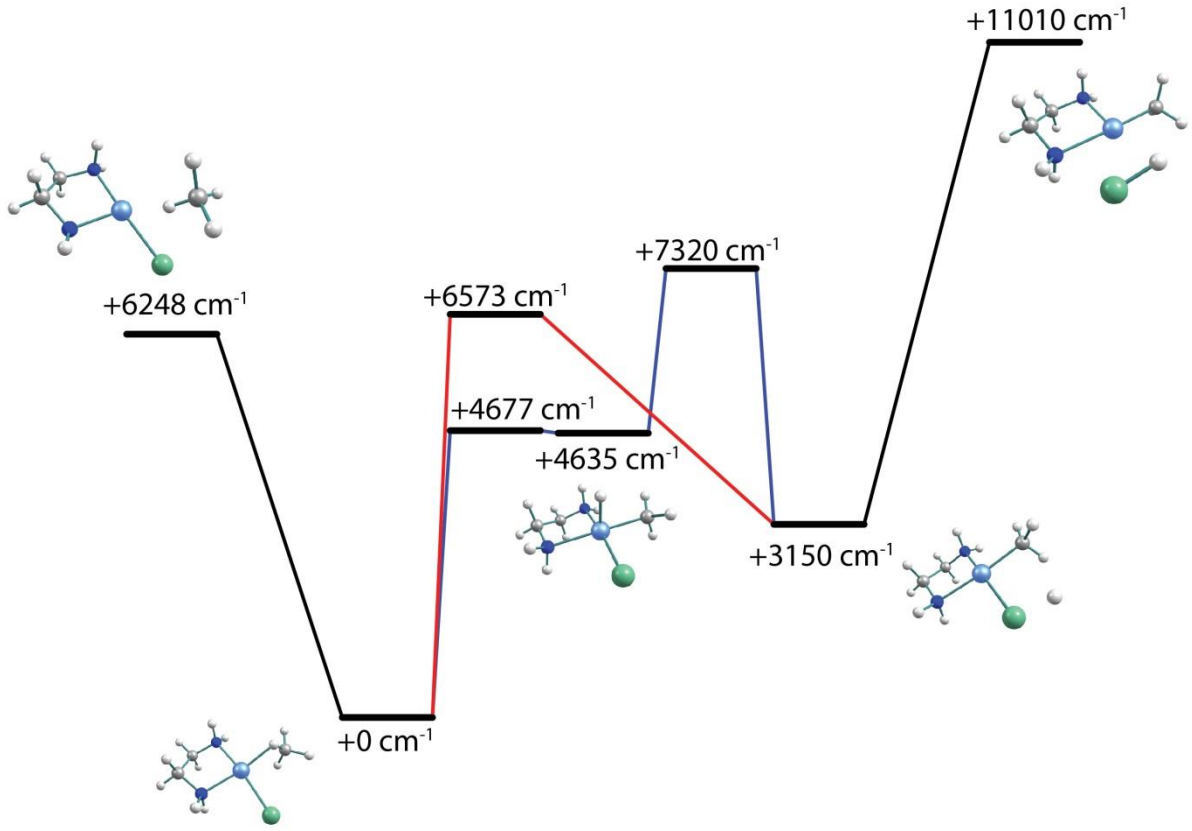

Figure 5.4- Potential energy surface for the reaction of $[Pt(en)Cl]^+$ with methane. The σ-bond metathesis and oxidative addition pathways are shown above in red and blue respectively.

metathesis pathway may be preferred due to the additional ~2700 cm^{-1} barrier to convert from the oxidative addition to the metathesis. At the temperature of the experiment (80 K) the σ-CH and oxidative addition intermediates have an internal energy of 256 cm^{-1} while the metathesis species has an energy of 274 cm^{-1}. This suggests that interconversion between the σ-CH and oxidative addition species is unlikely under our conditions. However, it is worth noting that the small difference between the energy of the oxidative addition intermediate and the σ-CH-oxidative addition barrier (~40 cm^{-1}) means that any oxidative addition intermediate is likely to undergo conversion to the σ-CH complex in our experiment.

The spectrum of $[Pt(en)Cl(CH_4)]^+ \cdot (D_2)_2$ is shown in Figure 5.5 (A) along with the calculated spectra of the three intermediates discussed above (B-C). The first species, known as the σ-CH complex, is shown in panel B. This species consists of a methane molecule bound directly to the Pt metal center of the $[Pt(en)Cl(CH_4)]^+$ complex. This complex has distinct vibrations arising from the CH_4 molecule at 1630 cm^{-1}, 1390 cm^{-1}, and 1284 cm^{-1}. The activated C-H stretch motion is calculated to occur at 2361 cm^{-1}.

The oxidative addition intermediate is shown in panel C. This intermediate results from insertion of the metal center into the C-H bond of the methane. This structure gives rise to a distinctive Pt-H stretching motion at 2376 cm^{-1} as well as significant shifts in peak position and intensity in the region from 1000 cm^{-1} to 1200 cm^{-1}. The N-H vibrations are more shifted from the water complex in this species than in the σ-CH complex.

The final species is the σ-bond metathesis product. As shown in figure 5.4. This species can be formed by either direct cleavage of the activated C-H bond or through the intermediate oxidative addition state. In this complex a distinct vibration is calculated to appear at 2698 cm^{-1}

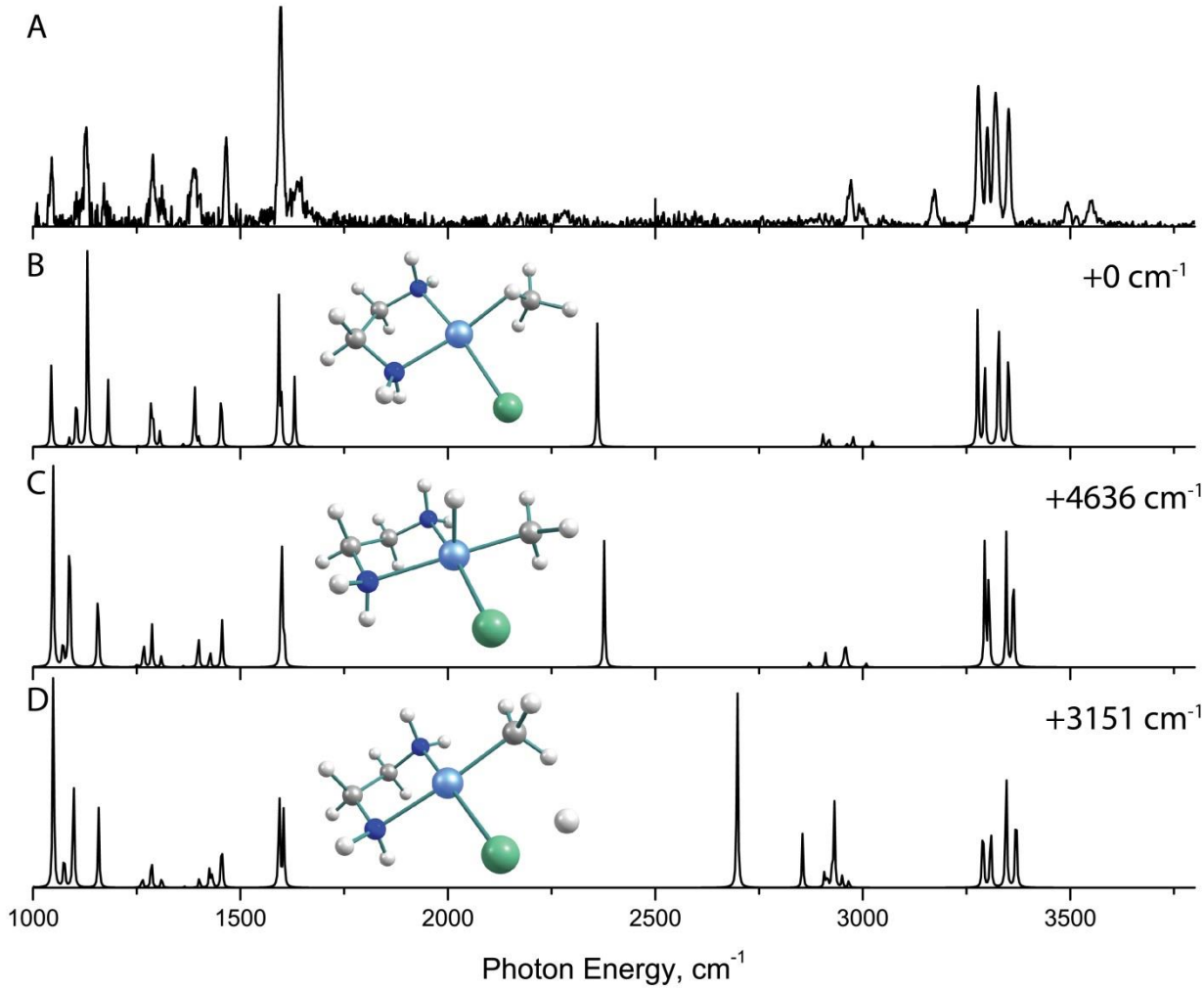

Figure 5.5- Experimental (A) and calculated spectra (B-D) for $[Pt(en)Cl(CH_4)]^+$. The energies displayed are referenced to the species in panel B.

due to the H-Cl bond that is formed. The spectrum from 1000 cm^{-1} to 1200 cm^{-1} is similar to that of the oxidative addition complex discussed previously.

Surprisingly, no intense features are observed in 2000 cm^{-1}-2800 cm^{-1} region. This lack of features could arise from the anharmonic nature of the peaks expected in this region. While the Pt-H and H-Cl vibrational modes are likely relatively harmonic in their behavior, the σ-CH vibrational mode may display significant deviations from the calculations due to anharmonic effects. The mode, which is redshifted over 600 cm^{-1} from the C-H stretches in free methane, is likely susceptible to coupling with combination bands and overtones which lie near the fundamental band. This would lead to peak broadening which decreases the observed intensity of the feature.

In contrast to the 2000 cm^{-1}-2800 cm^{-1} region the 1000 cm^{-1}-1700 cm^{-1} region contains many peaks which are indicative of the species present. This region is displayed along with the calculated spectra for each species in Figure 5.6. In this region the spectra of the oxidative addition (C) and sigma bond metathesis (D) species are quite similar whereas the σ-CH complex displays a similar spectrum to the water complex assigned earlier. The excellent fit of the σ-CH complex spectrum indicates that this species is present in the spectrum. This is supported by the presence of features at 1640 cm^{-1} (methane deformation) and 1127 cm^{-1} (methane bend) which are present only in the σ-CH complex due to the methane being relatively unperturbed. Furthermore, the while activity is predicted around 1390 cm^{-1} for each species, the activity is best reproduced in position and intensity in the σ–CH complex spectrum. The lack

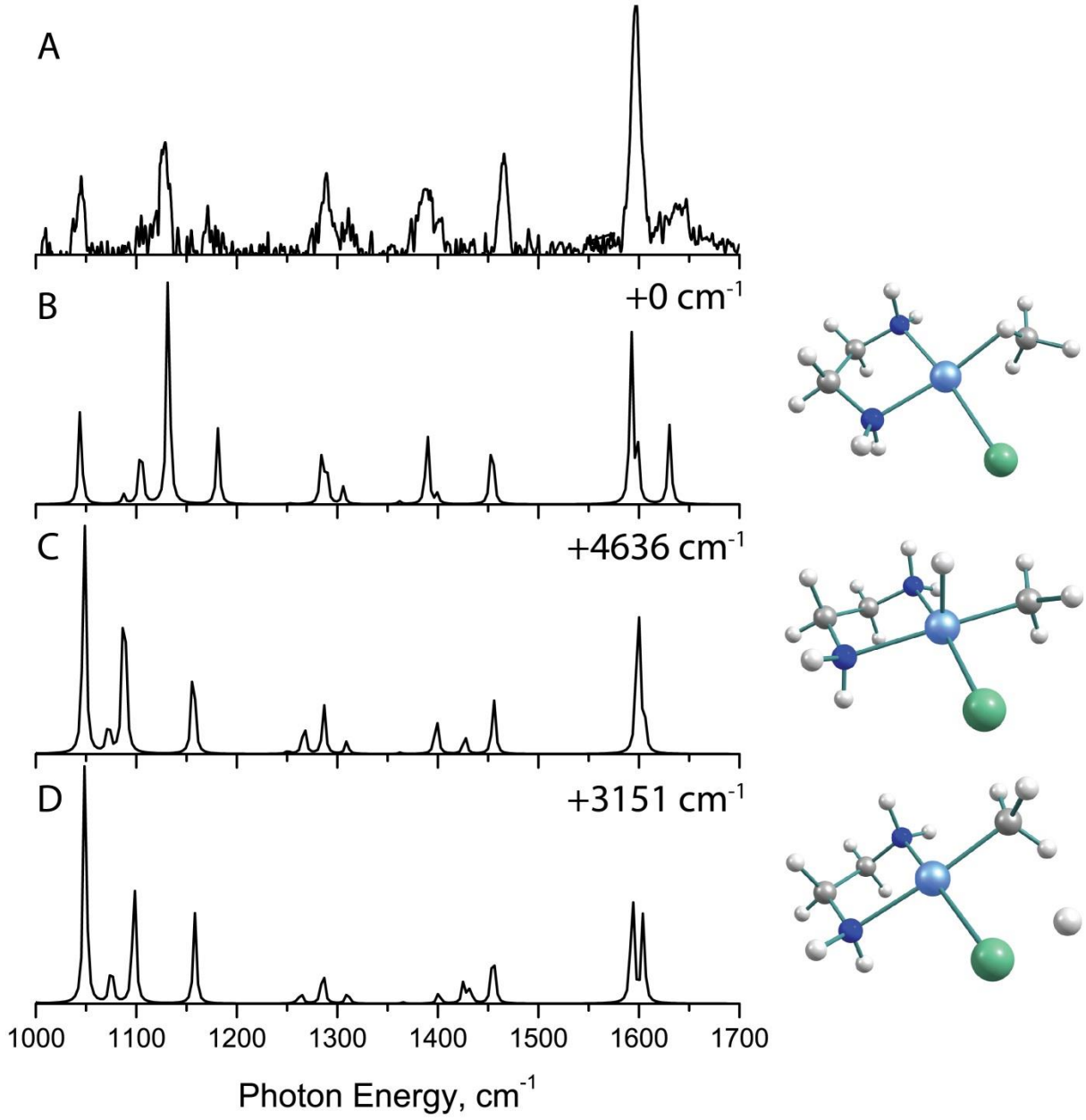

Figure 5.6- Experimental (A) and calculated spectra (B-D) of $[Pt(en)Cl(CH_4)]^+$ in the region from 1000 cm^{-1} to 1700 cm^{-1}.

of a satellite peak to the red of the 1289 cm^{-1} feature is another piece of evidence supporting the assignment of the σ–CH complex to this spectrum. Furthermore, the relative stability of the complex compared to the other species as well as the somewhat high barriers to convert to these species support this assignment as well.

With the species present in the spectrum assigned we can now assign the peaks present in the spectrum. Similar to the H_2O spectrum the lowest feature at 1043 cm^{-1} is assigned to the C-C stretching vibration of the ethylenediamine ligand. The peak at 1128 cm^{-1} is attributed to the C-N stretches. The 1288 cm^{-1} contains contributions from the CH and NH wags as well as methane bending vibrations. The 1389 cm^{-1} peak arises from a deformation mode of the methane ligand. The feature at 1465 cm^{-1} is composed of CH_2 bending motions with some contribution from the methane ligand. The intense feature at 1590 cm^{-1} is, as in the water spectrum, due to the NH_2 bending vibrations. The final peak, consisting of a broad feature around 1640 cm^{-1}, is due to a methane deformation mode that involves the activated C-H bond. While this feature is roughly the same frequency as the H_2O bending motion the calculations do suggest the presence of the methane deformation is to be expected here.

5.1.5 Conclusions

In this work the reaction of methane and the Pt complex $[Pt(en)Cl]^+$ is considered. The complex $[Pt(en)Cl(CH_4)]^+$ is generated by the reaction of methane and the ionic complex at 80 K in the conditions of a mass spectrometer. The complex is characterized by infrared spectroscopy and compared to the spectrum of the $[Pt(en)Cl(H_2O)]^+$ complex. The methane complex showed little change in peak positions and intensities related to the ethylenediamine backbone compared to the water complex but did show additional bands arising from the vibrational modes of the

methane molecule. Analysis of the calculated potential energy surface for the reaction indicates that the most likely outcome of the reaction is the formation of the σ-CH. Comparison of the experimental data with DFT calculations shows that we have indeed obtained the σ-CH complex. Furthermore, there is no evidence of the oxidative addition or metathesis intermediates in the spectrum presented. Intriguingly, while the calculated spectrum for the σ-CH complex shows excellent agreement in the range from 1000 cm^{-1}-1700 cm^{-1} and 2900 cm^{-1}-3800 cm^{-1} the activated C-H stretching frequency is not observed in the region from 2000 cm^{-1}-2500 cm^{-1}.

References:

1. A. E. Shilov and G. B. Shul'pin, *Chemical Reviews*, 1997, **97**, 2879-2932.

2. J. A. Labinger and J. E. Bercaw, *Nature*, 2002, **417**, 507-514.

3. K. J. H. Young, S. K. Meier, J. M. Gonzales, J. Oxgaard, W. A. Goddard and R. A. Periana, *Organometallics*, 2006, **25**, 4734-4737.

4. B. G. Hashiguchi, S. M. Bischof, M. M. Konnick and R. A. Periana, *Accounts of Chemical Research*, 2012, **45**, 885-898.

5. M. Lin, C. Shen, E. A. Garcia-Zayas and A. Sen, *Journal of the American Chemical Society*, 2001, **123**, 1000-1001.

6. J. L. Garnett and R. J. Hodges, *Journal of the American Chemical Society*, 1967, **89**, 4546-4547.

7. J. A. Labinger and J. E. Bercaw, *Journal of Organometallic Chemistry*, 2015, **793**, 47-53.

8. S. S. Stahl, J. A. Labinger and J. E. Bercaw, *Journal of the American Chemical Society*, 1996, **118**, 5961-5976.

9. G. Gerdes and P. Chen, *Organometallics*, 2003, **22**, 2217-2225.

10. B. Butschke and H. Schwarz, *Organometallics*, 2011, **30**, 1588-1598.

11. L. Johansson, M. Tilset, J. A. Labinger and J. E. Bercaw, *Journal of the American Chemical Society*, 2000, **122**, 10846-10855.

12. H. Heiberg, O. Swang, O. B. Ryan and O. Gropen, *The Journal of Physical Chemistry A*, 1999, **103**, 10004-10008.

13. S. S. Stahl, J. A. Labinger and J. E. Bercaw, *Angewandte Chemie International Edition*, 1998, **37**, 2180-2192.

14. W. H. Bernskoetter, C. K. Schauer, K. I. Goldberg and M. Brookhart, *Science*, 2009, **326**, 553-556.

15. S. D. Pike, A. L. Thompson, A. G. Algarra, D. C. Apperley, S. A. Macgregor and A. S. Weller, *Science*, 2012, **337**, 1648-1651.

16. J. A. Calladine, S. B. Duckett, M. W. George, S. L. Matthews, R. N. Perutz, O. Torres and K. Q. Vuong, *Journal of the American Chemical Society*, 2011, **133**, 2303-2310.

17. U. Mazurek and H. Schwarz, *Chemical Communications*, 2003, DOI: 10.1039/B211850E, 1321-1326.

18. D. Schröder and H. Schwarz, *Angewandte Chemie International Edition in English*, 1995, **34**, 1973-1995.

19. J. Roithová and D. Schröder, *Chemical Reviews*, 2010, **110**, 1170-1211.

20. G. Altinay, A. Kocak, J. Silva Daluz and R. B. Metz, *The Journal of Chemical Physics*, 2011, **135**, 084311.

21. G. Altinay and R. Metz, *J. Am. Soc. Spectrom.*, 2010, **21**, 750-757.

22. P. B. Armentrout, L. Parke, C. Hinton and M. Citir, *ChemPlusChem*, 2013, **78**, 1157-1173.

23. B. M. Marsh, J. M. Voss and E. Garand, *The Journal of Chemical Physics*, 2015, **143**, 204201.

24. B. M. Marsh, J. Zhou and E. Garand, *Physical Chemistry Chemical Physics*, 2015, DOI: 10.1039/C5CP01522G.

25. B. M. Marsh, J. Zhou and E. Garand, *The Journal of Physical Chemistry A*, 2014, **118**, 2063-2071.

26. E. M. Duffy, B. M. Marsh and E. Garand, *The Journal of Physical Chemistry A*, 2015, DOI: 10.1021/acs.jpca.5b04778.

27. A. Masson, E. R. Williams and T. R. Rizzo, *The Journal of Chemical Physics*, 2015, **143**, 104313.

Chapter 6: Future Directions

The work presented within this thesis is only the foundation of what is likely to be several fruitful projects. This section details some thoughts about possible projects building upon this foundation as well as some preliminary data. Some of these ideas have already demonstrated promise, some have a reasonable chance of success based on the work of others, and some are at this point only loose ideas. At any rate they provide a small sample of the sort of work which could be

Within the umbrella of C-H activation further exploration of the Pt-CH_4 reaction is warranted to capture the additional postulated intermediates. The effect of solvation on the reaction has also been debated and thus is worth investigating as well.[1, 2] We are particularly well suited to study such a system due to our unique abilities to reproducibly produce large cluster ions in our machine.[3]Additionally, reactions of Pt complexes with other hydrocarbons, such as benzene, have been of interest to several groups.[2, 4, 5] Thus, the study of these species in a manner similar to the Pt-CH_4 reaction has potential to be a particularly impactful experiment. In figure 6.1 a preliminary spectrum of $[Pt(en)Cl(C_6H_6)]^+$ is shown from 2400 cm^{-1} to 3800 cm^{-1}. Finally, the use of isotopically labeled hydrocarbon species should be considered for all of the reactions discussed here in order to more definitively assign spectral features related to those hydrocarbons.

Another area of interest is the solvation of biological molecules. Although this is a commonly studied phenomenon the spectra of large solvated systems are often difficult to disentangle due to the overlap of ion and solvent bands in the hydride stretching region. Although isotopic labeling schemes can overcome this problem, at room temperature the exchange of hydrogen and deuterium atoms occurs rapidly, resulting in isotopic scrambling.[6]

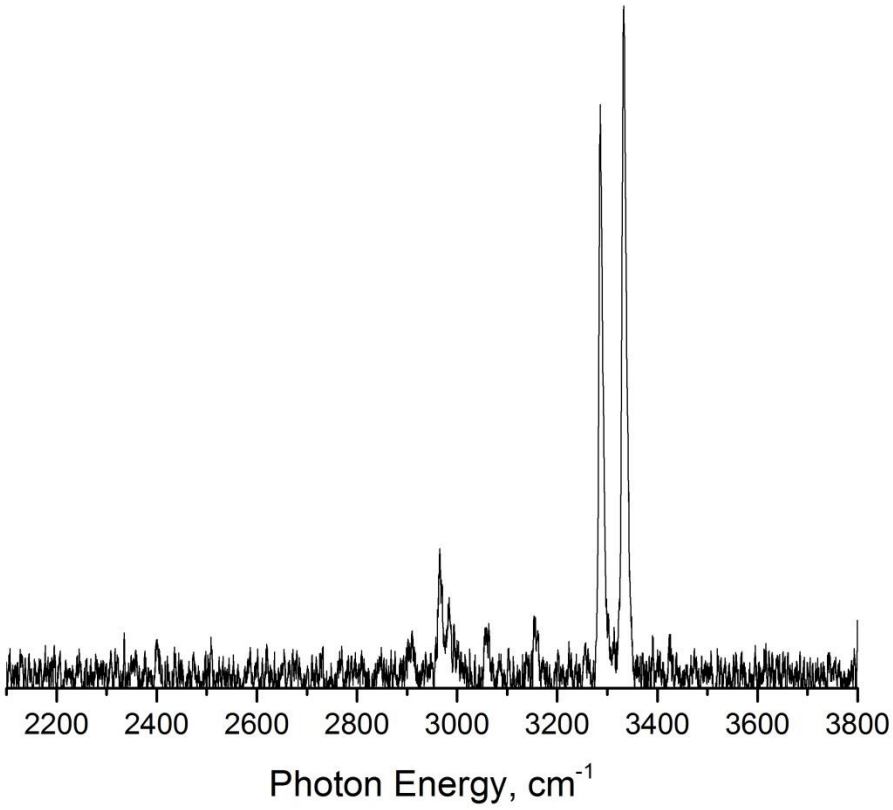

Figure 6.1- Spectrum of $[Pt(en)Cl(C_6H_6)]^+$.

Preliminary data from our lab (Figure 6.2) indicates that this exchange is largely suppressed at 80 K for a tetraglycine polypeptide. This allows for attachment of D_2O to the peptide without complicating the spectrum due to exchange. Comparison of $[Gly_4+H]^+ \cdot H_2O$ and $[Gly_4+H]^+ \cdot D_2O$ spectra (Figure 6.3) indicate that few if any peptide hydrogens are replaced with deuterium. This result holds for larger clusters as well. However, the results here have to be expanded to additionally systems to prove that this is a general technique. Additionally, investigation of the $H_2O/HOD/D_2O$ bending region of the spectrum could more conclusively prove the extent of H/D exchange in these systems. Still, this appears to be a promising way to isolate the solvent contributions from peptide contributions in these solvated species.

H/D exchange is also interesting in the context of C-H activation. H/D exchange has been performed on C-H bonds in reactions of carbanions and fluorophenyl anions.[7, 8] By seeding D_2O into the reaction mix used to generate the Pt-CH_4 complexes we may be able to observe the activated C-H bond directly. It is unclear if the barrier for H/D exchange would be favorable in this circumstance but if the reaction was observed it would provide additional details on the nature of this activated C-H bond.

An area that has been of interest to me recently is the creation of metals in unusual or high valent oxidation states. In most catalytic metal systems intermediate species are often postulated to exist in oxidation states which are uncommon or unstable in the condensed phase.[9, 10] In our work on $CuOH^+$ we observed formation of minor amounts of CuO^+, formally a Cu(III) species.[11] Additional studies by Armentrout and coworkers showed the generation of formally Cu(I) species is possible through collisional dissociation of $CuOH^+$.[12] This work, along with many other studies, suggests that the oxidation states of metal centers can be changed by gas phase collisions resulting in fragmentation. This opens up the possibility of isolating these

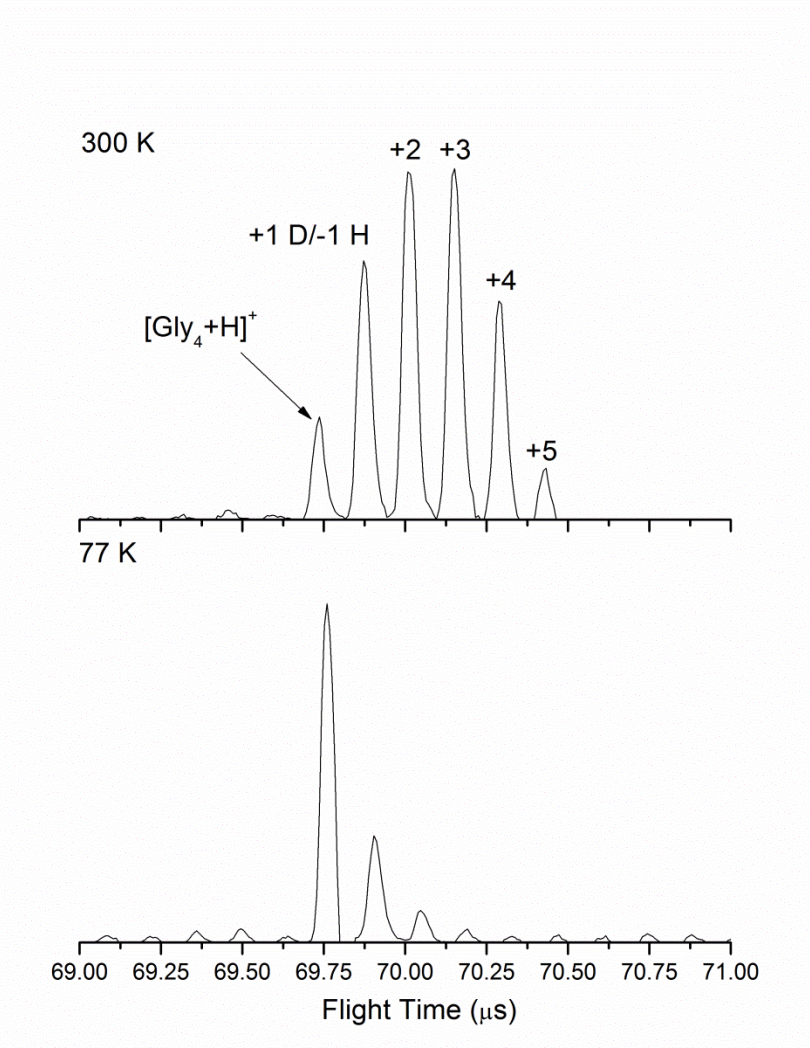

Figure 6.2- $[Gly_4+H]^+$ mass spectra in the presence of D_2O at 300 K (top) and 77 K (bottom) reaction trap temperatures. Note the suppression of H/D exchange at 77 K.

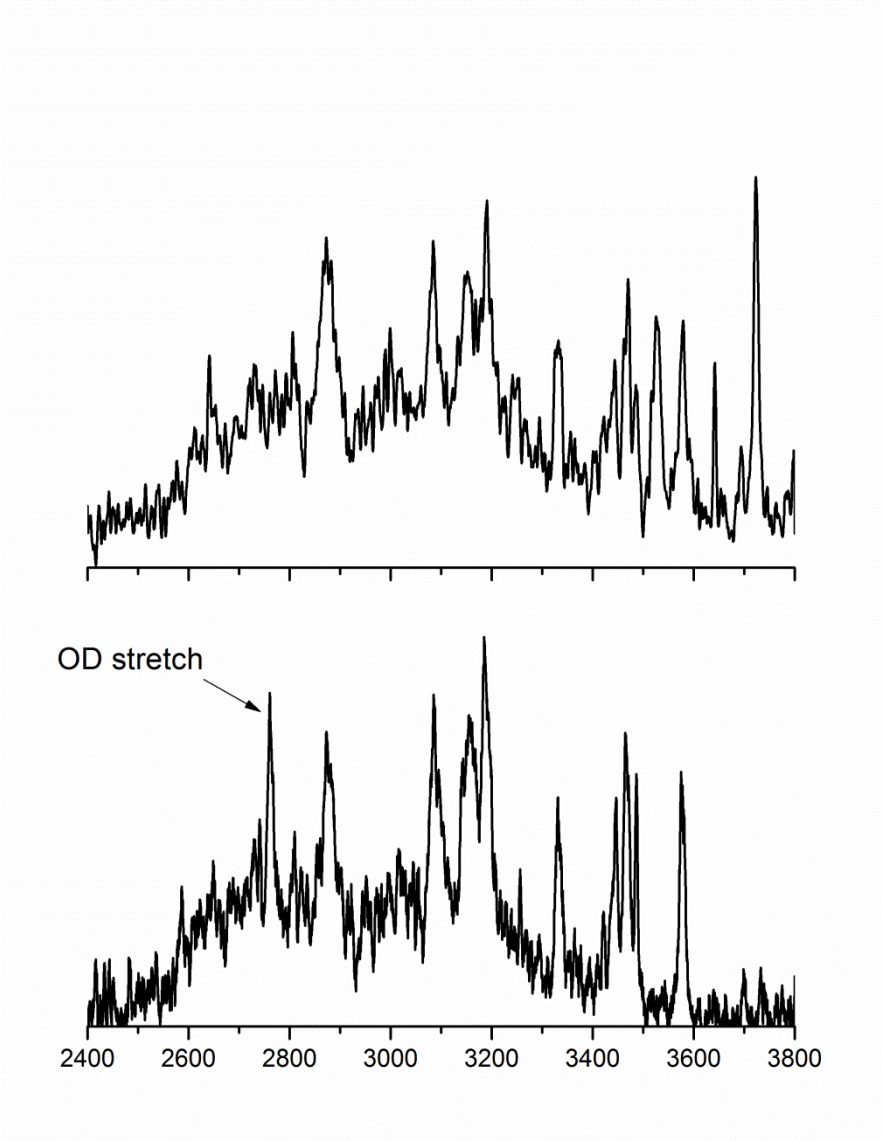

Figure 6.3- Spectra of $[Gly_4+H]^+ \cdot H_2O$ (top) and $[Gly_4+H]^+ \cdot D_2O$ (bottom). The most prominent O-D stretching feature is indicated in the bottom panel.

unusual states by fragmenting carefully designed complexes in the mass spectrometer. A thorough study of selected compounds could provide insight into systems which show promise for this work.

Photolysis of metal complexes can also generate unusual oxidation states as shown by Vohringer and coworkers.[13, 14] In this solution phase experiment an Fe(V) complex was generated by photolysis of an iron azide complex to release N_2. Although formally assigned as Fe(V), it is likely, as observed in our work on metal hydroxides, that there is significant charge transfer between the resulting nitride ligand and the Fe center. By fragmenting this complex photolytically in either the reaction trap region or main trap region of the spectrometer it would be possible to study this complex in isolation. This would allow for investigation of solvent effects and could give insight into the true nature of the iron center. It is also not difficult to imagine that other ligands and complexes could be used to generate oxo species such as the putative $Ru(V)=O^{2+}$ species implicated in water oxidation. Such a setup would require modification of the machine to accept UV/Vis radiation into either the main or reaction trap regions.

Finally, in perhaps the most esoteric piece of future work, the fragmentation pathways of species such as peptides could be investigated. It has been observed that UV photodissociation produced fragments of some peptide species differ from those produced by collisons with a buffer gas.[15, 16] By using UV/Vis photolysis as discussed in the above paragraph one could easily generate the photofragments while the collisional fragments can be generated in source. Characterizing the structures of these species could give insights into the processes that give rise to them.

References:

1. G. Gerdes and P. Chen, *Organometallics*, 2006, **25**, 809-811.

2. G. Gerdes and P. Chen, *Organometallics*, 2003, **22**, 2217-2225.

3. B. M. Marsh, J. M. Voss and E. Garand, *The Journal of Chemical Physics*, 2015, **143**, 204201.

4. L. Johansson, M. Tilset, J. A. Labinger and J. E. Bercaw, *Journal of the American Chemical Society*, 2000, **122**, 10846-10855.

5. B. Butschke and H. Schwarz, *Organometallics*, 2011, **30**, 1588-1598.

6. M. E. Hemling, J. J. Conboy, M. F. Bean, M. Mentzer and S. A. Carr, *J. Am. Soc. Spectrom.*, 1994, **5**, 434-442.

7. S. Kato, C. H. DePuy, S. Gronert and V. M. Bierbaum, *J. Am. Soc. Spectrom.*, 1999, **10**, 840-847.

8. J. H. Stewart, R. H. Shapiro, C. H. DePuy and V. M. Bierbaum, *Journal of the American Chemical Society*, 1977, **99**, 7650-7653.

9. M.-T. Zhang, Z. Chen, P. Kang and T. J. Meyer, *Journal of the American Chemical Society*, 2013, **135**, 2048-2051.

10. J. L. Fillol, Z. Codolà, I. Garcia-Bosch, L. Gómez, J. J. Pla and M. Costas, *Nat Chem*, 2011, **3**, 807-813.

11. B. M. Marsh, J. Zhou and E. Garand, *The Journal of Physical Chemistry A*, 2014, **118**, 2063-2071.

12. A. F. Sweeney and P. B. Armentrout, *Journal of Physical Chemistry A*, 2014, **118**, 10210-10222.

13. H. Vennekate, D. Schwarzer, J. Torres-Alacan and P. Vöhringer, *Journal of the American Chemical Society*, 2014, **136**, 10095-10103.

14. J. Torres-Alacan, U. Das, A. C. Filippou and P. Vöhringer, *Angewandte Chemie International Edition*, 2013, **52**, 12833-12837.

15. N. L. Burke, J. G. Redwine, J. C. Dean, S. A. McLuckey and T. S. Zwier, *International Journal of Mass Spectrometry*, 2015, **378**, 196-205.

16. J. C. Dean, N. L. Burke, J. R. Hopkins, J. G. Redwine, P. V. Ramachandran, S. A. McLuckey and T. S. Zwier, *The Journal of Physical Chemistry A*, 2015, **119**, 1917-1932.